AD-A188 348 DYNAMICS OF THE OCEANIC SURFACE MIXED LAYER PROCEEDINGS 1/4
OF 'AHA HULIKO'A (U) HAWAII INST OF GEOPHYSICS
HONOLULU P MULLER ET AL 1987 N00014-87-G-0091
UNCLASSIFIED F/G 8/3 NL

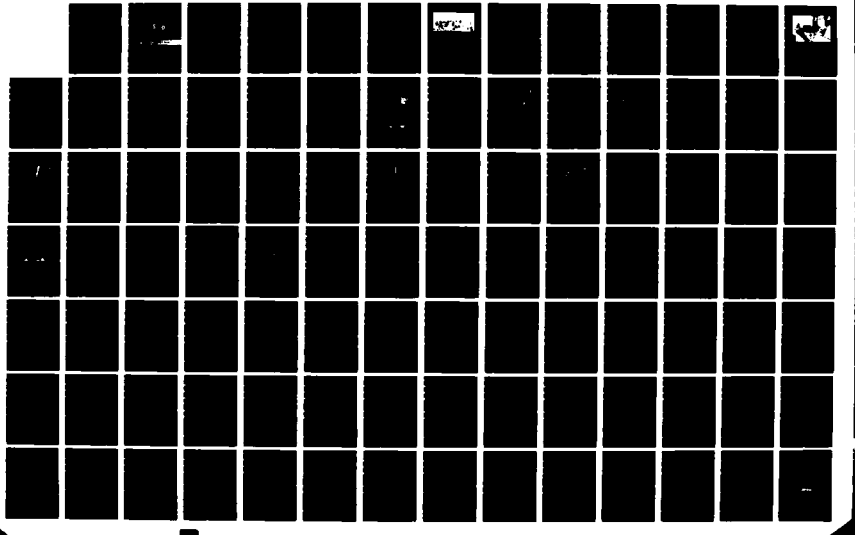

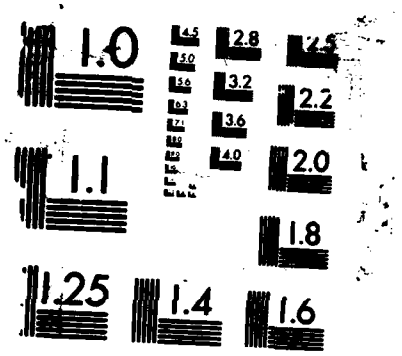

MICROCOPY RESOLUTION TEST CHART

'Aha Huliko'a

DYNAMICS OF THE OCEANIC SURFACE MIXED LAYER

Proceedings
Hawaiian Winter Workshop
University of Hawaii at Manoa
January 14-16, 1987

87 11 10 144

Dynamics of the Oceanic Surface Mixed Layer

PETER MULLER
DIANE HENDERSON
editors

PROCEEDINGS
'Aha Huliko'a
Hawaiian Winter Workshop
University of Hawaii at Manoa
January 14–16, 1987

Sponsored by the U.S. Office of Naval Research,
the Hawaii Institute of Geophysics,
and the Department of Oceanography, University of Hawaii

Hawaii Institute of Geophysics Special Publication • 1987

Cover: Nancy Hulbirt, Brooks Bays

FOREWORD

The fourth 'Aha Huliko'a Hawaiian Winter Workshop was held from January 14 to 16, 1987 to study "Dynamics of the Oceanic Surface Mixed Layer." ('Aha Huliko'a is a Hawaiian phrase meaning an assembly that seeks into the depth of a matter and describes it fully.) The participants were tasked to evalute recent developments and to offer suggestions for future research. Their lectures are published in these proceedings, as submitted in camera-ready form by the authors. The order of papers loosely follows the agenda of the workshop, covering observations, theory, modeling, and monitoring. Also included are reviews of the atmospheric turbulent boundary layer and of global biogeochemical mixed-layer fluxes.

The workshop, made possible by a grant from the U.S. Office of Naval Research, was hosted by the Hawaii Institute of Geophysics and the Department of Oceanography of the University of Hawaii. The excellent facilities of the East-West Center and the capable staff directed by James McMahon contributed greatly to the success of the meeting. The local organization and logistical arrangements were made by Karynne Chong Morgan. The following articles are the work of the creative and dedicated scientists who gathered in Hawaii this year.

Peter Muller
Diane Henderson
Editors

Department of Oceanography
Hawaii Institute of Geophysics
University of Hawaii
Honolulu, HI 96822

This work is related to Department of the Navy Grant N-00014-87-G0091 issued by the Office of Naval Research. The U.S. Government has a royalty-free license throughout the world in all copyrightable material contained herein.

Participants, 'Aha Huliko'a 1987

Back row: James Price, Federico Graef-Ziehl, Niklas Schneider, Thomas Spence, Gerbrand Komen, Chris Fairall, Pierre Flament, Peter Muller, Charles Eriksen, Frank Henyey, Benoit Cushman-Roisin, Eric Lindstrom.

Front row: Jerry Smith, Robert Pinkel, Michael Gregg, Hartmut Peters, Roland Garwood, Eric D'Asaro, William Large, Thomas Dillon, Roger Lukas.

Not present for photograph: Eric Firing, Catherine Gautier, Fred Mackenzie.

TABLE OF CONTENTS

STRUCTURES AND FLUXES IN A DEEP CONVECTING MIXED LAYER

M.C. Gregg

Applied Physics Laboratory and School of Oceanography, College of Ocean and Fishery Sciences, University of Washington, Seattle, Washington 98105

ABSTRACT

A sequence of microstructure profiles observed a strongly convecting mixed layer deepen from 25 m to over 140 m in two days. Dissipation rates and overturning scales reveal mixing rates and mechanisms in the layer and in the entrainment zone below. Preliminary analysis shows the strong role of convection and of entrainment.

INTRODUCTION

Mixed layer modeling appears to have reached an impasse, owing to an inability to test key assumptions. Comparisons with observations are usually limited to the bulk response of the upper ocean, such as the rate of deepening and budgets of heat and salt. These tests are inconclusive because different dynamical assumptions can produce similar bulk responses.

Two decades of extensive turbulence observations in the lower atmosphere have produced a much better foundation for modeling the planetary boundary layer. A similar interaction between observations and modeling of oceanic mixed layers has yet to begin. Although direct flux measurements are still lacking, turbulence observations in the upper ocean can be used to define important aspects of mixed layer dynamics and to improve the testing of models. Presently dissipation rates and overturning scales are the most reliable results and afford tests of similarity scaling, bulk energetics, and the parameterization of entrainment.

Convectively driven mixed layers are a high priority for study; they are the deepest layers and are presumably important agents ventilating the thermocline. Hoping to observe strong convection, we made shear and microstructure observations from the USNS BARTLETT off New England in January 1983. To obtain maximum surface heat fluxes, we chose a time when cold-air outbreaks are common; the measurements were taken in warm-core ring 82-I to enhance the air-sea temperature contrast. The turbulence measurements were made with the Advanced Microstructure Profiler (AMP).

Good fortune prevailed and a strong outbreak began on 18 January, following a strong storm. The outbreak was not immediately recognized, however, and a radial section was begun after AMP burst 19, when the mixed layer was 25 m deep. Regular observations of the convectively driven deepening began near the center of the ring on the 19th, with burst 26, which found the mixed layer base at 68 m. Owing to air temperatures slightly below

0°C, the 12°C mixed layer deepened from less than 25 m to over 140 m, mostly in two days (Fig. 1).

Sea smoke and snow accompanied the freezing temperatures, making memorable conditions on deck (Fig. 2). Exposure suits and ski masks provided protection, but we had not anticipated the difficulty of looking into snow coming at more than 30 knots. Fortunately, grinding goggles borrowed from the tool box provided some relief. While on deck during the rough weather, we wore harnesses attached to the ship with carabiners, as the chance of recovering someone over the side was nil.

The elation of the scientific party at witnessing the dramatic deepening wasn't shared by the crew, especially because the ship was usually laid over in the trough for AMP profiling. Average rolls were 20° and many peaks were twice that. Revenge came from the galley. In true Navy style, linen tablecloths were used, even in storms, requiring that they be watered before each meal to help hold down the plates. Although the covering of other tables was changed daily, the same cloth was kept on the scientists' table for 10 days. Watering before every meal and folding between meals soon produced rapidly growing colonies of black mold racing to claim the most real estate. Comparing growth rates from one meal to the next was our major diversion from a menu that culminated in spicy tripe the last night at sea.

Large, uniform dissipation rates were the most obvious feature of these deep convecting layers (Shay and Gregg, 1984 and 1986). Below the near-surface zone, ε followed the same similarity scaling as in convecting atmospheric boundary layers, i.e, $\bar{\varepsilon} \approx 0.6 J_b^0$, where J_b^0 is the surface buoyancy flux (Fig. 3). The dissipation rate dropped abruptly in the transition zone at the base of the layer, usually by several decades.

We are now examining the bulk energetics and the regions above and below the convectively dominated region, i.e., the near-surface zone of the mixed layer and the entrainment zone at its base. Preliminary results about three aspects are discussed, using data from bursts 19, 26, 30, and 32, which contained 5, 13, 8, and 9 drops, respectively. First, the extraordinary rate of deepening is compared with estimates of bulk changes in the potential energy and with the work done by the wind stress and by the buoyancy flux. Second, the very high dissipation rates found above 0.3 MPa are compared with previous measurements in mixed layers. Occurring above the convectively dominated regime considered by Shay and Gregg, these intense structures establish the integrated dissipation rates for the layers and are thus important to the overall energetics. Third, overturning scales, ε, and χ are examined in the transition zone, which is a sensitive region in models.

THE BULK RESPONSE

E_{10} was 2 W m^{-2} or less during the outbreak, compared with peaks of 13.5 W m^{-2} during the storm (Fig. 4). ($E_{10} \equiv \tau U_{10}$, where U_{10} is the wind velocity 10 m above the surface and τ is the wind stress.) During the outbreak the net work done by the wind was $\int E_{10} dt \approx 0.2$ MJ m^{-2}, about one third of that done in less than a day by the storm.

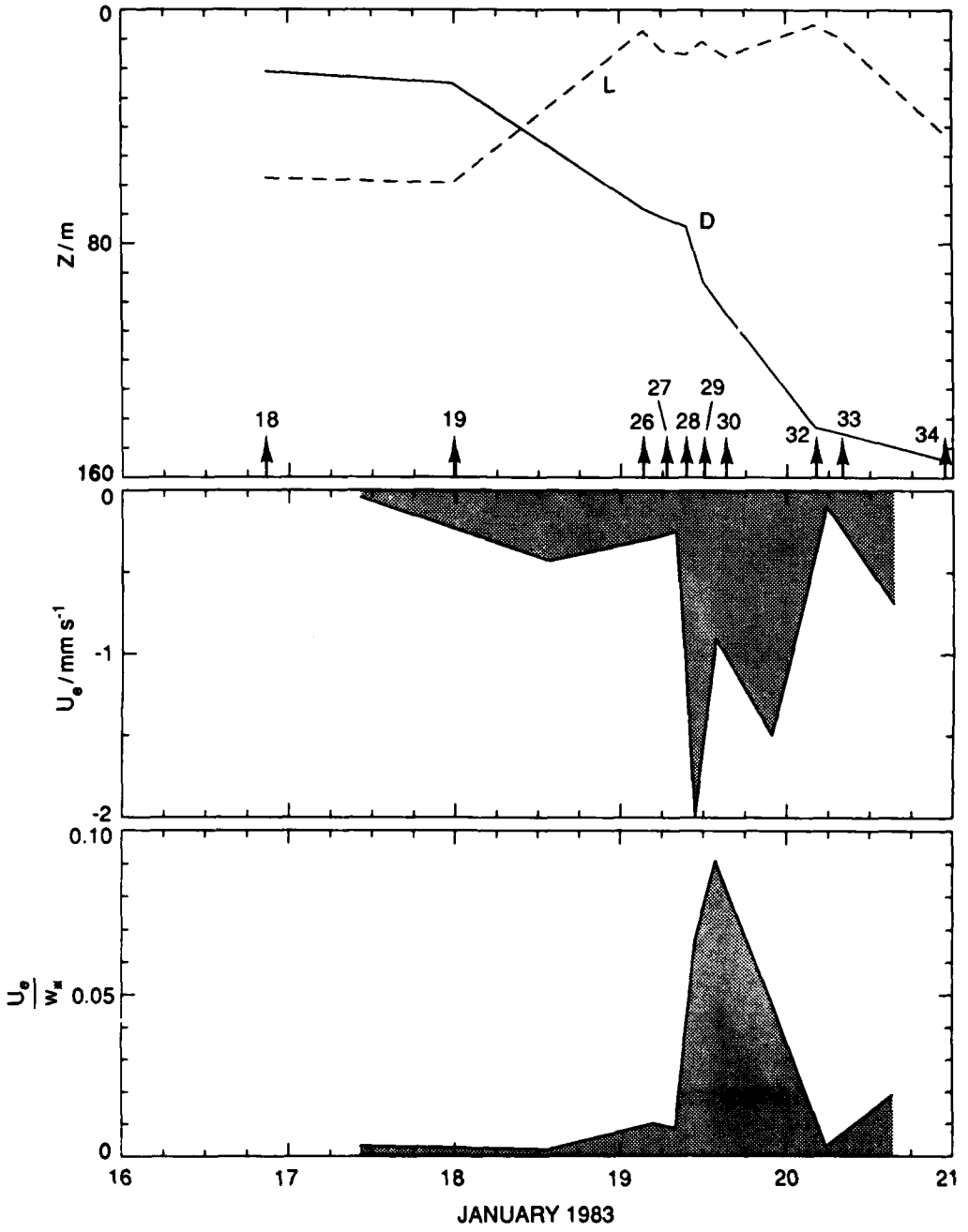

Fig. 1. Mixed layer deepening during the cold air outbreak. Times of AMP bursts are marked by arrows on the top panel. Between bursts 19 and 26, the Monin-Obukhov length, L, became smaller than the mixed layer depth, D. The most rapid deepening occurred on the 19th, when U_e was between 1 and 2 mm s $^{-1}$. During the most rapid deepening, $U_e \approx 0.1\ w_*$ (bottom panel).

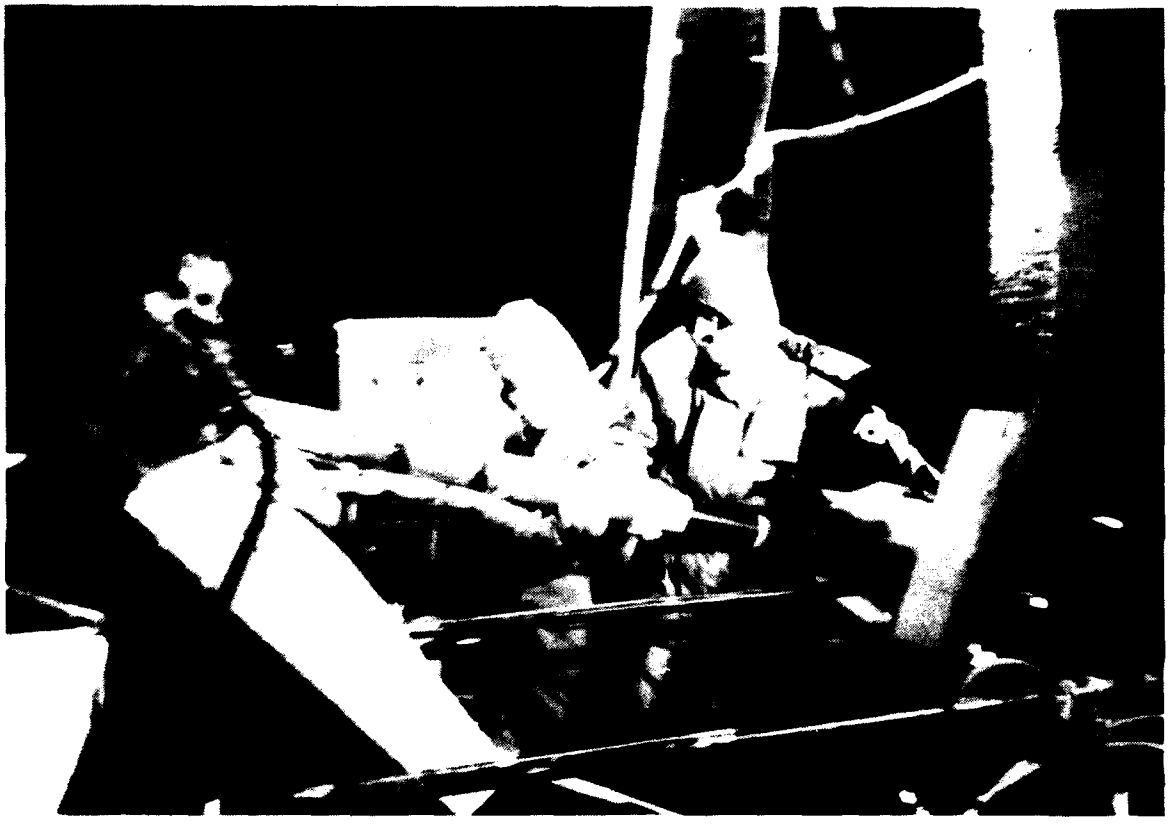

Fig. 2. Launching the AMP at night during the cold-air outbreak. Snow was coming in nearly horizontally from the left. Photo courtesy of Terry Joyce.

After the storm, J_b^0 dropped to 7×10^{-8} W kg^{-1} and then rose steadily to 3.6×10^{-7} W kg^{-1}. The latter corresponded to a heat flux of 1000 W m^{-2}. During the outbreak, the net density flux, $\int J_\rho^0\, dt = -\int (\rho/g)\, J_b^0 dt$, was approximately 5 kg m^{-2}, and the net heat flux was 8.6×10^7 J m^{-2}.

Although the storm produced little deepening, the outbreak caused a dramatic descent on the 18th and 19th, with D increasing from 25 m during burst 19 to 143 m during burst 32 (Fig. 1). The entrainment velocity, U_e, was less than 0.5 mm s^{-1} on 18 January but rose to 1 to 2 mm s^{-1} when the convection was most intense.

Similarity scaling of mixed layers is based on the assumption that turbulence is produced by wind stress and buoyancy flux acting on a profile with no background stratification. The corresponding velocity scales are $u_* \equiv \sqrt{\tau/\rho_w}$ and $w_* \equiv (DJ_b^0)^{1/3}$. The cube of their ratio, $(w_*/u_*)^3$, is a measure of the relative work done by the two processes. During the outbreak $u_* \approx 0.01$ m s^{-1}. As seen in Fig. 4, $(w_*/u_*)^3 \gg 1$ during the main deepening.

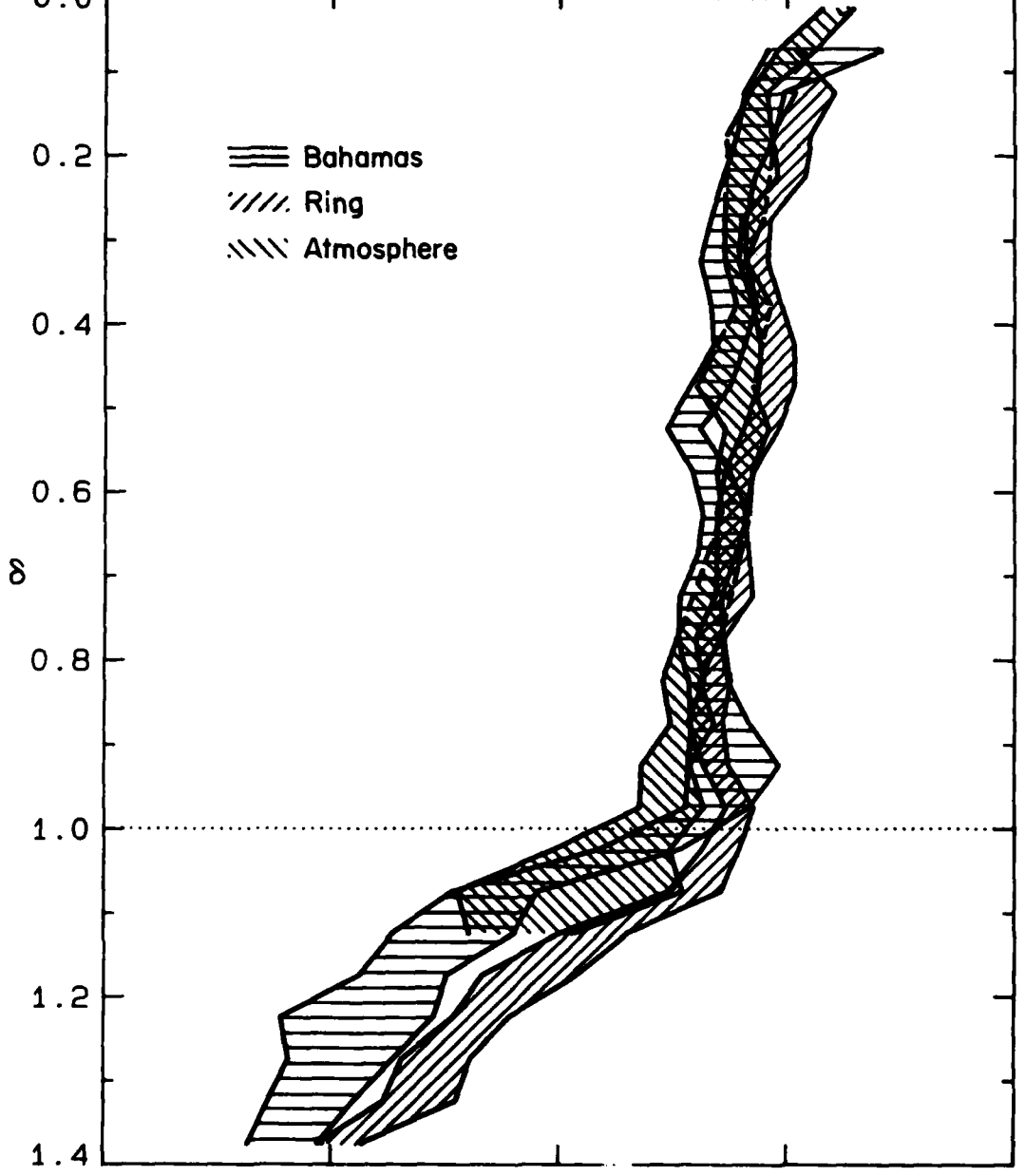

Fig. 3. Normalized dissipation rates, $\Psi \equiv \varepsilon/J_b^0$, as functions of normalized mixed layer depth, $\delta \equiv z/D$, in convectively driven surface layers. The Bahamas observations were made at night in a 100 m deep diurnal mixed layer, and the ring data are the ones being discussed in this paper. The oceanic observations show no significant differences from the atmospheric data. From Shay and Gregg, 1986.

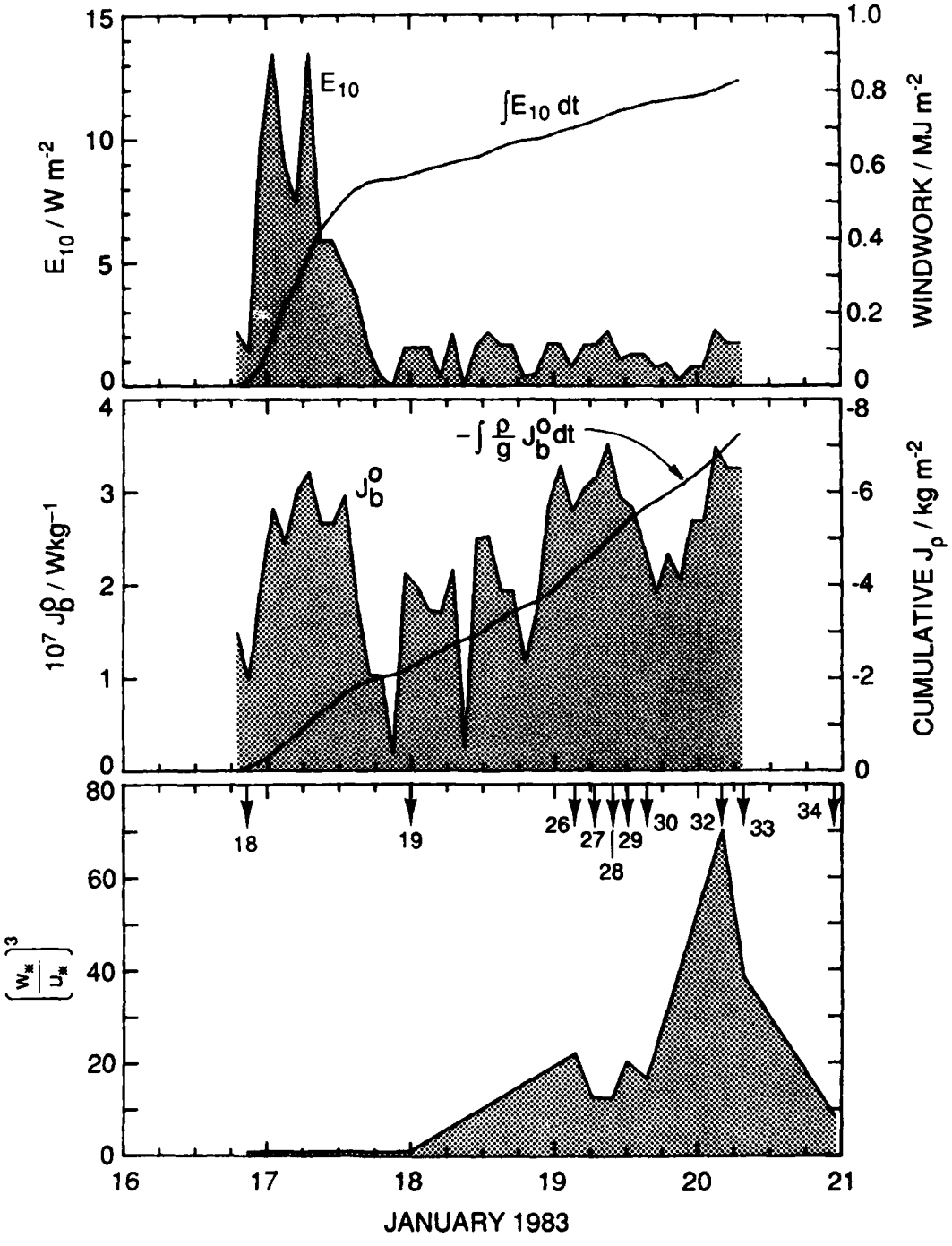

Fig. 4. Atmospheric forcing during the cold-air outbreak and the preceding storm. The storm ended on the 17th and the outbreak started on the 18th. Comparison with Fig. 1 reveals that the storm produced little deepening. The convectively driven deepening was most intense late on the 19th.

Asymptotic states of the similarity scaling describe turbulence produced only by wind stress, i.e., $J_b^0 = 0$, or only by convection, i.e., $\tau = 0$ (Wyngaard, 1983). In the former case a length scale is provided by the distance to the surface, yielding

$$\varepsilon = \frac{u_*^3}{\kappa z} \quad . \tag{1}$$

Thus dissipation should vary inversely with depth. By contrast, the purely convective case has no length scale, resulting in a uniform dissipation throughout the layer,

$$\varepsilon(z) = J_b^0 \quad . \tag{2}$$

Long observed in the atmosphere, the convective case has now been demonstrated in the ocean (Fig. 3).

The ratio of Eqs. (1) and (2) gives the depth at which the production mechanisms are equal. Known as the Monin-Obukhov length,

$$L \equiv \frac{u_*^3}{\kappa J_b^0} \quad [\mathrm{m}] \ , \tag{3}$$

where $\kappa = 0.41$ is Von Karman's constant and L is negative during convection. Convection is therefore dominant at depths greater than $|L|$. The mixed layer depth exceeded $|L|$ after burst 19 and increased to $D = 5\text{–}10\ L$ as the deepening proceeded (Fig. 1). Therefore, convection was dominant below 0.2 to 0.3 MPa.

During the outbreak, the mixed layer density increased 0.17 kg m^{-3} (Fig. 5). If the surface buoyancy flux and entrainment were solely responsible, the change from t_0 to t_1 would have been

$$\rho(t_1) = -\frac{1}{D(t_1)} \int_{t_0}^{t_1} \frac{\rho}{g} J_b^0(t)\, dt + \frac{1}{D(t_1)} \int_{-D}^{0} \rho(t_0, z)\, dz \quad . \tag{4}$$

The first term, the net density flux across the surface, accounts for an increase of only 0.031 kg m^{-3}. Entrainment, the second term, adds an additional 0.085 kg m^{-3}, leaving a shortfall of 0.054 kg m^{-3}. A similar problem was found with the heat budget of the ring by Joyce and Stalcup (1985). Based on XBT surveys before and after the microstructure profiling, they concluded that the net heat flux and the observed deepening were insufficient to explain the change in heat content and assumed that advection of slope water into the ring was responsible.

Given that advection was important, did it occur steadily or episodically? Using Eq. (4) as a diagnostic, the two components are shown in Fig. 6. for the three intervals being considered. The vertical balance works well between bursts 19 and 26 and between 26 and 30, but is drastically off between bursts 30 and 32. TS diagrams confirm a water mass change between bursts 30 and 32, but not earlier.

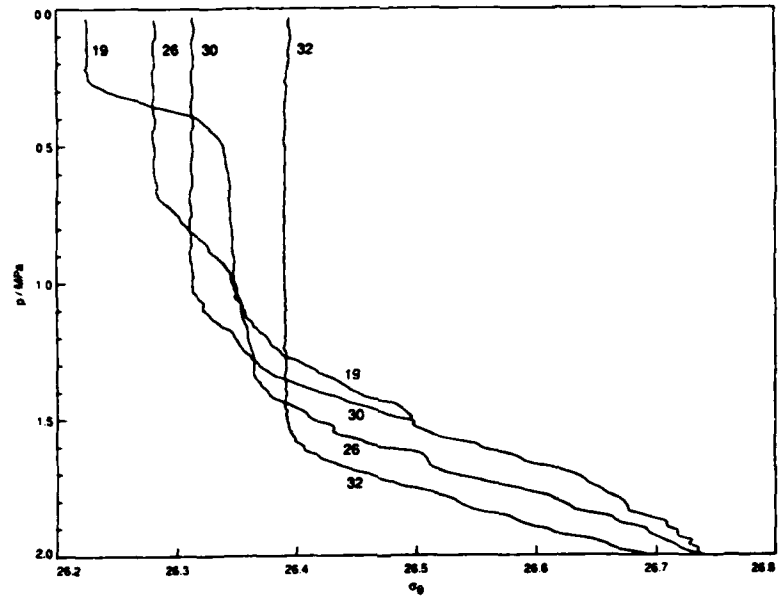

Fig. 5. Burst averages of σ_θ during the mixed layer deepening. The net density increase was 0.17 kg m^{-3}.

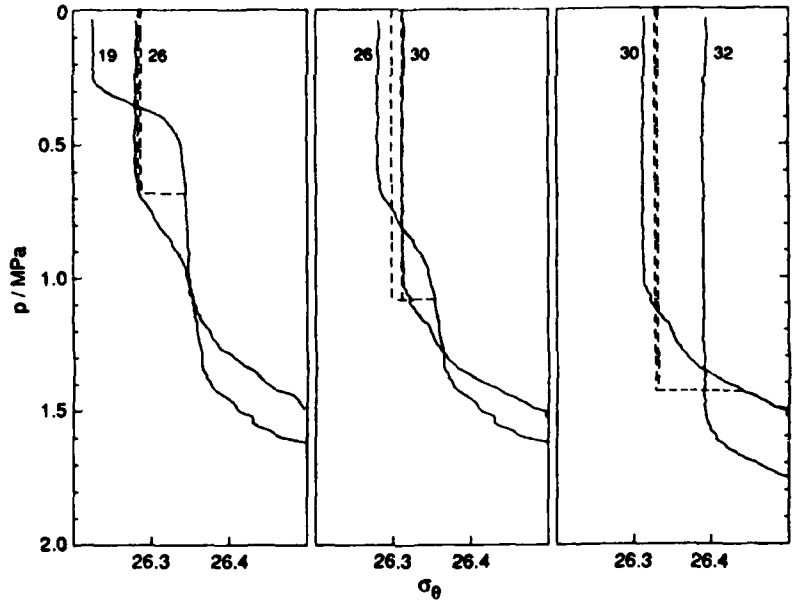

Fig. 6 Observed σ_θ changes (solid) compared with those given by Eq. (4) for the same increase in mixed layer depth. The leftmost dashed curve was obtained by homogenizing the initial profile to the mixed layer depth observed during the later burst; thus, it corresponds to the second term on the right in Eq. (4). The rightmost dashed curve includes the net density increase produced by J_b^0, and thus corresponds to the first term on the right of Eq. (4). The vertical balance accounts for the changes observed between bursts 19 and 26 and between 26 and 30, but not between bursts 30 and 32. Note that the surface contribution was significant between bursts 26 and 30.

Because of advection, increases in the potential energy of the stratification cannot be computed simply from the difference in density of two burst average profiles. Rather, estimates were made of the work required to homogenize an average profile to the depth of the mixed layer observed in the later burst. Thus, the mean density profile of burst 19 was homogenized to extend the surface layer from 25 to 68 m, the layer depth observed during burst 26.

The potential increases in energy varied between 536 and 880 J m^{-2} (Table 1). The rate of increase, however, rose from 5.5 mW m^{-2} between bursts 19 and 26 to 34 mW m^{-2} between bursts 30 and 32. For comparison, Denman and Miyake (1973) found that only a small fraction, 0.0012 E_{10}, of the work done by the wind was applied to increasing the mean potential energy. At this efficiency, the contribution of the wind stress was approximately 1/3 of the work done between bursts 19 and 26, but only 2% of that between bursts 30 and 32. Therefore, the wind stress was a minor factor in the initial deepening and was negligible subsequently.

Table 1. Energetics of the Mixed Layer Deepening.

BURST INTERVAL	D m	$\Delta P.E.$ J m^{-2}	$\Delta P.E./\Delta t$ mW m^{-2}	$0.0012E_{10}$ mW m^{-2}	$\rho D J_b^0$ mW m^{-2}	R_e
19-26	25-68	544	5.5	1.7	9.5	0.58
26-30	68-104	536	12.0	1.8	28.0	0.43
30-32	104-143	880	34.0	0.8	37.0	0.92

The work done by the surface buoyancy flux in releasing potential energy at the surface is $\rho D J_b^0$. In sinking through the mixed layer, the potential energy of the dense water formed at the surface is converted to kinetic energy, some of which is dissipated and some of which is converted to mean potential energy by entrainment at the base of the layer. The entrainment ratio,

$$R_e \equiv \frac{\Delta P.E./\Delta t}{\rho D J_b^0} \quad , \tag{5}$$

expresses the rate of increase of the part going into mean potential energy as a fraction of the total work done at the surface. With no dissipation in the layer and no generation of internal waves, $R_e = 1$. As noted by Cushman-Roisin (1982), entrainment rates in the literature range from 1, corresponding to no dissipation in the mixed layer, to 0, corresponding to all of the buoyancy work going into dissipation or internal waves. Laboratory convection experiments have yielded $R_e = 0.02$ (Deardorff et al., 1969) and $R_e = 0.10$ (Willis and Deardorff, 1974). No values in Cushman-Roisin's survey were based on oceanic observations.

Our entrainment ratios are large, 0.43 to 0.92 (Table 1). Indeed, they are too large to be consistent with $\bar{\epsilon}$ in the convectively dominated part of the mixed layer. Shay and Gregg (1986) found $\bar{\epsilon}/J_b^0 = 0.72$. Thus, only 28% of the work done by the surface buoyancy flux was available. Either $\Delta P.E.$ is overestimated or convection was not the only process deepening the layer.

Shear profiles taken during the deepening provide no evidence for shear instability at the base of the mixed layer (Fig. 7). Although shears were high in the upper part of the layer, they were small in the middle and lower sections. In both cases, $Ri \equiv N^2/S^2 > 1$ across the base of the layer. Thus there is no direct evidence that shear contributed to the deepening. It is possible, however, that shear over scales smaller than the 10 m vertical resolution of the XCP could have been sufficiently strong to produce dynamic instability.

HIGH DISSIPATION RATES AT SHALLOW DEPTHS

Although similarity scaling describes $\bar{\varepsilon}$ in the convective regime deep in the mixed layer, it fails near the surface, where burst average dissipation rates were several decades larger than the sum of Eqs. (1) and (2) (Fig. 8). The intense near-surface dissipation was produced by strong events in a majority of the profiles in each burst. For example, 8 of 12 profiles in burst 26 had near-surface events, with $\varepsilon \approx 10^{-5}$ to 10^{-4} Wkg^{-1} (Fig. 9). Some extended as deep as 0.3 MPa before cutting off abruptly.

The intense near-surface activity dominates the net dissipation, defined as

$$\varepsilon_I \equiv \int_{-D}^{-5} \rho \varepsilon dz \quad [Wm^{-2}] \; . \tag{6}$$

Integration was started at 5 m to avoid transients generated by release of the vehicle from the surface. Contamination by the ship's hull was not a factor because only the first drop in a burst was started close aboard. As seen in Table 2, ε_I varied from 30 mW m^{-2} to 410 mW m^{-2}. Comparison with Fig. 9 shows that the four low values of ε_I came from the drops without the intense near-surface activity, i.e., from drops 1282, 1283, 1288, and 1290.

For comparison, ε_I^c is defined as the contribution from the convectively dominated region below the intense near-surface activity. Values for individual drops ranged from 15 mW m^{-2} to 34 mW m^{-2}, and $\overline{\varepsilon_I/\varepsilon_I^c}$ ranged from 1 to 27. The variability was mostly due to ε_I, as ε_I^c varied less than a factor of 2. For the burst average, $\overline{\varepsilon_I}/\overline{\varepsilon_I^c} \approx 7$. Thus, even in these very deep layers, near-surface dissipation was much larger than that produced by convection.

The only data available for comparison were obtained by Oakey and Elliott (1982) in a layer where D increased slowly from 19 m to 22 m. Owing to the shallowness of the layer, their integration algorithm extrapolated the observed data to the surface,

$$\varepsilon_I = \frac{12}{5.5} \int_{-12}^{-5.5} \rho \varepsilon dz + \int_{-D}^{-12} \rho \varepsilon dz \; . \tag{7}$$

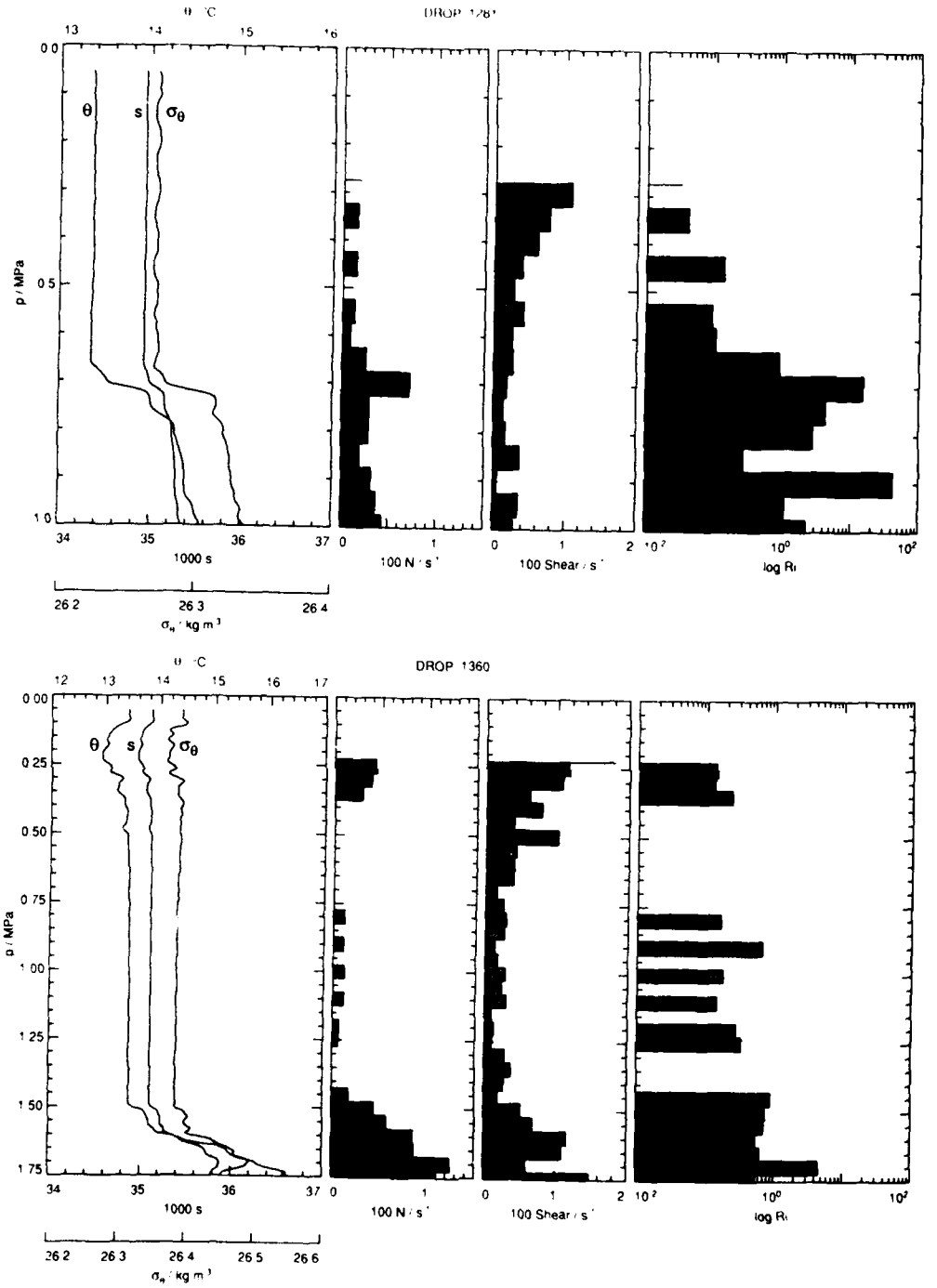

Fig. 7. Richardson numbers formed from XCP velocity and from AMP density taken in close proximity. Negative values of N^2 are set to a small positive value. The isolated positive N values in the mixed layer are the undersides of overturning structures. Ignoring them, $Ri \approx 0$ in the mixed layer but rises to greater than 1 across the entrainment zone. In XCP 1281 (top), shear is low throughout the mixed layer and does not increase across the entrainment zone. Shear increases across the entrainment zone in XCP 1360, but $Ri \approx 1$.

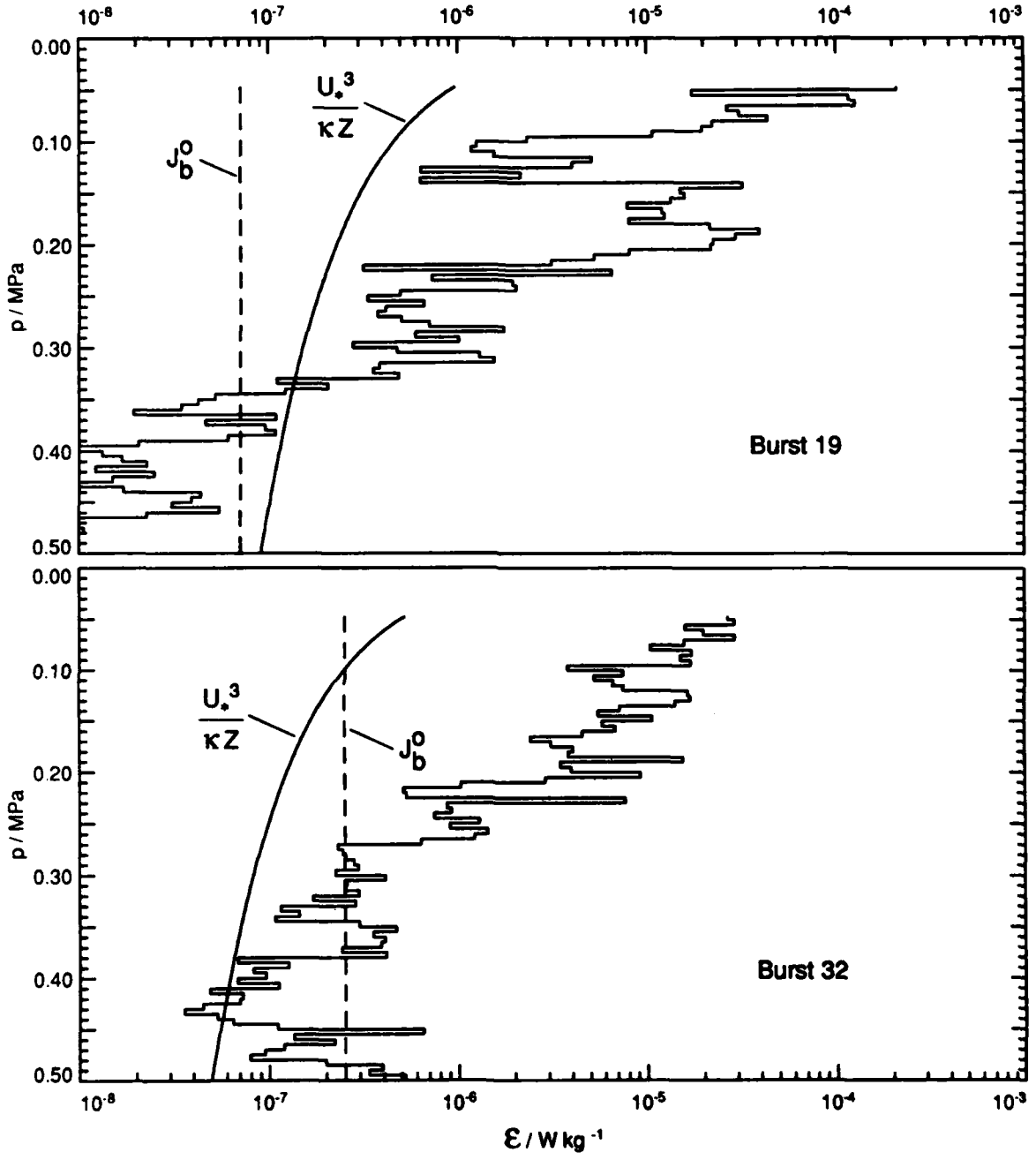

Fig. 8. Above 0.3 MPa, $\bar{\varepsilon}$ is much larger than the sum of the similarity scalings for turbulence produced by wind stress and by convection.

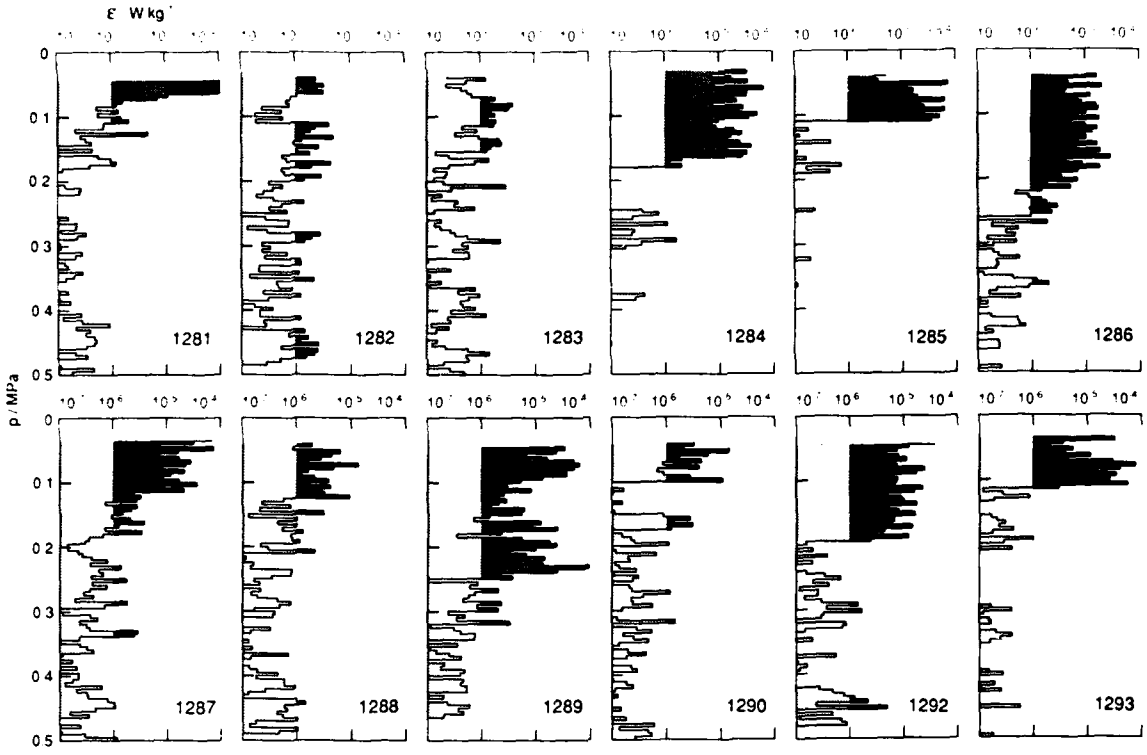

Fig. 9. Bursts of intense near-surface mixing occurred in 8 of 12 profiles from burst 26. Several of the intense events extended to between 0.2 MPa and 0.3 MPa and then cut off abruptly to the levels characteristic of the convective regime, e.g., drops 1284 and 1292. Some drops had little intensification near the surface, e.g., drops 1282 and 1283.

The upper 5.5 m were omitted from the direct integration for fear of contamination by the ship's hull. Finding an approximately linear dependence of ε_I on E_{10},

$$\varepsilon_I = 0.014\ E_{10} \quad , \tag{8}$$

all of the dissipation was attributed to the wind stress. Compared with $dP.E./dt = 0.0012\,E_{10}$ (Denman and Miyake, 1973), Oakey and Elliott found 10 times as much energy being dissipated as was going into the mean potential energy.

Integrating Eq. (1) by Eq. (7) yields $\varepsilon_I = 0.007\,E_{10}$, half of what Oakey and Elliott observed. By contrast, the average dissipation rate for burst 26 corresponds to $\varepsilon_I = 0.16\,E_{10}$, more than 10 times that found by Oakey and Elliott and 4 times the sum yielded by u_* and J_b^0 scaling.

Table 2. Integrated Dissipation Rates for Drops in Burst 26. Eight of the twelve drops have $\varepsilon_I \gg \varepsilon_I^C$, showing the large effect of the intense near-surface activity compared with that in the much thicker convectively dominated regime. The observed net dissipation was also much larger than given by previous parameterizations; e.g., scaling Oakey and Elliott (Eq. 4) gives $\varepsilon_I = 13$ mW m^{-2}.

DROP	D m	ε_I^C mW m^{-2}	ε_I mW m^{-2}
1281	70	15	410
1282	64	34	40
1283	68	23	30
1284	62	18	210
1285	76	22	140
1286	64	18	140
1287	82	23	130
1288	84	24	50
1289	74	21	290
1290	88	26	30
1292	86	26	130
1293	88	26	150
AVERAGE	76	23	145

Both convective plumes and breaking surface waves have been considered as sources of elevated near-surface mixing. The $\ln\varepsilon$ observed at a fixed height in the atmospheric marine boundary layer has a bimodal distribution (Businger and Khalsa, 1978). The quiescent background accounts for the lower peak, and passing plumes produce the upper one. The mode of the "on" distribution is three to four times larger than the mode of the "off" distribution and has tails extending to much higher values.

Estimates of turbulence produced by surface waves yield 10^{-4} of the wave energy during one wave period, yielding an average dissipation of

$$\varepsilon_{bw} = 10^{-4} \frac{g\, a^2}{2\tau\delta} , \qquad (9)$$

where a is the wave amplitude, τ is the wave period, and δ is the depth over which the energy is dissipated (Monin, 1977). Using $a = 3.3$ m, from the swell amplitudes estimated by the bridge watch, $\tau = 15$ s, and $\delta = 10$ to 30 m gives $\varepsilon_{bw} = 1\text{–}3\times10^{-5}$ W kg^{-1}, the same order of magnitude as the observed dissipations.

Snow and sea smoke obscured the sea surface much of the time, preventing observation of waves breaking near AMP. Temperature, however, reveals distinct "blobs" of cold water coinciding with most of the strong near-surface dissipation bursts (Fig. 10). Plumes, breaking surface waves, and Langmuir cells cannot be readily distinguished from uncorrelated temperature profiles. Nevertheless, these signatures are strong evidence that at least one of these mechanisms produced the intense near-surface dissipation.

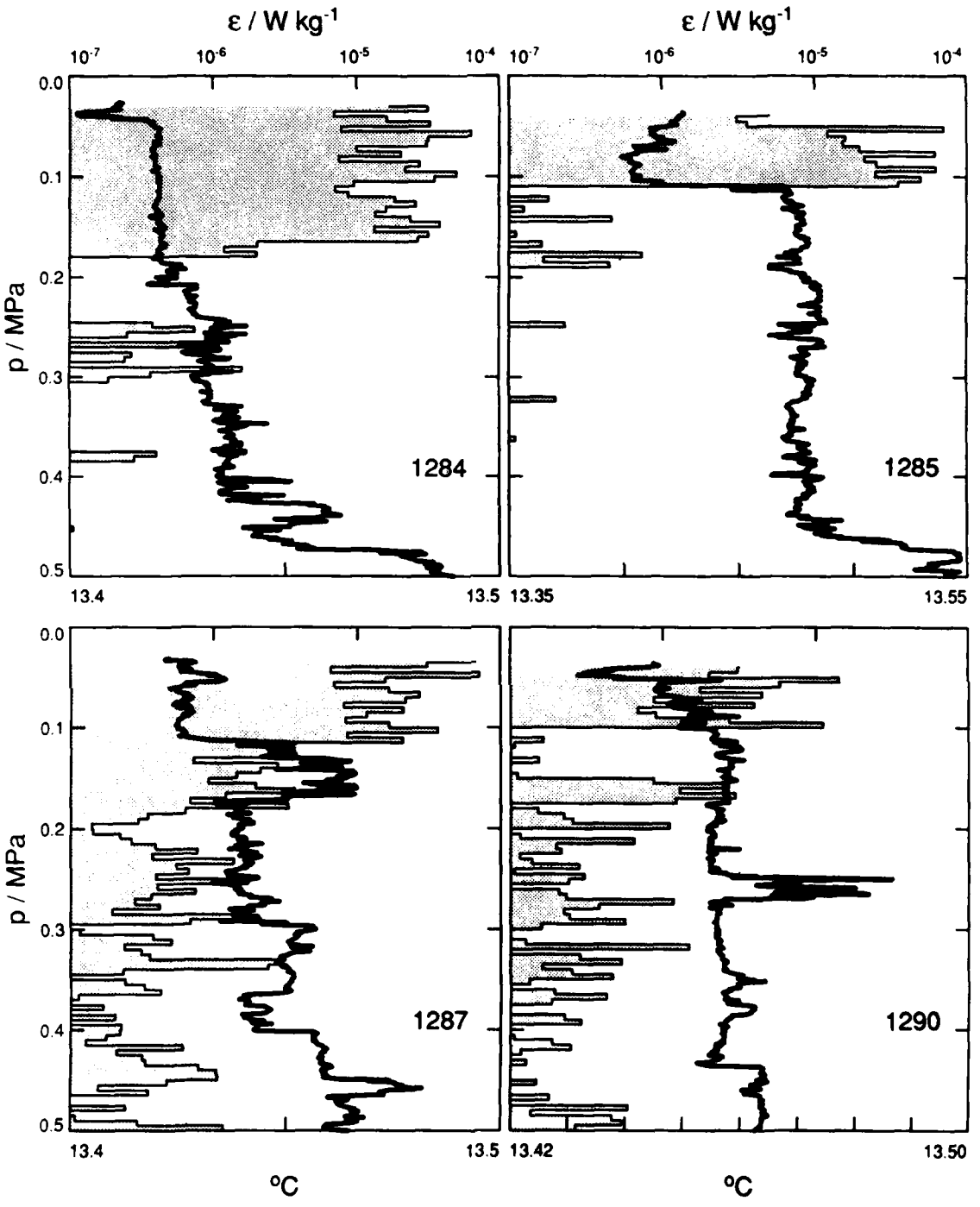

Fig. 10. Many of the near-surface high dissipation events coincided with blobs of cold, dense water.

In spite of their plausibility, the high dissipation rates must be viewed with some caution until more observations are made. Spurious high ε's are usually produced in the upper few meters by the vehicle's start-up, even under calm seas. We initially assumed that an extended vehicle transient in the heavy seas caused these much deeper dissipation bursts. Only later did we realize that the vehicle tilt changed little between drops having large differences in ε.

Tilt is monitored with a horizontal accelerometer. At low frequencies, it yields the inclination to the vertical, $\theta = \sin^{-1}(\dot{x}/9.8)$. Full scale is ± 0.45 m s^{-2}, corresponding to $\theta = \pm 2.6°$. As seen in Fig. 11, the largest tilts are only a few degrees and vary little between two records in which ε above 0.28 MPa differs by a factor of 300. Based on laboratory calibration studies, Osborn and Crawford (1980) concluded that angles of attack of $\pm 10°$ to $\pm 15°$ on airfoil probes cause minimal errors in the sensitivity. Hence, there is no evidence that such small angles could produce large, false signals.

In summary, these large near-surface dissipation rates appear to be correct measurements, and plausible mechanisms exist to produce them. Nevertheless, because of their novelty and the many errors affecting dissipation measurements, until further work is done they cannot be viewed with the same confidence as measurements from less energetic regimes. This intense activity must be taken seriously, however, because it completely dominates the net dissipation, even in very deep mixed layers.

OVERTURNS AND ENTRAINMENT

Close inspection reveals a wide variety of structures within the mixed layers. Some layers contained homogeneous sublayers near the surface that were more dense than any other water above the entrainment zone, for example drop 1345 in Fig. 12. Thick density minima existed within other layers, e.g., drops 1341, 1342, and 1344. Yet others had slightly stable profiles, e.g., drop 1346. Density inversions were more common late in the outbreak, when convection was strongest.

Overturning scales, computed from both θ and σ_θ using Thorpe's resorting technique, reflect the patterns of density instabilities. Some drops had overturns across the full depth of the layer, but others contained two or three sequential overturns collectively spanning the mixed layer, e.g., Fig. 13. Toward the end of the observations, many layers had density-compensated temperature and salinity contrasts, and thus were much more homogeneous in σ_θ than in θ or s. These showed smaller overturning scales in θ than in σ_θ.

The entrainment zone was defined as the region of strong average stratification between the mixed layer and the weakly stratified water below. When the mixed layer was only 25 m deep, the thickness of the entrainment zone, Δz, averaged 5 ± 2 m. After the layer had deepened to 143 m, Δz = 26 ± 23 m. Therefore, $\Delta z \approx 0.2D$, with an rms variability as large as the mean. Across the entrainment zone, ε decayed from $\geq 10^{-7}$ in the mixed layer to $\approx 10^{-9}$ in the quiescent water below (Fig. 14).

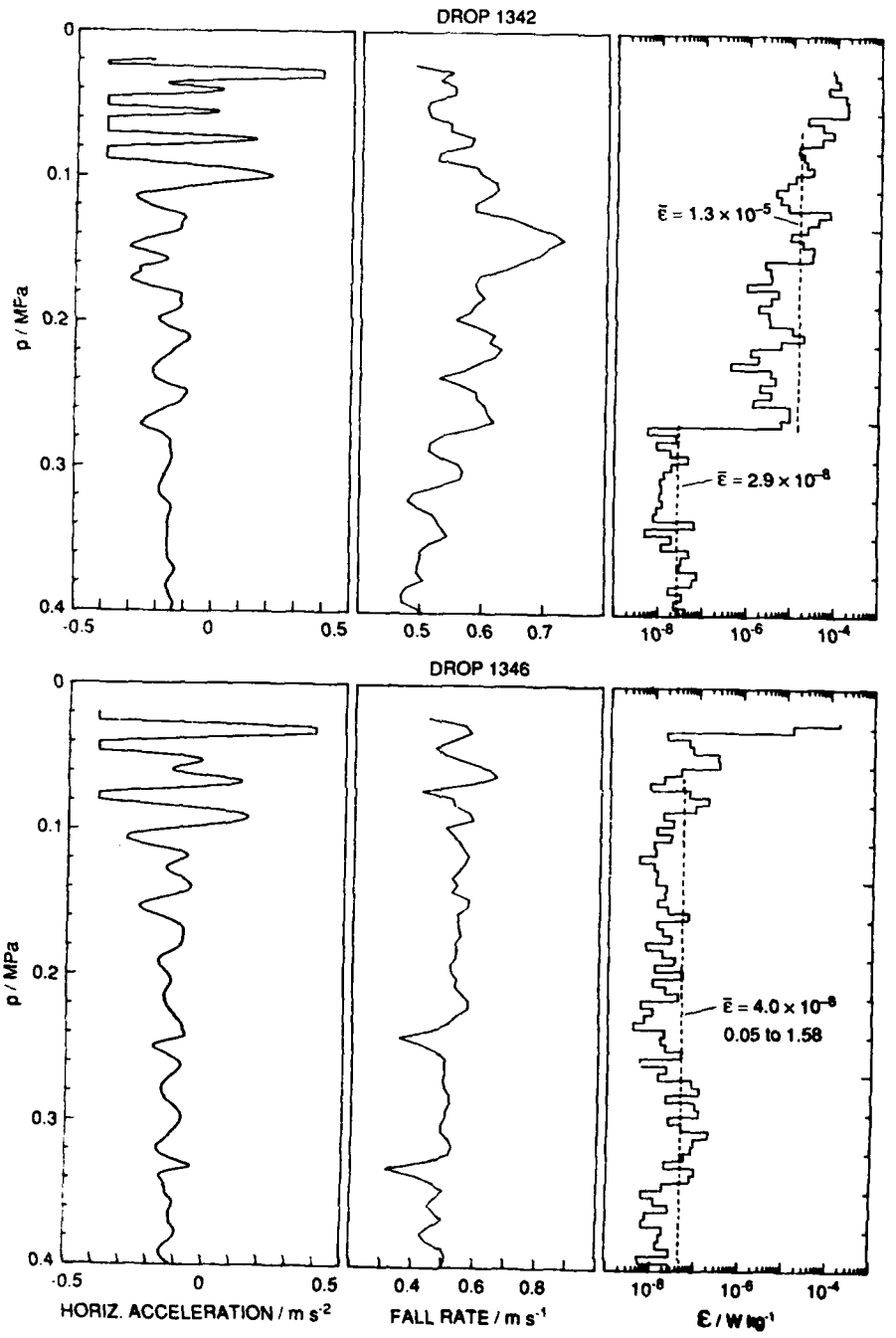

Fig. 11. Horizontal acceleration, fall rate, and ε for two drops taken in the same burst. Although the tilt was nearly the same, ε near the surface differed by a factor of 300.

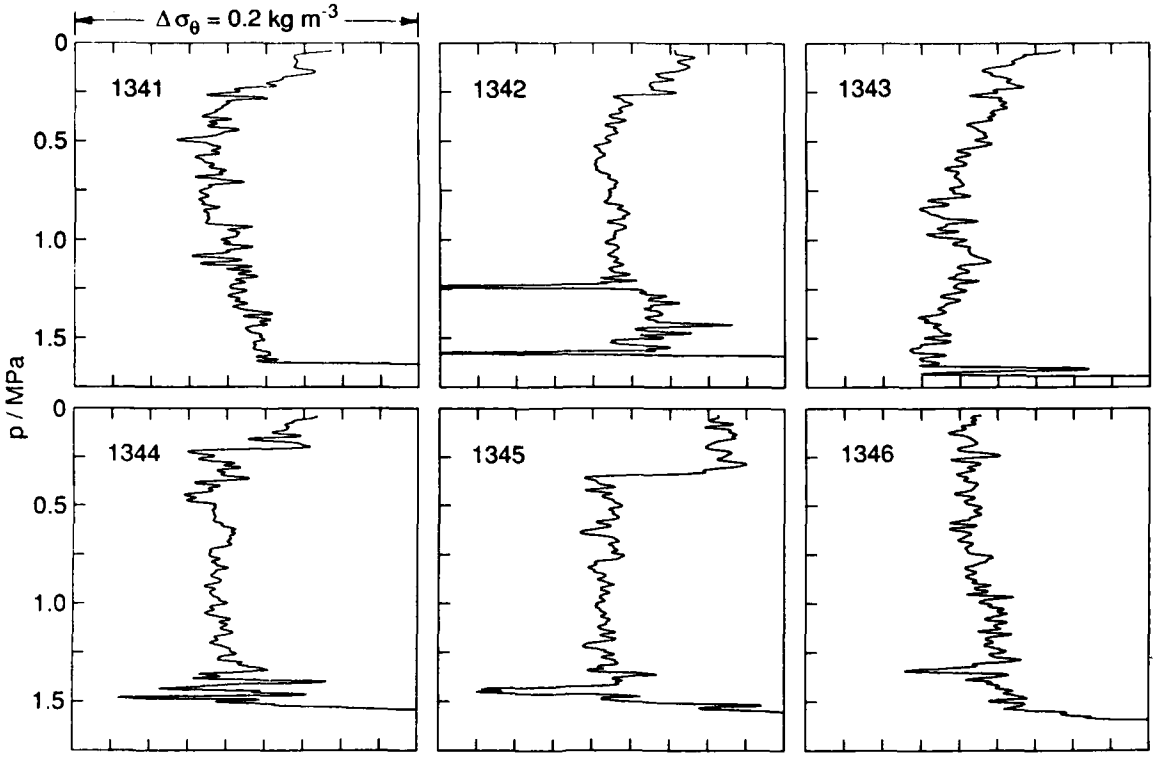

Fig. 12. σ_θ in the mixed layer during burst 32. Most profiles had distinct shallow density instabilities.

The turbulence was strong, with $\bar{\varepsilon} \gg \varepsilon_{tr}$, compared with the main thermocline, where $\bar{\varepsilon} \approx \varepsilon_{tr}$ (Gregg, 1984). The transition dissipation rate, $\varepsilon_{tr} = 24.5\nu N^2$, is the minimum level needed for stratified turbulence to support a buoyancy flux (Stillinger et al., 1983). The most intense mixing occurred in burst 19, when $\bar{\varepsilon} = 284\varepsilon_{tr}$. The entrainment zone was closer to the surface than in later bursts and more likely to have been affected by the strong near-surface activity. During the later bursts, $\bar{\varepsilon} \approx 130\varepsilon_{tr}$. The layers were much deeper, and presumably the entrainment zone was driven primarily by convective eddies from the mixed layer.

The buoyancy scale, $L_b \equiv (\varepsilon/N^3)^{0.5}$, was substantially less than observed overturning scales, unlike the situation in the main thermocline (Dillon, 1982) or in the Equatorial Undercurrent (Gregg et al., 1985). Apparently, the overturns were not produced by the local turbulence but by large mixed layer eddies impinging on the entrainment zone. The large fluctuations in Δz are consistent with this interpretation.

Overturns had scales of tens of centimeters to a meter or two — much less than the thickness of the entrainment zone. The rms scales were only $\frac{1}{3}\Delta z$ (Table 3). Often several steplike mixing zones separated by sharp interfaces comprised the zone.

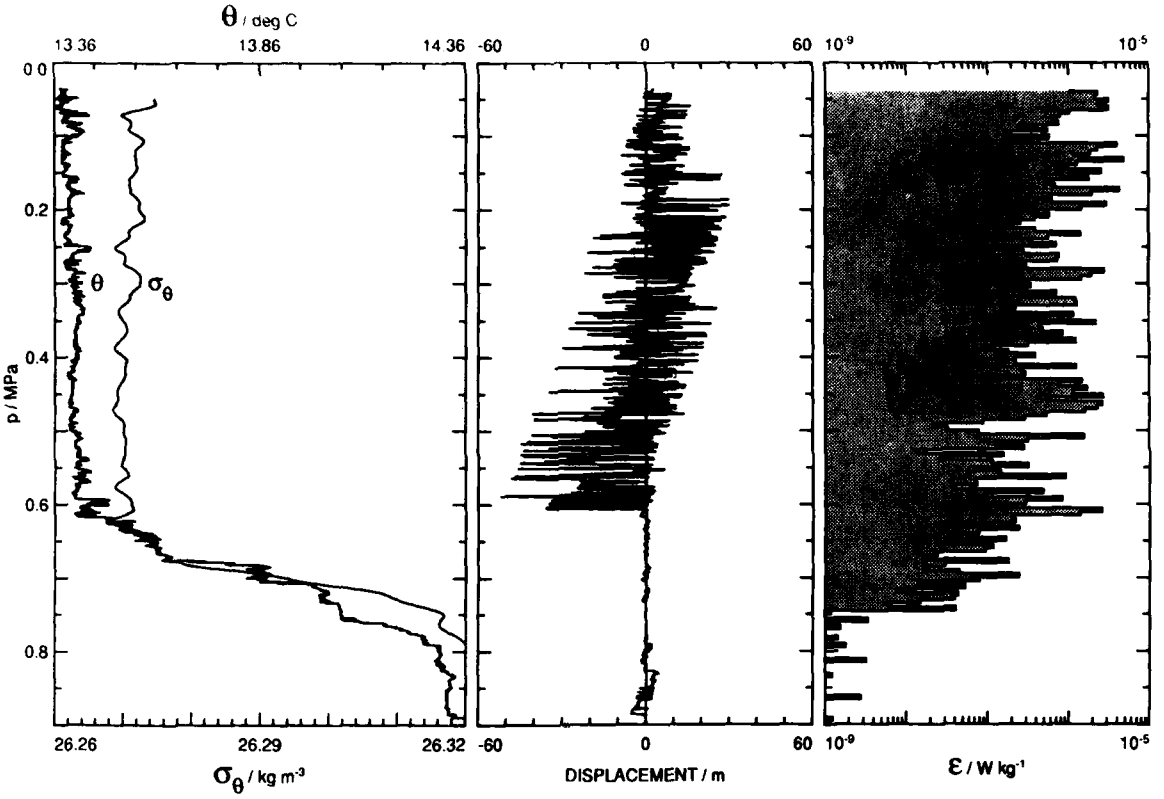

Fig. 13. Mixed layer structure during drop 1282. Potential temperature, θ, was plotted with a vertical spacing of 10 cm; σ_θ was averaged vertically to reduce salinity spiking. These overturning scales were computed from θ. Several large overturns spanned the mixed layer. Both the overturning scales and ε decreased strongly in the entrainment zone.

Table 3. Characteristics of the entrainment zone. Δz is the thickness of the zone, ε_{tr} is the transition dissipation rate, J_q is the vertical turbulent heat flux, l is the observed overturning scale, L_b is the buoyancy scale, and η is the density of the fluctuating potential energy.

BURST	D m	Δz m	$10^5 N^2$ s^{-2}	$10^7 \varepsilon$ W kg^{-1}	$\varepsilon/\varepsilon_{tr}$	$10^{-4} Cox$	$10^3 J_q$ W m^{-2}	l m	L_b m	$10^4 \eta$ J kg^{-1}
19	25	5±2	7.3±1.5	6.4	284	1.5	1.8±2.4	1.7	0.9	1.7
26	68	16±7	4.5±3.9	1.4	141	1.0	0.40±0.7	1.4	0.9	160
30	104	16±6	1.7±0.5	0.6	124	1.0	0.37±0.67	5.6	1.0	6.6
32	143	26±23	3.6±2.6	1.3	125			1.5	0.9	0.2

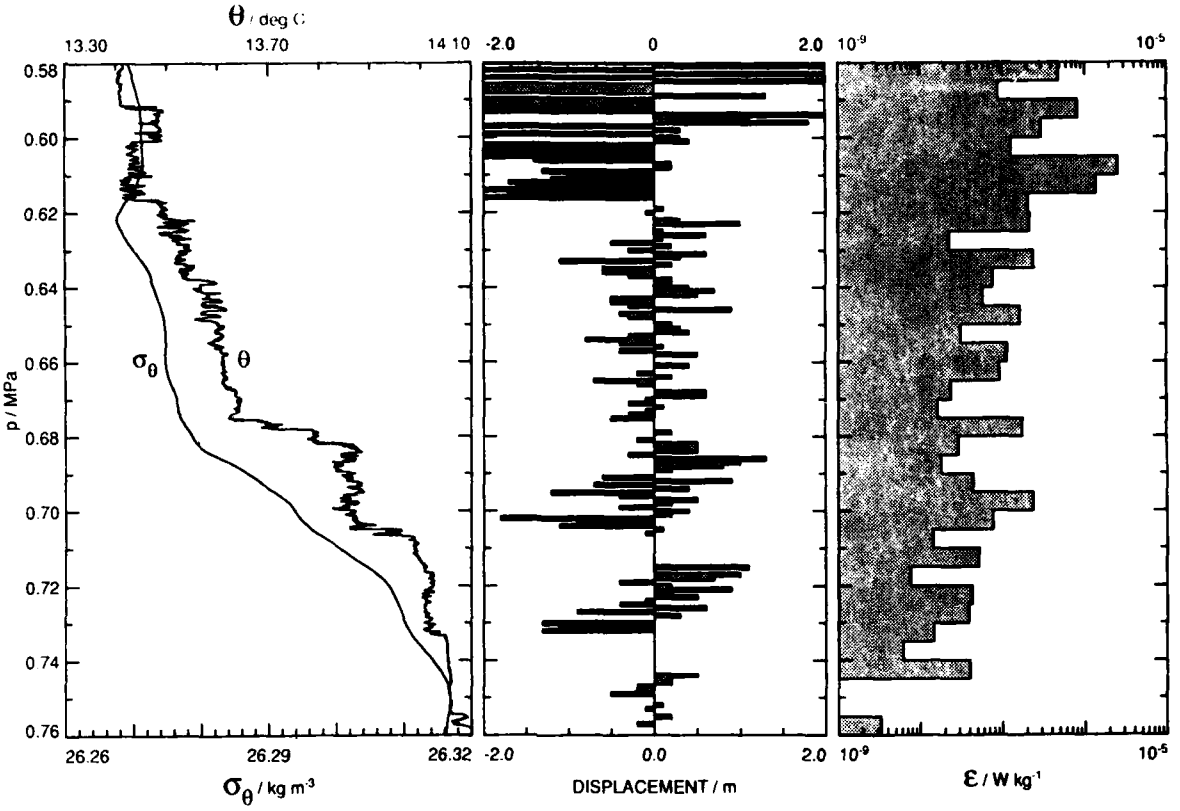

Fig. 14. Expanded plot of the entrainment zone of drop 1282 shows maximum overturning scales much less than the thickness of the zone. ε decreased steadily through the zone, reaching background levels at the base.

Temperature microstructure was measured with a cold film and a thermistor during three of the four bursts being considered. The average Cox numbers were very high, Cox ≈ 10^4. When turbulence exists as a steady local balance between production and dissipation, vertical eddy coefficients can be computed from the Cox numbers as

$$K_t = \frac{\tilde{\chi}}{2\,(\partial\bar{T}/\partial z)^2} = Cox\ \kappa_t \quad . \tag{10}$$

Similar assumptions (Osborn, 1980) yield the vertical eddy coefficient for density, based on the dissipation rate,

$$K_\rho = \frac{0.2\varepsilon}{N^2} \quad . \tag{11}$$

Somewhat surprisingly, K_t and K_ρ agree within a factor of 2 (Table 4), with K_t being the larger. The corresponding heat flux, $J_q = -\rho c_p K_t \partial\bar{T}/\partial z$, was 370 W m^{-2} to 1800 W m^{-2} and was directed upward into the mixed layer owing to the negative mean temperature gradient. These fluxes are significant compared with the surface fluxes and indicate the strong role of

entrainment. The bulk changes support this. For example, the net heat flux during the outbreak was sufficient to cool the final mixed layer by about 0.15°C, but the layer was observed to warm 1°C.

Table 4. Eddy coefficients in the entrainment zone computed using Eqs. (10) and (11).

BURST	K_t $m^2 s^{-1}$	K_ρ $m^2 s^{-1}$
19	2.1×10^{-3}	1.8×10^{-3}
26	1.4×10^{-3}	6.2×10^{-4}
30	1.4×10^{-3}	7.1×10^{-4}
32		7.2×10^{-4}

The large discrepancies between the observed overturning scales and the buoyancy scale, L_b, indicate that the turbulence was not in such a steady local balance. Hence, we should not expect fluxes based on microstructure to account for the entire heat flux, or even for most of it. Nevertheless, these estimates do demonstrate the importance of the small-scale component.

CONCLUSIONS AND DISCUSSION

- In two days a cold-air outbreak deepened the mixed layer in a warm-core ring from 25 m to over 140 m, increasing the potential energy of the mean stratification almost 2000 J m^{-2}.
- Using Denman and Miyake's observation that the increase in the mean potential energy is $0.0012E_{10}$, the role of wind-forcing was small to nil.
- Most of the deepening was consistent with a vertical density balance between the surface buoyancy flux and entrainment. The final deepening, however, coincided with a density increase much too large to be explained by a vertical balance.
- Entrainment ratios were 0.4 to 0.9. In view of $\bar{\varepsilon} = 0.72J_b^0$, these are too large for the deepening to be accounted for solely by convection.
- Richardson numbers computed with a vertical resolution of about 10 m, gave no evidence for shear instability at the base of the layer.
- Dissipation rates much larger than obtained from similarity scaling dominated the integrated dissipation in the mixed layer. Although not viewed with the same confidence as deeper measurements, the shallow ε profiles appear correct and are often correlated with cold blobs. Hence, breaking surface waves and plumes were possible mechanisms producing the elevated dissipation rates.

- Many σ_θ patterns were observed in the mixed layer. Density inversions across the entire layer were common late in the deepening, when convection was most intense.

- Strong turbulence and large vertical heat fluxes occurred in the entrainment zone, whose thickness was approximately 20% of the mixed layer depth.

- Overturning scales in the entrainment zone were much smaller than the thickness of the zone, indicating that mixing occurred as a sequence of small events. The overturning scales were also significantly larger than the buoyancy scales, evidence that the turbulence was not in local balance.

These results are incomplete, awaiting analysis of the rest of the bursts during the outbreak as well as examination of more aspects of the mixing. Nevertheless, they demonstrate the ability of microstructure measurements to examine the mechanisms of mixed layer dynamics. Even these preliminary results demonstrate that neglecting dissipation is a serious mistake, as is neglecting penetrative entrainment. Both omissions have been made in prominent models.

How far these data can be pushed is not yet clear; difficulties with lateral advection are already apparent. In spite of the limitations, mostly due to advection, it is important that they be pushed as hard as possible. In addition to the observations on the equator (Peters and Gregg, this issue), this is the fourth convecting mixed layer in which I have made observations, and it is the fourth in which significant lateral effects were observed. This was very striking in the first example, when the layer depth halved as a result of lateral motions (Gregg, 1976). Significant advection, particularly when the deepening is advanced, appears to be a general phenomenon and is likely to be closely coupled to what is now called subduction.

ACKNOWLEDGMENTS

This work was funded by the Physical Oceanography Program of the Office of Naval Research. Charles Lombardo provided valuable assistance in the analysis, and Donna Sorensen and Joe Peterson helped with the plotting. The analysis builds on the prior work of Tom Shay. Contribution 1692 of the School of Oceanography.

REFERENCES

Businger, J.A., and S.J.S. Khalsa, 1978: On the structure of convective elements in the air near the surface. Turbulent Fluxes Through the Sea Surface, Wave Dynamics, and Prediction, A. Favre and K. Hasselmann, Eds., pp. 5-19, Plenum Press, New York.

Cushman-Roisin, B., 1982: Penetrative convection in the upper ocean due to surface cooling. Geophys. Astrophys. Fluid Dyn., 19, 61-91.

Deardorff, J.W., G.E. Willis, and D.K. Lilly, 1969: Laboratory investigation of non-steady penetrative convection. J. Fluid Mech., 35, 7-31.

Denman, K.L., and M. Miyake, 1973: Upper layer modification at Ocean Station Papa: Observations and simulations. J. Phys. Oceanogr., 3, 185-196.

Dillon, T.M., 1982: Vertical overturns: A comparison of Thorpe and Ozmidov length scales. J. Geophys. Res., 87, 9601-9613.

Gregg, M.C., 1976: Finestructure and microstructure observations during the passage of a mild storm. J. Phys. Oceanogr., 6, 528-555.

Gregg, M.C., 1984: Persistent turbulent mixing and near-inertial internal waves. Internal Gravity Waves and Small-Scale Turbulence: Proceedings, January 17-20, 1984, P. Muller and R. Pujalet, Eds., Hawaii Institute of Geophysics, Honolulu, 1-24.

Gregg, M.C., H. Peters, J.C. Wesson, N.S. Oakey, and T.J. Shay, 1985: Intensive measurements of turbulence and shear in the equatorial undercurrent. Nature, 318, 140-144.

Joyce, T.M, and M.C. Stalcup, 1985: Wintertime convection in a Gulf Stream warm-core ring. J. Phys. Oceanogr., 15, 1032-1042.

Monin, A.S., 1977: On the generation of oceanic microstructure. Izvestiya, Atmos. & Ocean. Physics, 13, 798-803.

Oakey, N.S., and J. A. Elliott, 1982: Dissipation within the surface mixed layer. J. Phys. Oceanogr., 12, 171-185.

Osborn, T.R., 1980: Estimates of the local rate of vertical diffusion from dissipation measurements. J. Phys. Oceanogr., 10, 83-89.

Osborn, T.R., and W.R. Crawford, 1980: An airfoil probe for measuring turbulent velocity fluctuations in water. Air-Sea Interactions: Instruments and Methods, F. Dobson, L. Hasse, and R. Davis, Eds., Plenum, New York, 369-386.

Shay, T.J., and M. C. Gregg, 1984: Turbulence in an oceanic convective mixed layer. Nature, 310, 282-285.

Shay, T.J., and M.C. Gregg, 1986: Convectively driven turbulent mixing in the upper ocean. J. Phys. Oceanogr., 16, 1777-1798.

Stillinger, D.C., K.N. Helland, and C.W. Van Atta, 1983: Experiments on the transition of homogeneous turbulence to internal waves in a stratified fluid. J. Fluid Mech., 131, 91-122.

Willis, G.E., and J.W. Deardorff, 1974: A laboratory model of the unstable planetary boundary layer. J. Atmos. Sci., 31, 1297-1307.

Wyngaard, J.C., 1983: Lectures on the planetary boundary layer. Mesoscale Meteorology-Theories, Observations and Models. D.K. Lilly and T. Gal-Chen, Eds., 603-650.

EQUATORIAL TURBULENCE: MIXED LAYER AND THERMOCLINE

Hartmut Peters and Michael C. Gregg

Applied Physics Laboratory and School of Oceanography, College of Ocean and Fishery Sciences, University of Washington, Seattle, Washington 98105

ABSTRACT

In November 1984, the equatorial undercurrent in the central Pacific was strongly developed, with mean Richardson numbers as low as 1/4. Intense mixing in the shear zone above the core produced a diapycnal turbulent heat flux of 80 W m^{-2}. A diurnal cycle with changes in dissipation rates of a factor of 100 extended well into the thermocline. Internal waves radiating from the nighttime convecting mixed layer probably produced the deep component of the diurnal cycle; owing to the low mean Richardson numbers, any additional shear from internal waves was likely to cause breaking. The depth-integrated dissipation rate between 15 m and the undercurrent core at 110 m was largest near the equator and smallest at ±1.5° latitude. High dissipation in the thermocline produced the equatorial maximum.

INTRODUCTION

Small-scale turbulence is an essential component of the flux balances in the equatorial upper ocean; the undercurrent is thought to be frictionally balanced (McCreary, 1981), unlike geostrophically balanced currents at higher latitudes. Intense turbulence occurs in the high-shear regime above the velocity maximum of the undercurrent. Near the surface, a diurnal convective mixed layer couples the deeper zone of stratified turbulence to atmospheric forcing. This coupling appears to be an essential component of equatorial dynamics.

This paper is based on turbulence measurements taken in the equatorial Pacific at 140°W in November and December of 1984 as part of the Tropic Heat program (Niiler, 1982; Eriksen, 1985). Four north-south sections and one 4-1/2 day time series on the equator were taken by the RV THOMPSON. The data include some 900 microstructure/CTD profiles, continuous acoustic Doppler current measurements, and about 70 XCP drops (Fig. 1).

The methods, procedures, and uncertainties have been described by Peters et al. (1987b). Previous results from the Tropic Heat microstructure measurements have been reported by Gregg et al. (1985), Moum and Caldwell (1985), Moum et al. (1986), Chereskin et al. (1986), Toole et al. (1987), and Peters et al. (1987a). The measurements by Oregon State investigators were obtained from the RV WECOMA operating near the THOMPSON.

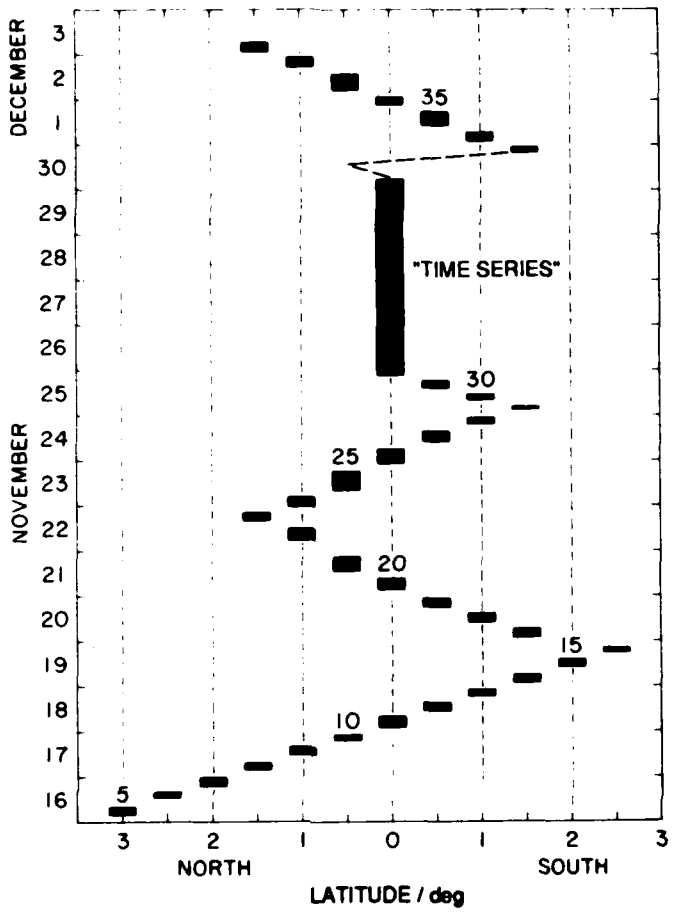

Fig. 1: Stations occupied by RV THOMPSON in 1984 during Tropic Heat at 140°W.

THE EQUATORIAL MIXED LAYER

The character of the undercurrent as a stratified shear current has some important implications for the mixed layer above the current. Here, the "mixed layer" is a weakly stratified, or unstratified, turbulent zone above a highly stratified turbulent region (Fig. 2). This contrasts with typical off-equatorial conditions, where the thermocline is essentially laminar, except for intermittent turbulent patches. The distinction between the equator and higher latitudes is not absolute, because a turbulent, stratified transition layer is sometimes found underneath the mixed layer. However, this transition zone is entirely forced by processes in the mixed layer, whereas on the equator, the stratified, turbulent zone is linked to the large-scale mean shear.

Thus, the definition of a "mixed layer" is not straightforward on the equator, and some explanation is necessary. We define the depth of the mixed layer, h_{ml}, to be the shallowest depth at which the surface density was exceeded by 0.01 kg m^{-3}. The result is close to the depth chosen visually (Fig. 2). As discussed below, stratification (and turbulence)

underwent a pronounced diurnal cycle. It is imperative that the definition of h_{ml} reproduce this cycle. Fig. 3 shows the good correspondence of N^2 contours and h_{ml}. The graph also shows that on average the nighttime mixed layer was not completely mixed ($N^2 < 10^{-6}$ s^{-2}, or $N < 0.6$ cph). In instantaneous profiles, N^2 showed considerable scatter, and instabilities were common.

Instrument wobble produced by release from the surface and by surface waves makes turbulence data from close to the surface less reliable than observations from greater depths. Therefore, we will not discuss the top 0.15 MPa here. This is unfortunate, because this layer is a crucial part of the mixed layer, containing most of the top boundary layer. The very high dissipation rates observed (order of 10^{-4} W kg^{-1}) appear to be correct, at least qualitatively. Without the top 0.15 MPa, no meaningful estimate of the total rate of dissipation per unit ocean surface area can be made (see Gregg, 1987, this volume, for a similar problem).

VERTICAL AND TEMPORAL VARIABILITY OF TURBULENCE ON THE EQUATOR

The undercurrent was strongly developed with eastward speeds of about 1.3 m s^{-1} at 1.1 MPa (110 m; Fig. 4a). The mean stability, N^2, and the mean shear were large, even close to the surface (Fig. 4b). Their combination yielded very low mean Richardson numbers, $\overline{Ri} = 0.25$-0.4 between 0.23 MPa and 0.8 MPa (Fig. 4c). This low dynamic stability is a major, unique property, distinguishing the undercurrent from other strong open ocean currents. Below 0.8 MPa, $\overline{Ri}$ had a strong maximum at the core.

The mean dissipation rate of kinetic energy, $\bar{\varepsilon}$, varied inversely with $\overline{Ri}$. From a maximum of about 10^{-6} W kg^{-1} at 0.3 MPa, $\bar{\varepsilon}$ decreased 2-1/2 decades to a minimum at the core (Fig. 4d). The maximum rate is high even compared with the little data available from the Gulf Stream (Gargett and Osborn, 1981). The minimum of 1.510^{-9} W kg^{-1} is comparable to levels found in the mid-latitude thermocline.

The mean eddy coefficient for heat, K_h, was obtained from the measured dissipation rate of temperature variance, $\bar{\chi}$, by applying the Osborn-Cox method (Osborn and Cox, 1972). K_h ranged from barely above the molecular diffusivity to a maximum of about 5×10^{-3} m^2 s^{-1} near 0.3 MPa (Fig. 4e). The maximum is a factor of 50 above the canonical "Abyssal recipes" value (Munk, 1966). The associated diapycnal turbulent heat flux, J_h, had a maximum of 80 W m^{-2} at 0.3 MPa, which was comparable to the net surface heat flux and an important factor of the upper ocean heat budget (Fig. 4f). (All turbulence parameters given are uncertain to a factor of 2.)

The eddy coefficient for momentum, K_m, and the associated momentum flux, computed by means of the dissipation method, showed characteristics similar to K_h and J_h (Fig. 4e,f). One key assumption in the computations is that the total shear is composed of the mean and of turbulence. If internal waves and other small-scale processes were important during the experiment, our estimates might be in error (see below, Gregg et al., 1985, and Dillon, 1987, this volume). Note that internal waves can transport momentum vertically without transporting scalars.

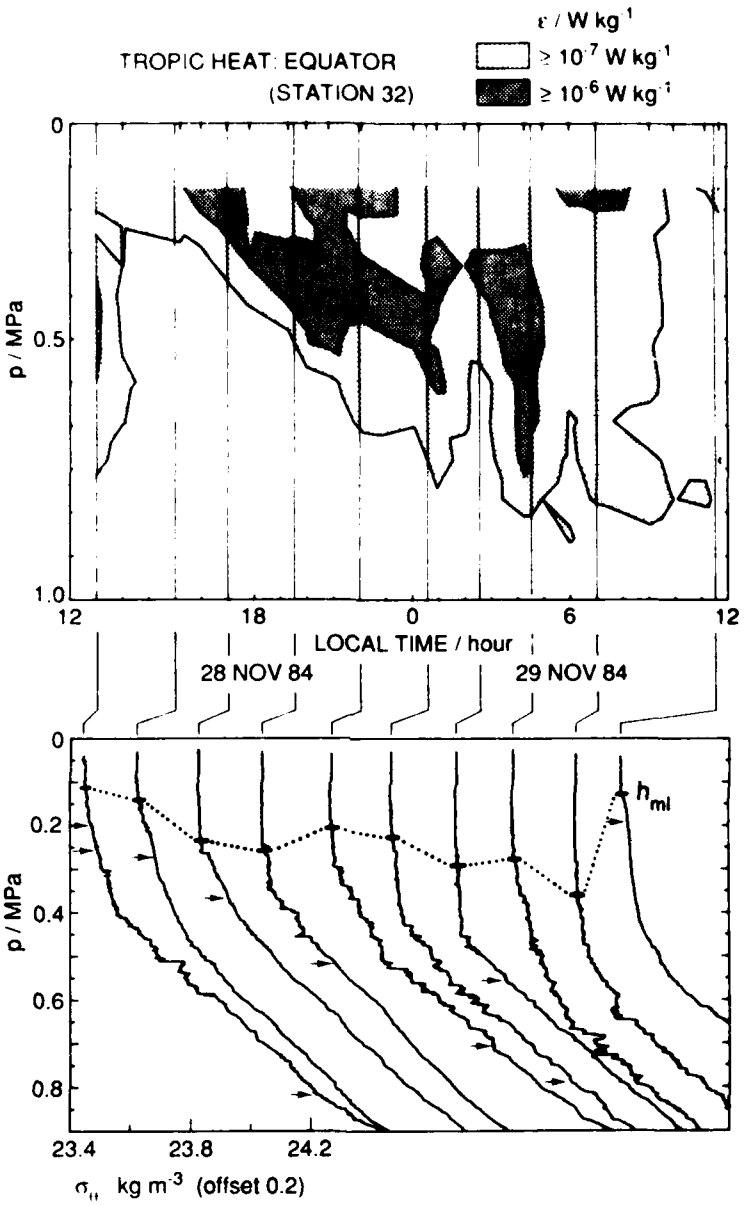

Fig. 2: Selected and smoothed contours of hourly averaged ε data and selected instantaneous density profiles. Pressure is in MPa; 1 MPa = 100 decibar. The horizontal bars on the σ_θ profiles indicate the mixed layer depth, h_{ml}, while the arrows mark the depth at which the $\varepsilon=10^{-7}$ contour is crossed. Note the large overturns in the high-ε zone. At the onset of the nocturnal intensification of turbulent mixing (≈1700 local time), the zone of high ε was restricted to the mixed layer and a small depth band below. Later, the highest dissipation values were found in a broad layer within the well-stratified thermocline. Note the vertically coherent burst of high ε between 0300 and 0600 local time.

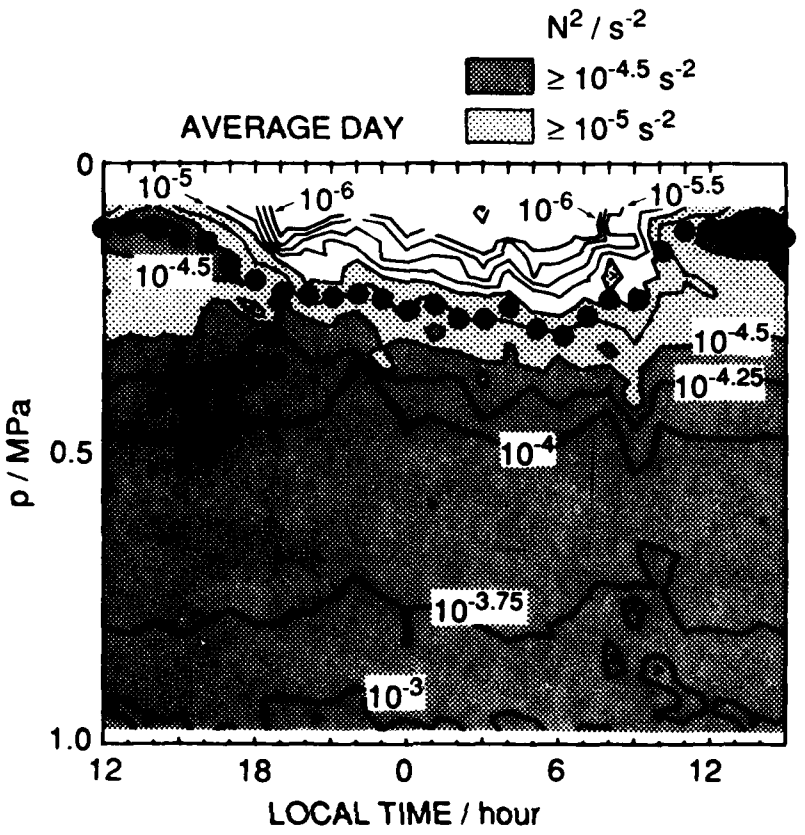

Fig. 3: Contours of N^2 from the daily average of the time series and average mixed layer depth (large dots). The first 3 hours are repeated at the end. A pronounced diurnal cycle of nighttime mixing and daytime restratification is seen above 0.4 MPa. The average mixed layer depth enclosed the weakly stratified region. N^2 was computed by differencing on a 0.03 MPa grid, and has thus been smoothed.

As functions of mean Richardson number, K_m and K_h showed an increase with decreasing $\overline{Ri}$, which was slow at $\overline{Ri} > 0.4$ and became very steep at $\overline{Ri} < 0.4$ (Fig. 5). These functions differ greatly from those currently used to parameterize mixing in equatorial models (Pacanowski and Philander, 1981), and can be exploited to improve the parameterizations (Peters et al., 1987b).

During Tropic Heat, the dominant variability of the turbulence parameters was a diurnal cycle coupled to the phase of the surface heat flux (Fig. 6). Maxima of ε occurred at night, exceeding the daytime minima by a factor of 100. Although the nighttime convection deepened the surface mixed layer to only 0.3 MPa, the diurnal ε signal extended to at least 0.7 MPa, far beyond the mixed layer into the stratified medium (Figs. 2 and 6). Although the shut-off was almost simultaneous, the onset of high ε showed a delay with increasing depth (Fig. 2). The turbulent overturning scales ranged from less than 0.1 m during daytime to up to 10 m at night (Fig. 2) and tracked changes in the Ozmidov scale computed from the

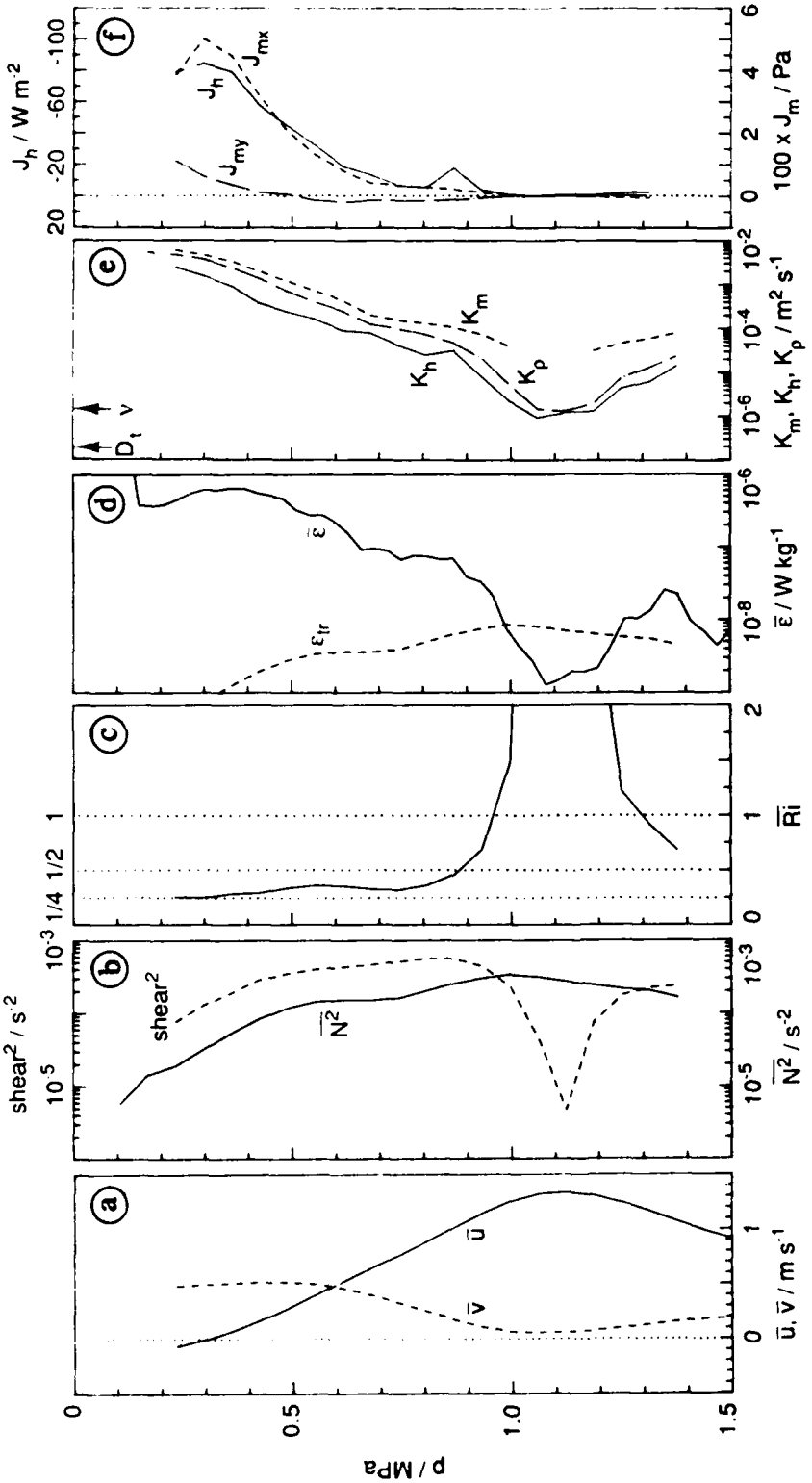

Fig. 4: Average profiles from the 4-1/2 day time series on the equator:
(a) Mean velocity profiles from the acoustic Doppler data (obtained by J.M. Toole), adjusted to match moored current meter data taken simultaneously at 20 km distance (D. Halpern, personal communication, 1986). The undercurrent core was located at 1.1 MPa. Above 0.3 MPa, the South Equatorial Current prevailed. The meridional current was strong above 0.8 MPa because the time series was located in a phase of maximum northward movement of the 21-day equatorial waves.
(b) Average $\bar{N}^2$ (filtered to match the Doppler data) and shear^2 = $(\partial\bar{u}/\partial z)^2+(\partial\bar{v}/\partial z)^2$. The mean stratification was strong even close to the surface; shear^2 was low in the core and paralleled $\bar{N}^2$ above.

(c) $\overline{Ri} = \bar{N}^2/\text{shear}^2$. The mean Richardson number was high in the core and low in the shear zones above and below. Note $Ri < 0.5$ above 0.85 MPa. These low values make the undercurrent unique among open ocean currents.

(d) Kinetic energy dissipation rate, $\bar{\varepsilon}$. $\bar{\varepsilon}$ was low in the core, close to the noise level of the data, and similar in magnitude to that found in the mid-latitude thermocline. Toward the surface, $\bar{\varepsilon}$ increased by 2-1/2 decades, and by 1 decade in the lower shear zone. The transition dissipation rate, $\varepsilon_{tr}=24.5\nu N^2$, exceeded ε where $Ri > 1$.

(e) Eddy coefficients for momentum K_m, heat K_h, and mass K_ρ, computed from the mean dissipation rates and mean gradients ($K_\rho = 0.2\ \varepsilon\ N^{-2}$; Osborn, 1980). The eddy coefficients were high near the surface, and very low in the core (compare with Munk's (1966) value of 10^{-4} m^2 s^{-1}, with the kinematic viscosity, ν, and with the thermal diffusivity, D_t). No realistic values of K_m could be obtained near the undercurrent core, because the dissipation method is not applicable where the mean shear vanishes. K_h and K_ρ were highly correlated; the offset could be due to uncertainties in the data.

(f) Average vertical turbulent heat flux, J_h, and momentum flux components, J_{mx} (E), J_{my} (N). The maximum J_h found near 0.3 MPa was comparable to the net surface heat flux. The mean surface wind stress during the measurements was 0.08 Pa, as compared with a total turbulent momentum flux of 0.05 Pa at 0.3 MPa. The fluxes dropped fast with increasing pressure, becoming negligible below about 0.7 MPa.

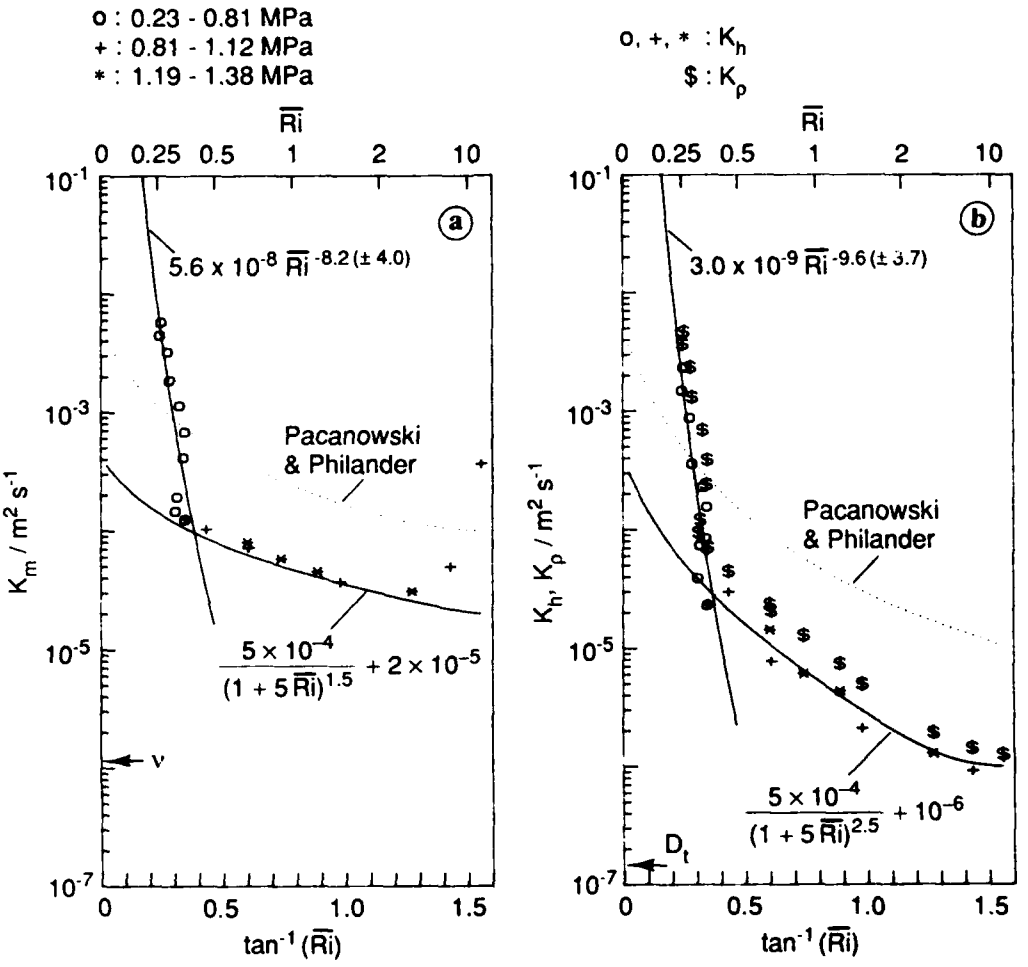

Fig. 5: K_m (a), K_h, and K_ρ (b) as functions of mean $\overline{Ri}$ from the time series. The data are the same as in Fig. 4e. K_m and K_h are marked "o" for the upper high-shear zone (23-81 m), "+" for the remainder of the zone above the undercurrent core (87-112 m), and "*" for the lower shear zone (119-138 m). For K_ρ "$" is used. The solid lines are fits to K_m and K_h, and dotted lines are the Pacanowski and Philander (1981) parameterization. Note the dramatic increase in the eddy coefficients with Ri decreasing toward 1/4. The shape and level of $K(Ri)$ at $Ri \gg 1/4$ are due to unresolved shear, especially from internal waves. (a) The dissipation method was not applicable near the current core; therefore K_m data from the core were ignored and the fit was extrapolated to high Ri somewhat arbitrarily. The approximate value of the molecular kinematic viscosity, ν, is indicated. (b) In the core, K_h and K_ρ, known to be overestimates, were less than a factor of 10 above the thermal diffusivity, D_t.

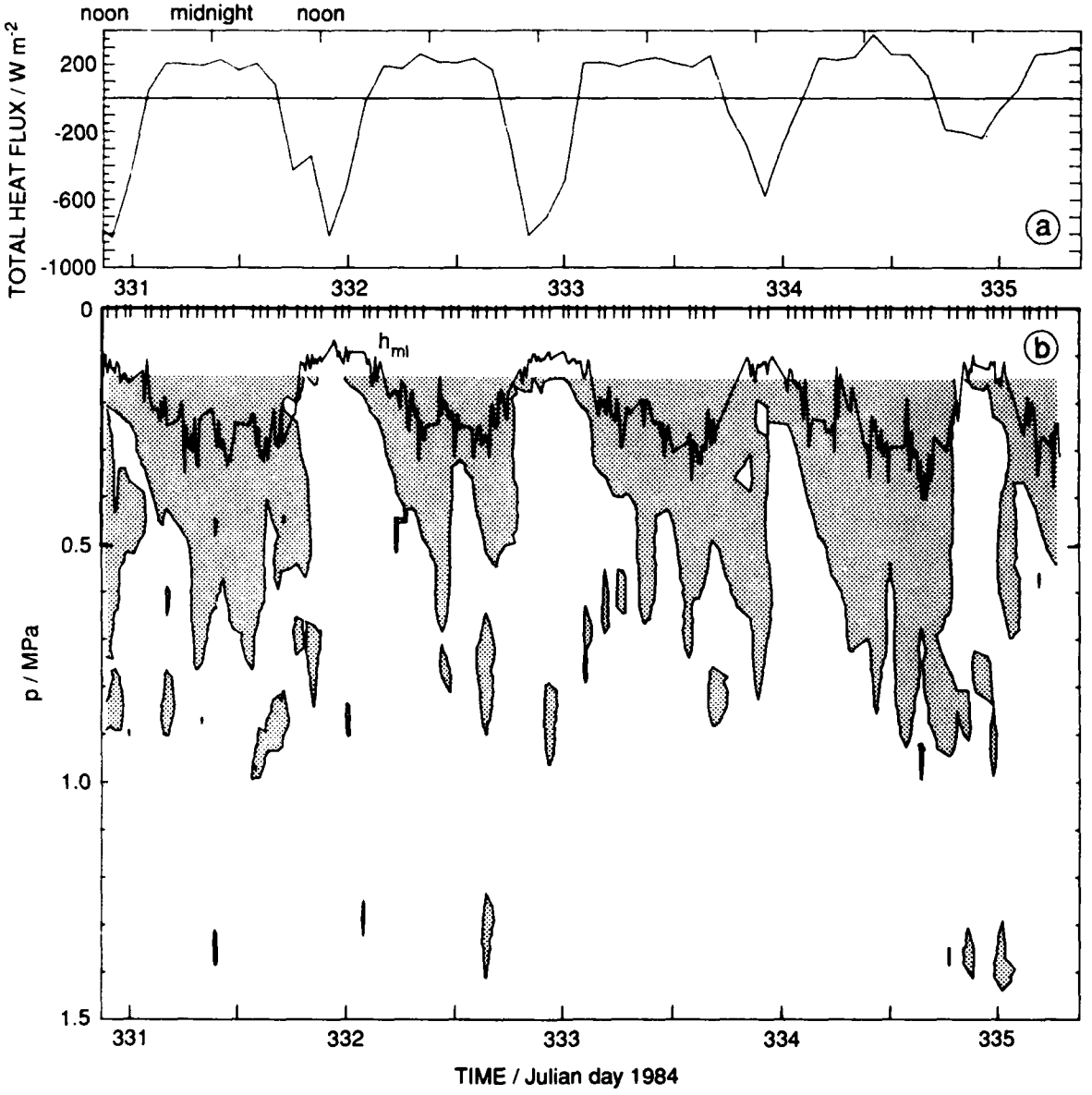

Fig. 6: (a) Surface heat fluxes, (b) mixed layer depth, and contour $\varepsilon = 10^{-7}$ W kg^{-1} of hourly averaged dissipation rate. The time series starts at 2100 GMT on 25 November. The heat fluxes were computed from the bridge log using bulk formulas. The ocean gained heat during local daytime and lost heat at night. The mixed layer depth varied in phase with the net surface heat flux. It reached 0.3 MPa at night, on average, 0.4 MPa occasionally. The diurnal cycle in dissipation rates reached much deeper than the cycle in mixed layer depth.

dissipation rate. Strong short-term variability occurred in the form of bursts of high dissipation, lasting up to a few hours and standing out of the background by a factor of 10 (Fig. 7). An example at 0400 local time in Fig. 2 shows the vertical coherence of the bursts. They appear to be an integral part of the deep diurnal signal in ε.

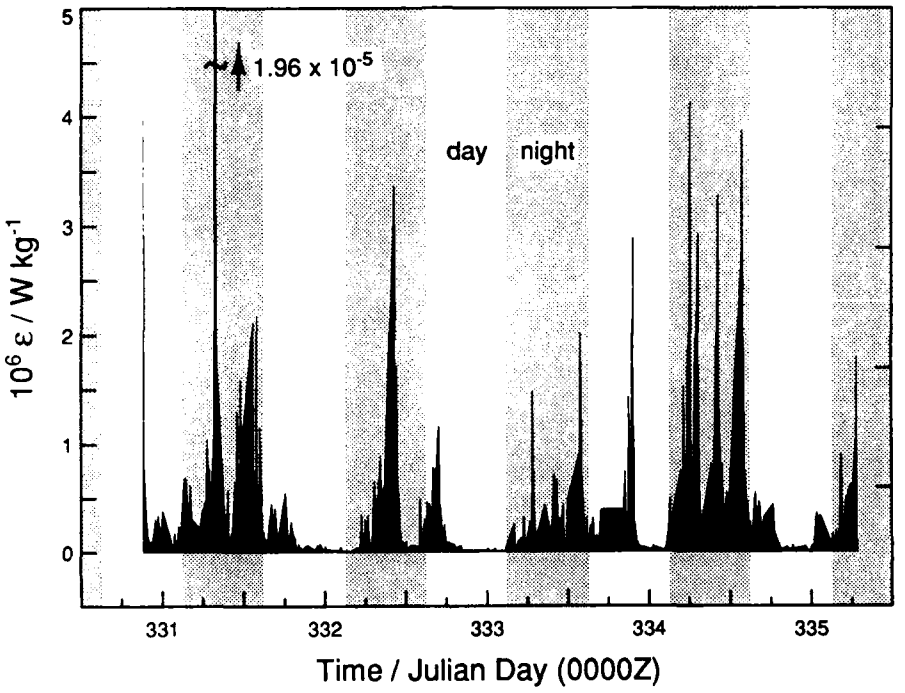

Fig. 7: ε averaged from 0.3 to 0.6 MPa as a function of time. The linear scale emphasizes "bursts" which mostly, but not exclusively, occurred at night, and lasted up to a few hours. The night sector (local time 1800-0600) is shaded.

Changes in Richardson number did not extend much below the mixed layer depth (Fig. 8), and therefore offer no explanation for the penetration of the diurnal ε cycle to beyond 0.7 MPa. As suggested in our first paper (Gregg et al., 1985), the deep diurnal cycle was possibly associated with high-frequency internal waves. Such waves and their breaking were observed off the equator during Tropic Heat (C. Paulson, personal communication 1987). The bursts observed in ε on the equator may well have been caused by breaking events.

A possible mechanism explaining the generation of high-frequency internal waves as well as a diurnal variation of their intensity is inspired by Bell (1978). Waves will be generated at the bottom of a mixed layer with irregular thickness directly from the vertical turbulent velocity and due to the relative, mean horizontal motion of the stratified water below. In this scenario, wave energy and momentum can be drawn both from the mixed layer turbulence and from the mean shear current. On the equator, the

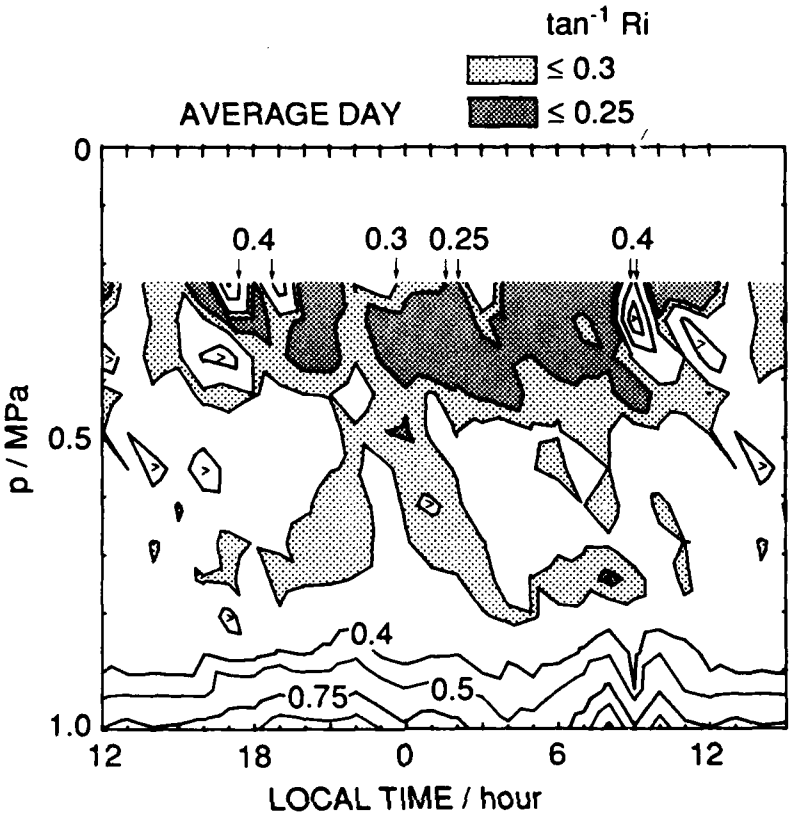

Fig. 8: Contours of $\tan^{-1} Ri$ for the daily average of the time series. The Ri values of the contours are 0.255, 0.309, 0.423, 0.546, and 0.932. Note the diurnal changes above 0.5 MPa, varying from <0.25 to >0.4. The higher values occurred in the early afternoon, and lasted only a few hours. This feature was well correlated with a similarly asymmetric variability of ε in the same pressure range. The signal was barely above the level of uncertainty, which was somewhat smaller than 20% in an rms sense. From 0.5 to 0.8 MPa, the fluctuations of Ri were smaller than above, and not correlated with fluctuations in ε.

mixed layer depth should be roughest during the nighttime convection, suggesting a diurnal variation in both forcing mechanisms. If true, this mechanism, together with the dissipation of the waves, provides a unique, complicated coupling of mixed layer and thermocline involving waves and turbulence.

MERIDIONAL STRUCTURE OF TURBULENCE

Extracting the meridional structure of turbulent dissipation is difficult. The strong temporal variability aliased the spatial variability in the north-south sections. Nevertheless, a pattern emerges when ε is analyzed in terms of the contributions within the mixed layer and within the thermocline. To assess the aliasing of the dominating diurnal signal, the data

at each latitude have been plotted as functions of local time (Fig. 9). Within ±1.5° of the equator a reasonable daily coverage was obtained, whereas farther away the distribution was sparse.

Comparing all mixed layer depths reveals maxima off the equator that were twice those on the equator (Fig. 10). Depths up to 0.4 MPa were found on the equator at night or just after dawn. Near noon h_{ml} was less than 0.2 MPa. Coverage off the equator was not as complete, but maximum values near 0.8 MPa were found at 2.5°N and 1.5°N, and 0.6 MPa occurred at 3°N and 1°S.

The occurrence of shallowest diurnal mixed layers on the equator is consistent with the equatorial density field (Fig. 11a), which is characterized by the "doming" of the isopycnals. The doming is directly related to the undercurrent through the beta effect. The average stratification above 1 MPa is generally much weaker outside the undercurrent, i.e., beyond ±1.5°, than in the undercurrent. The mixed layers should be deeper where the mean stratification is weaker, if the surface forcing does not counteract this tendency. In the climatological mean, the wind stress varies little across ±3° (Wyrtki, 1981), whereas the latent heat flux, the dominant contributor to the surface buoyancy flux, has a minimum at the equator (Weare et al., 1980). Thus, the mean mixed layer depth should indeed increase away from the equator.

In our data, local water mass shifts complicated this picture. No deep mixed layers were observed at and beyond 1.5°S. During the first section, a lens of warm and salty water enhanced the near-surface stratification, and so restricted mixed layer deepening. Later, the salty lens had been advected northward, and a rather deep mixed layer was found at 1°N (0.6 MPa). The adjacent station at 1.5°N during the last section was taken during the restratification phase so that h_{ml} was small. The temperature and salinity profile show that the nighttime mixed layer depth must have been about 0.65 MPa. Thus, disregarding the mentioned complications, mixed layer depths were observed to be up to two times deeper off, than at, the equator, with increases both south and north.

Using all our data to form the depth-integrated dissipation rate,

$$\varepsilon_I = \int_{-110}^{-15} \varepsilon \, dz \ ,$$

reveals a broad peak within 1.5° of the equator (Fig. 12). If only the contribution in the thermocline is considered, the peak is even more accentuated. The width indicates that this is the signature of mixing in the stratified high shear zone of the undercurrent (Figs. 11a,b). The pattern of ε_I was not simply an image of the surface forcing (Fig. 13), further substantiating our finding. Despite aliasing of the diurnal cycle, the pattern is shown in the first section, where between ±1° latitude the high dissipation occurred below the mixed layer. By contrast, most of the high dissipation at 2.5°N and 3°N was in deep mixed layers (Fig. 11c).

Our view differs from Moum et al. (1986), who concluded that dissipation was uniformly high across the entire equatorial zone (±3°) without examining the relative roles of dissipation in mixed layers and in the thermocline. Their data, as well as ours, show strong diurnal variations in turbulent dissipation rate on and off the equator.

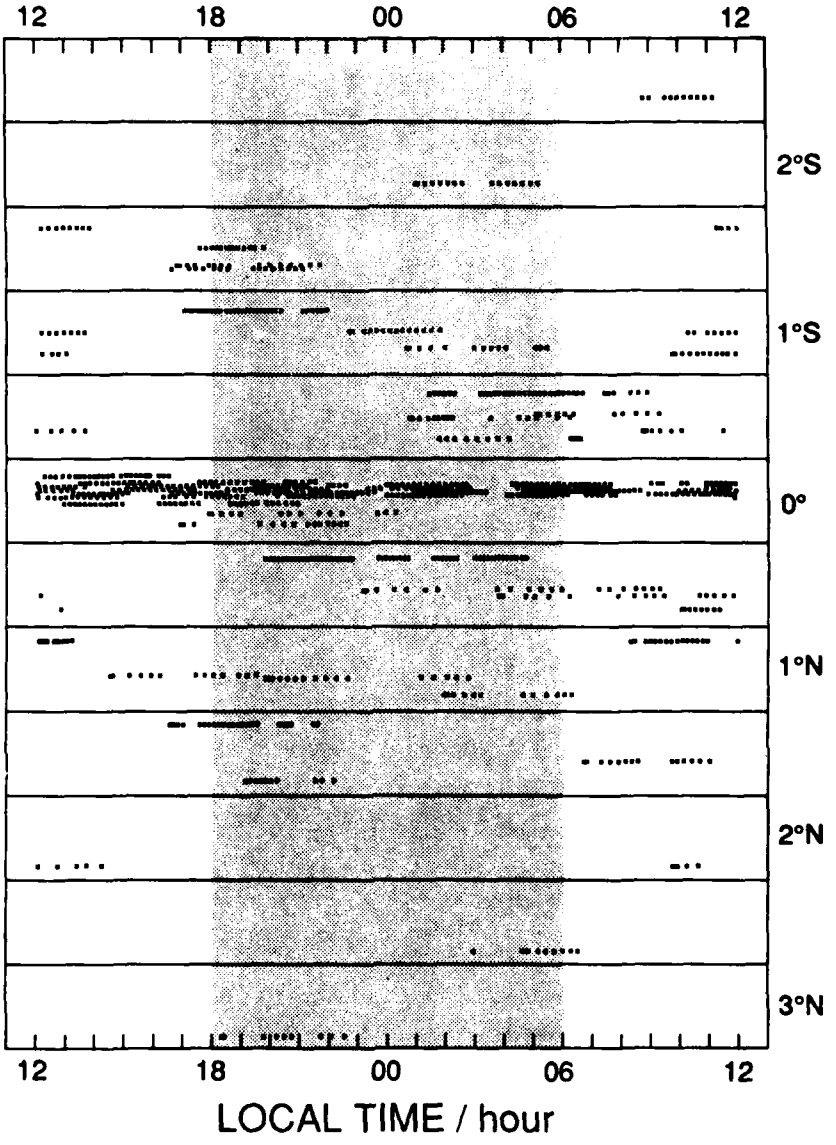

Fig. 9: Local time of microstructure drops as a function of latitude. The night sector from 1800 to 0600 local time is shaded. The vertical axis in the latitude boxes is time from Julian day 318, 0000Z, to 342, 0000Z. The graph shows that the local day was covered at least to some degree within ±1.5°. Outside, latitudes were occupied only once. The lack of nighttime measurements at 2°N and 2.5°S represents the most severe problem for the analysis.

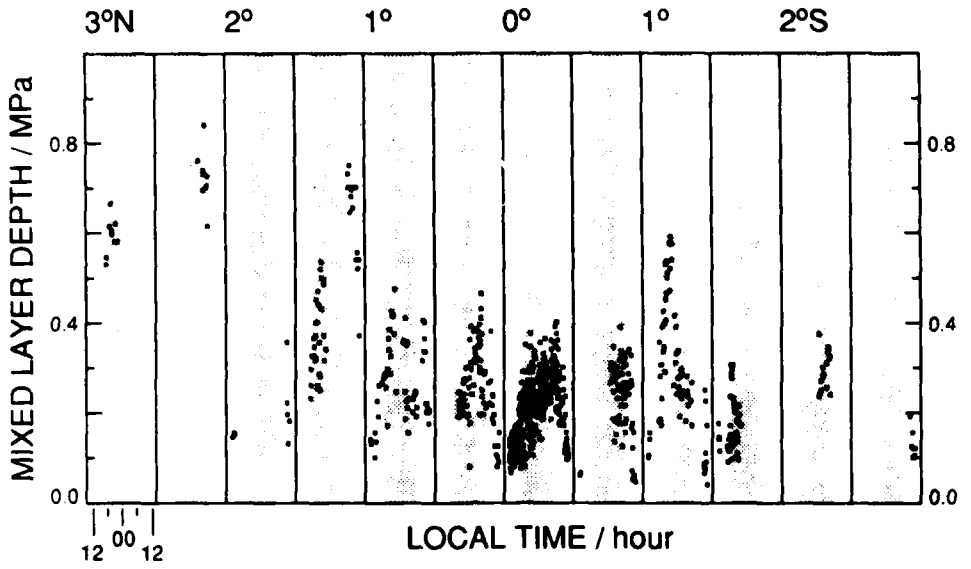

Fig. 10: Mixed layer depth as a function of latitude and local time. Wherever resolved, the data show a diurnal cycle in h_{ml}, indicating nighttime mixing and daytime restratification. The smallest maximum mixed layer depths were found on the equator. They clearly increased toward the north; this is less clear in the south. Partly there is a problem with poor coverage of the diurnal signal. More important, during the earlier part of the observation period, the doming of isopycnals was displaced toward the south, causing strong, near-surface stratification at southerly latitudes. Near the end of the experiment, the doming had been shifted north, and a deep mixed layer was found at 1°N.

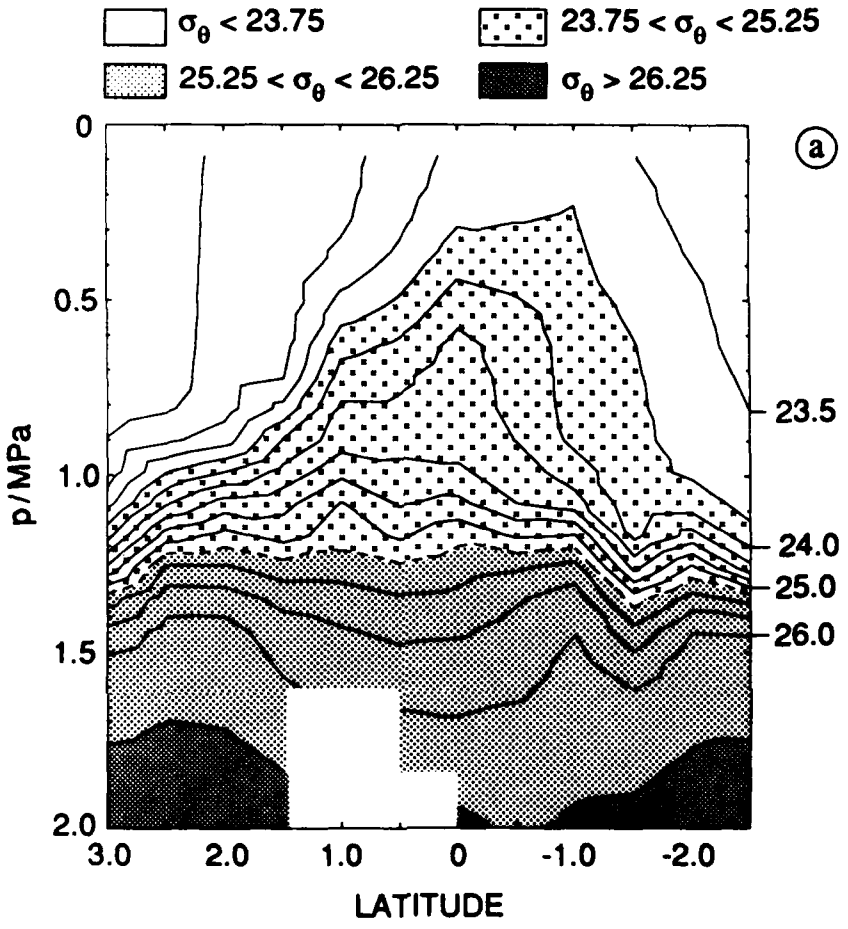

Fig. 11: First north-south section.
(a) Potential density. The contour interval is 0.25 kg m^{-3}. The dashed contour corresponds to the density level of the undercurrent core. The isopycnals show the usual equatorial doming. The minimum of surface density had been shifted south of the equator by the 21-day equatorial waves, resulting in an asymmetry. In relation to the doming, the stratification was weak in the top 0.8 MPa near the northern and southern end of the section, whereas nearly the whole column was stratified near the equator.

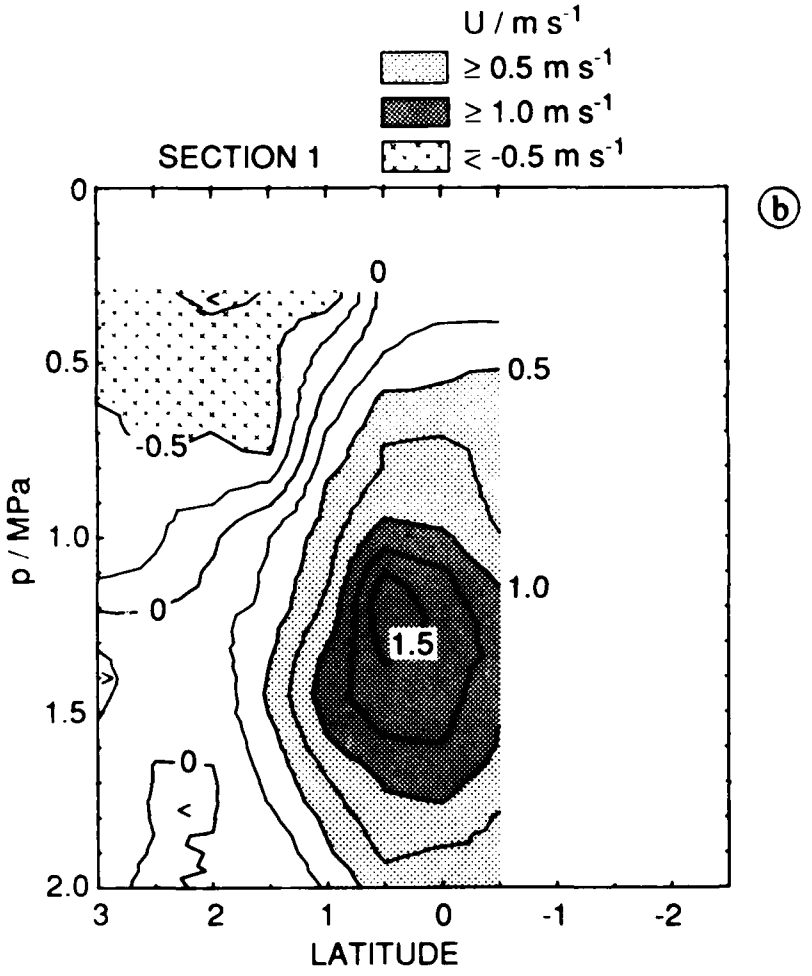

...zonal velocity from XCP data referenced to 5 MPa. Because of the proximity of the magnetic equator, no data could be obtained beyond ...5°S. During this section, the undercurrent core was located at ...5°N; later it moved to the equator. The contours show only part of the South Equatorial Current, which extended to and beyond the equator ... 1.25 MPa with speeds of about 0.5 m s^{-1}.

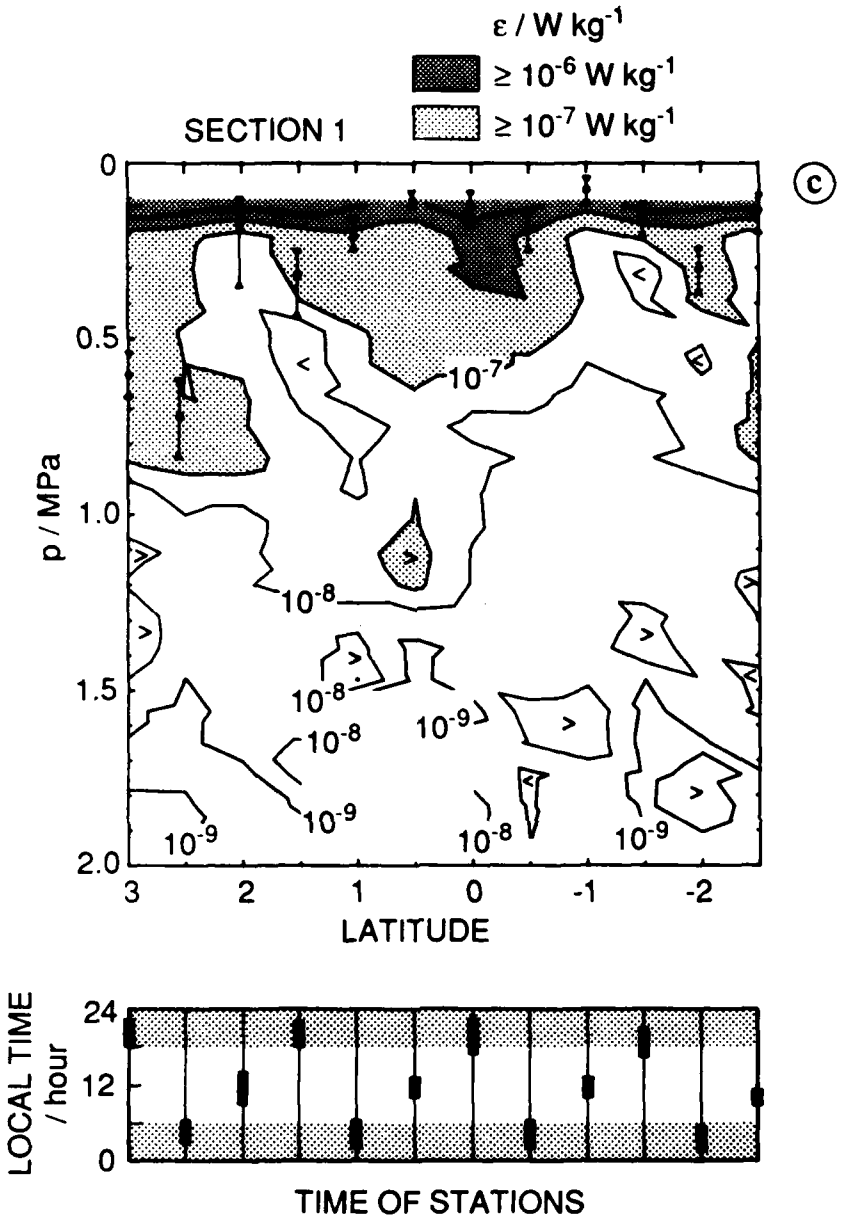

(c) Dissipation rate and mixed layer depth (minimum, mean, maximum, connected by a vertical bar). The pattern is biased by the unresolved diurnal cycle in ε. As a help for the interpretation, the time of the measurements is also indicated. In this section, high ε (> 10^{-7} W kg^{-1}) extended to larger depths near the northern and southern end, and near the equator. Note that the data at 0.5°N, taken in the undercurrent core, showed high values near local noon. At 3°N and 2.5°N most of the high ε zone was located in the mixed layer. There was no corresponding feature in the south, not only because the station at 2.5°S was occupied in the morning, but also because of the asymmetry of the density section (Fig. 11a). Near the equator, high ε extended deeper than the mixed layer both at night and during daytime.

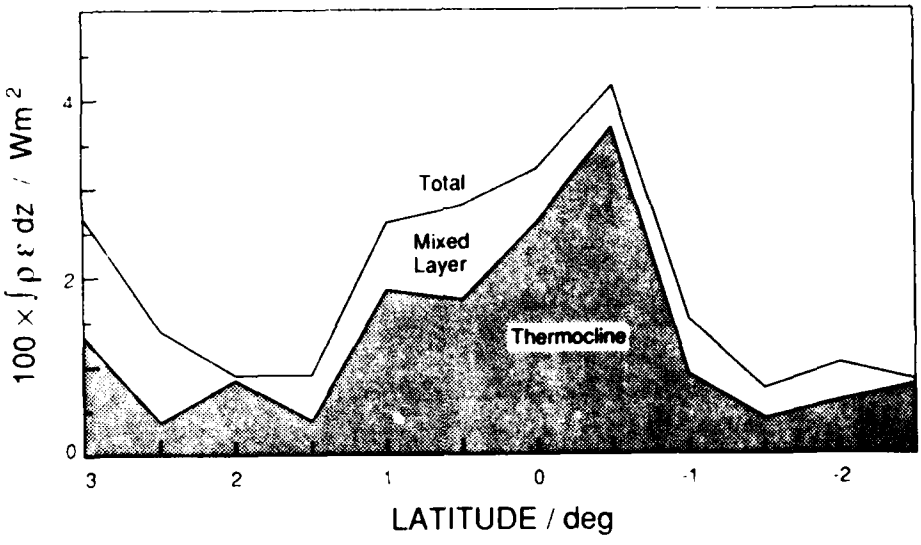

Fig. 12: Cruise average of vertically integrated kinetic-energy dissipation rate in the upper 0.15 to 1.1 MPa as a function of latitude, split into the contributions from the mixed layer and from the stratified column, below. The data were averaged from individual drops with $h_{uj} \geq 0.18$ MPa. The dominant diurnal variability of ε was covered only within ±1.5°; at higher latitudes positions were occupied only once. At 2°N and 2.5°S, measurements were taken only near local noon. The depth-integrated dissipation in the stratified layer had minima at ±1.5° and increased toward the equator. We interpret this equatorial maximum to be the signature of the undercurrent.

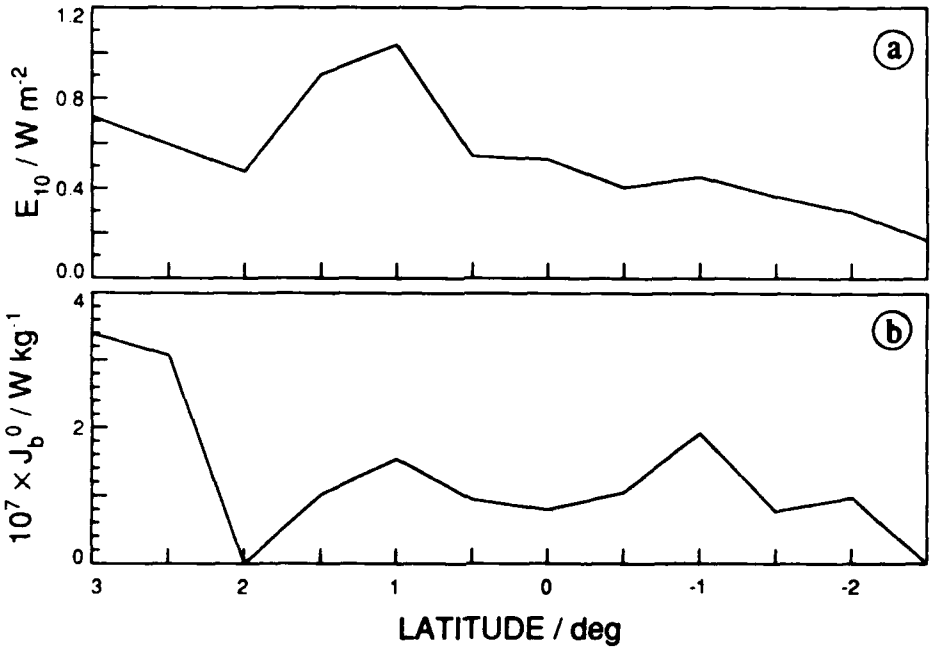

Fig. 13: Cruise average of surface forcing and shear as functions of latitude. (a) Surface wind work. (b) Surface buoyancy flux. Negative values (equivalent to a heat gain of the ocean) have been replaced by 0 prior to averaging. The two latitudes where only daytime measurements have been taken show up as $J_b^0 = 0$. The data were averaged in the same way as the turbulence data displayed in Fig. 12. It is not important how much the true spatial structure is represented, as the only concern is the correlation with the meridional patterns of turbulence parameters.

SUMMARY

During Tropic Heat, turbulent mixing was intense in the shear zone above the undercurrent core, producing a diapycnal heat flux of about 80 W m^{-2}, which is significant in the upper ocean heat budget. The flow was characterized by very low mean Richardson numbers, 0.25-0.4, and by dissipation rates varying inversely with $\overline{Ri}$. Eddy coefficients as functions of $\overline{Ri}$ rise dramatically when the Richardson number drops below 0.4.

At the equator, a diurnal cycle changed ε by a factor of 100 above about 0.7 MPa, dominating the variability of the dissipation rate. Nighttime convection probably caused the diurnal cycle, at least in the mixed layer. The extension of the cycle deep into the thermocline was probably produced by internal waves generated at the base of the mixed layer.

When studying the meridional structure of turbulence, it is imperative to distinguish between the surface mixed layer and the thermocline. Most depth-integrated dissipation in the top 1.1 MPa came from the thermocline at the equator and from deep mixed layers off the equator. The high dissipation signature in the thermocline coincides with the meridional extent of the undercurrent.

A number of questions remain open, such as the the role of high-frequency internal waves in the deep diurnal cycle of turbulence. These will be studied in a second field experiment in April 1987.

ACKNOWLEDGMENTS

This work was supported by the National Science Foundation as part of the Tropic Heat program. The acoustic Doppler current meter data were taken by John Toole of the Woods Hole Oceanographic Institution. Contribution No. 1691 of the School of Oceanography, University of Washington, Seattle, WA 98105.

REFERENCES

Bell, T. H., 1978: Radiation damping of inertial oscillations in the upper ocean. J. Fluid Mech., 88, 289-308.

Chereskin, T. K., J. N. Moum, P. J. Stabeno, D. R. Caldwell, C. A. Paulson, L. A. Regier, and D. Halpern, 1986: Fine-scale variability at 140°W in the equatorial Pacific. J. Geophys. Res., 91, 12,887-12,897.

Eriksen, C. C., 1985: The Tropic Heat Program: An overview. EOS, 66, 50-52.

Gargett, A. E., and T. R. Osborn, 1981: Small-scale shear measurements during the Fine and Microstructure Experiment (Fame). J. Geophys. Res., 86, 1929-1944.

Gregg, M. C., H. Peters, J. C. Wesson, N. S. Oakey, and T. J. Shay, 1985: Intensive measurements of turbulence and shear in the equatorial undercurrent. Nature, 318, 140-144.

McCreary, J. P., 1981: A linear, stratified ocean model of the equatorial undercurrent. Phil. Trans. Roy. Soc. London, A, 298, 603-635.

Moum, J. N., and D. R. Caldwell, 1985: Local influences on shear-flow turbulence in the equatorial ocean. Science, 230, 315-316.

Moum, J. N., D. R. Caldwell, C. A. Paulson, T. K. Chereskin, and L. A. Regier, 1986: Does ocean turbulence peak at the equator? J. Phys. Oceanogr., 16, 1991-1994.

Munk, W. H., 1966: Abyssal recipes. Deep-Sea Res., 13, 707-730.

Niiler, P., 1982: Tropic Heat: A study of the tropical Pacific upper ocean heat, mass, and momentum budgets. Unpublished manuscript, Oregon State University, Corvallis, Oregon.

Osborn, T.R., and C. S. Cox, 1972: Oceanic fine structure. Geophys. Fluid Dyn., 3, 321-345.

Osborn, T.R., 1980: Estimates of the local rate of vertical diffusion from dissipation measurements. J. Phys. Oceanogr., 10, 83-89.

Pacanowski, R.C., and S. G. H. Philander, 1981: Parameterization of vertical mixing in numerical models of tropical oceans. J. Phys. Oceanogr., 11, 1443-1451.

Peters, H., D. R. Caldwell, J. N. Moum, and M. C. Gregg, 1987a: Equatorial vertical mixing. Further Progress in Equatorial Oceanography: A Report of the U.S. TOGA Workshop on the Dynamics of the Equatorial Oceans. Held in Honolulu, HI, August 11-15, 1986, E. Katz and J. Witte, Eds., Nova University Press, Ft. Lauderdale.

Peters, H., M. C. Gregg, and J. M. Toole, 1987b: On the parameterization of equatorial turbulence. J. Geophys. Res. (submitted).

Toole, J. M., H. Peters, and M. C. Gregg, 1987: Upper ocean shear and density variability at the equator during TROPIC HEAT. J. Phys. Oceanogr. (in press).

Weare, B. C., P. T. Strub, and M. D. Samuel, 1980: Marine climate atlas of the tropical Pacific Ocean. Contribution in Atmospheric Science No. 20, University of California, Davis.

Wyrtki, K., 1981: An estimate of equatorial upwelling in the Pacific. J. Phys. Oceanogr., 11, 1205-1214.

ON THE ZONAL MOMENTUM BALANCE AT THE EQUATOR

T. M. Dillon, J. N. Moum, T. K. Chereskin, and D. R. Caldwell

College of Oceanography, Oregon State University,
Corvallis, Oregon, 97331

ABSTRACT

The conventional view of equatorial dynamics requires that the zonal equatorial wind stress be balanced, in the mean, by the vertical integral of "large-scale" terms, such as the zonal pressure gradient, mesoscale eddy flux, and mean advection, over the upper few hundred meters. It is usually presumed that the surface wind stress is communicated to the interior by turbulent processes. Turbulent kinetic energy dissipation rates measured at 140°W during the TROPIC HEAT experiment and a production rate-dissipation rate balance argument have been used to calculate the zonal turbulent stress at 30 m to 90 m depth. The calculated turbulent stress amounts to only 20% of the wind stress at 30 m depth, and decreases exponentially with depth below 30 m. Typical large-scale estimates of the zonal pressure gradient, mesoscale eddy flux, and advection have a depth scale larger than the turbulent stress, and are inconsistent with the vertical divergence of the stress as estimated from the dissipation rate measurements. It is concluded that either

(1) the measured estimates of dissipation rate are too small,
(2) the actual large-scale zonal pressure gradient, mesoscale eddy flux, and advection during our observation period were highly atypical and had a very shallow depth scale,
(3) some process other than the simple diffusion of momentum through shear instabilities is transporting the momentum, or
(4) the assumption of a production-dissipation balance in the turbulent kinetic energy budget is incorrect.

The first two possibilities are unlikely.

1. INTRODUCTION

Two important features of the upper 100 m of the equatorial ocean are large vertical shears of zonal velocity and energetic turbulence. The Equatorial Undercurrent flows toward the east beneath the westward-flowing South Equatorial Current. Between these two currents, vertical shears as large as 0.02 s^{-1} are commonly observed. The most recent measurements of equatorial turbulence were done as part of the TROPIC HEAT experiment, during which one ship occupied an equatorial station from November 19 to December 1, 1984 (Moum and Caldwell, [1985], hereafter MC), and another ship occupied a station a few tens of km distant from November 25 to 30 (Gregg et al [1985], hereafter GPWOS). Both groups took vertical profiles 24 hours per day. New records were set for the number of profiles collected, with MC obtaining 1749 good casts, and GPWOS obtaining 385 good casts.

The large number of profiles collected in TROPIC HEAT make possible the calculation of some elementary balances of the momentum budget in the upper 100 m. The most important contributions to the zonal momentum budget at the equator are the zonal convergence of zonal momentum, upwelling of eastward momentum, the zonal pressure gradient, the divergence of the mesoscale eddy flux, and the turbulent stress (Bryden and Brady, 1985). Balancing these factors leads to the conservation equation

$$U\frac{\partial U}{\partial x} + W\frac{\partial U}{\partial z} = -\frac{1}{\rho}\frac{\partial P}{\partial x} - \frac{\partial \overline{U'U'}}{\partial x} - \frac{\partial \overline{U'V'}}{\partial y} - \frac{\partial \bar{F}_x}{\partial z}, \qquad (1)$$

where U and V are mean zonal (positive eastward) and meridional (positive northward) velocities, P is mean pressure, ρ is density, x is the zonal direction (positive x eastward), and F_x is the vertical turbulent flux of zonal momentum. By "mean", we intend an average over several months to years, and thousands of kilometers; U' and V' are zonal and meridional velocity fluctuations in the mesoscale eddy band (i.e., fluctuations with time scales from a day to several weeks, length scales from tens of kilometers to hundreds of kilometers). Contributions of small-scale horizontal turbulent fluxes (i.e., turbulent fluxes with length scales smaller than tens of meters) are neglected on the grounds that horizontal velocity gradients are orders of magnitude smaller than vertical velocity gradients. The overbar indicates an average over several months to several years. It is assumed that the mean acceleration of fluid and the mean meridional velocity are small. The zonal balance of forces on a column of fluid of unit surface area extending from z=a to z=b is obtained by vertically integrating and rearranging eq.(1):

$$\int_a^b \left(-\frac{1}{\rho}\frac{\partial P}{\partial x} - U\frac{\partial U}{\partial x} - W\frac{\partial U}{\partial z} - \frac{\partial \overline{U'U'}}{\partial x} - \frac{\partial \overline{U'V'}}{\partial y}\right) dz - \bar{F}_x(b) + \bar{F}_x(a) = 0,$$

or

$$ZPG + ZD + UW + EF - \bar{F}_x(b) + \bar{F}_x(a) = 0 \qquad (2)$$

where -ZPG is the integral of the zonal pressure gradient divided by density, -ZD is the integral of the zonal divergence of mean zonal momentum, -UW is the integral of the upwelling of zonal momentum, and -EF is the integral of the mesoscale eddy flux.

If the momentum flux in the fluid interior is due to turbulent processes, $-F_x(z)$ equals $\tau(z)/\rho$, where τ is the zonal turbulent stress; at the sea surface, $-F_x(0)$ equals τ_0/ρ, where τ_0 is the zonal surface wind stress. An eddy viscosity K_m is defined by

$$- F_x(z) = K_m \langle \partial u/\partial z \rangle, \quad z < 0 , \qquad (3)$$

where the brackets < > denote some averaging process, for example, an ensemble average, an areal average, or perhaps a Monte-Carlo average. If a time average is used, it is an average over some arbitrary "short" time, longer than the time scale of turbulent fluctuations, but shorter than the overbar average. For the measurements described below, hourly averages of turbulence quantities are used, although it is more correct to think of these as ensemble averages rather than time averages.

Bryden and Brady (1985) (hereafter BB) made an order of magnitude estimate of K_m by assuming that the dominant term in eq.(2) is ZPG, the zonal pressure gradient term. Using historical measurements of $\partial P/\partial x$ and wind stress, BB estimated a mean equatorial eddy viscosity at 75 m depth of 1.7×10^{-3} m^2/s, an order of magnitude larger than has been estimated from dissipation measurements (GPWOS).

Our approach is to extend BB's method. We will use BB's estimates of the first four terms in eq.(2), and use MC's estimates of $K_m(\partial u/\partial z)$ and the surface wind stress to evaluate the last two terms of eq.(2) (see Fig. 1 for a schematic representation). We seek to determine whether eq.(2) can be balanced in this manner, and if not, which of the assumptions might be at fault.

In section 2, we review the dissipation method for estimating turbulent stresses. In section 3, we evaluate both sides of eq.(2), and are unable to find equality. At first sight, this approach seems peculiar. BB's estimates are for the mean circulation over a wide longitude range, while MC's turbulence data is for a single 12-day period at one location several years after BB's estimates were made. In principle, there is no reason to expect a balance to be achievable. BB's estimates can, however, be viewed as "typical" estimates, and the difference between BB's estimates and the actual realization can be viewed as an "anomaly". In section 4, we ask whether or not the zonal momentum budget residual can be explained by a <u>reasonable</u> anomaly in large-scale terms, and examine the consequences if reasonable anomalies cannot be found.

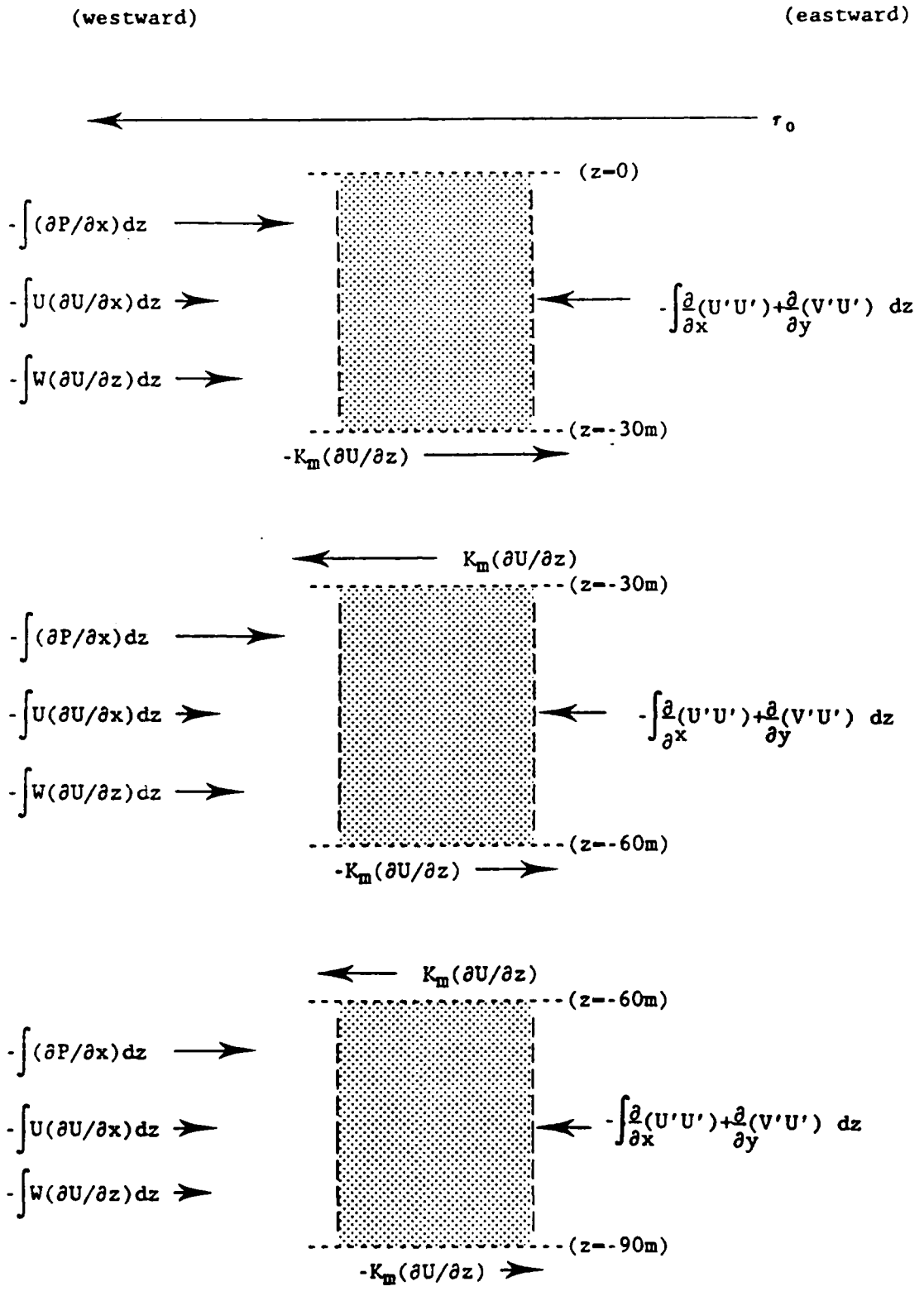

Fig. 1. Schematic view of balance of forces per unit surface area on control volumes in the upper three 30 m depth intervals. The terms represented are from eq.(2). The arrow length for each term is approximately scaled by the corresponding values in Table 1.

2. THE DISSIPATION METHOD

Estimates of eddy viscosities, diffusivities, and the turbulent fluxes of momentum and heat have been made using measurements of ϵ, the turbulent kinetic energy dissipation rate (e.g., Osborn, 1980; Crawford, 1982; GPWOS). The dissipation rate is calculated from measurements of large wavenumber vertical shears (vertical scale roughly between 0.01 and 1 m). Flux estimates are based on the turbulent kinetic energy equation (Wyngaard and Cote, 1971; Osborn, 1980; Dillon, 1984, or any standard text):

$$\frac{\partial \langle q^2 \rangle}{\partial t} + W\frac{\partial \langle q^2 \rangle}{\partial z} = \mathcal{P} - \epsilon + B - \frac{\partial}{\partial z}\{\langle w'p'/\rho \rangle + \langle w'q^2 \rangle\} . \qquad (4)$$

Here, q^2 is the turbulent kinetic energy, W is the mean vertical velocity, and $\mathcal{P}$ is the rate of production of turbulent kinetic energy by shear instabilities,

$$\mathcal{P} = - \langle w'u' \rangle \langle \partial u/\partial z \rangle - \langle w'v' \rangle \langle \partial v/\partial z \rangle \ ; \qquad (5)$$

ϵ is the rate of kinetic energy dissipation, $B = (g/\rho)\langle w'\rho' \rangle$ is the buoyancy flux, u' v' and w' are zonal, meridional, and vertical velocity fluctuations, and p' is a pressure fluctuation. In obtaining eq.(4), it has been assumed that gradients of terms like q^2, $\langle p'u_i' \rangle$, and $\langle w'q^2 \rangle$ are much larger in the vertical than in the horizontal because the forcing processes are, in an average sense, horizontally uniform over the region being considered.

The next step in using eq.(4) to obtain eddy viscosities is to assume the time scale for changes in the shear production is long compared to the time scale for adjustment of the fluctuation field, i.e., that $\partial q^2/\partial t$ is small compared to $\mathcal{P}$. This assumption makes no statement about the state of the turbulence in any single observation. In any single realization of a particular overturning event, $|\partial q^2/\partial t|$ may be much greater than $\mathcal{P}$ and the fluctuation field may be rapidly growing or rapidly decaying, yet the steady-state assumption is reasonable, provided only that enough samples are included in the average. An analogy may be useful here: the ensemble average of sea level changes slowly, even though any instantaneous measurement at a point may show rapid variations.

The second term on the left of eq.(4) is the advection of turbulent kinetic energy by a mean vertical velocity W. In many parts of the ocean this term may be safely neglected because W is small, but in equatorial waters, there is a net upwelling, with W in the range of 1 to 3 meters per day (BB). We can scale $W\langle \partial q^2/\partial z \rangle$ as Wq^2/h, where h is a typical equatorial mixing layer depth, say 50 m. Since ϵ scales as q^3/ℓ, where ℓ

is the typical size of an overturn (say, 1 to 5 m), we estimate that $W\langle\partial q^2/\partial z\rangle/\epsilon \approx (W\ell)/(hq) \approx 10^{-6}$. This term can be safely neglected.

Osborn (1980) argues that the last two terms on the right of eq.(4) are divergences, and hence can affect only the distribution of q^2 in space, not the total amount of turbulent energy, for stably stratified turbulent flows. This argument may be more nearly correct for the divergence of $\langle w'q^2\rangle$ than for $\langle w'p'\rangle/\rho$, because the former term is just the advection of turbulent kinetic energy by turbulent vertical velocity fluctuations, while the latter term is the internal wave energy flux. There is no a priori reason to believe that the amount of energy radiated away by internal waves is small, but we shall for the present assume that it is, and later will discuss the consequences of this assumption.
We are left with the common assumption that the rate of production of turbulent kinetic energy is balanced by its rate of dissipation plus the buoyancy flux. Experiments in the laboratory and in the atmospheric boundary layer (Osborn [1980] reviews some of these) indicate that the flux Richardson number, $R_f = B/\mathcal{P}$, is small, probably never exceeding 0.2. On these grounds, we neglect B in eq.(4), and arrive at a production-dissipation balance:

$$\mathcal{P} = \epsilon \quad . \tag{6}$$

If we define an eddy viscosity by

$$\langle u'w'\rangle = -K_m\langle\partial u/\partial z\rangle \ , \quad \langle v'w'\rangle = -K_m\langle\partial v/\partial z\rangle, \tag{7}$$

we can use eqs.(5), (6), and (7) to obtain the eddy viscosity and zonal shear stress in terms of measured dissipation rates:

$$K_m = \frac{\epsilon}{\langle\partial u/\partial z\rangle^2 + \langle\partial v/\partial z\rangle^2} \ , \tag{8}$$

$$-F_x = -\langle u'w'\rangle = K_m\langle\partial u/\partial z\rangle = \frac{\epsilon\langle\partial u/\partial z\rangle}{\langle\partial u/\partial z\rangle^2 + \langle\partial v/\partial z\rangle^2} \tag{9}$$

3. EQUATORIAL TURBULENCE ESTIMATES

Turbulent kinetic energy dissipation rates were determined from measurements made using the Rapid Sampling Vertical Profiler (RSVP; Caldwell, Dillon and Moum, 1985) and were averaged over one-hour time intervals and 12-m depth intervals. The zonal shear was measured using a hull-mounted Acoustic Doppler Current Profiler (ADCP) and averaged over the same time and depth intervals (the depth averaging is an inherent limitation to the ADCP; our averaging interval was chosen to obtain independent shear estimates). An evaluation of the ADCP measurements made from the R/V WECOMA during the TROPIC HEAT experiment may be found in

Chereskin, Halpern and Regier (1986). K_m and $-F_x$ were calculated from the one-hour average dissipation rates and shears, and then averaged over the entire 12-day period. GPWOS calculated 4-day average values for ϵ, and then used an estimate of the mean shear based on 8 XCP casts.

MC's dissipation rate measurements begin at 10 m depth and extend to 110 m. The 12-day average dissipation rate is nearly constant in the upper 30 m, but falls off exponentially in the 30 m to 70 m depth range (Fig. 2). The upper ocean is continuously stratified. The 12-day average buoyancy frequency is smallest near the surface, and increases from 1 cph at 10 m depth to about 7 cph at 60 m depth; from 60 m to 110 m, the buoyancy frequency is roughly constant at 7 to 8 cph. The estimates of K_m and $-F_x$ using eq.(8) begin at 33 m because that is the shallowest depth at which the shear could be independently determined from ADCP measurements. The momentum flux and eddy viscosity are largest nearest the surface, and monotonically decline with increasing depth (Fig. 3,4). GPWOS dissipation rates are somewhat larger than those measured by MC; the precise reason for the difference is unknown at present, but may be a result of different algorithms for calculating the dissipation rate.

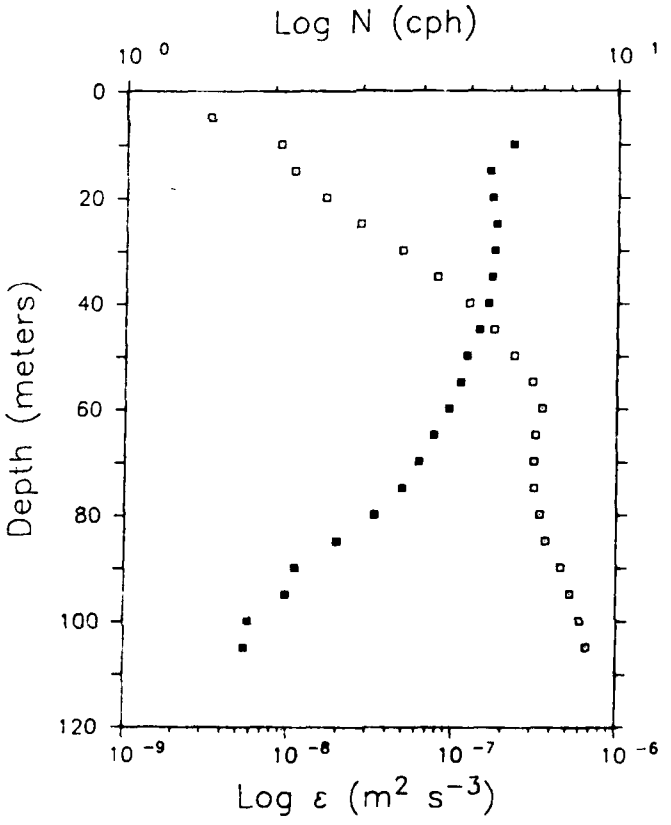

Fig. 2. Turbulent kinetic energy dissipation rates (solid square) and buoyancy frequency (open square) averaged over 12 days using Moum and Caldwell's (1985) data.

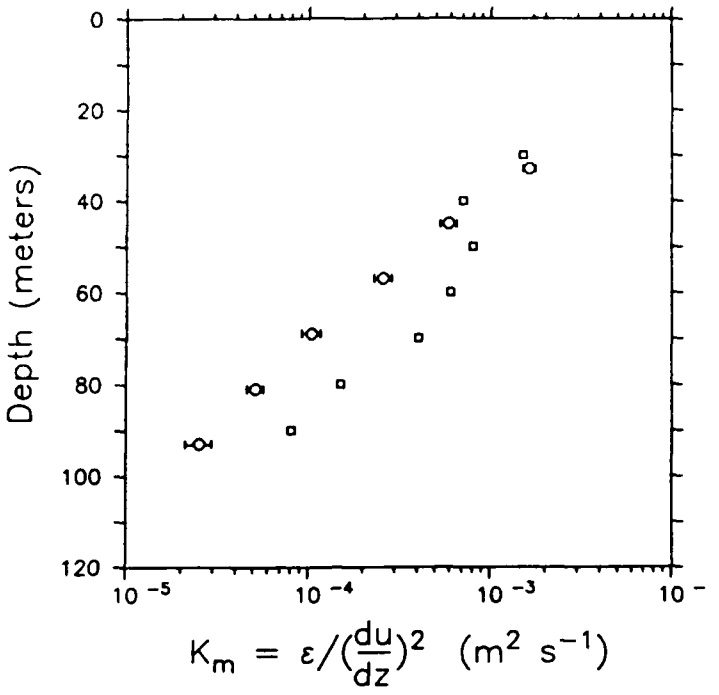

Fig. 3. Eddy viscosity estimates, K_m, vs depth. Boxes are from GPWOS. The open circles were estimated from eq.(8) using hourly averages of dissipation and velocity shears, and averaged over the 12-day station. The confidence limits of ±1 standard deviation were found from a bootstrap test using the parent population of the 288 hourly-averaged samples at each depth bin. Distributions of bootstrapped means are approximately Gaussian, and 68% of the values lie within the plotted confidence limits.

The shears used by GPWOS are from 8 XCP profiles made during their 4-day station and these do not agree in detail with the overlapping 4-day average from the MC data set. MC's eddy viscosities are surprisingly small; BB's estimate at 75 m is twenty times larger than the eddy viscosity estimated from MC's data using eq.(9).

Wind stress was calculated from R/V WECOMA observations. Wind speed and direction were recorded at 2 minute intervals, and first averaged over an hour. Atmospheric stability was determined from surface heat flux estimates using measured total downward solar radiation, the measured sea surface temperature, and humidity (measured with a dew-point hygrometer). Large and Pond's (1981) iterative bulk-aerodynamic procedure, which provides drag coefficients corrected for atmospheric stability and sensor height, was used to calculate the zonal stress. The hourly stress was then used to calculate τ_0, the average zonal stress. For the 12-day station, $\tau_0 = 0.097\ N/m^2$. The standard deviation was $0.030\ N/m^2$, and the sampling error in the mean is $0.002\ N/m^2$.

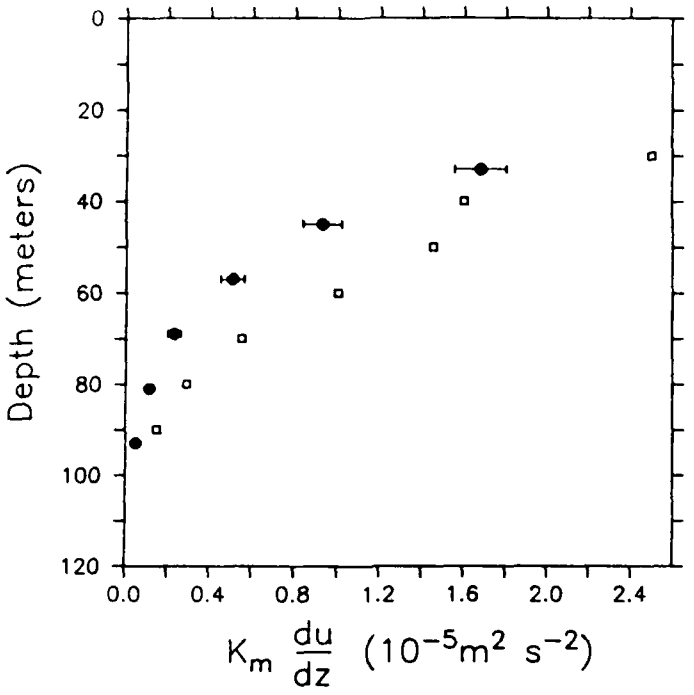

Fig. 4. Zonal component of the turbulent momentum flux estimated using eq.(9). Boxes are from GPWOS. Solid circles are from hourly averages of dissipation and vertical shears averaged over the 12-day station. Confidence limits are as in Figure 3.

Large and Pond (1981) found good agreement between stability-corrected bulk stress estimates, and direct eddy correlation measurements. They list an uncertainty of 30% for daily average bulk estimates, with the largest discrepancies noted when winds were rapidly rising or falling; others have noted deficiencies in the bulk method when the relative wind/wave direction changes. The wind speed was nearly constant over the 12 days spent on station, ranging between 6 and 12 m/s (see Moum and Caldwell [1985] for a plot), with no rapid changes of direction, and an infinite fetch. We therefore expect the WECOMA bulk estimates to have an uncertainty smaller than 30%; conservatively, we place the systematic uncertainty at 20%, and round the stress estimate to 0.10 N/m^2.

Surface stress must be continuous across a fluid boundary, assuming surface tension is negligible. Much of the surface stress can be taken up by the surface wave field in cases where the fetch is small. If surface wave transport were an appreciable part of the momentum budget in the infinite fetch case, however, the growth of the wave field would be unbounded. When the fetch is large, as in the tropical Pacific, surface wave transport must play a small role in the average zonal momentum budget.

The 12-day average stress $F_x(z)$ is reasonably well described by

$$-F_x(z) = \tau_0 \, e^{z/z_\tau} \qquad (10)$$

in the 30 m to 90 m depth range. The shallowest (33 m) estimate of the turbulent momentum flux is much smaller than τ_0. The shear above 100 m does not vary much with depth, and the eddy viscosity and dissipation rate, as well as F_x, have an approximately exponential depth dependence. The scale depth for the divergence of F_x is z_τ = 18 m, surprisingly small. We have no dynamical reason why ϵ, K_m, and F_x should be approximately exponential; rather, an exponential profile is simply a convenient way of summarizing the measurements. The fact that eq.(10) intercepts the surface at the measured surface stress is probably circumstantial. The exponential profile in eq.(10) simply illustrates a surprisingly small effective penetration depth for the surface stress.

4. A MOMENTUM IMBALANCE?

Mean zonal pressure gradient and advective accelerations were calculated by BB from a diagnostic model of equatorial circulation. The horizontal eddy flux of zonal momentum was estimated by Bryden, Brady and Halpern (1986; hereafter, BBH) using moored current meter arrays near 152°W from April 1979 to June 1980, and near 110°W from January 1979 to October 1981. Covariances were calculated using daily-average velocity measurements extending from the upper 15-20m to 250m depth. The BB and BBH estimates were made based on measurements of more than a year duration, and we interpret them here as "typical" estimates of large-scale quantities. The BB and BBH estimates are presented with the turbulence estimates in Table 1.

The dominant term estimated by BB and BBH is ZPG, the vertical integral of the zonal pressure gradient. The contribution to zonal momentum from upwelling (UW) is about half as large as the ZPG, and is positive in the upper 90 m. The contribution from large-scale eddies, EF, is about 2/3 of the ZPG, and is negative, reinforcing the wind stress and countering the ZPG. The only term small relative to the ZPG is ZD, the mean zonal divergence of zonal momentum.

MC's turbulence measurements extend from roughly 30m to 90m, and we have divided the upper ocean into 3 sections: 0-30m, 30m-60m, and 60m-90m (Table 1). We cannot expect to balance eq.(2) exactly, and so rewrite it with a residual term, R, representing the imbalance:

$$ZPG + ZD + UW + EF + \tau(b)/\rho - \tau(a)/\rho = R \qquad (11)$$

Here, $\tau_0(z)/\rho = -F_x(z)$ represents wind stress at the surface $z = 0$, and is estimated as $K_m\langle\partial u/\partial z\rangle$ in the fluid interior; a represents the depth of the top of each layer, and b represents the bottom. The right side of eq.(11) includes all of the terms we are unable to estimate, including the local acceleration $\partial u/\partial t$, as well as local anomalies in the zonal

Table 1. Momentum budget for the upper 90 m of the equatorial ocean in three 30 m segments. Units are 10^{-6} m^2/s^2. ZPG, ZD, UW, and EF, taken from Bryden and Brady (1985) and Bryden, Brady and Halpern (1986), are "typical" estimates of large-scale terms. The stress estimates are from Moum and Caldwell's (1985) TROPIC HEAT dissipation rate measurements. The uppermost 30 m segment has a large residual compared to the ZPG.

TABLE 1

Layer Depth Range	0 - 30m	30m - 60m	60m - 90m
$ZPG = \int -\frac{1}{\rho}\frac{\partial P}{\partial x}\,dz$	14	12	8
$ZD = \int -U\frac{\partial U}{\partial x}\,dz$	-0.9	-0.6	2
$UW = \int -W\frac{\partial U}{\partial z}\,dz$	5	6	1.5
$EF = -\int \frac{\partial}{\partial x}\overline{(U'U')} + \frac{\partial}{\partial y}\overline{(U'V')}\,dz$	-9	-6	-3
ZPG + ZD + UW + EF	9	11	9
τ/ρ, layer top	-100	-18	-4
τ/ρ, layer bottom	-18	-4	-0.6
$\delta\tau/\rho$, (top - bottom)	-82	-14	-3.4
Residual: R = ZPG + ZC + UW + EF + $\delta\tau/\rho$	-72	-3	5.6
(all units 10^{-6} m^2/s^2)			
R/ZPG x 100%	-514%	-25%	70%

pressure gradient, advective accelerations, and, possibly, contributions to the stress which we are unable to measure (for example, internal wave horizontal-vertical velocity covariances in the frequency range of 1/day to the local buoyancy frequency); by "anomalous" we mean "different from BB's 'typical' estimates".

The residual for the 60-90m depth range is large, amounting to 70% of the ZPG for that depth range. This is unexpectedly large, but not alarming. One must expect any 12 day period to have substantial differences from long term means. In the 30-60m depth range, the residual is only 25% of the ZPG.

The residual in the 0-30m depth range is extraordinarily large, 5 times larger than the ZPG. The imbalance is so large that we must suspect the dynamics near the surface are different than we have assumed, i.e., our formulation of the problem may be fundamentally wrong. But if our assumptions are so far off the mark in the upper depth range, we are not justified in making the same assumptions at deeper depths. We must consider the smaller residuals in deeper depth ranges as coincidental, and possibly having no physical significance.

5. DISCUSSION

A basic premise of equatorial dynamics is that the westward wind stress is transmitted from the sea surface to deeper waters by small-scale vertical transport, there to be balanced by larger-scale forces resulting from the mean zonal pressure gradient, the upwelling of eastward momentum, the convergence of zonal momentum, and the mesoscale eddy flux. (e.g. Gill,1982). An equally basic premise of small-scale turbulence dynamics is that the local rate of production of turbulent kinetic energy is balanced by the rate at which it is locally dissipated, allowing the turbulent stress to be calculated from dissipation rate estimates. We have demonstrated that "typical" large-scale forces cannot balance the resultant of wind stress and turbulent stress forces in the upper 30 m at 140°W. The eastward turbulent stress at 30 m depth is too small to account for more than 20% of the westward surface wind stress, and typical large-scale forces can account for only 10% of the wind stress. Clearly, something is seriously in error.

Two possibilities should be explored to resolve the momentum imbalance: (A) the large-scale horizontal forces at the time of the TROPIC HEAT experiment might have been much larger than our "typical" estimates; or (B) our estimate of the momentum flux may be unrealistically low. We examine each in turn.

A. Large-Scale Anomalies:

The average wind stress during the 12-day turbulence experiment was 0.10 N/m^2, approximately a factor of 2 larger than the mean annual surface stress at 140°W (Weare and Strub, 1981; Weare, Strub and Samuel, 1981). The detailed response of the equatorial ocean to anomalous changes in the wind is unknown, and it may be overly optimistic to expect a rapid

response in the zonal pressure gradient or other large-scale processes to fluctuations in the wind. Large-scale, annual average circulation terms can only balance the large-scale, annual average wind stress. If the mean annual surface stress (BB use 56×10^{-6} m^2/s^2) is used instead of the measured wind stress, the residual R drops from -72×10^{-6} m^2/s^2 to -28×10^{-6} m^2/s^2, still twice as large as the ZPG. In a perfect world, we would use the same time scale to average the wind stress, the turbulent stresses, and the large-scale terms. Since such measurements are not available, we cast the problem in a different sense: If estimates of typical large-scale terms can explain only annually averaged surface stress, can the local wind stress be balanced by anomalies in the ZPG, the upwelling velocity, or the mesoscale eddy flux?

If our estimate of the turbulent momentum flux is correct, momentum supplied by the local wind was not transmitted very deeply by turbulent stirring. Can the disposition of the momentum supplied by the wind but not transmitted below 30 m be explained by a local, unmeasured anomaly with a depth scale of 30 m or less? Candidate anomalies which might explain the large residual are (a) the local acceleration of the top 30 m of the ocean; (b) an anomalous zonal pressure gradient that is much larger than the mean pressure gradient; (c) the local meridional advection of zonal momentum (i.e., an anomalous mesoscale eddy flux); (d) a local anomaly in upwelling. Each of these is treated below:

(a) We have entirely neglected the local acceleration of the top 30 m of the ocean in eq.(11); we now ask, "how large would the acceleration have to be to explain the residual?" If $R = \int(\partial u/\partial t)dz$, the average acceleration of the top 30 m would be 2.4×10^{-6} m/s^2, equivalent to a gain in westward velocity of 2.5m/s over the 12-day period. No such acceleration was observed, and we consider this explanation unlikely.

(b) Suppose that the residual is in fact balanced by an anomalous pressure gradient. To evaluate $R = -\int \rho^{-1}\partial P_a/\partial x \, dz$, where P_a is the pressure anomaly, one must estimate the horizontal scale of the anomaly. Since "mean" zonal pressure gradients have the scale of thousands of km (typically, the mean zonal pressure gradient is calculated from sections taken at 150°W and 110°W, a distance of 4400 km), an "anomaly" should have a smaller horizontal scale, say, 500 km. R could be explained by a difference in dynamic height of 0.12 m over the 500 km distance, and such a difference has been noted by Lemasson and Piton (1968) over the longitudes 135°W to 145°W, in the region of large thermocline slope. However, the required anomalous pressure gradient must be concentrated entirely in the upper 30 m. The mean zonal pressure gradient has a depth scale of 100 m or more (Mangum and Hayes, 1984; Fig. 5); the anomalies shown by Lemasson and Piton (1968) are vertically variable, but have depth scales comparable to the mean zonal pressure gradient. An anomalous pressure distribution with a 30 m depth scale can be caused by an anomalous temperature distribution, but in this case, the required expansion is

0.12m/30m = 4 parts per thousand. A typical expansivity for sea water is 0.2 parts per thousand per degree, so the pressure gradient anomaly would require a temperature change of about 20 degrees over 500 km. No such temperature distribution has been observed on the equator, and we consider this explanation unlikely.

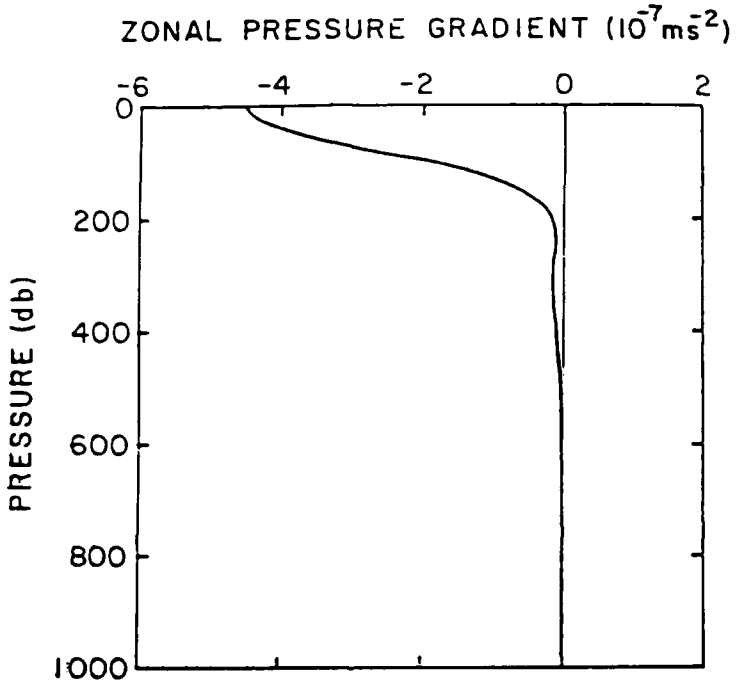

Fig. 5. Mean zonal pressure gradient from 1979 to 1981 (from Mangum and Hayes, 1984), calculated from NORPAX and EPOCS CTD sections at 150°W and 110°W, has a depth scale of greater than 100 m.

(c) Suppose the residual is balanced by a meridional advection anomaly. If $R = \int v(\partial u/\partial y)\, dz$, one must estimate the meridional scale. ADCP measurements from the MC vessel show a 6 day time interval midway through the measurement period when the meridional velocity averaged about 0.4 m/s northward (Chereskin et al, 1986; this appears to be related to the surface-intensified 21-day waveform discussed by Philander et al, 1985). To balance the residual requires a 260 km meridional length scale. The change δu in zonal velocity over a distance of δy = 260 km would have to be 1 m/s. Changes in zonal velocity of this size (to within a factor of 2 or so) are sometimes observed near the equator (Moum et al, 1986), with one crucial difference: <u>such fluctuations have a vertical coherence scale of order 50 m</u>, not less than 30 m as demanded by the residual. The sign is also wrong: BBH demonstrated that <u>the meridional advection of zonal momentum</u>

transports momentum westward, not eastward. We think it unlikely that this term could explain the residual, but because it is the large-scale term which has the shallowest depth scale, it should be investigated more carefully.

(d) If the residual is balanced by an upwelling anomaly, that is, $R = \int w(\partial u/\partial z)\, dz$, where w is an anomalous vertical velocity, one can estimate the size of w necessary for the balance. The vertical shear of zonal velocity during the 12 days of the turbulence experiment was of order 0.01 s^{-1} (Chereskin et al, 1986). Using this, we estimate that $w = 2.4 \times 10^{-4}$ m/s = 20 m per day. This is approximately 24 times as large as the mean upwelling velocity estimated by BB at 30m depth, and we think it unlikely that upwelling anomalies could explain the residual.

We can find no evidence that the large zonal momentum flux residual can be explained by anomalies in the large-scale effects. It is unlikely that zonal pressure gradient, horizontal advection, or upwelling anomalies are large enough to balance the residual; eq.(11) is so far out of balance that other explanations must be considered.

B. THE DISSIPATION METHOD REVISITED

The turbulent stress at 30 m depth is 20% of the surface stress. If we use the dissipation method for calculating eddy viscosity, we find that most of the momentum supplied by the local wind was not transmitted below 30 m depth, yet we know that momentum put into the ocean by the annual wind stress must penetrate deeply in order to balance the ZPG. We can only conclude that if the dissipation method is correct, local turbulent stirring in the upper 30 m does not respond rapidly to changes in the local surface stress. But there is direct evidence which indicates that turbulent mixing is a strong function of surface conditions: both MC and GPWOS found a very strong diurnal signal in the strength of turbulence above the undercurrent. Perhaps the truth is that the momentum supplied by the local wind is penetrating deeply, but our estimate of the momentum flux is wrong.

There are three potentially large sources of error which should be questioned: (a) Was the sampling adequate to determine the mean kinetic energy dissipation rate? (b) Is some process other than turbulent mixing responsible for vertically transporting most of the momentum at the equator? (c) Is the method of estimating turbulent stresses from kinetic energy dissipation rates formally flawed? We address each of these questions in turn:

(a) Is it possible that we have underestimated the dissipation rate by a factor of 4 because of sampling error? MC and GPWOS together made over 2,000 casts, each extending to 100 m depth or more. In all, well over 200 km of water was sampled; there is little hope of improving this record by another factor of 10 in the near future. We performed a bootstrap test of the significance of our mean turbulent stress calculation, using averages of the turbulent

stress over one hour and 10 m vertically to define a parent probability distribution having 288 elements in each 10 m depth bin. One thousand example averages were calculated by randomly drawing 288 samples from the parent distribution, and a histogram of the example averages was formed. It was found that 90% of the example averages were within 20% of the average of the parent distribution. We conclude that sampling error is an unlikely source of a factor of 4 error.

It is worth noting that GPWOS use the Cox number method (Osborn and Cox, 1972) to estimate the mean vertical heat flux, finding about -140 W/m^2 at 30 m depth. This estimate seems reasonable (at least within a factor of 2 or so), because the net surface heat flux was of roughly the same size. If the kinetic energy dissipation rates were grossly undersampled and underestimated, the Cox number would also be undersampled and underestimated. Both the vertical heat flux and the momentum flux would be seen as much too small if the turbulence were severely undersampled. Instead, the heat flux is roughly correct, but the momentum flux is much too small. If sampling error is invoked to explain the large residual, one must explain how the momentum flux could be increased without making the interior heat flux larger than the surface heat flux. Estimates of the vertical heat flux from the MC data set and dissipation measurements (Osborn, 1980) agree reasonably well (though perhaps only coincidentally) with the Cox number estimates of GPWOS and our own unpublished Cox number estimates.

(b) We have not considered vertical momentum transport by internal wave interactions. Internal waves can be excited by turbulence (Townsend, 1968; Wu, 1969), and can sometimes transfer momentum vertically (Muller, 1976; Booker and Bretherton, 1967). The present measurements are insufficient to determine whether or not internal wave radiation is the major momentum transport process. We only note that wave-like processes transport kinetic energy easily, but do not transport momentum very well, because horizontal and vertical velocity fluctuations are not well correlated in the internal wave band. While we cannot confidently evaluate internal wave momentum transport, in (c) below we demonstrate that internal wave kinetic energy transport by itself may be a major problem.

(c) It may not be possible to parameterize the vertical flux of horizontal momentum using the kinetic energy dissipation rate. The prescriptions for eddy viscosity and turbulent stress, eqs.(7), (8), and (9), all depend on eq.(6), the assumption that the local rate of production of turbulent kinetic energy is balanced by the local dissipation rate. Third-order correlations and pressure-velocity correlations have both been neglected in deriving eq.(6). Neither term has been measured in the ocean and there is no method to make such measurements directly. Wyngaard and Cote (1971) measured vertical velocity-turbulent kinetic

energy correlations in the atmospheric boundary layer, and found it to be a small quantity, sometimes positive and sometimes negative, when the stratification was stable. Wyngaard and Cote (1971) estimated the divergence of pressure-vertical velocity fluctuations as a residual in the unstable atmospheric boundary layer, but did not estimate it when the stratification was stable (presumably because there were too few examples when the atmospheric boundary layer was stable). We thus have no a priori reason to suppose that a local production-dissipation balance holds when the ocean is stably stratified.
There is some qualitative evidence that the pressure-velocity correlation divergence may be a significant term in the turbulent kinetic energy budget. C. Paulson (personal communication) observed a significant increase in internal wave isotherm amplitudes during the night, when turbulence was most energetic and dissipation rates were largest. We do not intend to discuss diurnal variations in equatorial turbulence, but simply note that increases in the internal wave energy content is observed to be correlated with increases in turbulent kinetic energy.

It may be possible for turbulent overturns to drive the internal wave field, because the rate of increase of wave energy is controlled by pressure-velocity correlations (Lighthill, 1978):

$$\frac{\partial E}{\partial t} = - \nabla \cdot (p\underline{u}) \quad , \tag{12}$$

where E is internal wave energy and $\underline{u}$ is the vector velocity. The mechanism described by eq.(12) is the radiative loss of turbulent energy to an internal wave field.

If the pressure-velocity correlation is large and confined to a restricted region of the fluid, internal waves can be excited, and energy can be radiated away, eventually to be dissipated elsewhere. If the energy is radiated away from the region it is generated, a local production-dissipation balance cannot hold, and kinetic energy dissipation rates may be only loosely related to the eddy viscosity and turbulent stress. In view of our inability to explain the large momentum budget residual with any other mechanism, we must consider the pressure-velocity correlation divergence as a possibly significant source of error, and we must treat estimates of the turbulent stress based on dissipation rates with skepticism.

6. SUMMARY AND CONCLUSION

We have shown that the momentum budget at 30 m depth and above on the equator at 140°W cannot be balanced using typical estimates of large-scale forces (zonal pressure gradients, upwelling of eastward momentum, convergence of westward momentum, and meridional eddy transport) and

conventional estimates of the turbulent stress. One of two conclusions must be drawn from this study: Either the large-scale processes during the time of measurement were highly atypical, or estimates of the momentum flux based on a production-dissipation balance are seriously flawed. For the present, we believe eddy viscosities estimated from measured dissipation rates must be treated with caution.
Estimates of anomalies in the large-scale forces which could explain the imbalance are unrealistically large, and do not have a realistic depth structure. Most of the problem may be attributable to the turbulent stress estimates because the stress estimate at 30 m depth is much smaller than the wind stress, and decreases exponentially below 30 m. It is possible that internal wave interactions play a crucial role in near-surface equatorial dynamics, either by transporting momentum directly, or by radiating energy and invalidating the hypothesis of a local production-dissipation balance.

ACKNOWLEDGMENTS

This work was supported by National Science Foundation, grant OCE-8214639, and the Office of Naval Research, contract number N00014-84-C-0218.

REFERENCES

Booker, J.R., and F.P. Bretherton (1967): The critical layer for internal gravity waves in a shear flow. J. Fluid Mech., 27, 513-539.

Bryden, H.L. and E.C. Brady (1985): Diagnostic model of the three-dimensional circulation in the upper equatorial Pacific ocean. J. Phys. Oceanogr., 15, 1255-1273.

Bryden, H.L., E.C. Brady and D. Halpern (1986): Lateral mixing in the equatorial Pacific. Unpublished manuscript.

Caldwell, D.R., T.M. Dillon and J.N. Moum (1985): The Rapid Sampling Vertical Profiler: an evaluation. J. Atmos. Oceanic Technol., 2, 615-625.

Chereskin, T.K., J.N. Moum, P.J. Stabeno, D.R. Caldwell, C.A. Paulson, L.A. Regier and D. Halpern (1986): Fine-scale variability at 140W in the equatorial Pacific. J. Geophys. Res., in press.

Chereskin, T.K., D. Halpern and L.A. Regier (1986): An evaluation of shipboard acoustic Doppler measurements at 140W in the equatorial Pacific. Unpublished manuscript.

Crawford, W. R. (1982): Pacific equatorial turbulence. J. Physical Oceanogr., 12 (10), 1137-1149.

Dillon, T. M. (1984): The energetics of overturning structures: Implications for the theory of fossil turbulence. J. Physical Oceanogr., 14 (3), 541-549.

Gill, A.E. (1982): Atmosphere-Ocean Dynamics. Academic Press, New York, 662 pp.

Gregg, M.C., H. Peters, J.C. Wesson, N.S. Oakey and T.J. Shay (1985): Intensive measurements of turbulence and shear in the equatorial undercurrent. Nature, 318, 140-144.

Large, W. G., and S. Pond: Open ocean momentum flux measurements in moderate to strong winds. J. Phys. Oceanogr. 11, 324-336, (1981):

Lemasson, L. and B. Piton (1968): Anomalie dynamique de la surface de la mer le long de l'equateur dans l'Ocean Pacifique. Cah. ORSTOM, Ser. Oceanogr., 6, 39-45. (the relevant figures appear in Gill, 1982, p 464.)

Lighthill, J. (1978): Waves in Fluids, University Press, Cambridge. 504 pp.

Mangum, L. J. and S. P. Hayes (1984): The vertical structure of the zonal pressure gradient in the eastern equatorial Pacific. J. Geophys. Res., 89 (C6), 10441-10449.

Moum, J.N. and D.R. Caldwell (1985): Local influences on shear flow turbulence in the equatorial ocean. Science, 230, 315-316.

Moum, J.N., D.R. Caldwell, C.A. Paulson, T.K. Chereskin and L.A. Regier (1986): Does ocean turbulence peak at the equator? J. Phys. Oceanogr., 16, 1991-1994.

Muller, P. (1976): On the diffusion of momentum and mass by internal gravity waves. J. Fluid Mech., 77, 789-823.

Osborn, T.R. (1980): Estimates of the local rate of vertical diffusion from dissipation measurements. J. Phys. Oceanogr., 10, 83-89.

Osborn, T.R. and C.S. Cox (1972): Oceanic finestructure. Geophys. Fluid Dyn., 3, 321-345.

Philander, G., D. Halpern, D. Hansen, R. Legeckis, L. Miller, C. Paul, R. Watts, R. Weisberg, and M. Wimbush (1985): Long waves in the equatorial Pacific ocean. EOS, 66, 154.

Townsend, A.A. (1968): Excitation of internal waves in a stably-stratified atmosphere with considerable wind shear. J. Fluid Mech., 32, 145-171.

Weare, B. and P. T. Strub (1981): Annual mean atmospheric statistics at the surface of the tropical Pacific Ocean. Mon. Wea. Rev., 109, 1002-1012.

Weare, B., P. T. Strub, and D. Samuel (1981): Annual mean surface heat fluxes in the tropical Pacific Ocean. J. Phys. Oceanogr. 11, 705-717.

Wu, J. (1969): Mixed region collapse with internal wave generation in a density stratified medium. J. Fluid Mech., 35, 531-544.

Wyngaard, J. C. and O. R. Cote (1971): The budgets of turbulent kinetic energy and temperature variance in the atmospheric surface layer. J. Phys. Oceanogr., 28, 190-201.

THE MIXED LAYER OF THE WESTERN EQUATORIAL PACIFIC OCEAN

Roger Lukas

Department of Oceanography and
Hawaii Institute of Geophysics
University of Hawaii
Honolulu, Hawaii 96822

Eric Lindstrom

CSIRO Division of Oceanography
GPO Box 1538
Hobart, Tasmania 7001
Australia

ABSTRACT

The mixed layer of the western equatorial Pacific and its dynamics are poorly known because of a general lack of data. The recent Western Equatorial Pacific Ocean Circulation Study (WEPOCS) conducted two expeditions to the near-equatorial region north of Papua New Guinea, performing high-resolution CTD profiling and other hydrographic observations.

The WEPOCS CTD profiles are analyzed for various measures of the upper layer or mixed layer thickness, using criteria which depend on vertical gradients of temperature, salinity, and density. From 243 profiles, the average mixed layer depth in the western equatorial Pacific during the two WEPOCS cruises was 29 m, which is about a factor of three shallower than had previously been thought. The depth of the top of the thermocline was found to be 51 m, so there is a nearly-isothermal layer which is deeper than the mixed layer. This discrepancy is attributable to salinity stratification. It is hypothesized that the waters in this layer between the bottom of the mixed layer and the top of the thermocline are formed to the east of the WEPOCS region, and subducted below the shallow and lighter mixed layer waters found in the west.

There was a significant, but weak, dependence of mixed layer depth on wind speed observed during the CTD stations. The scatter is partly due to the fact that spot wind measurements are not always representative of

the wind history that has determined the mixed layer depth, but another important factor is the strong stabilizing buoyancy forcing associated with heavy precipitation in the this region. Under light wind conditions, there was a tendency for warm and thin layers to form at the sea surface as a result of diurnal heating, however there did not appear to be any nighttime maximum to the mixed layer depth associated with convective overturn due to cooling. This contrast with the central Pacific is most likely due to the influence of salinity on the thermodynamics of the mixed layer.

A strong westerly wind burst was observed during WEPOCS II, and the mixed layer nearly doubled in depth, and cooled by more than 1°C. Evidence of downwelling near the equator, and upwelling off the equator, was seen in the distribution of temperature, salinity, and density in the meridional section along 143°E which was occupied immediately following the wind event. This event was apparently strong enough to erode through the salinity-stratified layer and into the thermocline, resulting in the obs rved cooling.

The results of this study suggest that, except during strong wind events, entrainment cooling may not be an important component of the heat budget of the western Pacific warm pool. Thus, a possible mechanism for interannual warming (and subsequent cooling) of the western Pacific has been identified as the intermittent wind forcing, and the switching on and off of entrainment cooling.

INTRODUCTION

The western equatorial Pacific has been identified as a region where the westerly wind anomalies associated with the onset of the El Nino/Southern Oscillation (ENSO) phenomenon first develop (Barnett, 1977). Our oceanographic database from this important region is relatively lean, and much of what we know about the hydrographic structure of this region is from discrete sampling with relatively poor vertical resolution, or from continuous temperature profiling using bathythermographs. As a direct result, many of our ideas about the structure and dynamics of the western equatorial Pacific are inaccurate and need to be improved. An excellent example of this problem is the almost universally accepted belief that the mixed layer in the western equatorial Pacific is very deep (100 m or more).

This notion has its roots in such observations as the trans-Pacific equatorial temperature section observed by Lemasson and Piton (1968) between 20 November 1964 and 8 March 1965 (Fig. 1, which is actually taken from Colin et al., 1971). In this often-cited section, the thermocline slopes upward from the central Pacific, intersecting the surface in the east. However, the thermocline is essentially flat between the central and western Pacific. The top of the thermocline is

found at about 100 m, and from this section it appears as if the bottom of the mixed layer is found at the top of the thermocline. It should be noted that this section was occupied in two pieces, with a 2-month-long break near 150°W (Cremoux, 1981). Also, the 1965 ENSO event was beginning during these observations, and they may well be anomalous.

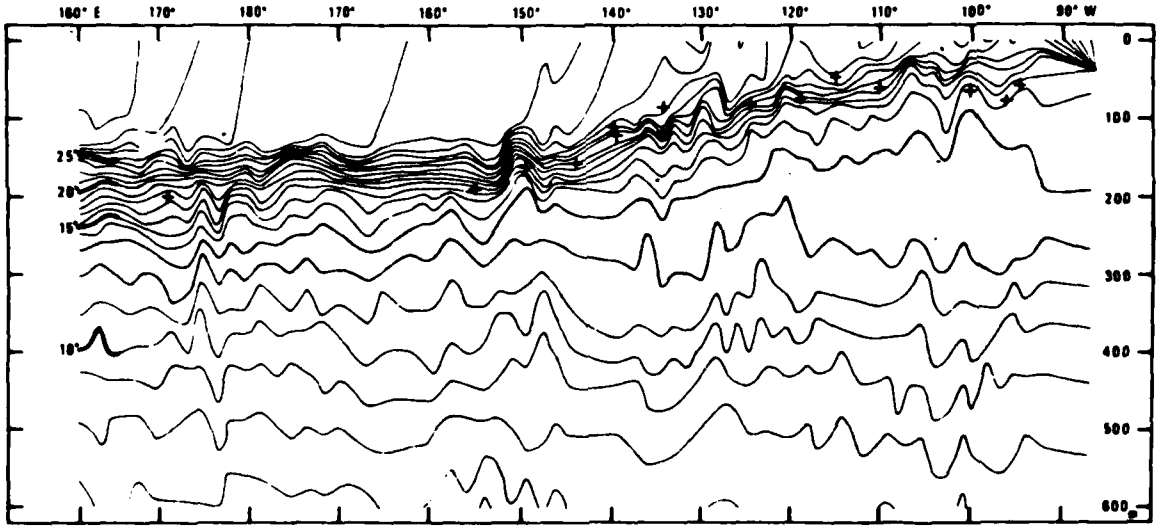

Figure 1. Thermal structure along the equator in the Pacific Ocean observed by Lemasson and Piton (1968) [After Colin et al., 1971].

An example of a deep mixed layer in the western equatorial Pacific is given in Fig. 2 which shows the temperature, salinity, and density observed at a near-equatorial station during the second cruise of the Western Equatorial Pacific Ocean Circulation Study (WEPOCS). All three properties are well-mixed down to a little more than 100 m. Figures 1 and 2 are consistent.

A very different situation is illustrated in Fig. 3, which shows a CTD profile from another near-equatorial station occupied during WEPOCS I. Here, the nearly isothermal layer is about 80 m deep. However, salinity is only well-mixed to 35 m, and thus the density profile has a sharp gradient near 35 m. A surprising result is that only 15-20% of the stations during WEPOCS I and II showed profiles like Fig. 2, and that, on average, the mixed layer in the western equatorial Pacific is quite shallow. In fact, the station shown in Fig. 2 was occupied immediately following a period of very strong winds associated with a westerly burst (cf. Luther et al. [1983] for a description of this phenomenon). This observation, as will be shown, has important implications for the ENSO phenomenon.

In the following, the WEPOCS observations will be presented in more detail, and the results of simple statistical analyses are discussed.

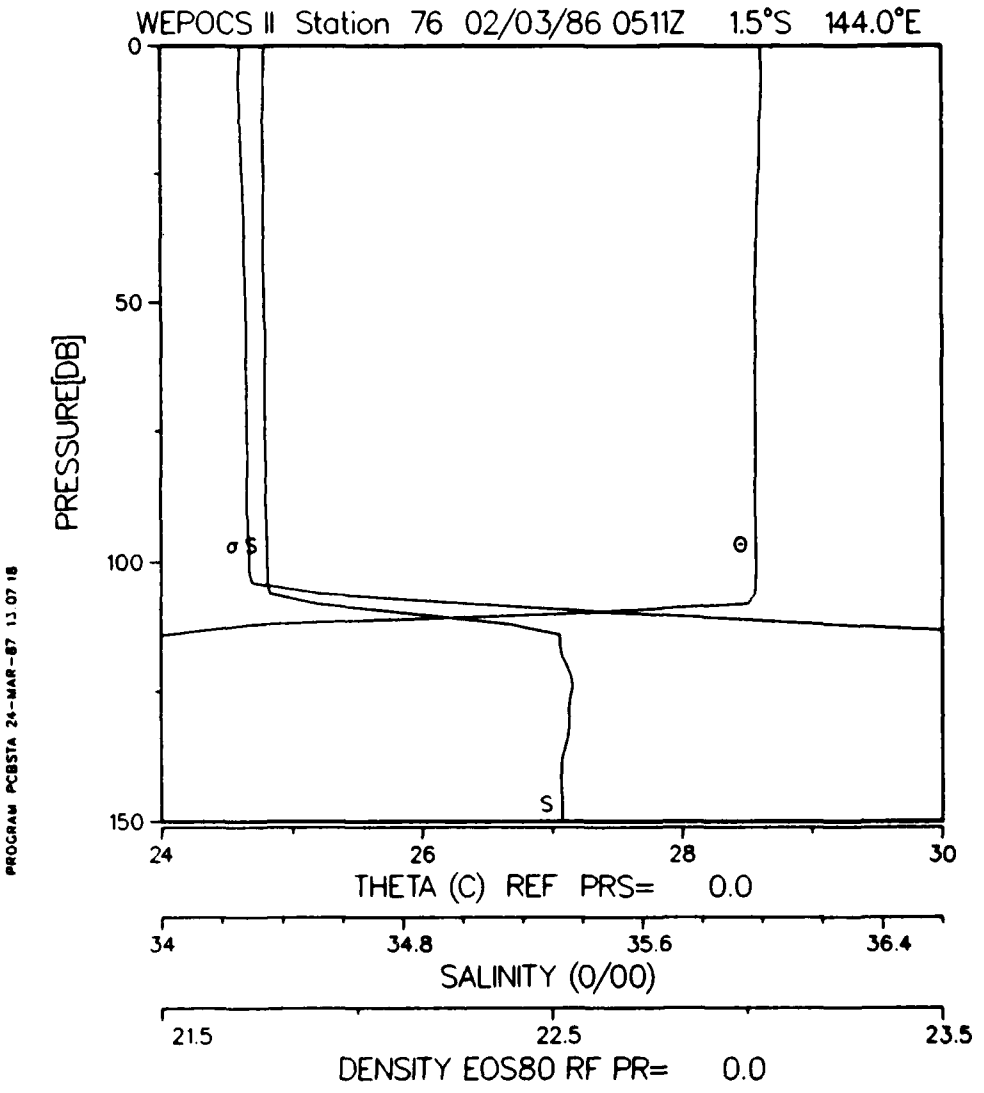

Figure 2. Potential temperature, salinity, and potential density from a CTD profile at 1.5°S, 144°E in February 1986.

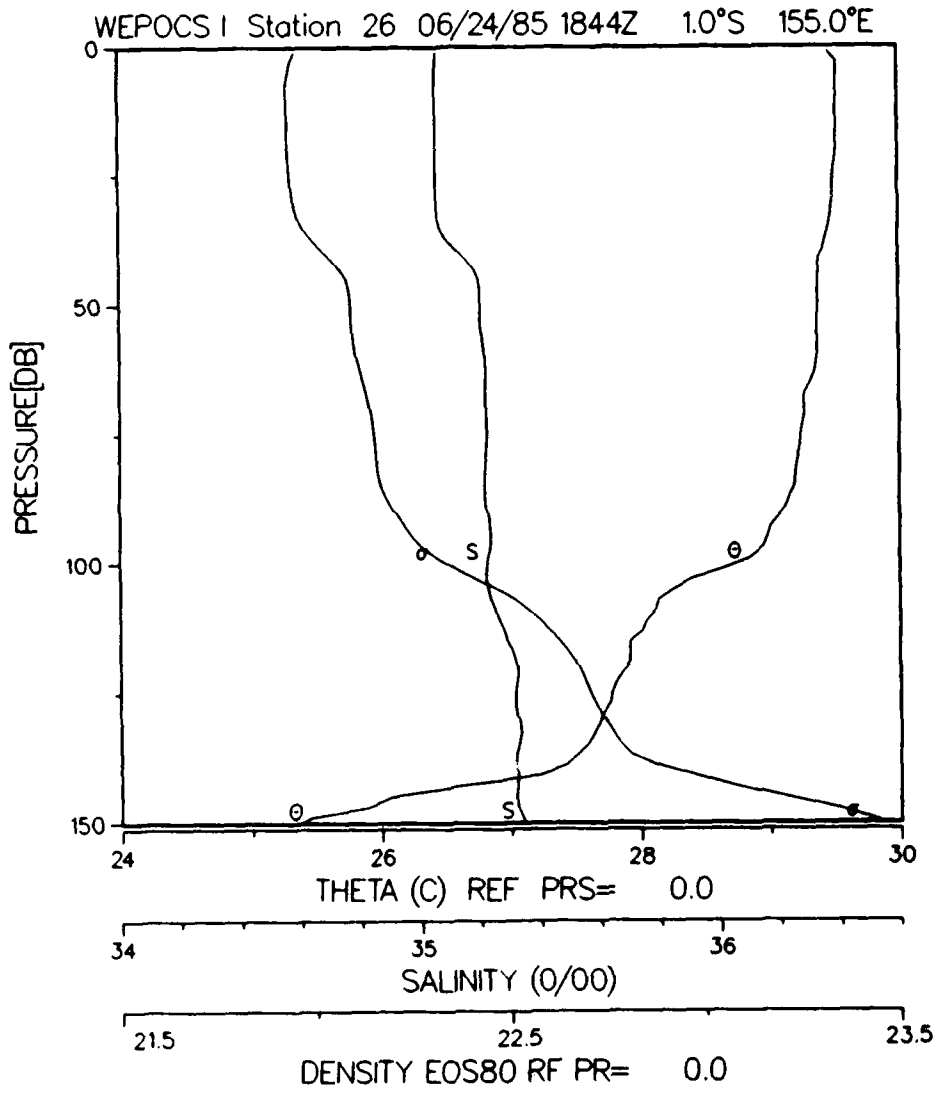

Figure 3. As in Fig. 2, except at 1°S, 155°E in June 1985.

The role of strong precipitation in the western equatorial Pacific and its influence on mixed layer dynamics is elaborated upon, and a hypothesis is outlined to explain the discrepancy between the nearly isothermal layer depth and the mixed layer depth.

DATA AND METHODS

WEPOCS

WEPOCS is a joint U.S.-Australian program to test a hypothesis concerning the source waters of the Equatorial Undercurrent, to improve our knowledge of the deep and intermediate circulation of the near-equatorial region north of Papua New Guinea, and to observe the oceanic response to the onset of the Northwest Monsoon (Lindstrom et al., 1987). Two expeditions were made (with U.S. and Australian vessels participating in each) at the two extremes of the seasonal cycle, the Southeast Trade season (June-August, 1985) and the Northwest Monsoon (January-February, 1986).

Hydrographic stations were occupied along the cruise tracks (Fig. 4), and moored current, temperature, and pressure measurements were made at key sites between the two expeditions. Acoustic current profiling measurements of the upper 150-450 m were made along the ships' tracks. Continuous temperature and conductivity observations were made at the depth of the ships' hulls, and wind speed and direction were recorded frequently during the cruises.

CTD Data

The temperature, salinity, and density data from CTD measurements are the primary data used in this study. Note that only data from the U.S. cruises have been included in the statistical analysis at this stage, but the statistics reported here will be updated soon. (However, upper ocean temperatures from a 24-hour sequence of CTD profiles on the equator at 150°E, performed from the Australian R/V Franklin, are included here.) The statistical results will not change significantly, because both ships were making observations nearly simultaneously, and the Australian cruise track filled in the center of the large polygon created by the U.S. cruise track (Fig. 4).

Neil Brown Mk IIIB CTD profilers were used during all cruises. Data acquisition and processing procedures are as developed at Woods Hole Oceanographic Institution and described by Fofonoff et al. (1974), with the exception of the U.S. WEPOCS II cruise, where the data were obtained and processed by the PACODF group of Scripps Institution of Oceanography. The modified processing procedures employed by PACODF are not yet documented, but the methods are not grossly different from those

employed at Woods Hole. Details of the processing of the hydrographic observations made from R/V Thomas G. Thompson during WEPOCS I can be found in Lukas and Tsuchiya (1986).

The CTD data are processed to 2 decibar averages, starting from the surface. The methods used by Woods Hole result in downcast profiles with averages centered on odd pressure values. The Scripps group processes all data to bins centered on even pressures. This difference is not important for the present study, with the exception of defining sea surface temperature (SST) and sea surface salinity (SSS). Here, I have ignored the surface values (p = 0) from WEPOCS II, as there are questions concerning the reliability of the CTD data in this interval. Thus, "SST" and "SSS" refer to the average temperature and salinity between 0 and 2 decibars for WEPOCS I, and between 1 and 3 decibars for WEPOCS II. For the shallow depths under consideration, we will take 1 decibar equal to 1 m, and a mixed layer depth of 1 m (2 m) for WEPOCS I (WEPOCS II) indicates the presence of strong property gradients right to the surface.

Mixed Layer Depth Criteria

Historically, mixed layer and thermocline depths have been estimated using temperature gradient criteria or by specifying a net temperature decrease from the surface. Defant, according to Wyrtki (1964), used a critical temperature gradient of 0.02°C/m to define the thermocline depth, while Wyrtki used a 0.5°C change from the surface value. Levitus (1982) used a net temperature change of 0.5°C from the surface to define the mixed layer depth, but also used a density change of 0.125 sigma-T units, as he recognized the importance of salinity in stabilizing the upper ocean, especially in the subarctic.

In this study, we employ a density gradient criterion as the most reliable estimator of mixed layer depth. The vertical density gradient is a measure of the buoyancy force which must be overcome by the turbulent kinetic energy of the wind forcing to deepen the mixed layer. In addition, we use temperature and salinity gradient criteria to estimate the mixed layer depth, and to estimate the depth to the top of the main thermocline and halocline. The reason for using gradients for criteria is that they are related to the mixing process. The reason for using temperature and salinity is that they have different source functions, and thus offer some independent information on mixing.

For temperature, the critical gradients used in this study are 0.05°C/m (dT1) and 0.025°C/m (dT2). For salinity, the gradients used are 0.02 °/oo (dS1) and 0.01 °/oo (dS2). In density, a gradient of 1×10^{-2} kg m^{-4} (0.01 sigma-T units/m; dD) was used. The values chosen for dT1 and dS1 are roughly equivalent in their influence on density, as are dT2 and dS2. (At T = 29°C, S = 34 °/oo, the ratio of the haline to temperature expansion coefficients is 2.25). The value specified for dD is slightly greater than the density change corresponding to dT2 or dS2.

Starting from the "surface" values, the data were searched downward until the gradient criteria were exceeded for the interval between adjacent 2 m values. The layer depth was assigned the depth value of the shallower of the two data values.

The initial analysis was performed by hand during the WEPOCS II cruise. As each station's data was scanned for the different layer depths, data plots were inspected to see how the various estimates performed under different oceanic and atmospheric conditions. In general, the dT1 criterion produced the deepest layer estimates (Table 1). This depth did not usually correspond to subjective estimates of the mixed layer depth; most often this depth corresponded to the depth of the top of the thermocline. Table 1 shows that the dT2 criterion produced mixed layer depth estimates that were 10 m shallower on average, though the maximum and minimum depths were the same. The density gradient criterion discussed above agreed most closely with subjectively determined mixed layer depths, as found by Peters (1987, this volume) in his Tropic Heat mixed layer work.

Table 1. Basic statistics for wind speed (WSPD), sea surface temperature (SST), sea surface salinity (SSS), and for five different measures of upper layer depth. Data are from 243 CTD stations during WEPOCS I and II.

	WSPD (m/s)	SST (deg C)	SSS (o/oo)	DT1 (m)	dS1 (m)	dT2 (m)	dS2 (m)	dD (m)
mean	5.3	29.10	34.22	51	41	36	31	29
median	5.2	29.10	34.27	57	40	36	26	23
std. dev.	3.4	.65	.46	30	28	28	25	26
max	14.9	30.70	35.14	106	157	106	106	106
min	.0	27.20	31.70	1	1	1	1	1

Many stations were observed to have relatively deep isothermal layers which were not isohaline. In fact, this observation during the WEPOCS I cruise motivated the present study. Obviously, the mixing is not complete over the deeper layer if there are substantial salinity gradients within it. A priori, it was not clear what was "substantial". A variety of salinity gradient criteria could be tried until one is found that produces the same average mixed layer depth determined by one's favorite temperature gradient. This is not the most satisfactory way to proceed, but such a value (0.02 °/oo) was found (Table 1). However, because of the different surface forcing for temperature and salinity, such an estimate will still vary considerably from the temperature gradient criterion at times. The correlation between layer depths estimated from dT2 and dS2 was only 0.55.

RESULTS

Basic Statistics

Surface variables observed at CTD stations will be used in later sections as proxies for wind and buoyancy forcing. It is recognized that these are poor substitutes for the time integral of wind stress and buoyancy flux which is responsible for the observed mixed layer structure, however such time histories are unfortunately not available.

Table 1 shows basic statistics for wind speed, SST, and SSS observed during WEPOCS. In general, the winds are relatively light at 5.3 m/s, but they are quite variable. Average SST is 29.1 degrees, and does not vary strongly over the WEPOCS region in general; the large range of SST is a reflection of significant warming of the region between cruises, and the rapid cooling associated with a strong wind event encountered during WEPOCS II. As mentioned, the SSS is relatively low, and varies over a large range. Some of the extremely low salinity values are associated with river runoff, which is a significant source of fresh water in the coastal portions of the WEPOCS area, however substantial precipitation (1.7-2.6 m/yr) occurs over the oceanic portions of the WEPOCS region (Rao et al., 1976).

The mean depth to the top of the thermocline (as defined by the dT1 criterion) was 51 m. This depth varied considerably in time and space. The main halocline (dS1) was slightly shallower on average, but exhibited comparable variability.

The mixed layer depth estimated from temperature, salinity, and density gradients all showed comparable variability, and identical ranges. However, the mean depths varied systematically, with the density gradient yielding the shallowest depths, even though the 0.01 kg m^{-4} criterion was larger than the equivalent density change of the dT2 and dS2 criteria. The average mixed layer depth of 29 m is shallower by a factor of 3 than the commonly accepted value of 100 m.

The upper layer thickness (Fig. 5a) exhibits a bimodal distribution, so the average and standard deviation are inadequate descriptors. There is a minimum frequency near 20 m, which suggests that the dT1 criterion is picking the top of the thermocline most of the time, but it also picks out the mixed layer depth a substantial fraction of the time. The minimum in the frequency distribution illustrates the substantial separation between the bottom of the mixed layer and the top of the thermocline.

The three mixed layer depth estimators are also not normally distributed (Fig. 5b-d), with each having a mode in the 0-5 m class. The general shape of these distributions is exponential. Such a probability density function is characteristic of a Poisson process (cf. Mohanty, 1986). The implications of this are pursued in the discussion.

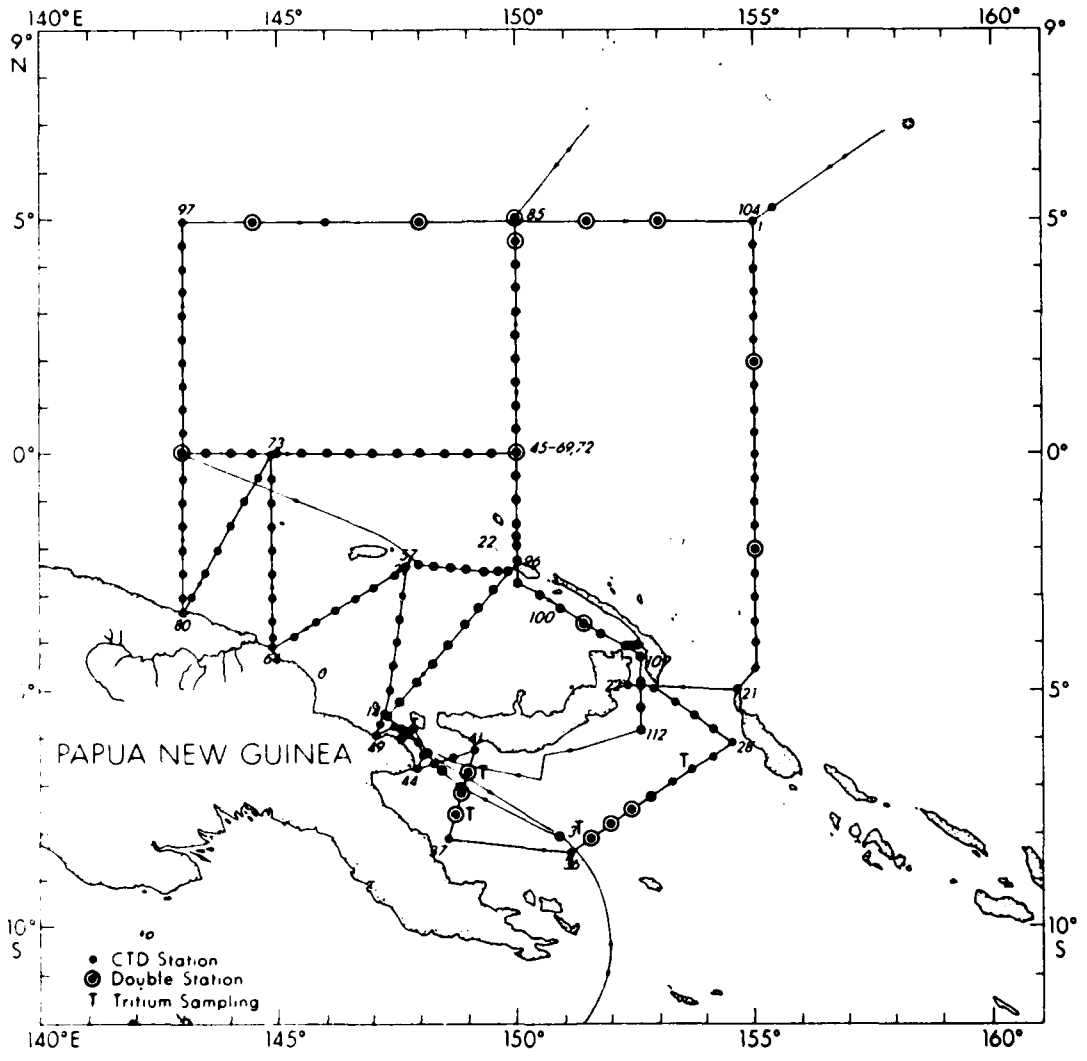

Figure 4. The cruise tracks and hydrographic station locations occupied by the R/V Moana Wave and the R/V Franklin during the WEPOCS II expedition, January-February 1986. The WEPOCS I cruise tracks and station positions were only slightly different.

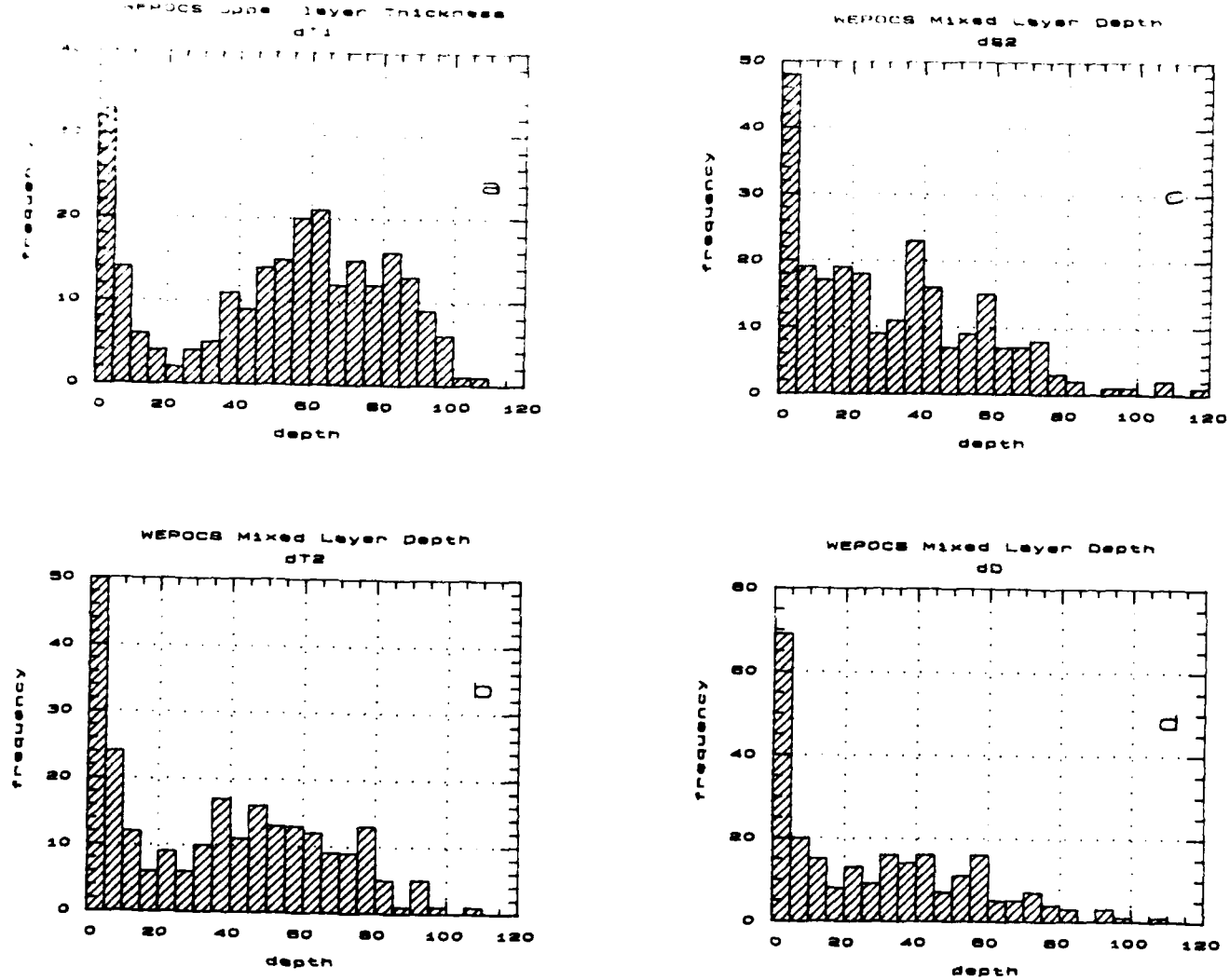

Figure 5. Histograms of the upper layer depth (a), and estimates of the mixed layer depth using temperature (b), salinity (c), and density (d) gradient criteria. See text for definitions and methods.

These mixed layer depth distributions suggest that shallow layers are fairly common in the western equatorial Pacific. In fact, these observations might be typical of summer in midlatitudes under light or no wind conditions, where diurnal warming is important. Pronounced effects of diurnal warming have been observed in the central equatorial Pacific mixed layer during Tropic Heat by Gregg et al. (1985). To investigate this possibility, the mixed layer depth observations were plotted against the time of day that the station was started (Fig. 6). It is obvious that there is no general correspondence between mixed layer depth and time of day. The observations were stratified into three different wind speed classes in the figure. Only during very light winds (speeds less than 3 m/s) is there a hint of a diurnal dependence, with these observations being shallow between 0600 and 1800. However, these very shallow mixed layers were found frequently during stronger winds as well (Fig. 7). Also, there is no apparent tendency for deep values to occur during the night hours, as is the case for the central Pacific (Gregg et al., 1985).

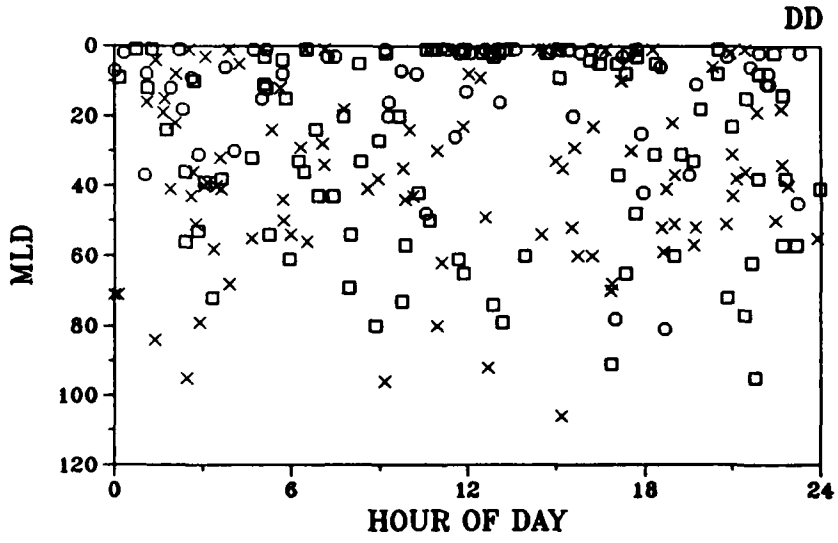

Figure 6. Mixed layer depth estimated from density gradient versus hour of the day (local time), for wind speed less than or equal to 3 m/s ([]), for wind speeds between 3 and 6 m/s (0), and for wind speeds greater than 6 m/s (X).

The average temperature and salinity of the mixed layer (as defined by density) were computed for each station, and the resulting frequency distributions are shown in Fig. 8. The mixed layer temperature shows a large peak in the 28.75-29.00°C class, for which an explanation does not exist. Further, there is a tendency towards a bimodal distribution which was quite pronounced when data from WEPOCS II were analyzed separately.

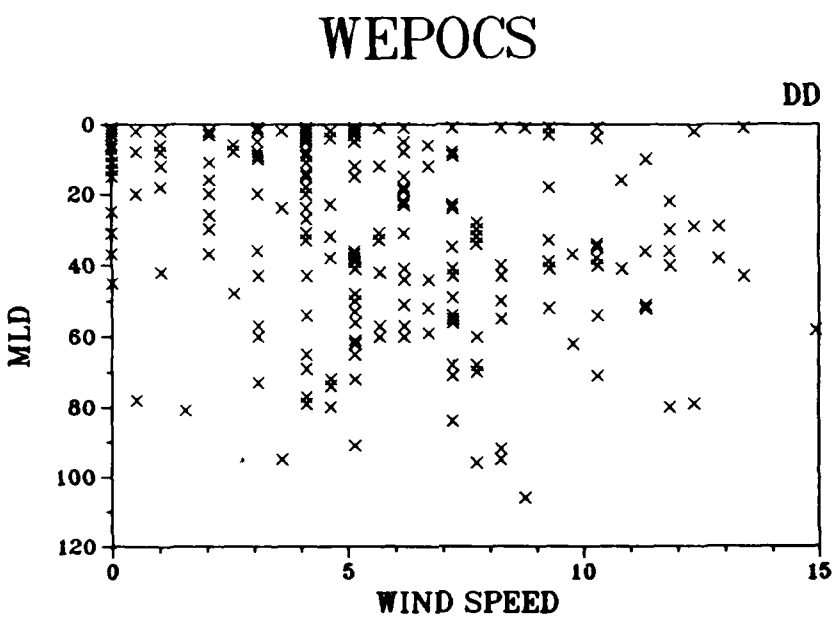

Figure 7. Mixed layer depth estimated from density gradient versus wind speed observed during CTD stations.

For those cases, there were sharp peaks in the 28.75–29°C and 29.75–30°C classes, with very few cases occurring in the 29–29.25°C class. The likely explanation for this situation is the strong burst of westerly winds that occurred in the middle of the WEPOCS II cruise, with wind speeds up to 15 m/s. The mixed layer temperatures during and after this wind event were cooler by one degree on average.

The mixed layer salinity distribution is highly skewed towards negative values, illustrating the influence of precipitation on the mixed layer of the western equatorial Pacific Ocean. The counter balancing influence on the high salinity side of the distribution is the high salinity layer of southern hemisphere subtropical water found in the thermocline over much of the WEPOCS region (Lindstrom et al., 1987).

A new variable was formed to estimate the thickness of the layer between the bottom of the mixed layer and the top of the thermocline. This is called the "barrier layer" by Stuart Godfrey (personal communication, 1987), and its existence in the western equatorial Pacific was previously unknown. The top of the thermocline is estimated using the dT1 temperature gradient criterion, but the first 10 m of the CTD profiles are ignored so that the shallow mixed layer is not distorting the signal. The difference between this depth and the mixed layer depth is then the thickness of the barrier layer. The frequency distribution for this variable is shown in Fig. 8c. Again, the distribution suggests an exponential density function. The mean thickness of this layer is 31 m, with half the observations deeper than 24 m. An explanation for the existence of this layer is suggested in the discussion.

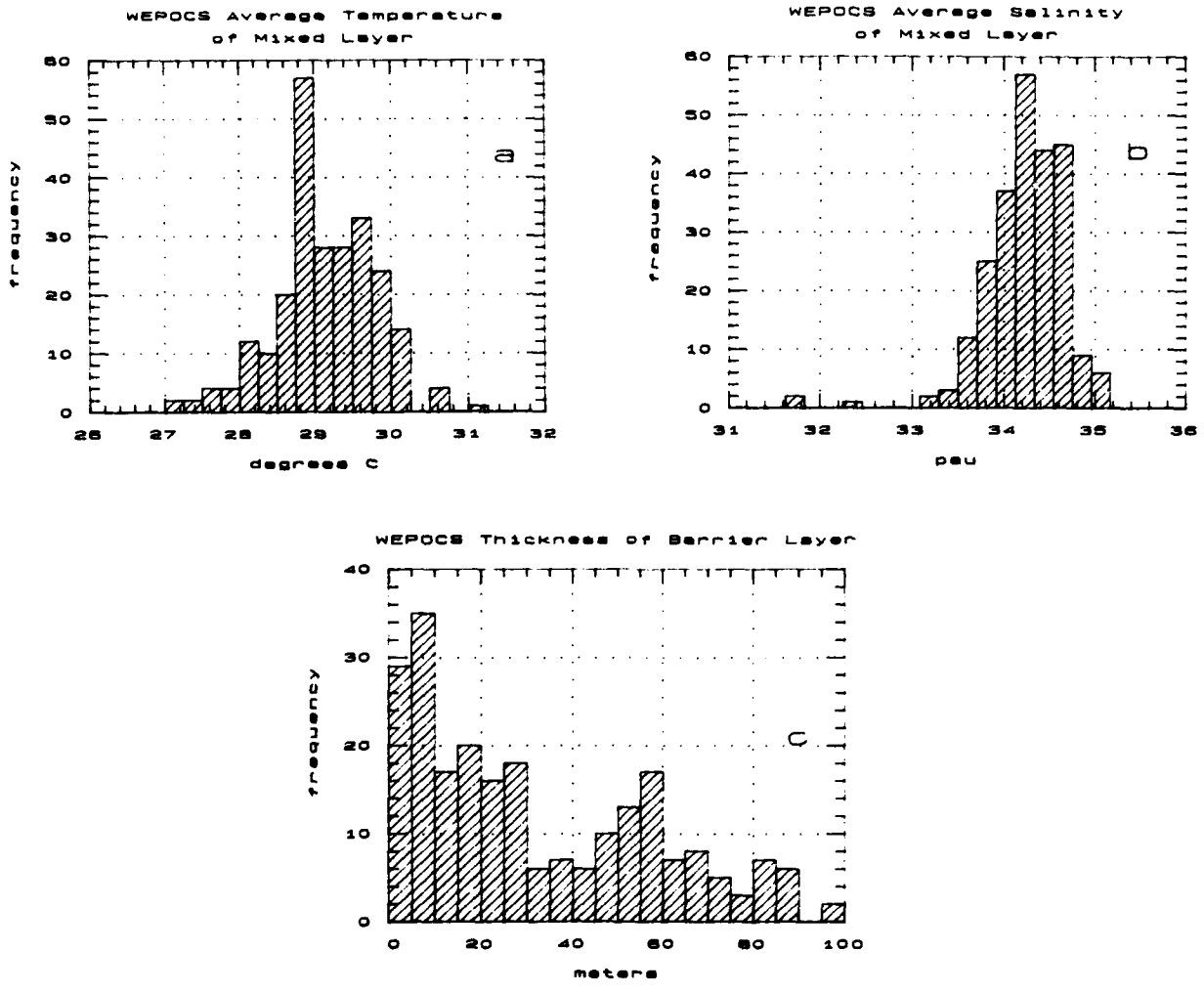

Figure 8. Histograms of average mixed layer temperature (a), average mixed layer salinity (b), and thickness of the layer between the bottom of the mixed layer and the top of the thermocline (c).

Figure 9 shows the temperature during the 24-hour time series CTD station on the equator at 150°E. The profiles were made at one hour intervals to a maximum depth of 400 m, though only the upper 100 m is shown. There are several features to point out in this figure. First, warmest SST occurs at 1600 local and coolest SST is found at 0800, consistent with the diurnal surface warming discussed earlier. Second, the mixed layer depth changes with the diurnal warming, but doesn't get deeper than about 20 m. Third, there is a large separation between the 29.4 and 29.3 isotherms relative to neighboring isotherms. Fourth, there is persistent temperature inversion of about 0.2°C near 70 m. This inversion is stable, being compensated by the salinity stratification. Finally, the top of the thermocline (as defined earlier) is found at about 75 m, and the layer between the top of the thermocline and the bottom of the mixed layer is about 50 m thick.

Correlation Results

It might be useful to examine the correlations between the surface variables and the mixed layer depths. Table 2 presents the correlations of the three different mixed layer depth estimators with the wind speed, SST, and SSS. These latter three variables are treated as proxies for the surface forcing from wind, heating, and precipitation. Also shown are the correlations of the discrepancy between the temperature and salinity gradient estimates of mixed layer depth with the three "forcing" variables.

Table 2. Correlation matrix of surface variables versus mixed layer depth estimated using density (dD), temperature (dT2), and salinity (dS2) gradient criteria from 243 CTD stations. Underlined values are considered statistically significant at the 95% confidence level, assuming 60 degrees of freedom (standard error of correlation coefficient = 0.13).

	WSPD	SST	SSS
dD	.31	-.19	.24
dT2	.36	-.22	.20
dS2	.20	-.10	.33
dT2-dS2	.20	-.15	-.11

The standard errors of the correlation coefficients were calculated using 60 degrees of freedom. This value assumes that each day's data during the cruise is independent from the other data. This is not strictly true, but perhaps the lack of perfect correlation within each day's observations offsets this factor. Future analysis will attempt to derive a better estimate of the degrees of freedom of these data.

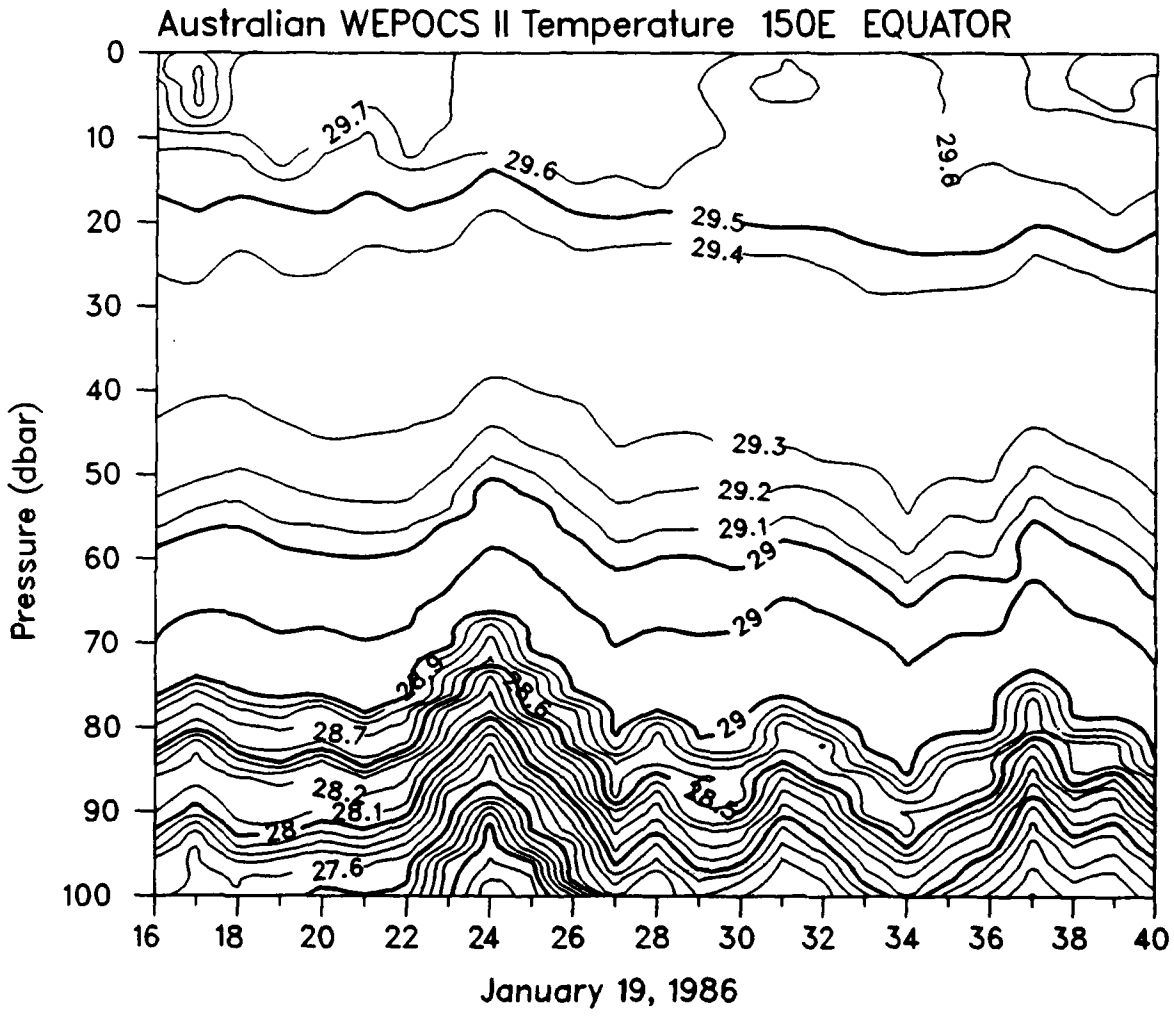

Figure 9. Time series of upper ocean temperature from hourly CTD casts on the equator at 150°E. The times are local.

At the 95% confidence level (r=0.26), there are three significant correlations. Both the density and temperature mixed layer depth estimates are positively correlated with the wind speed, suggesting a tendency for increased mixed layer depth with stronger wind. Figure 7 illustrates this correlation, though the percent of variance explained by the correlation is relatively small. The correspondence of wind speed and dS2 is not significant, but is of the same sense. The correlation of dS2 with SSS is significant though, which might explain the reduced dependence on wind speed. Note that these correlations were also run with wind speed squared (psuedostress), but the correlation coefficients actually were smaller.

At 90% confidence, dD shows the same correlation with SSS as dS2, which is consistent with the idea that surface buoyancy forcing associated with precipitation is an important factor in determining the mixed layer depth. Also, dT2 shows a negative correlation with SST, which indicates a tendency for the mixed layer depth to be shallower when SST is high, which might occur after maximum diurnal heating.

While there are no significant correlations between the surface variables and the difference of dT2 and dS2, the signs of the correlations are consistent with the idea that precipitation and heating are responsible for the mismatch in depths.

DISCUSSION

The Shallow Mixed Layer, and the Importance of Salinity

The western equatorial Pacific is a region where the warmest open-ocean sea surface temperatures in the world are found, and it is characterized by relatively low surface salinity due to frequent and heavy precipitation (Weare et al., 1981). In contrast to the central equatorial Pacific, the winds in the west are weak on average, and highly intermittent. The relative importance of wind and buoyancy forcing between these two regions is very important for understanding the distribution of mixed layer depth.

The new WEPOCS observations demonstrate that the mixed layer in the western equatorial Pacific is shallow in general, averaging 30 m. The top of the thermocline is found at an average depth of about 50 m. (DT1 in Table 1). The situation in Fig. 2 is quite exceptional. In the central Pacific, the observations from Tropic Heat show that the mixed layer is about 40-50 m deep, and there is a pronounced diurnal cycle of mixing associated with convective overturn due to nighttime cooling at the surface (Gregg et al., 1985). In the western Pacific, the stratification is almost always stable because of the strong buoyancy forcing associated with an excess of precipitation (P) over evaporation (E). This gradient in E-P can be seen in Fig. 10. The most negative values of E-P are centered in the WEPOCS region, and relatively small values are found on the equator near 140°W where Tropic Heat was conducted.

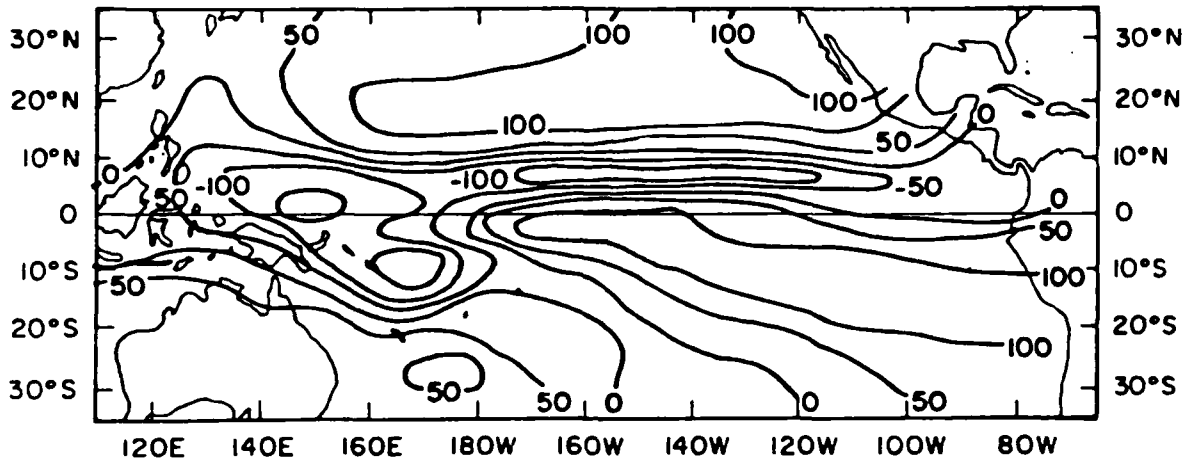

Figure 10. The annual average distribution of net evaporation over precipitation in heat flux units (W m^{-2}) [After Weare et al., 1981].

Salinity is usually neglected in models of the mixed layer. However, Miller (1976) investigated the effects of including salinity in the one-dimensional mixed layer model of Denman (1973). He found that the vertical salinity profile can play a critical role in determining the evolution of the depth of the mixed layer, and can even determine whether the mixed layer warms or cools, for given surface forcing. In one particular experiment, the addition of a stable salinity stratification with all other factors held constant resulted in an equilibrium mixed layer depth of 50 m versus 90 m without salinity.

This effect can be simply understood by comparing the available turbulent kinetic energy supplied by the wind versus the work that must be done to overcome potential energy when deepening the mixed layer. If the mixed layer is shallower as a result of the stabilizing effect of the salinity profile, then the net heat flux at the sea surface is distributed over a thinner layer, which will result in a warmer mixed layer. This assumes, however, that there are no external feedbacks between net heat flux, precipitation, and wind stress, and no feedbacks between any of these variables and SST. This assumption is of course absurd for the western equatorial Pacific, where the coupling between atmosphere and ocean is quite strong and complex.

The Subduction Hypothesis

The warm, nearly-isothermal upper layer of the western equatorial Pacific is deeper than in the central and eastern equatorial regions. Garwood et al. (1985) attribute this to greater mixing, but three-dimensional equatorial circulation models (eg., Busalacchi and O'Brien [1980]) clearly show that this situation is explainable in terms

of the horizontal convergence of mass in the warm upper layer, driven by the mean wind stress distribution. This provides the backbone for a hypothesis to explain the mismatch in vertical scales between the mixed layer depth and the nearly-isothermal layer in the western Pacific. As in the model of Atlantic 18°C water formation by Woods and Barkmann (1986), we believe that mixed layer waters formed in the near-equatorial region in the vicinity of the dateline are subducted below the extremely light surface waters of the western equatorial Pacific, as they are moved westward in the South Equatorial Current. Meridional circulation in the western Equatorial Pacific may well contribute.

In much the same way that the large-scale meridional distribution of net E-P and heating determines the vertical T-S relationship (see Worthington [1981] for a thorough discussion), the horizontal distribution of net E-P and heating in the tropical Pacific determines the vertical T-S relationship of the upper ocean in the western equatorial Pacific.

The central equatorial Pacific is a region of net evaporation, while the western equatorial Pacific is a region of heavy net precipitation. The strong zonal gradient of E-P can easily be seen in Fig. 10. Therefore, the mixed layer waters formed near the dateline are saltier than those formed further to the west, but are of nearly the same temperature (Reynolds, 1982). As these denser waters are advected westward, they must be subducted below the mixed layer of the western region. In this way, the warm upper layer of the western Pacific can increase in thickness, while the layer where active mixing occurs can be quite a bit shallower.

Recall that temperature inversions of up to 0.5°C were observed frequently during WEPOCS I (Fig. 11), and Meyers (personal communication, 1987) observes these in XBT traces from this region at other times. Also, the mean temperature at 50 m was warmer than that at 15 m as measured from the WEPOCS equatorial mooring at 150°E during the period between the two expeditions. This could be a signature of the subduction process. If the warmest surface waters are found further to the east, as in an average July or August (Reynolds, 1982), then the subducted water can be even warmer than that of the mixed layer in the WEPOCS region. However, such a stable temperature inversion at the base of the mixed layer can also result from strictly one-dimensional processes as found by Miller (1976). Further observations must be made to determine the cause of these persistent temperature inversions.

Intermittent Westerly Bursts

The subduction hypothesis can explain the mean upper ocean structure, but there are seasonal and faster time scale variations of winds, currents, and heat fluxes which may mask this process. An example of this is seen in the response of the western equatorial Pacific upper ocean to a westerly wind burst such as observed during WEPOCS II. Between 27 January and 2 February 1986, westerly winds between 15 and 30 knots were blowing over the near-equatorial region north of New Guinea.

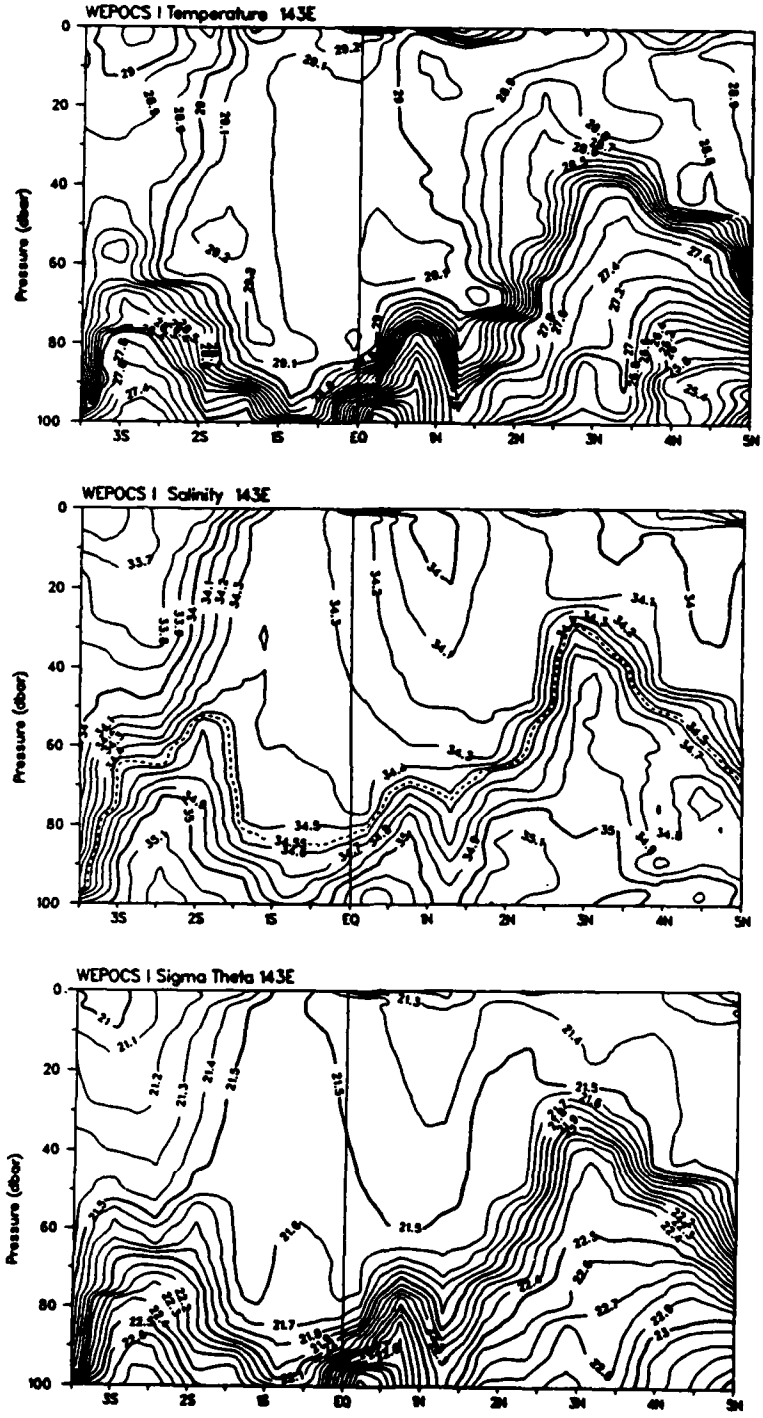

Figure 11 (a). Temperature, salinity, and density (from top to bottom) for WEPOCS I along 143°E. Data from CTD stations at 0.5° latitude spacing.

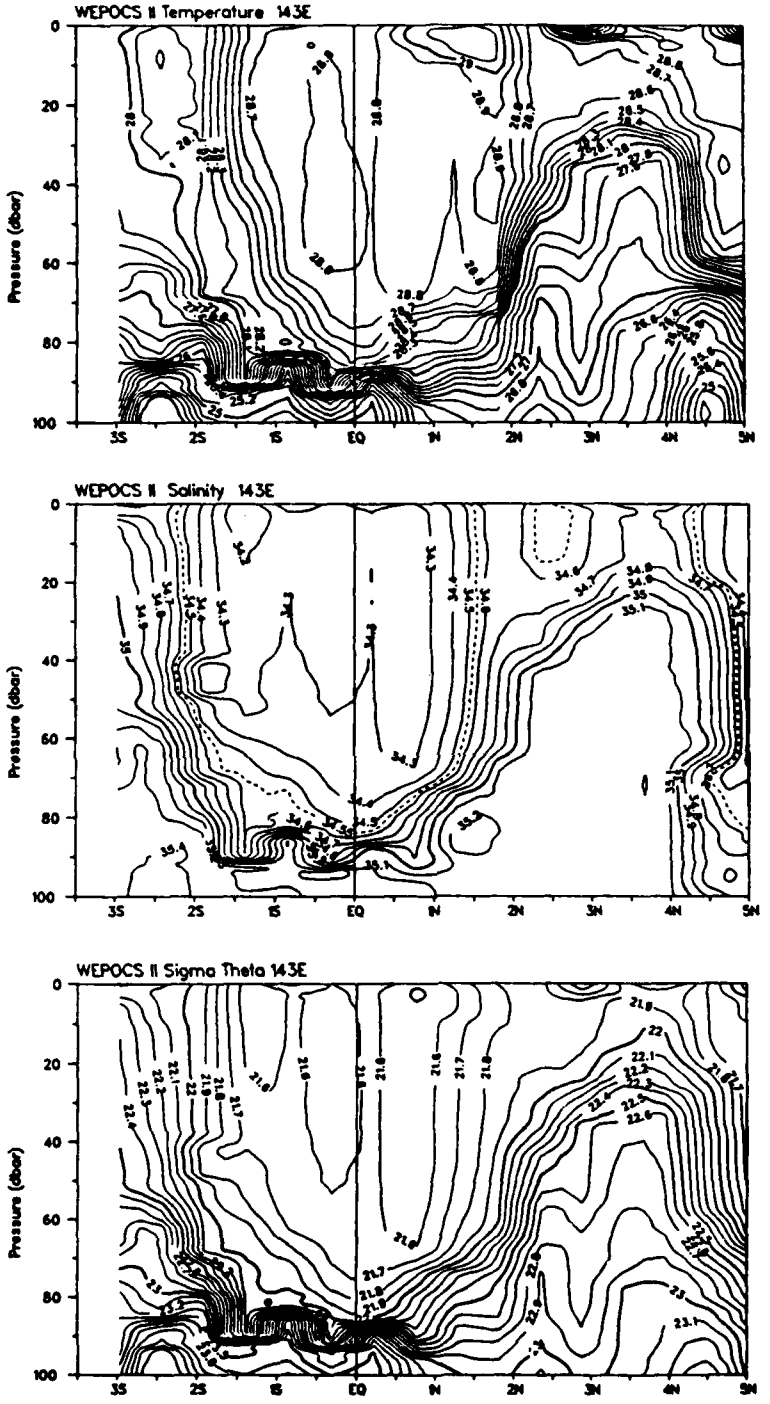

Figure 11 (b). Temperature, salinity, and density (from top to bottom) or WEPOCS II along 143°E. Data from CTD stations at 0.5° latitude spacing.

The climatological winds for January from the Australian Bureau of Meteorology Research Center (Fig. 12) show that, on average, the winds in the western equatorial Pacific are very light at this time of year, and the wind field is highly convergent. The winds veer from northeasterlies north of the equator to northwesterlies south of the equator. However, this smooth picture is the result of a highly variable wind field, both within the month and from year-to-year. Keen (1987) has developed a climatology of westerly wind bursts which shows that this area experiences such wind events more often than regions to the east, and that these events are far more frequent in the northern winter season. It is important to note that there are exceptionally few cases of easterly bursts, and the distribution of zonal wind in this region is highly skewed towards positive (eastward) values (Lukas et al., 1984).

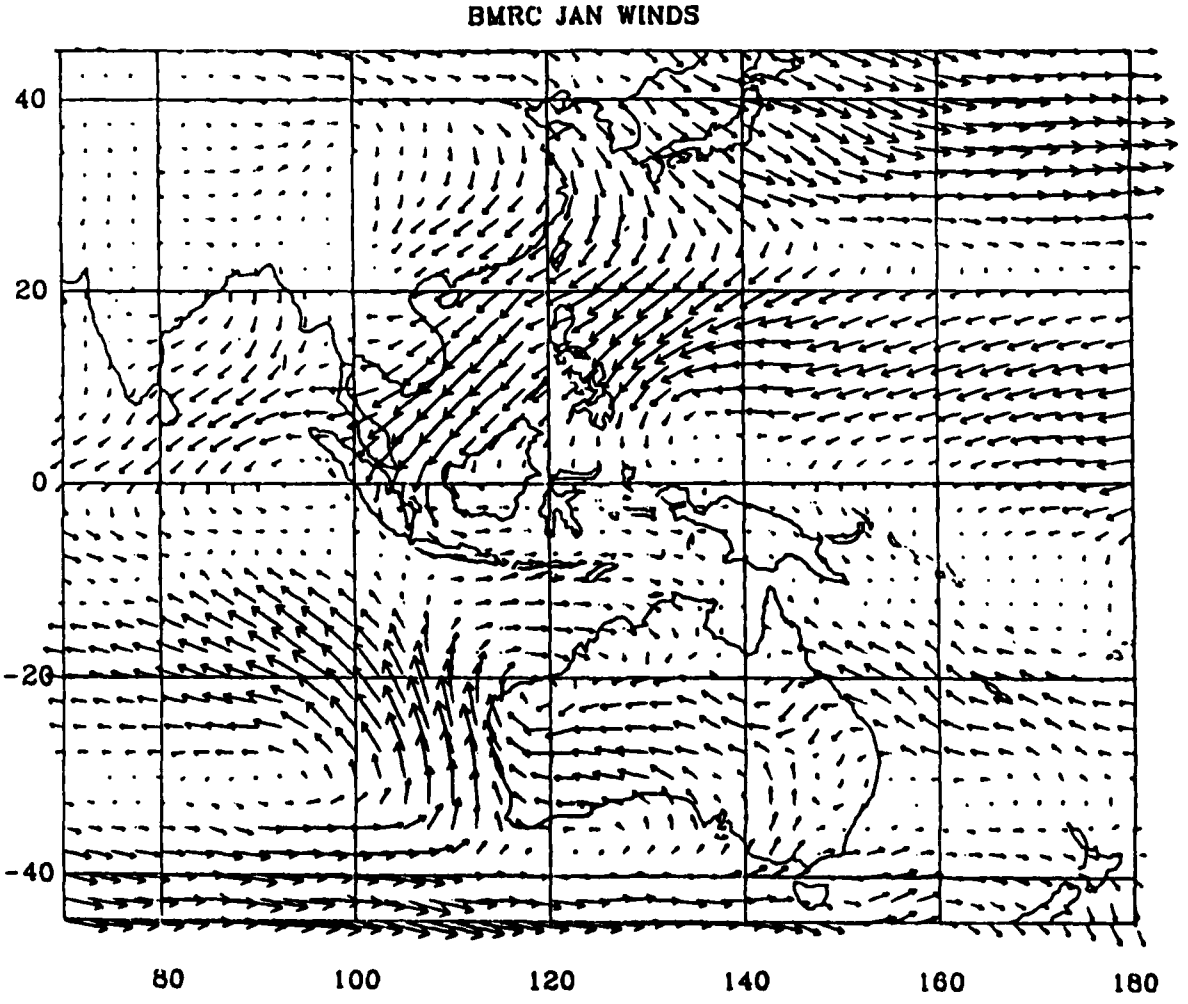

Figure 12. Climatological mean January wind vectors from the Australian Bureau of Meteorology Research Center (courtesy of G. Meyers).

Such intermittent and strong wind forcing events impulsively force the ocean, and they are responsible for the generation of equatorial Kelvin wave pulses (Lukas et al., 1984), among other effects. It is highly likely that these westerly bursts cause a substantial change from the usual fluxes of moisture and heat as well. (Evidence for such a change is found in the mean mixed layer temperatures observed before and after the burst.) There is certainly greater evaporative cooling, but the fresh water balance is not clear. Also, the cloud patterns associated with a westerly burst may affect the insolation in a way that is not obvious.

It was noted earlier that there was a bimodal distribution of mixed layer temperature during WEPOCS II, and that when these observations were separated into the two dominant classes, the observations fell into two time periods separated by the westerly wind event. As the cruise track did not repeat, it remains a possibility that spatial gradients were partly responsible. However, there were no strong spatial gradients of SST observed in the thermosalinograph records along the cruise track, as would be required to explain such a bimodal distribution. The mean SST before the event was 29.8°C, and 28.6°C after the event. The average mixed layer depth was 22 m before, and 44 m during and after the wind event. A portion of this difference may be due to real spatial variations, however. The change in SST is quite large by historical measures of western equatorial Pacific SST variability, and is associated with latent heat fluxes (Meyers et al., 1986), though entrainment of cooler thermocline waters into the mixed layer was probably a contributing factor.

The effect of such impulsive forcing on the western equatorial Pacific upper ocean can be seen in Fig. 11 from the contrast of the temperature, salinity, and density fields along 143°E from WEPOCS I (light winds) and WEPOCS II (just after the westerly burst). The near-equatorial temperatures are higher during WEPOCS I than during WEPOCS II, and the salinity is lower. This is consistent with a cooling of the upper ocean by the strong winds, and with enhanced evaporation. Also, the density field is markedly different. During WEPOCS II, density is symmetric with respect to the equator, and the mixed layer is deeper especially on the equator. Westerly winds straddling the equator cause an Ekman convergence at the equator, resulting in a downwelling response there. This circulation sets up in a matter of only a few days (Cane, 1980), and has the effect of concentrating mixed layer waters at the equator, which are then possibly detrained from the actively mixed layer. Upwelling occurs away from the equator as warm upper layer waters close to the equator are advected more rapidly than waters further away. The exceptionally large change in the hydrographic structure apparent near 3°S during WEPOCS II is due to upwelling along the Papua New Guinea coast induced by the westerly wind burst.

Recall that the distribution of mixed layer depths was found to be exponential which is characteristic of a Poisson process. This suggests physics which are intermittent or event-like. Either the boundary

conditions (the winds stress and buoyancy flux) or the dynamics (e.g., entrainment) or both may be intermittent. The combined influence of intermittent forcing and the barrier layer is illustrated schematically in Fig. 13, where entrainment cooling switches on when the mixed layer deepens enough to reach the substantial temperature gradients found at the top of the thermocline. In a Poisson process, events occur randomly, but there is an average recurrence rate. It is appropriate to treat westerly wind bursts as discrete events because a) they are relatively rare, and b) there are no easterly bursts. For a nonstationary Poisson process, the rate parameter is a function of time, and for the westerly wind bursts, the rate parameter varies seasonally and interannually as evidenced by the climatology of such events constructed by Keen (1987).

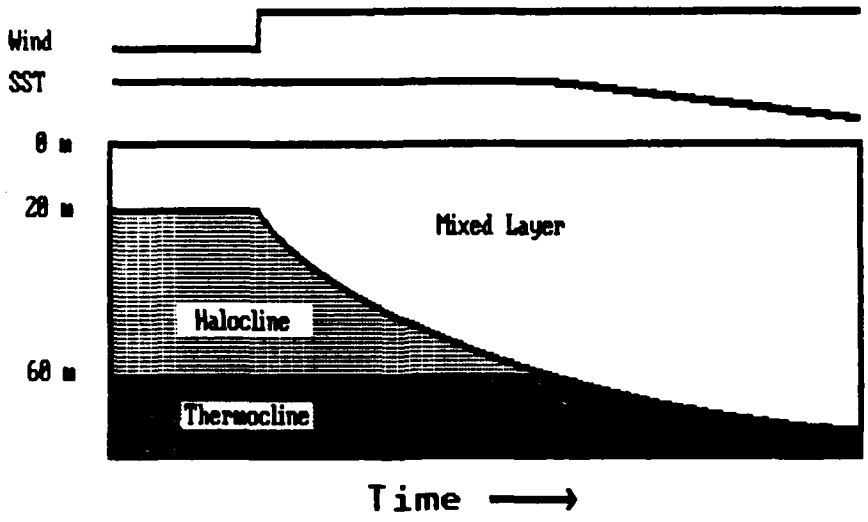

Figure 13. Schematic showing development of mixed layer depth and sea surface temperature when strong winds are turned on. Entrainment cooling of the mixed layer only begins when mixed layer has deepened through salt-stratified barrier layer.

CONCLUSIONS

The new observations from the Western Equatorial Pacific Ocean Circulation Study have shown that the mixed layer in this important region is much shallower than previously thought, averaging only about 30 m. This appears to be a result of strong positive buoyancy fluxes associated with heavy precipitation, combined with highly variable wind forcing.

The vertical scale of temperature in the upper ocean in the equatorial Pacific is larger than for salinity, which is a reflection of the larger zonal scale for SST and

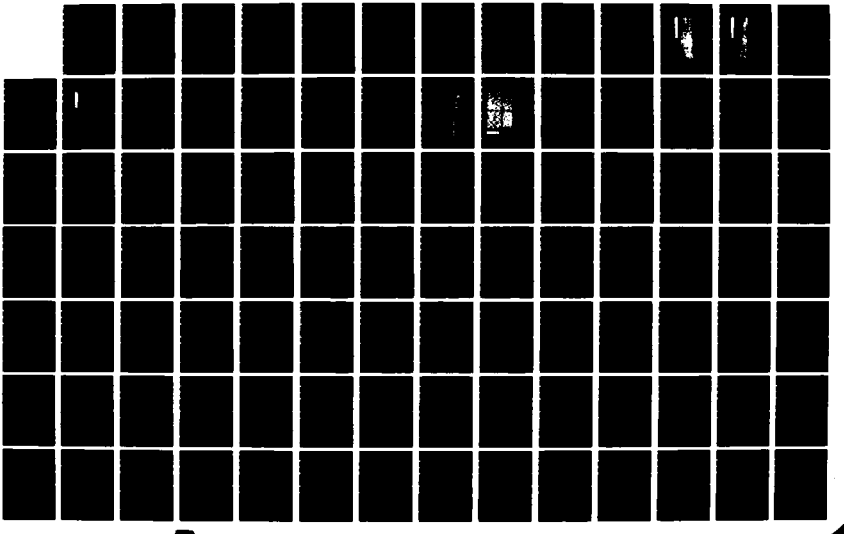

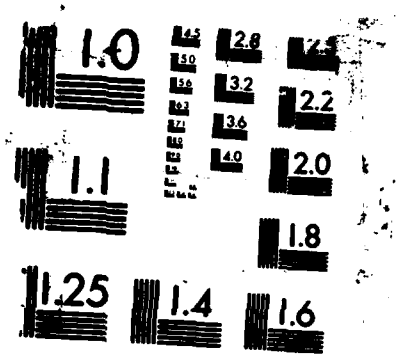

MICROCOPY RESOLUTION TEST CHART

precipitation. A hypothesis of subduction of saltier mixed layer waters from the east below the fresh mixed layer of the western equatorial Pacific appears to explain this aspect of the WEPOCS observations. New datasets are required to properly test this hypothesis.

The primary implication of the vertical mismatch in scales of the upper ocean thermal and haline structures in the western Pacific is that there is very little vertical heat flux out of the mixed layer since there is usually only a very weak vertical temperature gradient at the base of the mixed layer. There can be no entrainment of thermocline waters into the mixed layer except during very strong wind events, because of the strong stratification associated with the vertical salinity profile. Such entrainment was considered to be a continuous process by Niiler and Stevenson (1982), but these new observations suggest that entrainment might be very rare in the western equatorial Pacific. Thus, the mixed layer can easily warm in the absence of westerly wind bursts, which can erode the salinity-stratified warm upper layer and switch on entrainment cooling as a mechanism to modify the mixed layer heat budget (Fig. 13). This would imply that net cooling only occurs during the onset of ENSO events, when westerly bursts are more frequent (Luther et al., 1983; Keen, 1987). For the long term mean, there can be no net temperature increase of the mixed layer of course, but the ENSO phenomenon may exist solely because there is an inadequate removal of heat from the upper layer of the western tropical Pacific Ocean by the mean ocean circulation, as suggested by Wyrtki (1985).

We hypothesize that the switching on of the entrainment mechanism by the frequent and strong westerly bursts observed prior to the onset of ENSO conditions (Keen, 1987) is the essential process needed to allow the ocean warm pool/atmospheric convection supercluster to break away from the western boundary region and begin its eastward migration characteristic of the early phase of ENSO (Gill and Rasmussen, 1983). Further, we speculate that warming of the western equatorial Pacific sea surface increases the frequency and strength of such westerly bursts, effectively resulting in a negative feedback mechanism that is an essential part of the ENSO cycle. New observations are planned which will help to refine and test this hypothesis.

ACKNOWLEDGMENTS

The Western Equatorial Pacific Ocean Circulation Study (WEPOCS) is supported by the U. S. National Science Foundation and the Australian Commonwealth Scientific and Industrial Research Organisation. The assistance of Drs. Richard Lambert and Angus McEwan was crucial to the success of the program. This support is gratefully acknowledged. The first author was supported during the writing of this manuscript by NSF grant OCE84-16383.

The seamanship of the captains and crews of the research vessels FRANKLIN, MOANA WAVE, and THOMAS G. THOMPSON, as well as their interest in the scientific program, were essential to the success of the field work. The excellent technical support by the PACODF group of Scripps Institution of Oceanography, the CTD Group of Woods Hole Oceanographic Institution, the nutrient chemistry group of Oregon State University, and the CSIRO Division of Oceanography was responsible for the high quality of the WEPOCS dataset. Graduate students from the University of Washington and the University of Hawaii contributed their time and enthusiasm to the data gathering efforts. Sharon DeCarlo has efficiently managed the large and numerous datasets obtained in WEPOCS, and her skillful programming in the computer analysis of these data is appreciated.

Drs. Gary Meyers and J. Stuart Godfrey have been most generous in sharing their ideas in numerous discussions about the western equatorial Pacific mixed layer.

Valerie Ono provided professional word processing support in the several iterations of this manuscript. This is Hawaii Institute of Geophysics Contribution No. 1861 and Joint Institute for Marine and Atmospheric Research Contribution No. 87-0132.

REFERENCES

Barnett, T. P., 1977: Statistical relations between ocean and atmosphere fluctuations in the tropical Pacific. J. Phys. Oceanogr., 11, 1043-1058.

Busalacchi, A. J. and J. J. O'Brien, 1980: Seasonal variability in a model of the tropical Pacific. J. Phys. Oceanogr., 10, 1929-1951.

Cane, M., 1980: On the dynamics of equatorial currents, with application to the Indian Ocean. Deep-Sea Res., 27A, 525-544.

Colin, C., C. Henin, P. Hisard, and C. Oudet, 1971: Le courant de Cromwell dans le Pacifique Central en fevrier 1970. Cah. ORSTOM ser. Oceanogr., 9, 167-186.

Cremoux, J. L., 1981: Resultats des croisieres faites le long de l'Equateur par le Centre ORSTOM de Noumea. Rapp. Sci. et Tech., #16, ORSTOM, Noumea, New Caledonia.

Denman, K. L., 1973: A time-dependent model of the upper ocean. J. Phys. Oceanogr., 3, 173-184.

Fofonoff, N. P., S. P. Hayes, and R. C. Millard, 1974: WHOI/Brown microprofiler: Methods of calibration and data handling. WHOI Tech. Rept. 74-89.

Garwood, R. W., P. Muller, and P. C. Gallacher, 1985: Wind direction and equilibrium mixed layer depth in the tropical Pacific Ocean. J. Phys. Oceanogr., 15, 1332-1338.

Gill, A. E. and E. M. Rasmussen, 1983: The 1982-83 climate anomaly in the equatorial Pacific. Nature, 306, 229-234.

Gregg, M. C., H. Peters, J. C. Wesson, N. S. Oakey, and T. J. Shay, 1985: Intensive measurements of turbulence and shear in the equatorial undercurrent. Nature, 318, 140-144.

Keen, R., 1987: Equatorial westerlies and the Southern Oscillation, submitted to Mon. Wea. Rev.

Lemasson, L. and B. Piton, 1968: Anomalie dynamique de la surface de la mer le long de l'Equateur dans l'Ocean Pacifique. Cah. ORSTOM Ser. Oceanogr., 6, 39-45.

Levitus, S., 1982: Climatological atlas of the world ocean. National Oceanic and Atmospheric Administration Professional Paper 13, Rockville, Md., 173 pp.

Lindstrom, E., R. Lukas, R. Fine, E. Firing, J. S. Godfrey, G. Meyers, and M. Tsuchiya, 1987: The Western Equatorial Pacific Ocean Circulation Study. In preparation.

Lukas, R., S. P. Hayes, and K. Wyrtki, 1984: Equatorial sea level response during the 1982-83 El Nino. J. Geophys. Res., 89, 10,425-10,430.

Lukas, R. and M. Tsuchiya, 1986: Hydrographic observations from the first U.S. cruise of the Western Equatorial Pacific Ocean Circulation Study (WEPOCS). JIMAR Data Rept. 1, Joint Institute for Marine and Atmospheric Research, U. Hawaii, 350 pp.

Luther, D. S., D. E. Harrison, and R. A. Knox, 1983: Zonal winds in the central equatorial Pacific and El Nino. Science, 222, 327-330.

Meyers, G., J. R. Donguy, and R. K. Reed, 1986: Evaporative cooling of the western equatorial Pacific by anomalous winds. Nature, 323, 523-526.

Miller, J., 1976: The salinity effect in a mixed layer ocean model. J. Phys. Oceanogr., 6, 29-35.

Mohanty, N., 1986: Random Signals Estimation and Identification. Van Nostrand Reinhold Co., New York, 626 pp.

Niiler, P. and J. Stevenson, 1982: The heat budget of tropical ocean warm-water pools. J. Mar. Res., 40 (suppl.), 465-480.

Rao, M. S. V, W. V. Abbot III, and J. S. Theon, 1976: Satellite-derived global oceanic rainfall atlas (1973 and 1974). National Aeronautics and Space Administration special publication, NASA SP-410, 31 pp + 5 Appendices.

Reynolds, R. W., 1982: A monthly averaged climatology of sea surface temperature. NOAA Tech. Rep. NWS 31, 35 pp.

Weare, B. C., P. T. Strub, and M. D. Samuel, 1981: Annual mean surface heat fluxes in the tropical Pacific Ocean. J. Phys. Oceanogr., 11, 705-717.

Woods, J. D. and W. Barkmann, 1986: A Lagrangian mixed layer model of Atlantic 18°C water formation. Nature, 319, 574-576.

Worthington, L. V., 1981: The Water Masses of the World Ocean, Some Results of a Fine-Scale Census. In: Evolution of Physical Oceanography, B. A. Warren and C. Wunsch, eds., MIT press, Cambridge, 42-69.

Wyrtki, K., 1964: The thermal structure of the eastern Pacific Ocean. Deut. Hydrogr. Zeit., Suppl. Ser. A(8), 6-84.

Wyrtki, K., 1985: Water displacements in the Pacific and the genesis of El Nino cycles. J. Geophys. Res., 90, 7,129-7,132.

OBSERVATIONS OF WAVES AND LANGMUIR CIRCULATION WITH DOPPLER SONARS

J.A. Smith and R. Pinkel

Marine Physical Laboratory A-013, Scripps Institution Oceanography
University of California, San Diego La Jolla, California 92093

ABSTRACT

In October-November 1983, Doppler sonars mounted on the Research Platform FLIP were used to scatter 75 kHz sound from the underside of the sea surface at low angle, as well as from the interior of the mixed layer. Surface gravity waves were easily seen in velocity estimates from the surface scattering sonar, even though the wave conditions were unusually calm. Valid measurements of sea surface motion were obtained over the range interval 600 to 1400 m from FLIP. A second sonar, which transmitted horizontally and scattered from the interior of the mixed layer, also sensed surface waves, although with amplitude reduced in proportion to the decay of the motions with depth. Wavenumber frequency spectra of the observed motions are consistent with linear theory. In addition, lower frequency motions were detected, which are consistent with Langmuir circulation. While the sonars lack the resolution to see the smallest scale structures, cell-like structures with cross-wind scales comparable to mixed layer depth were seen in both scattering intensity and Doppler velocity. The emergence of this technology enables the synthesis of kilometer-long surface current arrays in the open sea, without the cost and logistical support usually associated with large aperture arrays.

INTRODUCTION

We present preliminary results of a new application of acoustic technology. High frequency sound is scattered at low angle from the underside of the sea surface. From the Doppler shift of the backscattered sound, surface velocities can be estimated over ranges in excess of 1.4 km, with roughly 20-m range resolution. Surface gravity waves are evident in these velocity measurements. The velocity measurements can also be time-averaged, to determine low-frequency surface currents and their spatial variability.

In this work, two examples of surface scattering data are presented. Both were obtained on the 1983 Mixed Layer Dynamics Experiment, MILDEX. The first example is a one-hour record showing wave (swell) propagation. A full three-dimensional wavenumber frequency spectrum $F(k,l,\omega)$ is estimated, using data from two orthogonal sonar beams. The second example presents an eight-hour view of low-frequency surface currents, during a period of particularly strong Langmuir circulation (Langmuir, 1938).

In previous work, the intensity of acoustic returns from surface-scanning sonars has been used to detect surface wave breaking, internal waves and fronts, and even Langmuir circulation (e.g., Thorpe, 1986 and references therein). This is possible because the variations in intensity are related to sub-surface bubble densities, which are modulated by the observable phenomena. In this work, the modulation of surface and subsurface scattering intensity is also clearly seen. New in this work is the ability to correlate the observed intensity fluctuations with the flow field, as estimated from the Doppler shift of the same sonar returns.

THE DATA

During October and November 1983, the Research Platform FLIP was a participant in the Mixed Layer Dynamics Experiment (MILDEX). A number of sensor systems were simultaneously operated in the attempt to observe the mixed layer. The principal sensing systems on board FLIP included fixed and profiling arrays of Vector Measuring Current Meters, operated by R. Weller of Woods Hole Oceanographic Institution; wind, wave, solar radiation, and other environmental sensors; a repeatedly profiling CTD; and six Doppler sonars. The sonars were mounted at a depth of 36 m on FLIP's hull (Fig. 1). They were operated at frequencies between 67 and 80 kHz. Two of the six sonars had nearly horizontal beams while the remaining four pointed downward. A servo controlled thruster, linked to the ship's gyrocompass, was used to maintain the azimuthal orientation of the sensors.

This paper presents data from the two quasi-horizontal sonars. These were oriented at right angles in azimuth. The starboard sonar pointed about one degree up from horizontal on the average. The 75-kHz sound it transmitted scattered from the volume of the mixed layer for the first 500 m of range. Sea surface scattering dominated the return for the subsequent 900 m of sampled range. The port sonar was operated at 80 kHz, and had a mean elevation angle slightly downward from horizontal, much less than 1°. Volume scattering data was collected from the interior of the mixed layer for the first 600 to 900 m. At greater ranges, the beam exited the base of the mixed layer, and profiled the upper thermocline.

The horizontal beamwidth of the sonar is ±1.1°, as measured to the -3db points of the beam pattern. Thus at a "typical" range of 1 km, the surface footprint of each velocity estimate from the starboard (surface grazing)

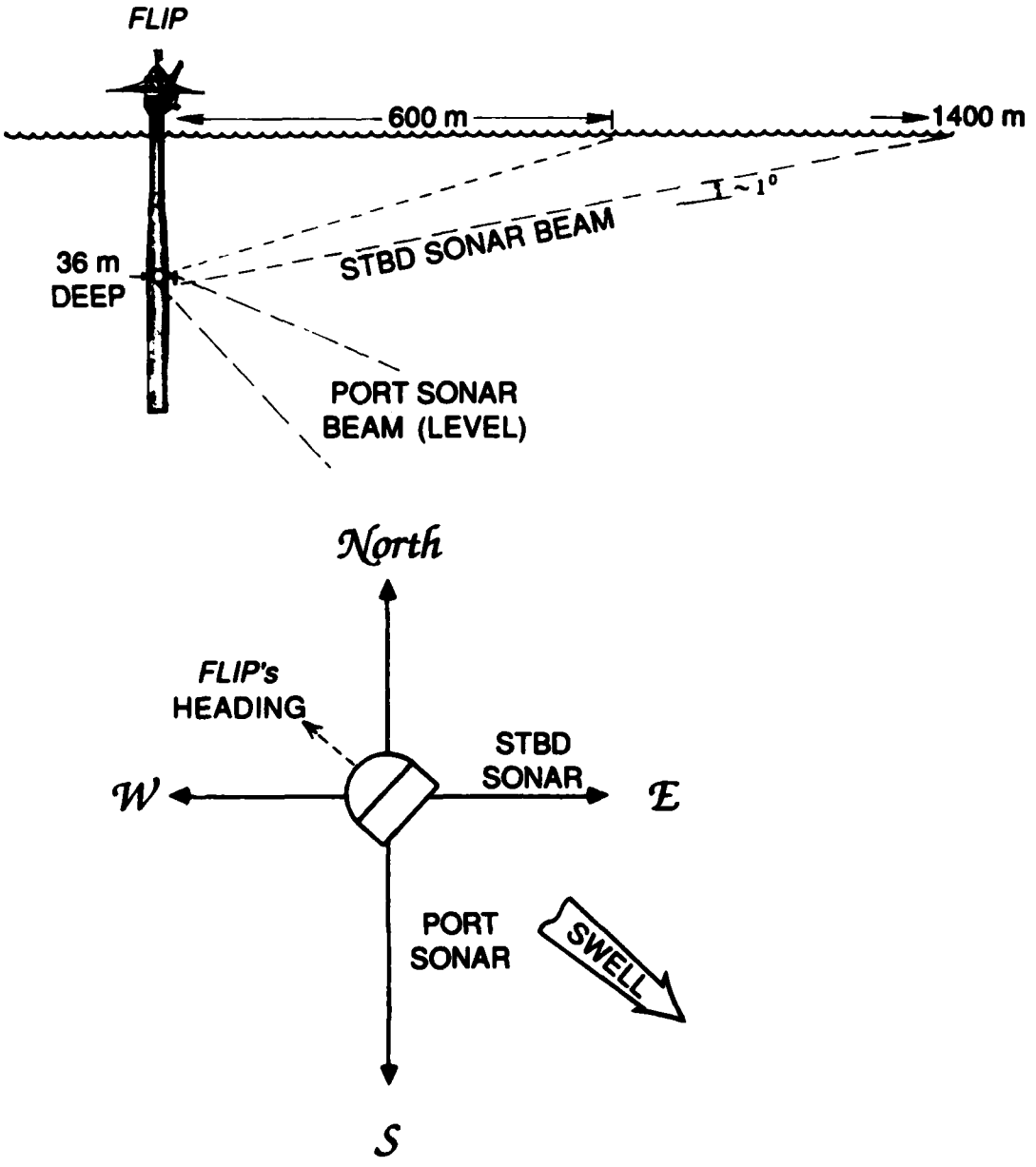

Fig. 1. a) Schematic and b) plan view of FLIP during the raw data collection. The East sonar grazed the surface, the other remained near 35 m below.

sonar is about 22.5 m (range) by 40 m (across beam). For the port beam, the vertical spread of about 0.44° also enters, yielding a sample volume at 500 m range of about 20 × 20 m horizontally by 4 m vertically, centered somewhere between 25 and 45 m depth (depending on the instantaneous tilt of FLIP).

In operation, each sonar transmitted a sequence of four tones every two seconds. The duration of each tone was 30 ms, corresponding to a 22.5-m averaging range. Velocity estimates were formed using the complex covariance technique of Rummler (1968), using 2-ms lagged covariances. Covariance estimates were averaged over 18 ms in time (13.5 m in range) prior to estimating the velocity. For this signal processing configuration, a "Cramer-Rao" lower bound for error variance in the velocity estimate for a single ping, in the limit of infinite signal-to-noise ratio and uniform scatterer velocity (Theriault, 1986), yields about 3 cm/s RMS error. Using the measured pulse-to-pulse velocity variability of the data, 9 cm/s RMS precision is indicated. However, this includes any real velocity variance within the roughly 20 × 20 m "samples". Twelve-second waves of 0.5 m amplitude were present at the time of the precision measurement. These have steepness (ak) of about 1/70. Averaging over phase, the RMS velocity gradient is then about 1/200 s^{-1}. For an average separation of 10 m, the resulting velocity variance is about 5 cm/s, which is therefore a reasonable estimate of the physical velocity variance. The sum of the physical and lower bound measurement variances is close to the empirical noise estimate.

In operating the full complement of the six sonars, it is necessary to record and process 25 thousand numbers per second. To permit continuous operation of the system over periods of weeks, a CSPI Map 300 array processor is used to form averaged estimates of the covariances in real time over 30-s intervals. However, on the night of 26 October, about an hour's worth of unaveraged data from all six sonars was recorded on tape, filling one tape roughly every 7 min. This was the only segment of such "raw data" recorded during MILDEX, and comprises a "trial sample" for open ocean surface wave detection.

For the eight-hour "Langmuir circulation" segment, the velocity estimates were further averaged over 3 min (90 pings), reducing the RMS statistical noise estimate to about 1 cm/s. In this case, the high frequency variation of surface wave velocities must be considered as a noise source for the mean motion measurement. Worst-case contamination of the 3-min average occurs if there are half-integral numbers of waveperiods in time T = 3 min. Using $u^{orb} = a\sigma \sin \sigma t$ and setting $\sigma = n\pi/T$ where n is any odd integer, an average over time T then results in a worst-case of $u^{contamination} = 2^{3/2}h/T$, where h is the RMS displacement of the surface. During the Langmuir circulation segment, the maximum RMS displacement was of order 1 m, leading to worst-case contamination of 1.6 cm/s. The

directional spread, frequency spread, and exponential decay of the orbital velocity with depth would all decrease this aliasing estimate.

In the fluid volume, the dominant scattering targets at 80 kHz are zooplankton. A clear diurnal cycle in scattering strength is seen in all of the volume reverberation data. Surface scattering may arise from either capillary waves at the surface or bubbles just below. The 80-kHz sound used here scatters resonantly from bubbles of about 40 μm radius near the surface, which is near the observed peak in bubble size spectra (Johnson and Cooke, 1979). It is felt that the subsurface bubble cloud is the dominant scatterer (McDaniels and Gorman, 1982; Thorpe, 1986 and references therein). This bubble cloud has been observed to decrease roughly exponentially with depth, with a depth scale which increases slightly with wind, from about 0.4 m for 4 m/s winds (at 10 m height) to about 0.7 m for 10 m/s winds (Thorpe, 1986). For given wind conditions, this depth scale remains nearly constant, although the absolute intensity at a specific depth can vary by about two orders of magnitude (Thorpe 1986). Thus, the depth-scale of the "surface-measurements" shown in the surface wave section may be taken as about a half meter below the instantaneous surface, increasing to about 3/4 meter during the Langmuir circulation segment. Sheltering of parts of the surface from this sonar beam probably occurred occasionally. At the farthest range of 1400 m, the upward angle to the surface from 35 m depth is about 1/40. For 12-s swell (wavelength 225 m) with an amplitude of 0.5 m, as was present during the first (surface wave) segment, the steepness is about 1/70. Thus, the RMS slope was just slightly over half the slope of the beam, and so such sheltering was infrequent during that time period. In this data, the surface-backscattered (starboard) intensity was observed to be about 35 to 40 db greater than the non-surface (port) intensity at the greatest ranges. Thus, although the farthest subsurface ranges are lost to noise, the surface scattering sonar signal remains quite strong over the full 1400 m.

SURFACE WAVES

During the raw data run, FLIP was oriented with the starboard, surface grazing sonar pointing due east and the port sonar pointing due south. The wind was steady at about 4 to 5 m/s from the NNE, and a 12-s swell of about 1 m height (crest-to-trough) was incident from the WNW. Wave propagation away from FLIP is evident in the data from both sonars (Figs. 2 and 3). Also, a range-independent response at the wave frequency exists, due to the movement of FLIP by the swell's orbital motion. This signal was removed from the data shown, for clarity. Notably, the range-independent response is roughly equal in the two beams, whereas the propagating component is attenuated in the South (subsurface) sonar due to the exponential decay with depth of the waves.

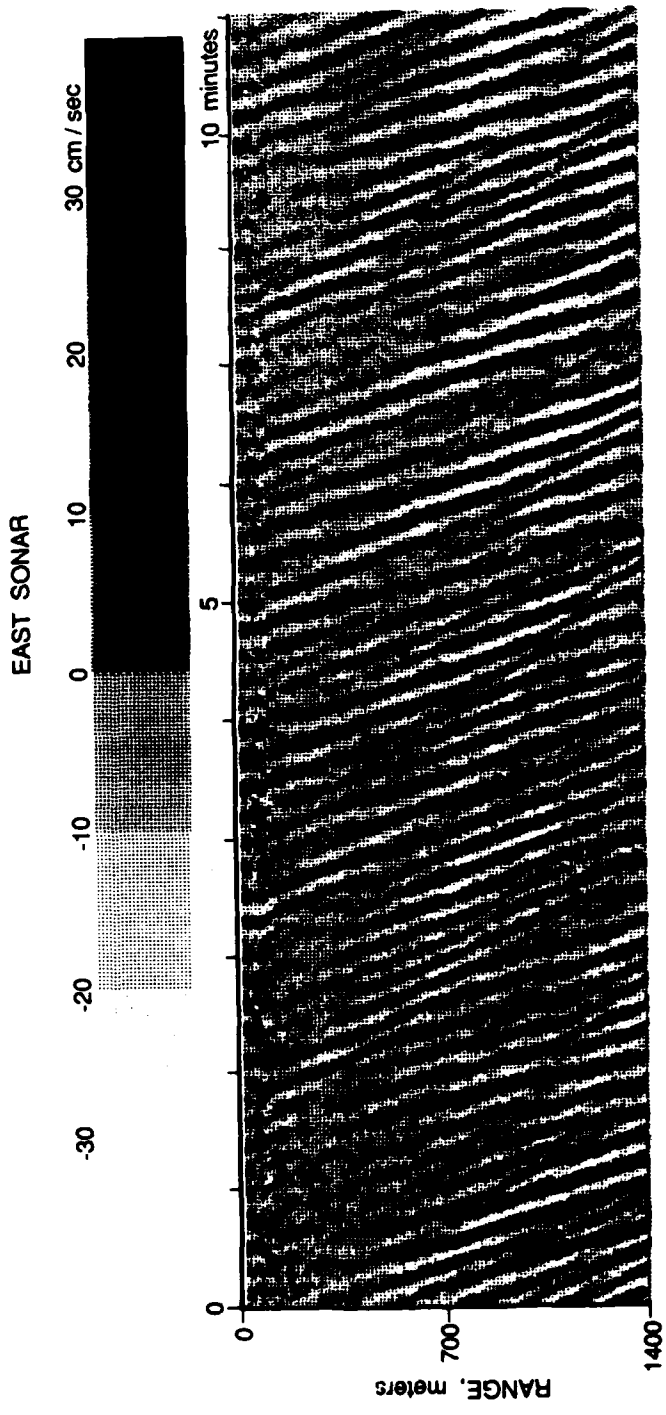

Fig. 2. Eleven minutes worth of velocity data from the East sonar. Surface return dominates from about 600 m to 1400 m. Note the wave-like disturbances propagating away from FLIP.

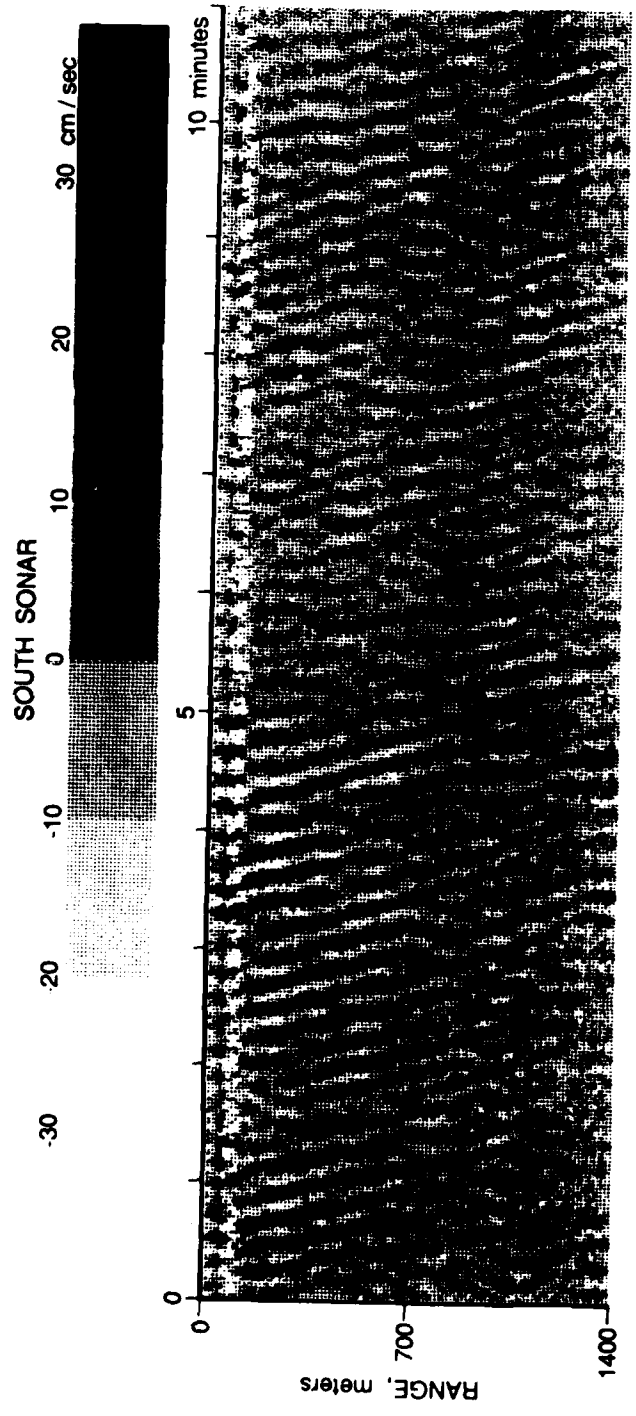

Fig. 3. The same eleven minutes from the South sonar. Beyond about 1 km, the signal strength dropped into noise. Short of 120 m or so, the data is contaminated by side-lobe return. Note the weaker wave propagation, with a cross-hatched appearance due to both Northward and Southward propagating components.

Wavenumber-frequency spectra were calculated for each beam separately, and are shown in Figures 4 and 5. These were formed from 26 sequential data segments each consisting of 64 ranges by 64 pings (864 m by 128 s). The total averaging time is thus about 55 min. At any given frequency, waves incident on a single beam at some angle θ will produce a signal with an along-beam wavenumber component $|k| \cos \theta \leq \omega^2/g$. In addition, the sonar detects only the component of orbital velocity parallel to the beam, $u^{det} = u^{orb} \cos \theta$. For example, with an isotropic directional distribution of free waves at a given frequency "ω", the one-beam wavenumber spectrum would have sharp high wavenumber cutoffs at $k = \pm \omega^2/g$ (at the dispersive values). Also, because only the along-beam component of orbital velocity is detected, the "raw" power estimates $|u|^2 \cos^2 \theta$ would decrease relative to the true values $|u|^2$ as the observed component $k_x = |k| \cos \theta$ decreases. Thus, the response-function of the one-beam spectra for free waves at a fixed frequency is a parabola, increasing from zero at $k_x = 0$ to sharp cutoffs at $|k_x| = \pm \omega^2/g$. Bound harmonics, at $2k_x$ and 2ω, would also be confined well within these limits.

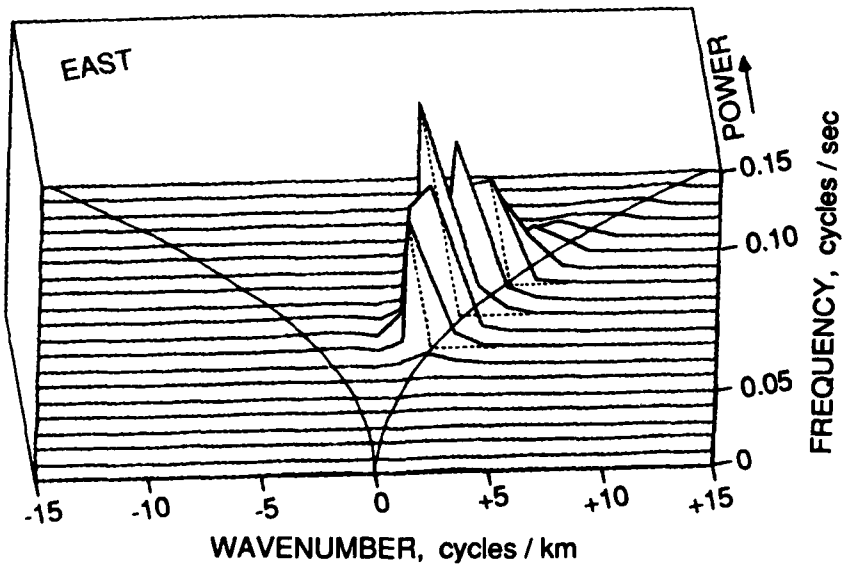

Fig. 4. Frequency-Wavenumber spectra from the East sonar. Each transverse line represents a set frequency. The two curves crossing the frequency lines represent surface-wave dispersion, $\omega^2 = gk$. Positive k (right) corresponds to eastward propagation (away from FLIP).

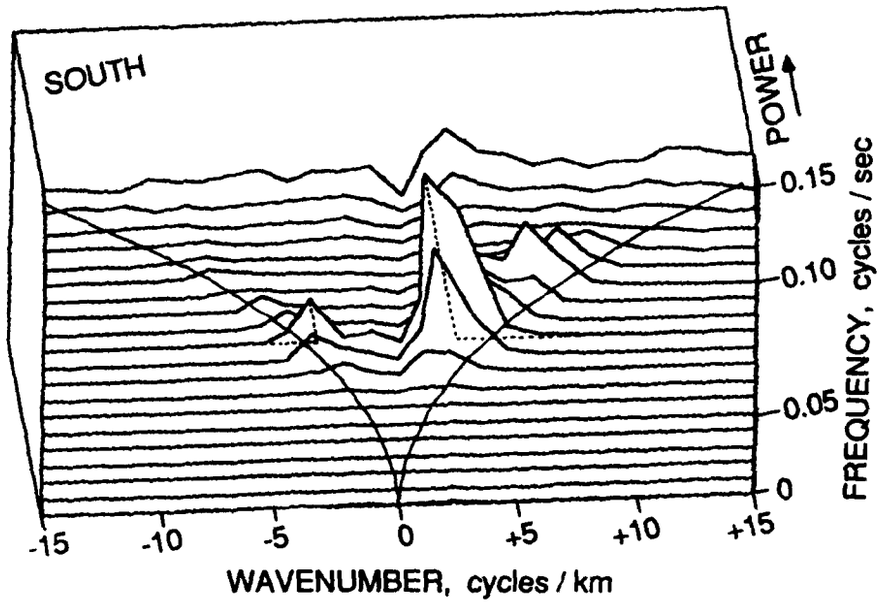

Fig. 5. Frequency-Wavenumber spectra, as in Figure 4, but for the South sonar. Positive k (to the right) corresponds to southward propagation (away from FLIP).

The starboard sonar grazes the surface from about 600 m out to 1400 m. The wavenumber-frequency spectrum (Figure 4) was calculated from just these far ranges. The zero wavenumber band was set to zero, to remove the signature of range independent noise associated with FLIP motion. As shown, almost all the detected energy is on the +k half, corresponding to eastward propagation. In addition, the energy is very strongly concentrated near the maximum (dispersion) value, indicating that the swell is propagating very nearly straight down the beam (i.e., from the west). These trial spectra resolve the wave motions to periods as short as 7 s, or 70 m in wavelength. Shorter wavelengths are suppressed by the 22.5-m along-beam smoothing. The influence of linear dispersion is clearly seen.

Swell propagation also appears in the intensity signal of this "surface scattering sonar". To bring this out, a time-averaged intensity at each range is removed, reducing the effects of beam spreading and attenuation with range. A least-squares-fit parabola was then removed at each timestep, to counter the effects of the slight tilting of the beam in the vertical. A sample of the resulting intensity anomalies is shown in Figure 6. In the farther ranges, patterns appear in the intensity signal, which move with the same "phase speed" as in the velocity signal. The middle-ranges are somewhat confused, due to the vertical side-lobe structure of the beam. As an alternate approach, the coherence between East sonar velocity and intensity anomaly was calculated for various wavenumbers (Table 1), averaging over all 1683 pings. To provide a rough estimate of the effective degrees of freedom and hence of statistical significance, the total averaging time

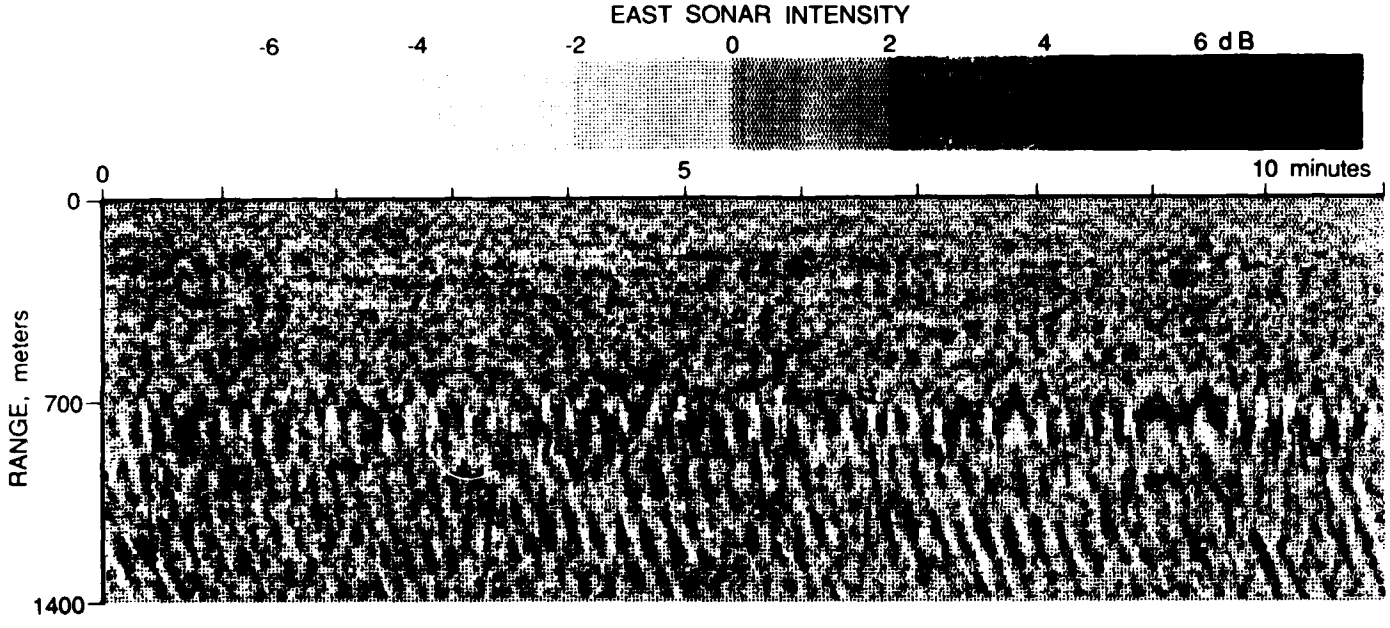

Fig. 6. Intensity anomalies vs. range and time, from the East sonar, as for velocity in Figure 2. Note the suggestion of ripples moving away from FLIP, especially at the far ranges. Surface returns dominate from roughly 600 m out to 1400 m.

(~56.1 min) was divided by the maximum period corresponding to the wavenumber k (i.e., as if the waves were going due east). The most significant correlations, for wavenumbers 3 (λ = 285 m) and 5 (λ = 170 m) correspond to the brightest spot being located about 65° to 70° toward FLIP from the trough, on the face tilted toward the beam (also the rising face of the waves, since they are propagating away from FLIP). The detected fluctuations in intensity could be independent of wave direction (e.g., if they are induced by variations in scatterer density with wave phase), or could depend on wave direction as does the velocity measurement (e.g., if they are purely an effect of tilting the surface across the beam).

Table 1. Co-spectrum $\langle V(k)I^{*}(k)\rangle$ of Velocity and Intensity from the East sonar. Phase angle increases toward FLIP from the wave trough (at 0°).

CYCLES PER 864 m	WAVELENGTH(m)	PHASE(deg)	|C| COHERENCE	<|C|> 68% ESTIMATE
1	864	12.8345	.0166	.0840
2	432	111.3184	.0141	.0707
3	288	65.1740	.2351	.0639
4	216	50.9758	.0848	.0594
5	173	71.6068	.1646	.0562
6	144	73.2922	.0910	.0537
7	123	79.7480	.0900	.0517
8	108	74.8335	.0777	.0500
9	96	83.3032	.0685	.0485
10	86	77.7762	.0680	.0473
11	79	69.6089	.0339	.0462
12	72	84.0478	.0226	.0452

To demonstrate the potential of this observational system, a full directional-frequency power spectrum $F(k,l,\omega)$ was estimated (Fig. 7). The method used was a Mills cross technique, as described by Pinkel (1981) for a pair of orthogonal sonar beams. Several aspects of this method should be noted. First, there is a $\sin\theta\cos\theta$ response: only the radial component of velocity is detected along each beam, and only cross-correlations between beams are used. No estimate is produced along either axis (N or E). This information is contained in correlations along each beam separately, but is neglected in the simple approach used here. In Figure 7, the spectral estimates along the axes were set to zero, and then smoothing in the (k,l) planes applied. Second, estimates adjacent to each axis are contaminated by noise, due to amplification by the $1/\sin\theta\cos\theta$ correction for this response. This effect is noticeable in Figure 7A (the highest frequency plane): ridges appear near the axes at higher wavenumbers (though spread slightly by the 3 by 3 smoothing). Third, statistical sampling error leads to larger-than-zero correlations (estimates) along crosses centered on any large "true" power estimate (see, e.g., Fig. 7E). Finally, this is a surface velocity, not elevation, spectrum. A surface wave elevation spectrum with an ω^{-5} frequency dependence would correspond to an ω^{-3} velocity spectrum.

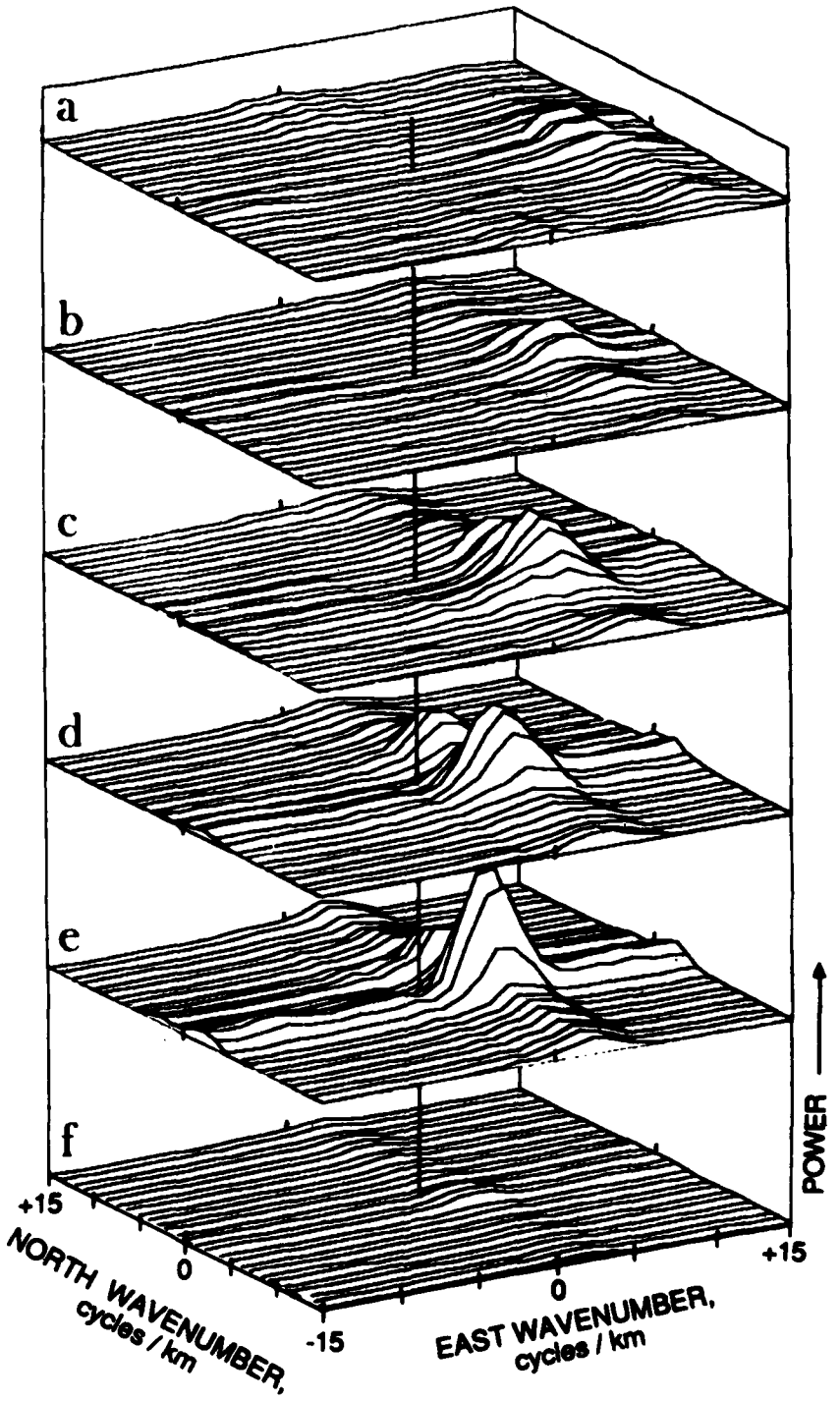

Fig. 7. Three dimensional power spectrum, $F(k,l,\omega)$, from the sonar velocity data. Each surface represents the wave component energies (vertical displacement) at each location on the (k,l) plane, in the frequency band corresponding to periods of (A) 7.1 to 8.0 sec, (B) 8.0 to 9.1 sec, (C) 9.1 to 10.7 sec, (D) 10.7 to 12.8 sec, (E) 12.8 to 16 sec, (F) 16 to 21 sec.

The directional-frequency spectrum shown in Figure 7 is consistent with the visual observations and with the one-beam results. The swell was highly directional, from the WNW. While the peak amplitude in Figure 7 appears in the 13-s to 16-s band, the mean period is closer to 12 s, owing to the sharp low-frequency cutoff and broader high-frequency decay. As frequency increases, the peaks in Figure 7 move toward higher wavenumbers, but also move closer to the East axis. This latter effect is plausibly an artifact of the analysis. The South sonar data was amplified to compensate for exponential decay with depth. Thus, the higher the frequency, the noiser the South sonar data. Finite sampling results in non-zero correlation estimates near the East axis between the amplified noise and the detected (genuine) East-component amplitudes. These are further amplified by the $\sin\theta\cos\theta$ correction. Thus, the true peaks may be further from the East axis than shown in Figure 7.

These trial estimates demonstrate the clear potential of surface-grazing Doppler sonars for estimating directional-frequency spectra of open ocean surface waves. The difficulties discussed above would be reduced by using two surface-grazing beams. With more sophisticated analysis techniques (c.f. Long and Hasselmann, 1979; or Lygre and Krogstad, 1986), greatly enchanced estimates should be possible. Our intent here is to point out the existence and potential of the surface-scanning acoustic Doppler technique for measurement of directional spectra and breaking events.

LANGMUIR CIRCULATION

Discussion of Langmuir circulation focuses on data taken between 2000 local time 9 Nov. to 0600 10 Nov. This eight-hour data segment, just prior to the highest winds of the experiment, provided some of the clearest spatial patterns in the Doppler data. During this time, the winds held from the SSW, with half-hour averaged values of 15 to 20 m/s. The surface layer remained well mixed to a seasonal thermocline at 40 to 60 m depth. The RMS wave elevation increased to just over 1 m in this time, with the waves directed predominantly downwind (toward the ESE). The orientation of the wind and FLIP during this time, and the relative positions of the sonar beams and current meters, are shown in Figure 8.

Downwelling velocities exceeding 30 cm/s were observed by Robert Weller of Woods Hole, using his Real-Time Profiler during MILDEX. Values in the range 15 to 30 cm/s were fairly common, especially in this eight-hour period. As described in previous works (Weller et al., 1985; Smith, Pinkel, and Weller, 1987), these downwelling events are associated with surface convergences. The convergence could be easily inferred from the rapid alignment of material on the surface. They often had downwind horizontal velocity fluctuations roughly as large as those in the vertical.

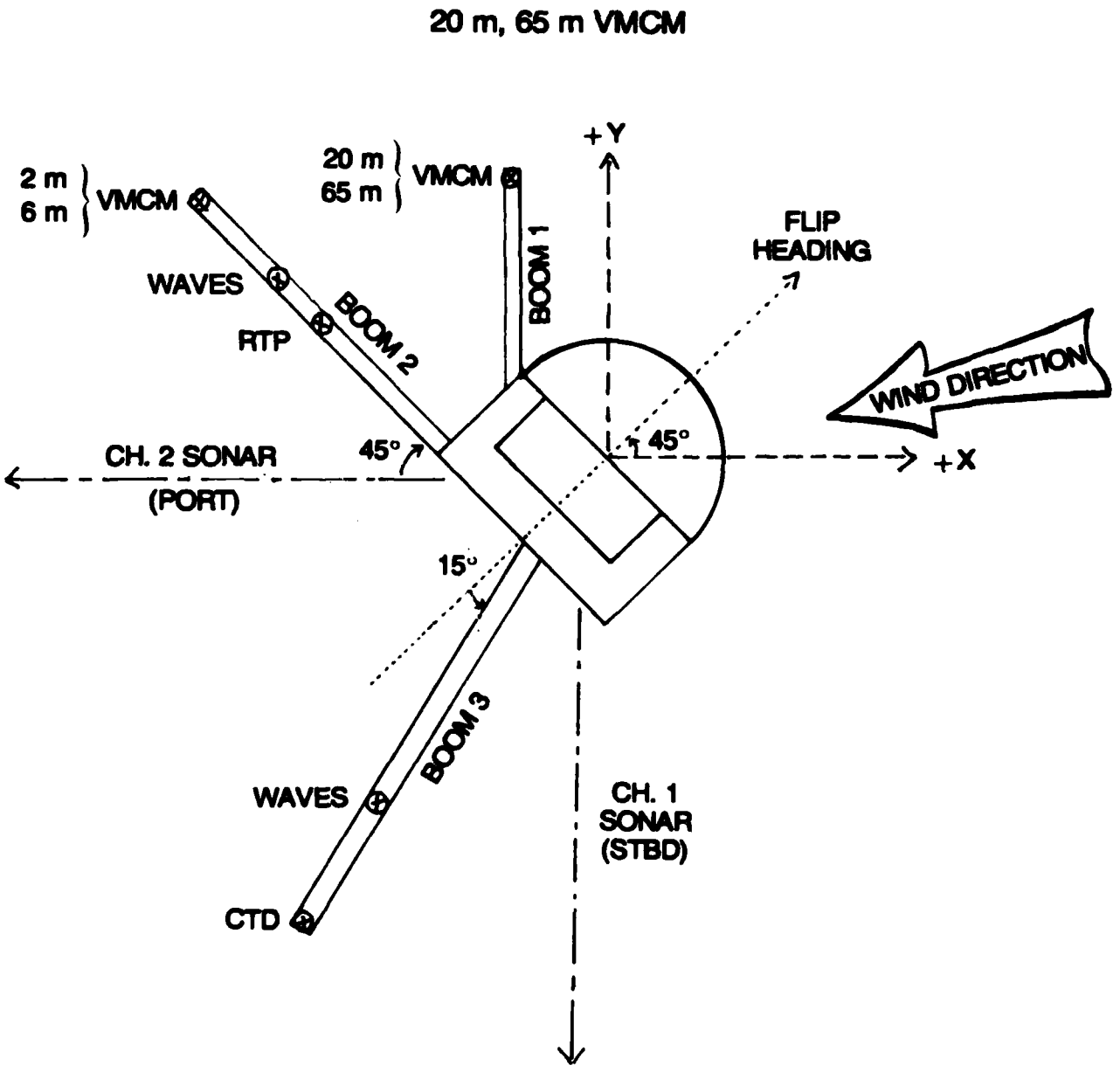

Fig. 8. Plan view of R/P FLIP, showing relative locations of the current meters and sonar beams, and the orientation with respect to the wind during the Langmuir circulation segment.

Thus, the net fluid velocity under the windrows is directed downward about 45° at mid-depth in the mixed layer, relative to the mean velocity of the layer as a whole.

Sonar derived velocities can be compared to point measurements from a Vector Measuring Current Meter (VMCM) which was fixed at 20-m depth during the time discussed here. A vector velocity was formed from the sonar data by averaging over ranges from 100 m to 450 m along each beam, corresponding to sub-surface velocity estimates in both directions. The resulting centers of averaging for the two sonar derived components are separated by about 390 m. In spite of this, the comparison with the 20 m VMCM data is quite favorable (Fig. 9): both the magnitude and direction agree closely. As expected, the point measurements have greater fluctuations about the mean. In both data sets, the fluctuations tend to be asymmetric, with somewhat larger 'squirts' in the downwind direction.

The dominant feature seen in the velocity data is the relative movement of FLIP through the near-surface layer. This is due to the balance of windage on FLIP's superstructure and drag on FLIP's hull, which extends to 90 m below the surface. The downwind velocity of FLIP ranges up to almost 30 cm/s, tracking closely the increasing windspeed over the same time period. The cross-wind velocity changes sign, with the water moving to the left initially (as seen facing downwind from FLIP) and later moving to the right.

To reduce the effects of FLIP's trajectory through the mixed layer and of slow variations in tilt, windspeed, wave height, etc., the data were high-passed filtered. A six-hour running mean was removed, at each range, from both the velocity and intensity data. Backscattered acoustic intensity is discussed in terms of db ($10 \log_{10} I$) relative to this time mean at each range. Removing the time-mean intensity reduces greatly the effects of beam spreading and attenuation. Tilting combined with mean vertical shear can introduce large-scale velocity 'noise' along each beam; thus, the spatial mean, trend, and wavelengths 480 m and longer (up to 3 cycles in 128 times 11.25 m) were also removed at each time-step. The resulting data are shown in Figure 10. FLIP's position is along the bottom edge of each square. The data segment is eight hours long, resolved in 3-min intervals. Black represents larger than average values, white less than average. The full height of each contour plot represents 1400 m in range, with 11.25 m by 3 min pixels. Again, the port sonar data (Figs. 10a,b) corresponds to averages over roughly 25 to 45 m depth by about 20 m across beam (at 500 m range), by 22.5 m in range. This will also be referred to as the "downwind" or "x" beam. The starboard sonar beam (Figs. 10c,d) reflects off the sea surface at ranges greater than 600 m. It corresponds to an average over a surface area of 22.5 m by approximately 20 m at 600 m, increasing to 40 m width at 1200 m. The vertical scale depth of the near-surface scattering layer is about a half meter. This "surface scattering beam" will also be referred to as the "crosswind" beam.

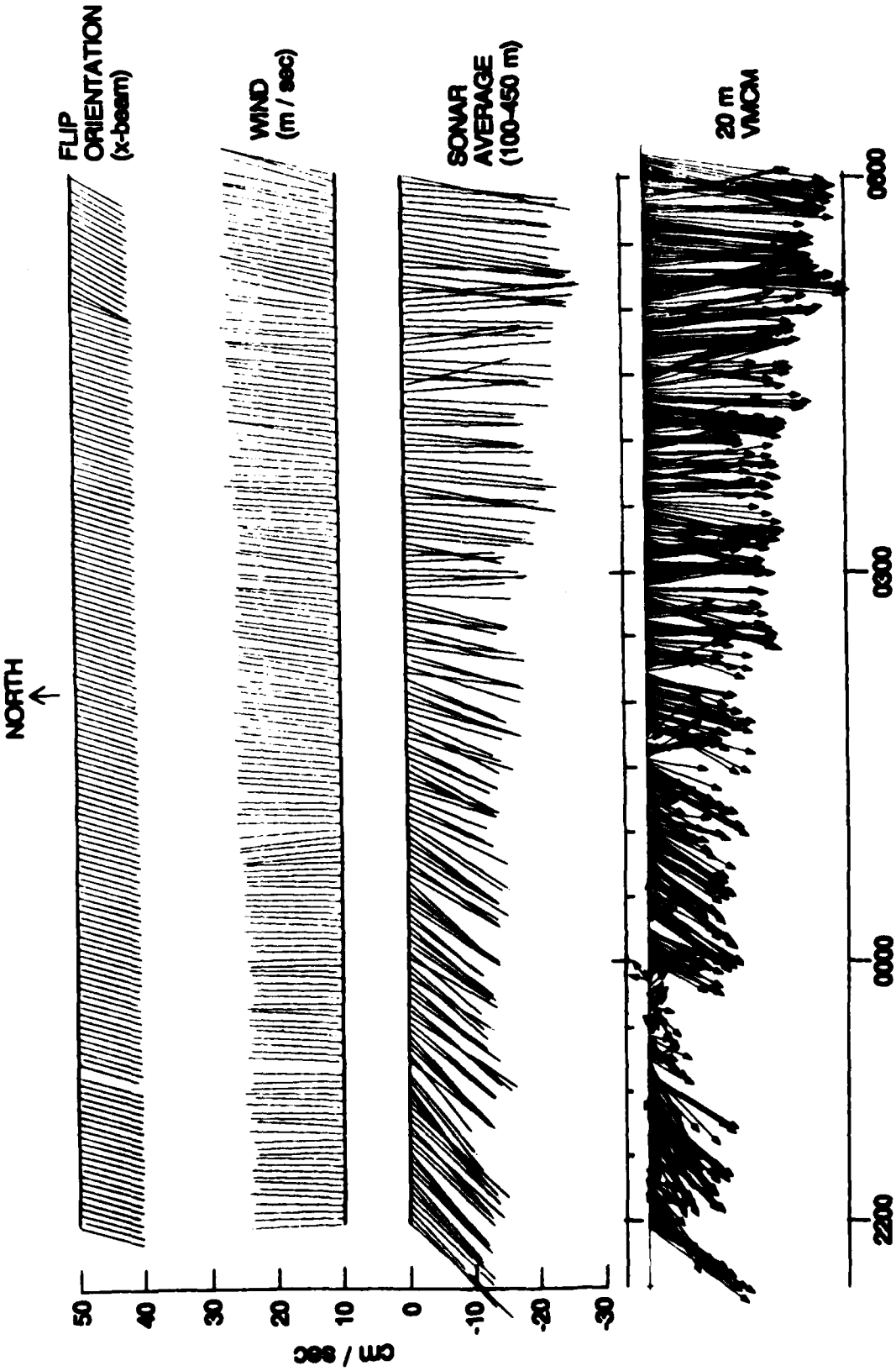

Fig. 9. The VMCM record from 20 m depth (bottom; in cm/s), the 'mean sonar velocity' obtained by averaging from 100 to 450 m along each beam (3rd row; cm/s), the wind (2nd; in m/s), and FLIP's orientation (top row; the length of these sticks are arbitrarily set to 10 units).

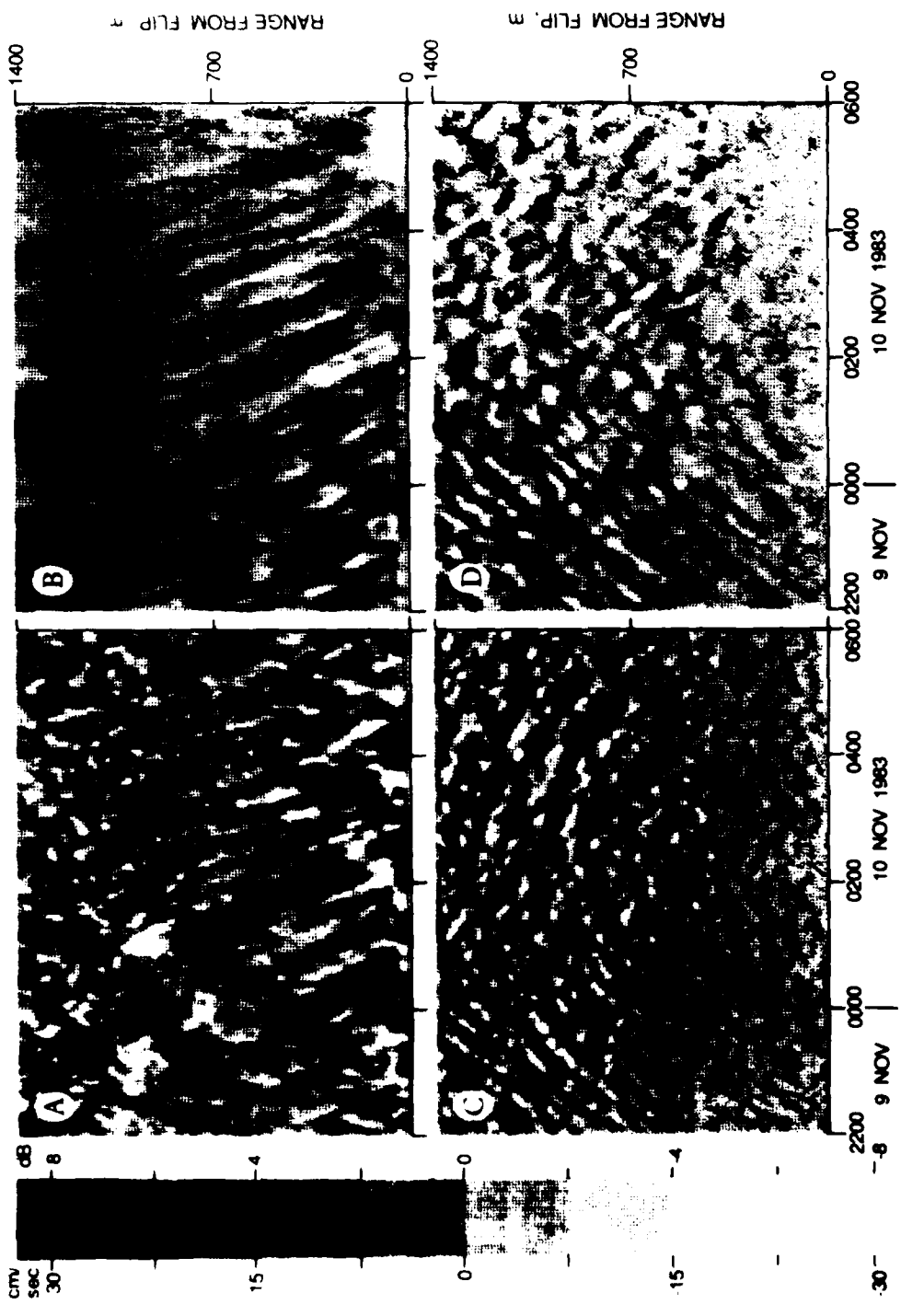

Fig. 10 (a) Shaded contours of high-pass filtered downwind velocity over the period of 2200 9 Nov. to 0600 10 Nov. Contour interval is 1.0 cm/s. (b) I_x, the high-pass filtered downwind intensity fluctuations. Contour interval is 0.5 db. The diagonal stripes represent regions of anomalous intensity (black = bright, white = dim), which appear to approach FLIP. Due to windage and shear across the thermocline, FLIP is moving downwind (toward these "lumps") at about 20 cm/s, in good accord with the angle made by these stripes. (c) dV_y/dy, the high-passed filtered crosswind convergence rate. Contour interval is 0.0009 s^{-1}. (d) I_y, the crosswind intensity variations. Contour interval is 0.25 db. The 6-beam returns from the surface about 600 m out to 1400 m from FLIP.

The movement of FLIP downwind through the water relative to nearly stationary features produces steep, straight "streaks" in the downwind-data and curved ones in the crosswind. The reversal in the crosswind advection of features is evident near 0200 of the 10th. Referring to the stick-plot comparison between the sonars and 20 m VMCM (Fig. 9), this 'reversal' actually represents a relatively small rotation of the total velocity (relative to FLIP) across the downwind direction.

The downwind beam reveals features in both velocity and intensity which appear to approach FLIP from the greatest detectable range (about 1 km) to the nearest (100 m) in roughly one and one half to two hours (Figs. 10a,b), corresponding to a mean downwind-velocity of about 20 cm/s relative to FLIP. Typical amplitudes of these fluctuations are about ± 5 cm/s for high pass filtered velocity intensity and ± 2.5 db in I_x. In this period, just prior to the peak winds observed during MILDEX, the bulk flow relative to FLIP increased from 16 to 23 cm/s, so the speed of the streaks visible in both intensity and velocity are consistent with advection by this bulk flow. Also, very faint and broad scale modulations appear in the x-velocity data at about 35°, "propagating" downwind (away) faster than FLIP (Fig. 10a). One possible explanation is that the cross-wind velocity of about 5 cm/s could advect elongated stationary features sideways across the downwind beam; thus, long features ("streaks") oriented at various angles about the wind could have virtually any apparent "propagation" speed, yet be quasi-stationary in the water. Another (and quite likely) possibility is that internal gravity waves, propagating in the seasonal thermocline, are responsible for the streaks. The internal wave explanation can be rejected for the smaller, steep streaks on the grounds that these propagate too slowly relative to the mean flow. The converse is not true: long stationary features advected at an angle can have any apparent phase speed, and so cannot be rejected even for the broad, "propagating" features observed here.

In the crosswind direction, the surface divergence dV/dy is shown (Fig. 10c), rather than high-pass filtered velocity. The observed features in $\partial V/\partial y$ and I'_y (Fig. 10c,d) appear to reverse direction somewhere near 0200, again consistent with advection by the mean flow (Fig. 9). The typical amplitudes are ± 2.5 db in I_y, and ± 0.003 s^{-1} for the convergence rates. If the features were long enough in the downwind direction and lasted long enough, they could be observed for longer than the two hours it took to progress the entire length of the other beam. However, the features can be traced for only about two hours, as before. We conclude that the individual features are limited to either two hours duration or to the 1-km to 2-km length scale covered by FLIP in that time. The features may persist longer, or have longer extent alongwind, but not both. The crosswind length scale (half the distance between convergence zones) is in the range 50 to 80 m; thus, the features appear to be about 10 to 20 times longer in the downwind direction than in the crosswind.

These crosswind convergence data are interesting in that they reveal the evolution in time of the crosswind scales of the flow. To examine this, wavenumber spectra of surface convergence rates were formed using data from ranges 700 to 1400 m (surface return). The spectra are plotted at 2-h intervals over the two days surrounding the maximum winds, from 1800 8 Nov. to 1800 10 Nov. (Fig. 11). Each spectrum shown is an average of 40 realizations, each calculated from a 3-min average of the sonar data. A best-fit quadratic in range was removed from each 3-min sample prior to Fourier transformation. The eight-hour "close-up" segment is bounded by heavier lines.

A low-wavenumber "cutoff" in crosswind convergence appears on the evening of the 9th, as the activity at higher wavenumbers increases. The peak just above this cutoff progresses from about 100 m wavelengths near 2000 to about 150 m by 0400 of the 10th, intensifying as the scale grows. During this time, cards thrown on the surface aligned into rows with a much smaller spacing, due to activity at higher wave-numbers. In the presence of multiple scales, visual observation of cards on the surface leads to a bias toward the smaller scale windrows, due to the relatively short observation times and distances. In contrast, the sonars are able to detect a maximum spacing scale under these circumstances. Thus, correspondence of this maximum scale to other environmental factors (e.g., mixed layer depth) can be explored more reliably with the sonar data than previously possible. Over the same time period, the mixed layer depth increased from roughly 40 to 60 m depth (Fig. 12). The maximum spacing between convergences remained close to three times the mixed layer depth over the whole period. In subsequent days, the mixed layer thickness oscillated with about a 12-h period, a consequence of the baroclinic tide. We conjecture that the largest scale circulations 'tracked' the mixed layer depth as long as the wind was strong, adjusting relatively quickly to a maximum streak spacing of nearly three times the layer thickness.

SUMMARY

During a period of fairly gentle 12-s swell, a surface-grazing Doppler sonar was used to observe surface wave propagation along a nearly 1-km path. The sonar sampled the motions every 2 s, with 22.5 m range resolution. Propagating surface waves were seen in the Doppler velocity estimates, and also, to a lesser extent, in the backscattering intensity. A weak maxima in scattering intensity appeared to occur on the forward faces of the waves.

Three-dimensional wavenumber-frequency spectra were estimated using the Doppler output. The trial spectra resolve the wave motions to periods as short as 7 s, 70 m wavelength. The influence of linear dispersion is clearly seen. Considerable improvement can result by using two (or more) surface-scattering sonar beams, rather than one surface and one sub-surface

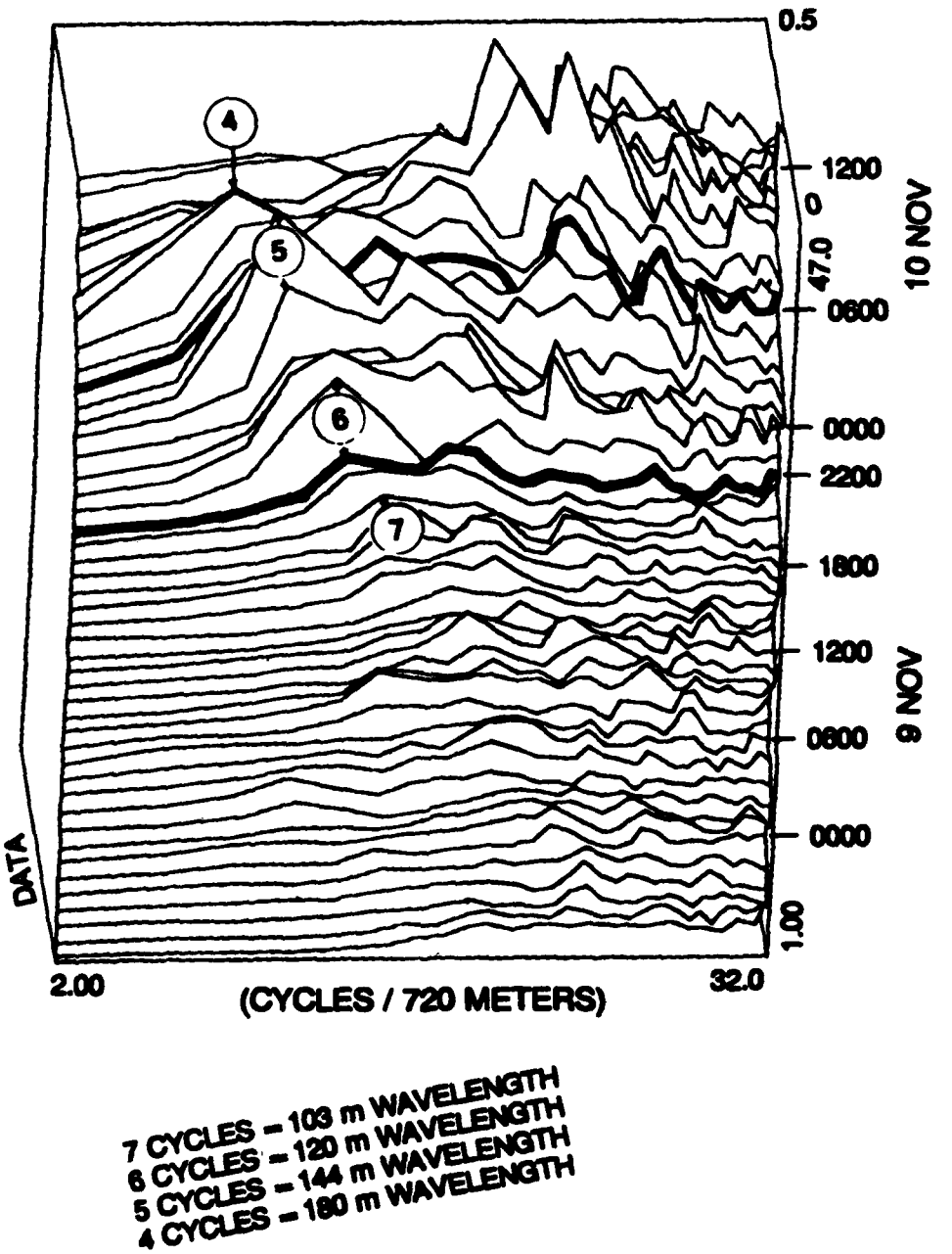

Fig. 11. 2-h mean power spectra of crosswind surface convergence, dV/dy, at 1-h intervals from 1800 8 Nov. to 1800 10 Nov. Note the appearance of a peak between 1800 (7) and 2200 (6) of the 9th, progressing to lower wavenumbers with time. Peak wavelengths designated are (7 cycles) = 103 m, (6) = 120 m, (5) = 144 m, and (4) 180 m.

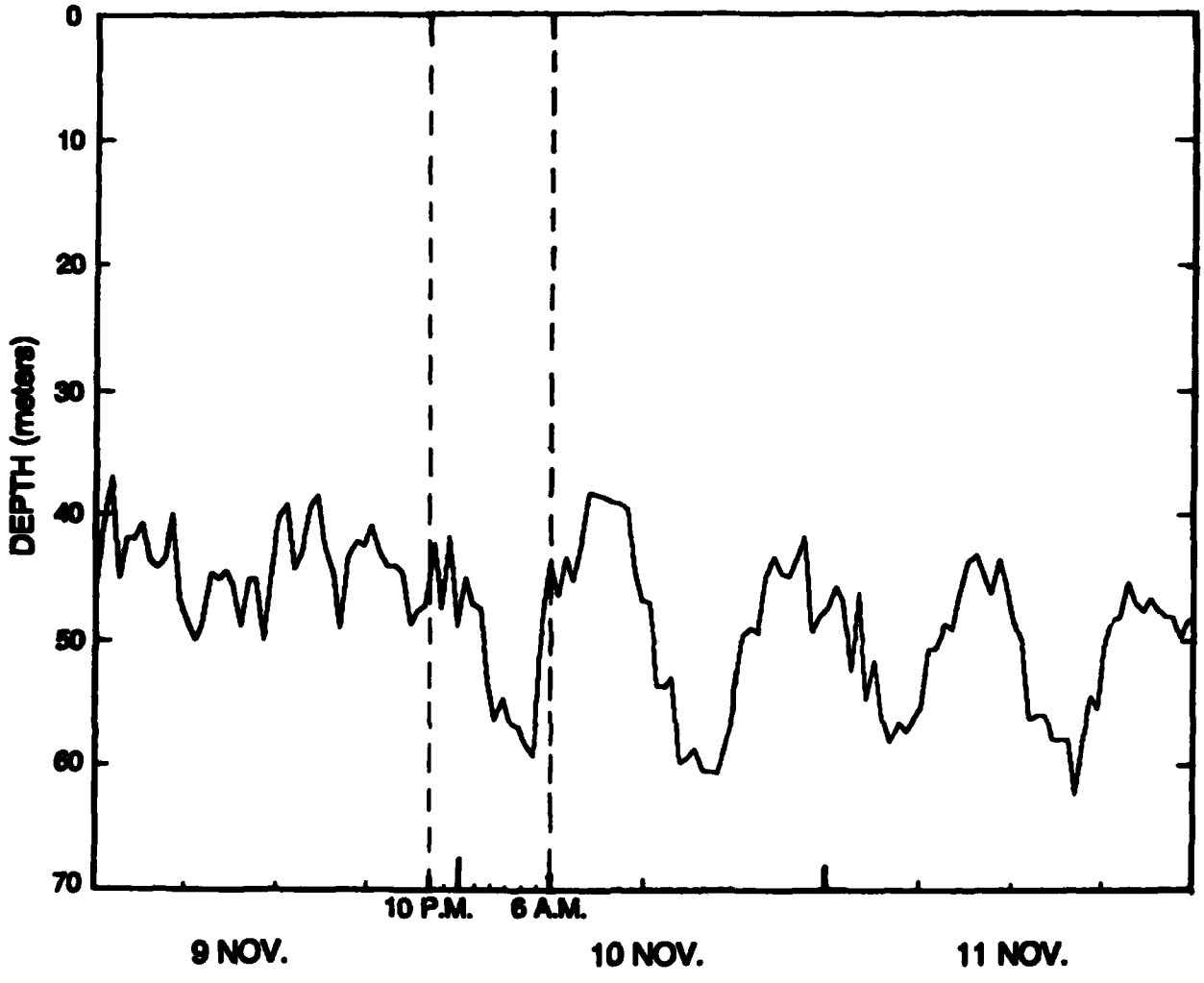

Fig. 12. The mixed layer depth showing the near-tidal frequency oscillations occurring during and after the eight-hour segment chosen for close examination of Langmuir Cell activity.

beam, as here. Also, more sophisticated analysis techniques should produce greatly enhanced estimates. Our intent here is simply to point out the existence and potential of a surface-scanning acoustic Doppler technique for measurement of directional spectra and breaking events.

During a separate period of moderate to high winds, the sonars detected lower frequency organized motions, which appear to be Langmuir cells. As surface convergence zones in this eight-hour 'close-up' period passed through the sonar beams, individual features (streaks) were observed. These features, identified through both velocity and intensity fluctuations, were roughly static with respect to the mean velocity of the layer, and persisted for up to two hours. In this time, FLIP drifted downwind about 2 km relative to the water, implying that these features stretched over 2 km parallel to the wind. The half-wavelength across the wind was about 60 to 90 m. The features were thus about 20 times as long as wide. The maximum crosswind spacing between convergences stayed close to three times the mixed layer depth, while that depth varied from about 40 to 60 m.

An ideal sonar for this type of work would transmit a fan-shaped beam broad in the vertical plane, narrow in azimuth. With fan shaped beams, pitch and roll of the transducer affect the output very little. Only yaw, variation in azimuth, needs to be suppressed. Thus, surface current measurements from sub-surface moorings or from slowly moving ships is a possibility. The intensity variations can also be used to observe breaking events and the subsequent decay of the resulting bubble cloud (Thorpe, 1986; Vagle and Farmer, 1986), providing a useful supplement to the current field and surface-wave directional information.

The prospect of being able to measure surface wave propagation continuously over distances greater than a kilometer, to get a measure of breaking activity (bubble formation), and to sense the surface currents which interact with the wavefield and with the mixed layer all with a single instrument encourages further study and development.

ACKNOWLEDGMENTS

This work was supported under ONR code 1122 PO contract N00014-79-C-0472. We would like to thank Lloyd Green, Steve Beck, Eric Slater, Mike Goldin, and the crew of FLIP for assistance in collection of the data. R. Weller of Woods Hole Oceanographic Institution provided the data in Figure 9, as well as several useful discussions.

REFERENCES

Johnson, B. D. and R. C. Cooke, 1979: Bubble Populations and Spectra in Coastal Waters. J. Geophys. Res., 84, 3761-3766.

Langmuir I., 1938: Surface motion of water induced by wind. Science, 87, 119.

Long R.B. and K. Hasselmann , 1979: A Variational Technique for Extracting Directional Spectra from Multi-Component Wave Data. J. Phys. Oceangr., 9, No. 2, 373-381.

Lygre A. and H.E. Krogstad, 1986: Maximum Entropy Estimation of the Directional Distribution in Ocean Wave Spectra. J. Phys. Oceangr., 16, No. 12, 2052-2060.

McDaniel S. T. and A. D. Gorman, 1982: Acoustic and Radar sea surface backscatter. J. Geophys. Res, 87, 4127-4136.

Pinkel, R., 1981: On the use of Doppler sonar for internal wave measurements. Deep Sea Res., 28A, 269-289.

Rummler, W. D., 1968: Introduction of a new estimator for velocity spectral parameters. Bell Telephone Labs, Murray Hill, NJ, MM-68-4141-5.

Smith J. A. , R. Pinkel, and R. A. Weller, Velocity Structure in the Mixed Layer during MILDEX. Journal Physical Oceanography. to appear .

Theriault K. B., 1986: Incoherent multibeam Doppler current profiler performance: Part I-Estimated Variance. IEEE Journal Oceanic Eng., OE-11, 7-15.

Thorpe S. A. , 1986: Bubble Clouds: A review of their detection by sonar, of related models, and of how K_v may be determined,. Oceanic Whitecaps and Their Role in Air-Sea Exchange, 294 pp..

Vagle S. and D. Farmer, 1986: Sea surface studies using underwater sound FASINEX. preliminary results, EOS, 67, 1034.

Weller R.A., J.P. Dean, J. Marra, J. Price, E.A. Francis, and D.C. Boardman, 1985: Three-Dimensional flow in the upper ocean. Science, 227, 1552-1556.

UNSTEADY SHALLOWING MIXED LAYER

Roland W. Garwood, Jr.

Department of Oceanography
Naval Postgraduate School
Monterey, California 93943

ABSTRACT

An analytical analysis of the mechanical energy budget for an unsteady shallowing oceanic surface mixed layer with a downward surface buoyancy flux B_o and a water surface friction velocity u_* provides insight into the relative roles of vertical mixing by turbulence generated within the Obukhov depth zone, $L = 2u_*^3/B_o$, and by turbulence generated by a mean flow dynamic instability below L.

An increase in the downward surface buoyancy flux decreases the Obukhov length and causes an initially well-mixed turbulent boundary layer to be separated into a surface layer, which decreases in thickness to L, and a region below L which is isolated. The turbulence in the new surface layer achieves an equilibrium state on an adjustment time scale L/u_*, and the turbulence in the isolated region is dissipated. The thickness δ of the interface between these two mixed layers grows due to a mean flow dynamic instability, achieving its maximum value of about $0.18\ u_*/f$ after about 0.37 of an inertial period.

INTRODUCTION

The purpose here is to examine the unsteady ocean surface mixed layer which shallows in response to a change in atmospheric forcing. This situation may arise if either the downward surface buoyancy flux, B_o, is increased or if the surface wind stress, u_*^2, is decreased, causing the Obukhov length scale,

$$L = 2\ u_*^3/B_o \qquad (1)$$

to be reduced to a value less than the previously established depth of turbulent mixing, z_i.

Many applications of the vertically integrated turbulent kinetic energy (TKE) budget (see reviews by Zilitinkevich et al., 1979; Garwood, 1979; and Price et al., 1987) have shown the length scale attributed to Obukhov (1946, 1971) to be the steady state solution for a shallowing, buoyancy-flux dominated ocean surface mixed layer. Recently, Price et al. (1986) have focused interest on the development of transient thermoclines due to the diurnal increase in the downward buoyancy flux. From such observations as these it has become evident that it is insufficient to consider entrainment alone in developing and verifying mixed layer models. In fact, some of the theoretical differences between alternative mixed layer parameterizations may be better examined and understood by simulation of the shallowing mixed layer than by simulation of the mixed layer which is being deepened by strong entrainment. Although much attention has been paid to the unsteady response of a deepening mixed layer, little attention has been given to the dynamics and thermodynamics of the shallowing surface mixed layers in the ocean.

DeSzoeke and Rhines (1976) first demonstrated the asymptotic regimes of an unsteady TKE budget for a mixed layer during the initial deepening into a linearly stratified pycnocline, $\partial b/\partial z = N^2$, where N is the buoyancy frequency and b is the mean buoyancy. They found that unsteadiness in the TKE was significant in determining mixed layer depth only during the first stage of deepening, or for $t \leq 1/N$. However, DeSzoeke and Rhines considered only the wind-driven case, and they did not include a surface buoyancy flux. Therefore a principal difference here is the inclusion of a downward surface buoyancy flux, resulting in the restratification of a previously well mixed layer. Following DeSzoeke and Rhines, however, this study shall include the unsteadiness in the TKE (first suggested by Zilitinkevich, 1975, in an application to the atmospheric turbulent boundary layer) in order to reveal the time scale for the TKE budget to approach equilibrium and for the surface mixed layer depth to achieve an approximate steady state, $h \sim L$.

The Obukhov scale L is not the only possible length scale for turbulent boundary layers in equilibrium. In the case of the neutral atmospheric planetary boundary layer (zero surface buoyancy flux), the limiting depth of the turbulence has traditionally (Rossby and Montgomery, 1935) and in observational studies (Clarke, 1970) and in model applications of the atmosphere (Deardorff, 1972; Wyngaard et al., 1974) been assumed to be proportional to the neutral planetary boundary layer scale,

$$L_o = u_*/f. \qquad (2)$$

For the oceanic planetary boundary layer (OPBL), and in particular for

the stable ($B_o > 0$) OPBL, the relative importance of L_o and L has not been clear. The effort here may help resolve this question.

The method will be to examine the energetics of the turbulence, via the TKE equations and of the mean flow with regard to the possibility of dynamic instability below the surface-controlled turbulent boundary layer. A sudden change in the surface forcing will result in the transient decay of turbulence in the surface layer. A new shallower turbulent boundary layer will be established as the turbulent kinetic energy budget approaches a new equilibrium. As the surface buoyancy flux and wind stress cause the mean buoyancy and momentum to increase in the new shallower layer, both the mean shear and the mean buoyancy gradient at the base of the new layer will be expected to increase. Apart from the surface-generated TKE, a mean flow instability may occur below the new layer, causing momentum and buoyancy to be mixed to a greater depth (below $z = -L$).

THE UNSTEADY TKE BUDGET

The turbulent kinetic energy equations for the three constituents, $\overline{u'^2}$, $\overline{v'^2}$ and $\overline{w'^2}$, are integrated vertically across a well-mixed and turbulent layer of depth h:

STORAGE	WIND-SHEAR PRODUCTION	PRESSURE REDISTRIBUTION	VISCOUS DISSIPATION	BUOYANT DAMPING	
$\langle \overline{u'^2} h/2 \rangle_t$	$= \cos^2(\theta) m_3 u_*^3 +$	$m_2 E^{1/2}(E-3\langle \overline{u'^2} \rangle)$	$- M_1/3\, E^{3/2}$		(3)
$\langle \overline{v'^2} h/2 \rangle_t$	$= \sin^2(\theta) m_3 u_*^3 +$	$m_2 E^{1/2}(E-3\langle \overline{v'^2} \rangle)$	$- M_1/3\, E^{3/2}$		(4)
$\langle \overline{w'^2} h/2 \rangle_t$	$=$	$m_2 E^{1/2}(E-3\langle \overline{w'^2} \rangle)$	$- M_1/3\, E^{3/2}$	$-B_o h/2$	(5)

The functional parameterization of the pressure redistribution and dissipation terms above follow the methods of Garwood (1977). The brackets, $\langle\ \rangle$, denote averages over the vertical extent (h) of the surface mixed layer. The wind direction is θ, and $E = \langle \overline{u'^2} + \overline{v'^2} + \overline{w'^2} \rangle$ is the total TKE. In eq. (5) there is no entrainment buoyancy flux because it is required that there be no entrainment at the base of the mixed layer. Here the entrainment is not occurring because $\overline{w'^2}$ is assumed to vanish at

the base of the mixed layer, z = -h. In this special state of no entrainment, the ratio of net vertical TKE to total TKE is required to follow the similarity constraint,

$$r = 3 \langle \overline{w'^2} \rangle / E, \tag{6}$$

where r is expected to be a small dimensionless constant. For isotropic turbulence, r would have a value of unity, and in general r would vary with changes in the entrainment buoyancy flux. However, in the limiting case here of strong buoyant damping and vanishingly small $\overline{w'^2}$ at z = -h and no entrainment, it is expected that r will achieve a limiting value much less than unity. Although there is no direct experimental evidence for the size of r in the OPBL, a reasonable value for r may be determined from laboratory observations of stable grid-stirred turbulence. In any case, with r prescribed, eqs. (3-6) provide a closed system of equations for mixed layer depth, h, and the three constituent components of the vertically averaged TKE, $\langle u'^2 \rangle$, $\langle v'^2 \rangle$, $\langle w'^2 \rangle$. For the purposes here, an approximate and very direct solution for a shallowing h is achieved by assuming r ~ 0 and solving eq. (5) simultaneously with eq. (7), the total TKE equation:

$$\langle Eh/2 \rangle_t = \underbrace{m_3 u_*^3}_{\text{"G"}} - \underbrace{m_1 E^{3/2}}_{\text{"D"}} - B_o h/2 \tag{7}$$

Steady state solution

The steady state solutions for mixed layer depth and dissipation are given by

$$h_\infty = \left[\frac{m_2/m_1 - 1/3\ (1 - r)}{m_2/m_1 + 2/3\ (1 - r)} \right] \left[\frac{2\ m_3\ u_*^3}{B_o} \right] \tag{8}$$

$$D_\infty = m_1 E^{3/2} = 6 m_3 u_*^3 / (7 - 3r) \tag{9}$$

where D is the vertical integral of TKE dissipation over the mixed layer. The values r = 0, m_2/m_1 = 0.5, and m_3 = 7 as taken as representative values for the model constants, m_i. These values are based upon laboratory observations and model vertification (Garwood, Gallacher and Müller, 1985 a, b; Martin, 1985; Gallacher, 1987; Gaspar, 1987). Then eqs. (8) and (9) give

$$h = 2u_*^3/B_o = L, \text{ and}$$

$$D = (6/7)\, G$$

where $G = m_3 u_*^3$ is the total wind-shear production. Hence, for the steady balance, 6/7 of the wind stress-generated turbulence (G) is dissipated, and only 1/7 of this energy is used to increase the system potential energy via the buoyancy flux.

Unsteady adjustment of shallowing mixed layer

The total TKE, the mixed layer depth, and time are both nondimensionalized on the boundary condition parameters, the downward surface buoyancy flux, B_o, and the water surface friction velocity, u_*:

$$E^* = (D/D_\infty)^{2/3} = 0.3028E/u_*^2 \qquad (10)$$

$$h^* = h/L = B_o h/(2u_*^3) \qquad (11)$$

$$t^* = B_o t/u_*^2 \qquad (12)$$

The dimensionless coefficients are included in eqs. (10-11) so as to normalize both the TKE and the mixed layer depth on their respective steady state values. Thus eq. (7) for the total TKE budget becomes

$$(6)^{2/3} \langle E^* h/2 \rangle_{t^*} = 7 - 6(E^*)^{3/2} - h^* \qquad (7a)$$

and the vertical TKE budget, eq. (5), reduces to

$$0 = (E^*)^{3/2} - h^* \qquad (5a)$$

Figure 1 shows the solutions for E^* (t^*) and h^* (t^*), assuming that the mixed layer was much deeper than L at the time the downward buoyancy flux was initiated (and the wind stress was held steady). Notice that the depth of mixing is immediately reduced to 7L/6, regardless of how deep z_i was prior to the inception of the buoyancy flux (as long as $z_i < -7L/6$. The remnant mixed region which is below the shallowing surface layer and above z_i, $-h > z > z_i$, will initially still be turbulent. However, this

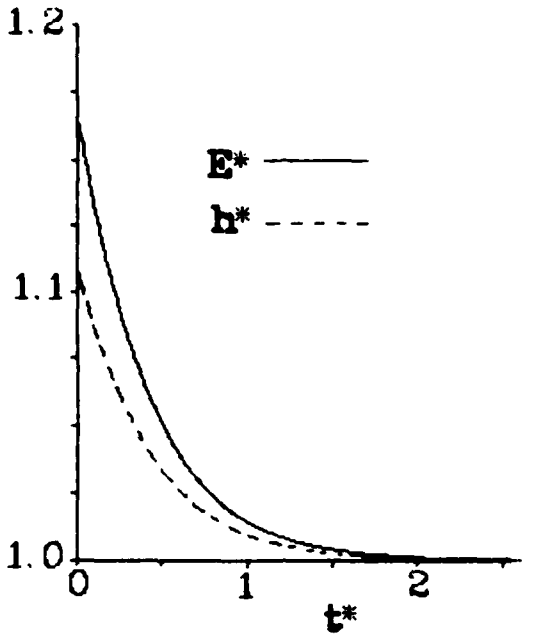

Fig. 1. Unsteady response of the dimensionless TKE, $E^* = E/u_*^2$, and the dimensionless mixed layer depth, $h = h/L$, versus the dimensionless time, $t^* = B_o t/u_*^2$, for a wind-forced (friction velocity = u_*) turbulent boundary layer which has a downward buoyancy flux (B_o) imposed at time $t = 0$.

region will now be isolated from surface fluxes, and the turbulence will necessarily decay by viscous dissipation unless there is an alternate source of turbulence (other than the wind stress). The schematic diagram in Figure 2 depicts the new surface layer which remains fully turbulent and the underlying remnant of the mixed layer with decaying turbulence.

The dimensionless solutions in Figure 1 show the time scale for adjustment by the new surface layer to a new equilibrium to correspond to $t^* = 1$, or $t = u_*^2/B_o$. For example, with a net downward heat flux of 400 W/m^2 and a wind speed of 8 m/s, the decay time period is about 1000 s for h to decrease to a new value of L = 20 m and for the total TKE to be about $E = 0.0003\ m^2 s^{-2}$. If the prior depth of mixing had been $z_i = -100$ m, for example, the remnant region between z = -20 m and z = -100 m would contain decaying turbulence. Because this region is isolated from the surface buoyancy flux, the decay time of the turbulence is not expected to be dependent upon the surface boundary conditions, and therefore will differ from the adjustment time for the surface mixed layer turbulence. Scale analysis of the TKE budget for this region suggests a decay time on the order of $(|z_i| - L)/u_*$, which could easily be much longer than the adjustment time scale for the turbulence in the surface layer.

Interfacial dynamic instability

In the hypothetical case here of a sudden step increase in the downward buoyancy flux, a turbulent boundary layer which is initially well mixed is separated into two distinctly different mixing layers. Typically, for a diurnally shallowing oceanic mixed layer, the turbulence in the lower remnant layer might be expected to decay on time scales of 10^3-10^4 s, provided there were no other sources of energy such as local breaking internal waves or turbulent transport from another shear production source region. Hence, because the buoyancy flux ceases throughout its vertical extent, this remnant layer is expected to continue to be well mixed until the time when another source of turbulence can penetrate the region.

An anticipated principal source of energy is that produced by a local dynamic instability. Both momentum and buoyancy will be relatively well mixed down to $z = -L$ as they are fluxed into the surface layer. However, at the lower interface between the two mixing layers, a dynamic instability of thickness,

$$\delta = (\Delta U^2 + \Delta V^2)\ (4\ \Delta\ b)^{-1} \tag{13}$$

is predicted (Garwood, 1977) to develop from the requirement that

$$Ri_\delta = \Delta b/\ (\Delta U^2 + \Delta V^2) = Ri_{cr} \sim 1/4$$

in the interfacial region between the surface mixed layer and an underlying dynamically stable and nonturbulent region, where Ri_δ is the gradient Richardson number and Δb, ΔU and ΔV are the buoyancy and mean velocity changes across the interface. See Figure 2.

Although the intensity of the turbulence and dissipation may be relatively large in the interfacial region, it will not be well mixed. Rather, the shear and mean buoyancy gradient will be governed by eq. (13), together with equations for the mean kinetic energy and the mean buoyancy:

$$\Delta U^2 + \Delta V^2 = 2u_*^4 f^{-2}\ (1 - \cos ft)\ (L + \delta/2)^{-2} \tag{14}$$

$$\Delta b = B_o\ t(L + \delta/2)^{-1}. \tag{15}$$

For the case of a constant wind stress and constant buoyancy flux, an analytical expression for $\delta(t)$ may be derived from the mean kinetic energy and mean buoyancy budgets, giving

$$\delta + \delta^2/(2L) = 0.25\ u_* f^{-1}\ (1 - \cos ft)\ (ft)^{-1}. \tag{16}$$

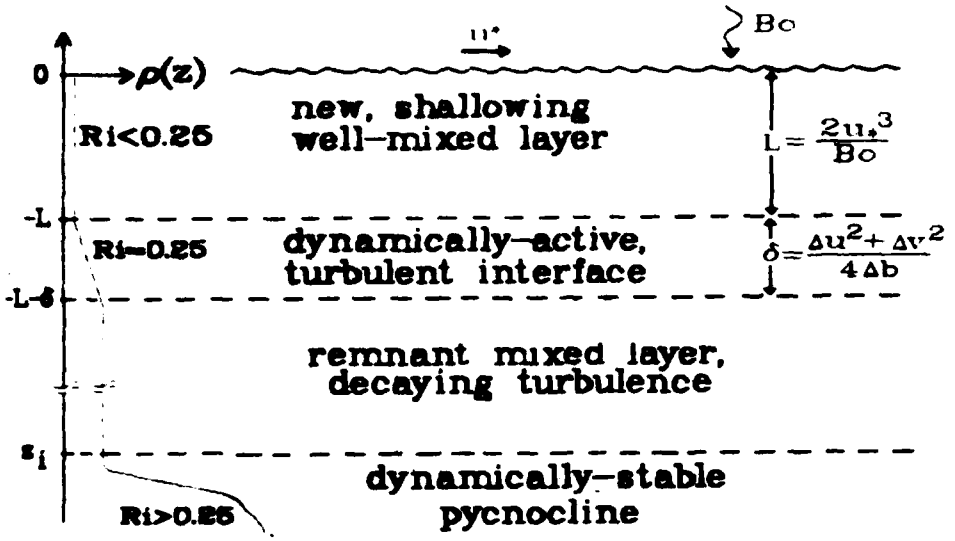

Fig. 2. Schematic diagram of the vertical domains of the ocean surface turbulent boundary layer as it responds to a downward buoyancy flux imposed on the surface. The density profile will evolve into two well- mixed regions separated by a stratified but dynamically active interface region of thickness δ. The surface layer turbulence will tend to maintain a well-mixed profile of thickness L after decaying from an initial depth of 7L/6.

Figure 3 shows the time dependence of $\delta(t)$ upon the dimensionless parameter,

$$B^* = u_*/(fL) = B_o/(2fu_*^2). \tag{17}$$

The parameter B^* is a measure of the relative importance of the neutral planetary boundary layer scale to the Obukhov scale, L_o/L.

For the small time, $ft \ll 1$, eq. (16) reduces to a linear dependence in time,

$$\delta \sim u_* t/4,$$

but the Coriolis effect limits this initial tendency. Although the maximum mean kinetic energy occurs at $ft = \pi$, deepest penetration of the dynamic instability occurs at $ft = 2.33$, or about 0.37 of an inertial period. For large L (small B^*), the limiting size of δ is

$$\delta_{max} = 0.18\, u_*/f \tag{18}$$

which is independent of B_o. For increasingly large B_o, the thickness δ

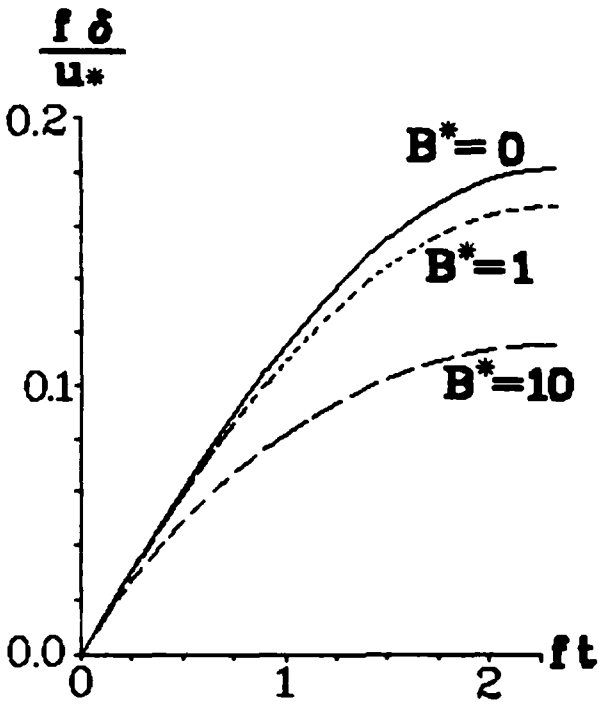

Fig. 3. Time-dependent growth of the interface thickness, δ, for three different cases of the buoyancy-to-rotation parameter, $B^* = u_*/(fL)$. Values of B^* less than unity correspond to transient thermocline formation for temperate oceanic regions. Values of B^* greater than 10 may occur regularly in tropical oceans.

becomes more dependent upon L. However, for $B^* \leq 10$ as for the summertime mixed layer in temperate oceans, δ_{max} depends mostly upon the Rossby and Montgomery neutral planetary boundary layer scale, $L_o = u_*/f$.

A fundamentally different scaling of the below-L interface will occur at low latitudes. With f vanishingly small, and $B^* \gg 1$, the mean kinetic energy budget given by eq. (14) becomes incorrect. Without the Coriolis limitation on the surface layer buildup of wind-driven mean kinetic energy, lateral friction and advection must have increasingly greater importance in the momentum budget. Also, the TKE itself may be influenced by planetary rotation in tropical regimes (Garwood, Müller and Gallacher, 1985). Nevertheless, as f is made smaller, δ will tend to increase proportionately, by eq. (18). Hence tropical and equatorial turbulent boundary layers might be expected to have relatively thick δ-regions created by intermittent dynamic instability and possibly strong turbulence below relatively shallow well-mixed layers of thickness L.

SUMMARY

A mechanical energy budget analysis of the unsteady shallowing oceanic surface mixed layer provides insight into the relative roles of vertical mixing by turbulence generated within the Obukhov depth zone, $0 < z < -L$, and by turbulence generated by mean flow dynamic instability below the Obukhov depth.

The special case of interest here is when the downward surface buoyancy flux (B_o) increases or the friction velocity (u_*) decreases sufficiently to cause the Obukhov depth, $L - u_*^3/B_o$, to decrease to a value less than the previously established turbulent boundary layer depth. Then equilibrium theory requires that there be no entrainment caused by the vertical transport of turbulence generated by wind-shear production. However, unsteadiness in the turbulent kinetic energy budget has an important effect upon the depth of the well-mixed part of the turbulent boundary layer for a period of time of approximately u_*^2/B_o. After this adjustment period the surface flux-controlled turbulent boundary layer depth approaches L asymptotically.

Mixing in the interfacial region below $z = -L$ must depend upon a source of energy other than turbulent transport. As both momentum and buoyancy which are fluxed through the surface are confined initially to the layer of depth L, with increasing time a local mean flow dynamic instability is expected at the base of the well-mixed layer. This instability causes mixing to penetrate below $z = -L$ to a maximum thickness of $\delta = 0.18u_*/f$. Hence the "interface" thickness, δ, is independent of the surface buoyancy flux and is a function of the history of the surface wind forcing and rotation. Thus both Obukhov scale and the neutral planetary boundary layer scale are shown to have important but different roles in the evolution of the shallowing transient oceanic turbulent boundary layer.

REFERENCES

Clarke, R. H., 1970: Observational studies in the atmospheric boundary layer. Quart. J. Roy. Meteor. Soc., 96, 91-114.

Deardorff, J. W., 1972: Numerical investigation of neutral and unstable planetary boundary layers. J. Atmos. Sci., 29, 91-115.

DeSzoeke, R. A. and R. B. Rhines, 1976: Asymptotic regimes in mixed layer deepening. J. Mar. Res., 34, 11-116.

Gallacher, P. C., 1987: Importance of rotation shear stress for entrainment in the ocean mixed layer. Ph.D. thesis, Naval Postgraduate School, 142 pp.

Garwood, R. W., Jr., 1977: An oceanic mixed layer model capable of simulating cyclic states. J. Phys. Oceanogr., 7, 455-468.

Garwood, R. W., Jr., 1979: Air-sea interaction and dynamics of the surface mixed layer. Rev. Geophys. Space Phys., 17, 1507-1524.

Garwood, R. W., Jr., P. C. Gallacher and P. Müller, 1985a: Wind direction and equilibrium mixed layer depth: General theory. J. Phys. Oceanogr., 15, 1325-1331.

Garwood, R. W., Jr., P. C. Gallacher and P. Müller, 1985b: Wind direction and equilibrium mixed layer depth in the Tropical Pacific Ocean. J. Phys. Oceanogr., 15, 1332-1331.

Gaspar, P., 1987: Modelling the seasonal cycle of the upper ocean. J. Phys. Oceanogr., in press.

Martin, P. J., 1985: Simulation of the mixed layer at OWS November and Papa with several models. J. Geophys. Res., 90, 903-916.

Obukhov, A. M., 1946: Turbulence in an atmosphere with a nonuniform temperature. Trudy Inst. Teoret. Geofiz. ANN SSSR, Vol. 1. Reprinted in Bound.-Layer Meteor., 2, 7-29, 1971.

Price, J. F., R. A. Weller and R. Pinkel, 1986: Diurnal cycling: observations and models of the upper ocean response to diurnal heating, cooling and wind mixing. J. Geophys. Res., 91, 8411-8427.

Price, J. F., E. A. Terray and R. A. Weller, 1987: Upper ocean dynamics. Rev. Geophys., in press.

Rossby, C. G. and R. B. Montgomery, 1935: The layer of frictional influence in wind and ocean currents. Pap. Phys. Oceanogr. Meteor., 3, 101 pp.

Wyngaard, J. C., O. R. Cote and K. S. Rao, 1974: Modeling the atmospheric boundary layer. In Advances in Geophysics, Ed. by F. N. Frenkiel and R. E. Munn, Vol. 18A, 193-211.

Zilitinkevich, S. S. 1975: Comments on 'A model for the dynamics of the inversion above a convective boundary.' J. Atmos. Sci., 32, 991-992.

Zilitinkevich, S. S., D. V. Chalikov and Y D. Resnyanskiy, 1979: Modelling the oceanic upper layer. Oceanol. Acta, 2, 219-240.

SOME EFFECTS OF HEATING ON THE WIND-DRIVEN VELOCITY IN THE UPPER OCEAN

James F. Price, Robert A. Weller, and Rebecca R. Schudlich

Woods Hole Oceanographic Institution
Woods Hole, MA, 02543

ABSTRACT

The relationship between the mean wind stress and the mean, wind-driven, upper ocean velocity is analyzed using measurements made by a surface mooring in the open Sargasso Sea. Mean values are estimated by ensemble averaging daily averages which have been rotated to a common wind direction. Velocity is referenced to 50 m depth to suppress tides and eddies. The resulting mean velocity is strongly surface trapped, e-folding over about 12 m, and rotates slightly to the right (cum sole) with increasing depth. This vertical structure of the mean velocity spiral is a result of diurnal cycling, and can be simulated well by a one-dimensional model driven with the estimated wind stress and diurnally varying surface heat flux. Volume transport is within about 10% of that expected from a steady Ekman balance, and is nearly 90° to the right of the wind.

INTRODUCTION

The direct, local effect of a steady wind stress, τ, upon a homogenous ocean was calculated by V. W. Ekman at the turn of the century. Ekman assumed that the horizontal momentum flux from the surface wind stress was transmitted through the water column by a Fickian diffusion process with constant effective viscosity, A, and was balanced by the Coriolis acceleration. The velocity profile which satisfies these dynamics has an elegant spiral shape, called the Ekman spiral (Pond and Pickard, 1983), whose depth integral is the Ekman transport,

$$M = \tau \times k/\rho f \quad ,$$

where k is the vertical unit vector, f is the Coriolis parameter, and ρ is the density of sea water. The magnitude and direction of M depend only upon there being a balance between wind stress and Coriolis acceleration, and not at all upon the effective viscosity or any other detail of the vertical mixing. As such, the Ekman transport is on much firmer theoretical ground than the Ekman spiral itself. However, the dynamics of the spiral, and specifically the parameter dependence of its trapping depth, determines where the Ekman transport occurs in the water column,

and thus determines which waters make up the Ekman transport. A sound observational and theoretical understanding of the mean velocity spiral and the accompanying transport is thus an integral part of the larger problem of the wind-driven ocean circulation. Here we give a progress report on our effort to understand these phenomena based upon an analysis of *in situ* velocity observations and numerical modelling.

Most previous attempts to make *in situ* observations of the mean wind-driven velocity and Ekman transport have been frustrated by a difficult signal-to-noise ratio with which we must also contend; the mean wind-driven velocity is small ($O(0.05\ m\ s^{-1})$) compared to the orbital motion of surface waves (which are about an order of magnitude larger in this case), and compared to the currents due to tides, inertial motions and nearly geostrophic eddies (which are about five times larger). To observe such a small mean velocity in the upper ocean requires both a current meter which rejects virtually all surface wave motion, and a record length sufficient to average out tides and eddies.

LOTUS FIELD OBSERVATIONS AND THEIR ANALYSIS

For this study we have a five month-long time series of upper ocean velocity and wind made from a surface mooring as part of the Long Term Upper Ocean Study (LOTUS) carried out in the western Sargasso Sea (Briscoe and Weller, 1984). Ocean velocity measurements were made by Vector Measuring Current Meters (VMCMs) which are able to reject nearly all surface gravity wave motions (Weller and Davis, 1980). VMCMs were set at depths of 5, 10, 15, 25, 50, 75, 100 m (and deeper) to give reasonably good resolution in the upper ocean. Meteorological measurements were made with calibrated, state of the art instruments, and surface fluxes were estimated from bulk transfer formulae (Deser et al., 1983; Large and Pond, 1981). We use the longest continuous record of velocity obtained during the LOTUS project, the LOTUS 3 record made from 14 May 1982 to 20 October 1982 (160 days). This period saw mainly summer conditions of strong daytime heating, and light winds (Stramma et al., 1986).

Recent field studies have shown that even the small stratification that occurs as part of the diurnal cycle (O(0.2 C)) (Price et al., 1986) can block the downward penetration of momentum flux from the surface. Thus, the effect of direct wind-driving may be confined to a comparatively thin surface layer during midday, but reaches deeper during the evening when cooling and wind-mixing erode away the diurnal stratification. This insight into the effects of diurnal heating (or stratification) leads to a fairly straightforward analysis method applied here in order to detect the mean velocity spiral and the Ekman transport.

First, given that the directly wind-driven velocity is going to be much more strongly surface-trapped than is the "noise" velocity due to tides and eddies, then it is appropriate and generally necessary to analyze a velocity vertical anomaly rather than the absolute velocity itself. We calculate a vertical anomaly by subtracting the velocity at a reference level, 50 m, from the upper ocean velocity (Davis et al., 1981a; Price et al., 1986). This reference depth was within the seasonal thermocline for all but the last few weeks of the LOTUS 3 record, and we see no evidence of any important direct wind-driving at that level or below. Moreover, the use of other plausible reference depths, 25 or 75 m, gives nearly the same result for the mean velocity spiral.

Further suppression of the non-wind-driven velocity is possible only by long-term averaging, and here we introduce a way to coherently average the data to enhance the signal-to-noise ratio. The aim is to account for the effects of varying wind direction. Wind stress and velocity data are first averaged over a day, and then an ensemble average is formed by rotating the daily averages of wind and velocity to a common wind direction ("up" in Figure 1). (The choice of a daily averaging interval for the record pieces is not crucial for the ensemble average, and essentially the same result comes from averaging over pieces of, say, two days, or over pieces of one or several inertial periods.) The coherently averaged wind stress has an amplitude of 0.068 Pa, while the simple time-mean average of wind stress during LOTUS 3 was 0.015 Pa, or about a fourth as large. Thus the coherent ensemble averaging applied here serves to enhance considerably the amplitude of the mean wind stress and Ekman transport detectable in this data set. The ensemble average is interpreted as if the wind had held a constant amplitude and direction over the observation period.

MEAN VELOCITY SPIRAL AND VOLUME TRANSPORT

The mean velocity at the four VMCM depths above 50 m is shown in Figure 1 (left), and uncertainties on the mean velocity at each depth are listed in Table I as standard errors. The integral time scale of the daily values was found to be surprisingly short, only 1.5 days, (most variability is contributed by tides and inertial motions rather than geostrophic eddies), and hence the number of effective degrees of freedom used to estimate standard error was taken to be $160/(2 \cdot 1.5) = 53$. Mean values at 15 m and above are thus fairly well defined, but the 25 m value is not distinguishable from zero.

The mean velocity spiral is strongly surface trapped in the LOTUS 3 data set. The 5 m velocity has an amplitude of about 0.04 m s^{-1}, and is well off to the right of the wind, about 78°. Velocity amplitude decays fairly rapidly with depth, e-folding over about a 12 m scale. The velocity vector rotates only about 20° over the e-

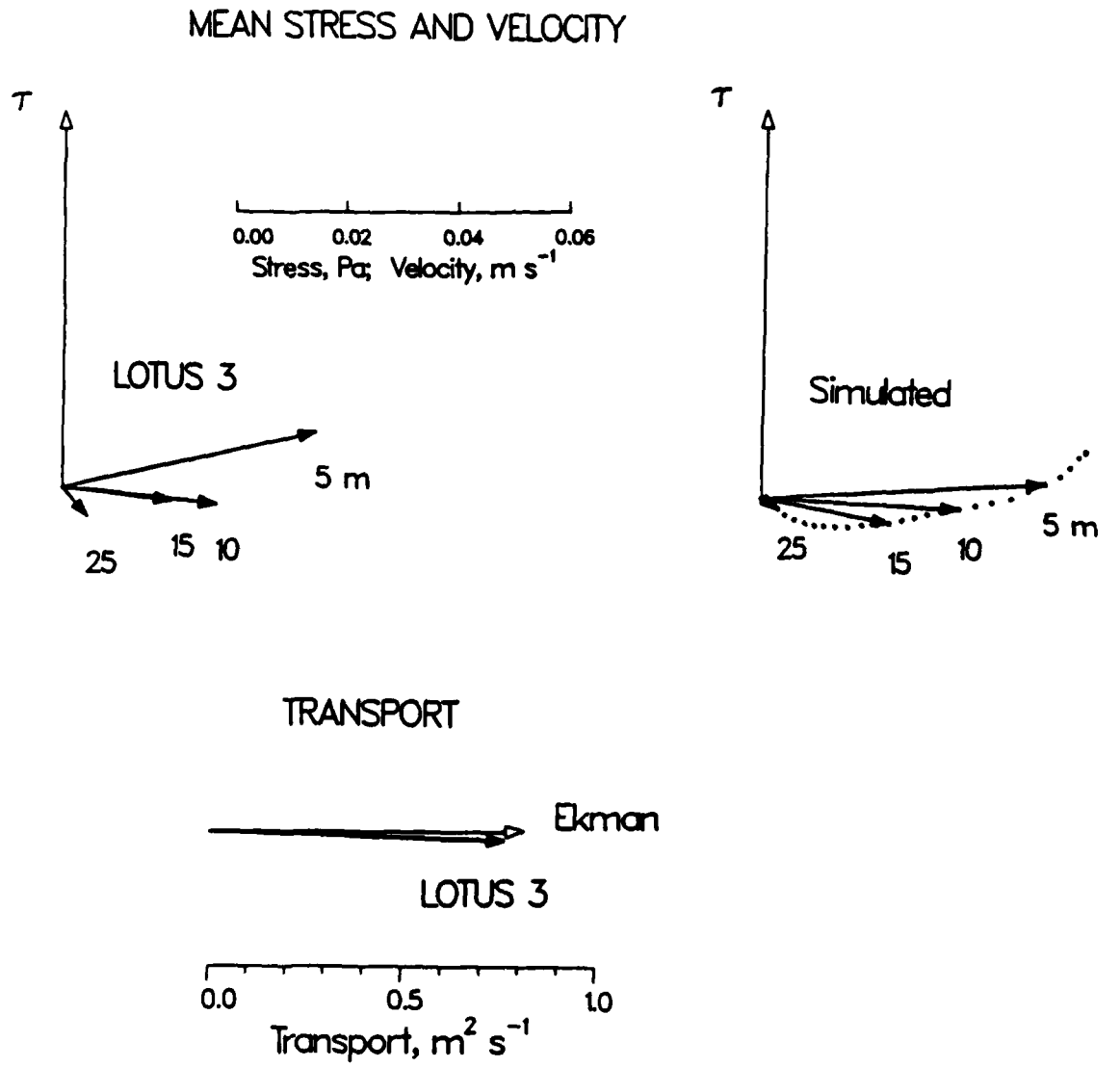

Figure 1. (Left) Mean velocity spiral from the LOTUS 3 data set. The mean has been estimated by an ensemble average over daily averages which have been rotated to a common wind direction (arbitrarily "up" in this figure). Uncertainties on the mean values are listed in Table I. (Lower) The observed transport is plotted (solid arrow head) along with the Ekman transport, (open arrow head). (Right) Mean velocity spiral simulated by the numerical model. The vectors correspond to the depths sampled by LOTUS 3, and the dots are at 1 m intervals.

TABLE I

STATISTICS ON MEAN VELOCITY AND TRANSPORT

Mean Velocity, m s^{-1}

Depth, m	Cross-Wind	Down-Wind
5	0.046 ± 0.012[a]	0.010 ± 0.007
10	0.028 ± 0.007	-0.003 ± 0.004
15	0.020 ± 0.007	-0.002 ± 0.005
25	0.004 ± 0.004	-0.005 ± 0.004
50[b]		
75	0.006 ± 0.003	-0.002 ± 0.004
100	0.011 ± 0.006	-0.007 ± 0.006

Transport, m^2 s^{-1}

	Cross-Wind	Down-Wind
Observed	0.76	-0.02
Ekman[c]	0.82	0

---

a. Uncertainty is standard error. 90% confidence limits are larger by a factor 1.7, and 95% confidence limits are larger by a factor 2.0.
b. The simple time – mean velocity at 50 m was 0.181 m s^{-1} westward, and 0.007 m s^{-1} northward.
c. Computed from a mean stress of 0.068 Pa.

folding depth so that the spiral found here has a rather flat (and not particularly elegant) shape when compared to the classical Ekman spiral. This has been noted before for other mean, wind-driven velocity spirals (Price et al., 1986, and Weller, 1981). (Elegant or not, the mean velocity does have an unmistakable spiral shape which makes analogy with diffusion models compelling. We do not pursue diffusion models in detail here, but simply note that an effective viscosity which decreases from a surface value of about 400 x 10^{-4} m^2 s^{-1} to zero at 30 m depth gives a spiral much like the one observed.)

Volume transport was calculated by a trapezoidal rule integration from 50 m to the surface and is plotted in Figure 1 (lower) along with the theoretical Ekman transport. Perhaps the most striking result is that the estimated volume transport closely approximates the theoretical Ekman transport in both magnitude and direction. We believe that this is the first reasonably sound, quantitative verification of the steady Ekman balance made from direct velocity observations in the upper ocean.

DIURNAL VARIABILITY OF VELOCITY SHEAR

There is an important and in some ways quite dramatic diurnal variability in the wind-driven velocity which is part of the diurnal cycle process of the upper ocean (Kondo et al., 1979; Price et al., 1986; Woods and Strass, 1986). The dynamics of this diurnal variability are central to understanding the surface trapping of the Ekman transport. Diurnal variability is, of course, lost in forming the ensemble average over the full data set, but can be seen by forming ensemble averages for the nighttime, 20 LST to 8 LST (Local Solar Time) and the daytime, 8 LST to 20 LST, Figure 2. This clearly shows that most of the shear in the upper ocean is supported by the stable stratification of the diurnal thermal cycle. Upper ocean shear is greatly reduced during the early morning when cooling by heat loss and wind-mixing have caused the mixed-layer to deepen well below its midday value.

SIMULATIONS

A consistent picture of the mean velocity spiral and the diurnal variability emerges from numerical simulations made with a simple one-dimensional numerical upper ocean model (Price et al., 1986). This model has a surface mixed-layer within which the effective viscosity is infinite and whose depth is controlled by a bulk Richardson number, a transition layer within which a gradient Richardson number controls mixing, and zero diffusion or mixing in the fluid below. The model was forced with the 160-day series of wind stress and surface heat flux from LOTUS 3. With this wind and buoyancy forcing, the depth of the mixed-layer goes through diurnal excursions from typically about 5 m near noon, to about 30 m before sunrise.

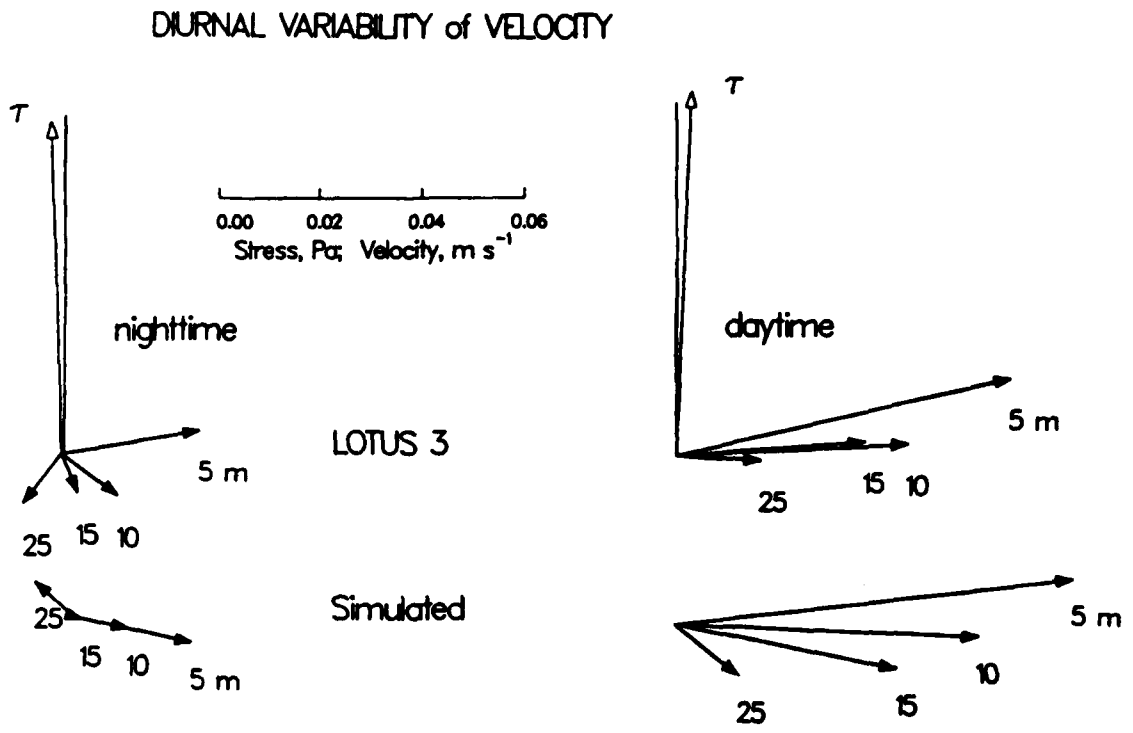

Figure 2. The ensemble average velocity during nighttime (left) and during the daytime. The wind stress for the corresponding time of day is plotted as a vector, with the mean value shown as a solid line. Note that there is very little diurnal variability of wind stress. This figure shows that there is much larger near-surface velocity and overall vertical shear during the day than at night.

Wind-driven velocity was analyzed exactly as it was from the LOTUS data, Figure 1. In the model solution there is, trivially, an exact Ekman balance (over any stable averaging period) since only wind stress and Coriolis forces act on the water column, and hence the transport balance is not plotted.

The important, nontrivial model results are the amplitude of the diurnal cycle, Figure 2, and the overall shape and trapping depth of the mean velocity spiral, Figure 1. The night-to-day variation of the velocity profile is fairly realistic, Figure 2, suggesting that the model responded to surface heating in a realistic way and the trapping depth of the simulated velocity profile is close to that actually observed, e-folding in about 15 m. We know of nothing that makes these results unique to this model, and expect that other upper ocean models (e.g., Mellor and Durbin, 1975; Kondo et al., 1979; Davis et al., 1981b) would perform as well as this one given the same wind stress and diurnally varying heat flux.

DISCUSSION

The principal result of this analysis is that the LOTUS 3 record was found to have a long-term mean upper ocean volume transport consistent with a steady Ekman balance, and that this transport was found to be fairly strongly surface trapped. The model results, together with the observed diurnal variability of the velocity and shear, show that this surface trapping is a consequence of surface heating and the diurnal cycling process. The upper ocean Ekman transport is thus found to be a much more dynamic phenomenon, and with a much richer parameter dependence than might have been supposed from the classical theory. It is heartening to see that modern observational tools like the LOTUS surface buoy and VMCM instruments can measure the upper ocean with enough fidelity and detail, and over sufficiently long periods, to at last provide a solid descriptive basis for developing new and better theories for the upper ocean.

ACKNOWLEDGMENTS

We are grateful to the Office of Naval Research for their support of the LOTUS project through contract N00014-76-C-0197, NR 083-400, and for support of J.F.P., R.A.W, and R.R.S. through contract N00014-84-C-0134, NR 083-400 with the Woods Hole Oceanographic Institution. We thank Ms. Nancy Pennington and Ms. Christina Light for their assistance with data processing and analysis.

REFERENCES

Briscoe, M. G., and R. A. Weller, 1984: Preliminary results from the Long Term Upper Ocean Study (LOTUS). *Dyn. Atmos. Oceans*, 8, 243-265.

Davis, R. E., R. DeSzoeke, D. Halpern, and P. Niiler, 1981a: Variability in the upper ocean during MILE. Part I: The heat and momentum balances. *Deep-Sea Res.*, 28, 1427-1451.

Davis, R. E., R. DeSzoeke, and P. Niiler, 1981b: Variability in the upper ocean during MILE. Part II: Modeling the mixed layer response. *Deep-Sea Res.*, 28, 1453-1475.

Deser, C., R. A. Weller, and M. G. Briscoe, 1983: Long Term Upper Ocean Study (LOTUS) at 34°N, 70°W: Meteorological sensors, data and heat fluxes for May-October 1982 (LOTUS 3 and LOTUS 4). *Woods Hole Oceanographic Inst. Tech. Rep.* WHOI-83-32, 68 pp.

Kondo, J. Y., Y. Sasano, and T. Ishii, 1979: On wind-driven current and temperature profiles with diurnal period in the oceanic planetary boundary layer. *J. Phys. Oceanogr.*, 9, 360-372.

Large, W. G., and S. Pond, 1981: Open ocean momentum flux measurements in moderate to strong winds. *J. Phys. Oceanogr.*, 11, 324-336.

Mellor, G. L., and P. A. Durbin, 1975: The structure and dynamics of the ocean surface layer. *J. Phys. Oceanogr.*, 5, 718-728.

Pond, S., and G. L. Pickard, *Introductory Physical Oceanography*, Pergamon Press, Oxford, 241 pp.

Price, J. F., R. A. Weller, and R. Pinkel, 1986: Diurnal cycling: Observations and models of the upper ocean response to diurnal heating, cooling and wind mixing. *J. Geophys. Res.*, 91(C7), 8411-8427.

Stramma, L., P. Cornillon, R. A. Weller, J. F. Price, and M. G. Briscoe, 1986: Large diurnal sea surface temperature variability: Satellite and *in situ* measurements. *J. Phys. Oceanogr.*, 16, 827-837.

Weller, R. A., and R. E. Davis, 1980: A vector measuring current meter. *Deep-Sea Res.*, 27, 565-582.

Weller, R. A., 1981: Observations of the velocity response to wind forcing in the upper ocean. *J. Geophys. Res.*, 86, 1969-1977.

Woods, J. D., and V. Strass, 1986: The response of the upper ocean to solar heating, II, The wind-driven current. *Q. J. R. Meteorol. Soc.*, 112, 29-42.

MIXED-LAYER SHEAR RELATED TO WIND STRESS IN THE CENTRAL EQUATORIAL PACIFIC

Fernando Santiago-Mandujano

Department of Oceanography and Hawaii Institute of Geophysics, University of Hawaii at Manoa, Honolulu, Hawaii 96822.

Eric Firing

Joint Institute for Marine and Atmospheric Research, University of Hawaii at Manoa, Honolulu, Hawaii, 96822.

ABSTRACT

Sixteen months of wind and current profile observations in the central equatorial Pacific show the response of the upper ocean shear to local wind forcing. The shear at the ocean surface is significantly correlated with the wind stress in direction, but not in magnitude. This implies that the vertical eddy viscosity coefficient (A_v) is proportional to the square of the wind speed or to the stress.

Using this variable eddy viscosity coefficient in Stommel's (1960) model of the Equatorial Undercurrent, we calculate shears in the mixed layer that compare well with the observations. The flow is downwind on the equator and tends toward an Ekman spiral off the equator. The depth to which the model applies increases with the wind speed and is close to the Ekman depth $(2A_v/|f|)^{1/2}$ at 2° from the equator. The application of the model to the observations is insensitive to the method of estimating the layer depth.

1. INTRODUCTION

The central equatorial Pacific surface layer is characterized by small vertical density gradients and a strong pycnocline that separates it from the deeper ocean. These conditions lead to the rapid development of ageostrophic shear flows directly driven by the wind and decoupled from the deeper circulation (Hisard et al., 1970, Wyrtki et al., 1981, Donguy et al., 1984, Leetmaa and Wilson, 1985). Previous studies have been based on occasional current profile sections, or, in the NORPAX Tahiti Shuttle, on a period of time in which the winds were quite steady. Here we investigate the relationship between local winds and upper ocean shear in a 16-month time series including 41 sections, and spanning a period of major wind changes: the 1982-83 El Niño.

2. DATA

During March 1982 through June 1983, as part of the PEQUOD project (Pacific Equatorial Ocean Dynamics), 21 cruises were made in the central equatorial Pacific (Firing et al., 1983). Profiles of absolute current velocity and temperature together with shipboard wind observations were obtained every half degree from 3°N to 3°S along 159°W (Fig. 1).

Current velocities and temperatures were sampled at about 10-m vertical intervals using the Pegasus acoustic dropsonde (Spain et al., 1981). The surface velocity was averaged from the drift of the Pegasus before recovery, an interval ranging from a few minutes to an hour. Descending and ascending Pegasus profiles were averaged and linearly interpolated at 2-m intervals, then smoothed and interpolated to 20-m intervals starting at 40 m. The 20-m velocity was calculated using a parabolic fit to the surface velocity, the smoothed 40-m velocity, and the unsmoothed intermediate data. The endpoints were given extra weight.

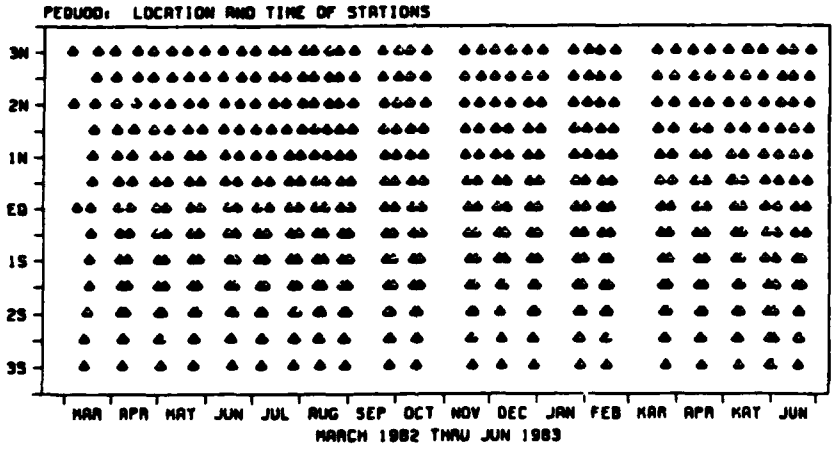

Fig. 1. Location of the stations along 159°W during the PEQUOD program.

Vertical shear of the horizontal currents was computed at each station at various levels. For the surface, the shear was calculated from a parabolic fit to the processed velocities at 0, 20, and 40 m. First order finite differences were used to calculate the shear at 10, 30, 50 and 70 m. The coarseness of these shear estimates was primarily due to limits imposed by the current profiling method. The relationship of these estimates to the actual shear structure of the ocean will require more investigation, including new measurements with better resolution and accuracy.

The wind stress was assumed proportional to the wind velocity squared: $\underset{\sim}{\tau} = \rho_a C_D |\underset{\sim}{U}| \underset{\sim}{U}$ with ρ_a the air density, $\underset{\sim}{U}$ the wind velocity at 10 m above the sea surface and C_D the drag coefficient. C_D was considered constant ($C_D = 1.14 \times 10^{-3}$, Large and Pond, 1982)) since only wind speeds smaller than 10 m/s were included in the study.

Confidence limits for correlation analyses were estimated using an integral time scale of 25 days (Davis, 1976, 1977), calculated from the time series at 3°N (Fig. 1) where the sampling interval was the most regular. The corresponding number of equivalent degrees of freedom, 17, was considered as representative for the time series at each latitude, and as a very conservative estimate for the data set as a whole, disregarding latitude.

3. SHEAR - WIND STRESS CORRELATIONS.

Using all 492 profiles, the correlation between the magnitudes of the wind stress and shear vectors at the sea surface was not significantly different from zero; but the directions of the vectors were significantly correlated (over the 99% confidence level, Fig. 2). This has important consequences for the eddy viscosity coefficient (A_v), given as: $A_v = \tau/\rho u_z = \rho_a C_D U^2/\rho u_z$, with ρ the density of water and u_z the surface shear magnitude. If the surface shear magnitude does not depend on the wind speed, then A_v must be proportional to the square of the wind speed. This was confirmed by the following alternative analysis, involving the Cartesian rather than the polar components of the vectors.

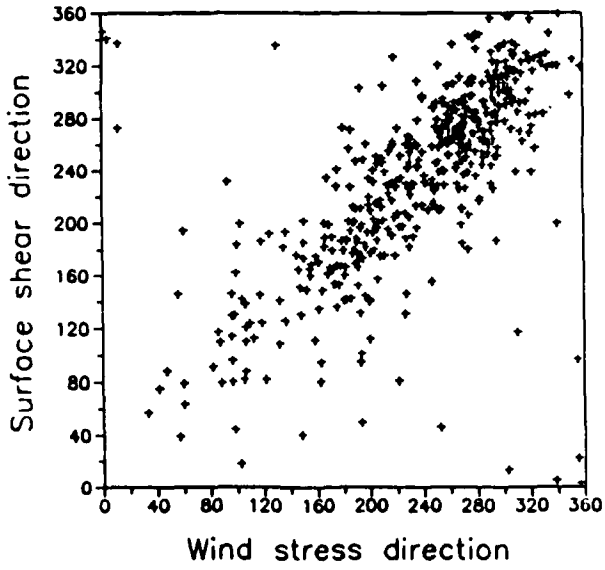

Fig. 2. Surface shear vs. wind stress directions from 492 data pairs. The directions increase clockwise from true North. The correlation coefficient is 0.7.

Values for A_v at different wind speeds were obtained from the correlations between wind stress and surface shear, separating zonal and meridional components. The correlations in the range of 1 - 10 m/s at 1 m/s intervals were all significant at the 95% confidence level, and for wind speeds higher than 4 m/s they were over the 99% level. A linear regression of A_v vs. wind speed (Fig. 3) gave:

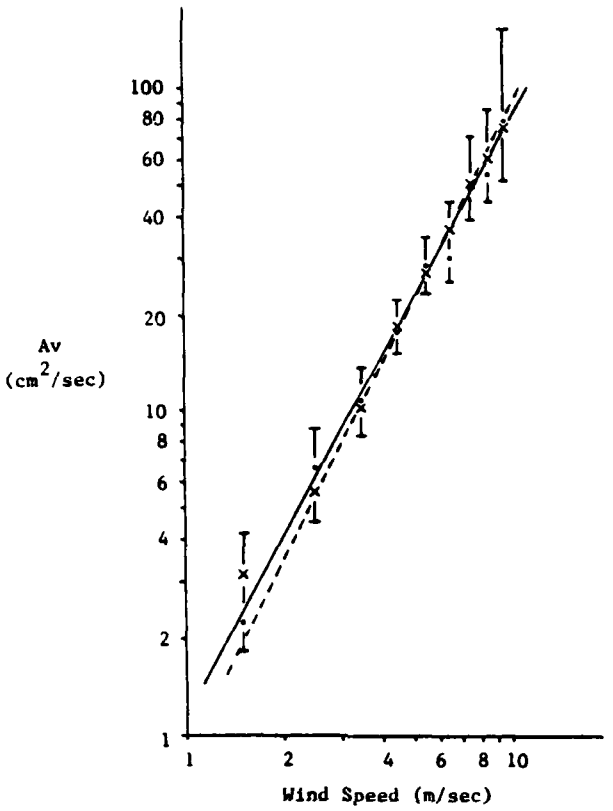

Fig. 3. Logarithmic plot of the vertical eddy viscosity coefficient (A_v) for different wind speeds (U). The crosses (X) correspond to the zonal and the dots (.) to the meridional components. The solid line is the linear regression fit, and the dashed line corresponds to $A_v \sim U^2$. The bars are the 95% confidence limits.

$$A_v = a\,(U/Uo)^b \quad ; \quad 1 \text{ m/s} < U < 10 \text{ m/s} \qquad (1)$$

with U = wind speed in m/s, Uo = 1 m/s, a = 1.16 cm^2/s and b = 1.85.

This shows A_v varying nearly as the square of the wind speed. The quadratic relation, also shown for comparison in Fig. 3, is:

$$A_v = c\,U^2 \quad ; \quad c = 1 \times 10^{-4} \text{ sec} \qquad (2)$$

This result implies that any approximation of A_v as constant in the mixed layer can be valid only over a narrow range of wind speeds. It is expected that eddy diffusivity responds to the wind speed in a similar manner.

Only the correlations between colinear components of the wind stress vs. surface shear were significant. The correlations of the cross components (e.g., meridional shear vs. zonal stress), which could have indicated a turning of the shear due to the Coriolis force, were not statistically significant. At deeper levels the turning appeared to be a consistent feature. To study this turning and to estimate the depth of direct

influence of the wind on the surface layer, the inner covariance (Mooers, 1973) and inner correlation were calculated.

The inner covariance between the shear vector (u_z, v_z) and the wind stress vector (τ^x, τ^y) for a sample of N observations is defined as:

$$\mathrm{Cov}(T^*,U_z) = \sum_{j=1}^{N} |T'_j|\,|U_z'_j|\,\exp\{i(\phi_j - \theta_j)\}$$

$$= |\mathrm{Cov}(T^*,U_z)|\,\exp(i\Phi_{inn})$$

where T and U_z are the complex representations of the wind stress and shear in terms of their zonal and meridional components (i.e., $T = \tau^x+i\tau^y = |T|\exp(i\theta)$ and $U_z = u_z+iv_z = |U_z|\exp(i\phi)$), and the primes denote demeaned quantities. Φ_{inn} gives the turning of U_z with respect to T. The normalized covariance is the inner correlation:

$$K_{inn} = \mathrm{Cov}(T^*, U_z) \,/\, [\mathrm{Var}(T)\,\mathrm{Var}(U_z)]^{1/2}$$

$$= |K_{inn}|\,\exp(i\Phi_{inn})$$

where $\mathrm{Var}(X) = \mathrm{Cov}(X^*, X)$.

The inner correlations between wind stress and shear at 10 and 30 m for each latitude are shown in Fig. 4. The magnitude of the vectors in the complex plane gives the correlation between the variables, and the phase is a measure of the mean angle from the stress vector to the shear vector. At 10 m the correlations were significant at almost all latitudes, but the angles were near zero. The 30-m shears were not significantly correlated (at the 95% level) with the stress but were consistently rotated clockwise north of the equator, and, to a lesser degree, counterclockwise south of the equator.

The inner correlations between the shear at 10 and 30 m, 30 and 50 m, and 10 and 50 m depth were obtained in order to observe the shear turning (Fig. 5). The phase of the complex vectors showed clearly a rotation of the shear with respect to depth, with clockwise turning in the northern hemisphere and counter-clockwise in the southern. This was observed regularly in the three cases. The correlations between 10 and 30 m depth were all significant at the 95% confidence level, and between 30 and 50 m they were over the 99% confidence level. Between 10 and 50 m the correlations were not significant (at the 95% confidence level), but were consistent with the 10 to 30 m and 30 to 50 m rotations.

The observed correlation between wind and shear, and the anticyclonic rotation of the shear with depth, suggest Ekman layer dynamics. The simplest model of Ekman dynamics near the equator is that of Stommel (1960). In the next section this model is used to predict the shear generated from the observed winds, which is then compared with the observed shear.

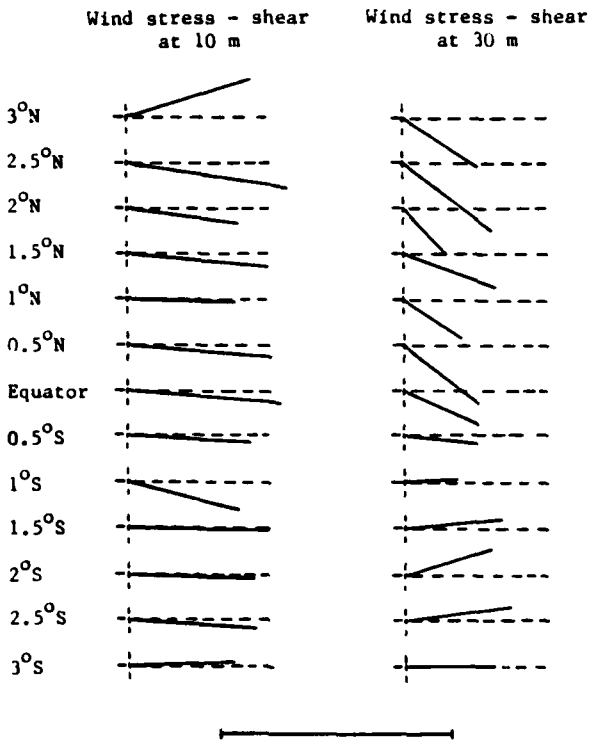

Fig. 4. Inner correlations in the complex plane between wind stress and shear at 10 and 30 m depth respectively, at each latitude. The phase indicates the turning of the shear with respect to the wind stress. The bar at the bottom of the figure represents a correlation of magnitude one.

4. APPLICATION OF STOMMEL'S MODEL

Stommel's 1960 model was originally applied to the Equatorial Undercurrent but is actually better suited to the study of shear in the mixed layer. It assumes steady linear flow in a homogeneous surface layer driven by the wind stress. The surface layer is decoupled from the deeper circulation by imposing a condition of zero momentum flux at the bottom of the layer. Only vertical friction is considered. The model gives a parabolic downwind velocity profile on the equator, blending smoothly into a surface Ekman layer far from the equator. There are two free parameters: A_v and the mixed layer depth h. A third parameter, the Ekman depth $(2A_v/|f|)^{1/2}$, is a function of latitude. In the following we will explore the behavior of the model in several ranges of wind speed with various methods for choosing the free parameters.

First, the shear at 10 and 30 m was modeled using a constant A_v = 35 cm^2/s and with the base of the layer defined as the shallowest point where the vertical temperature gradient exceeded 0.05°C/m. Comparing modeled versus observed shears for 440 stations (Fig. 6), the correlation coefficients were 0.59 (significant at 95%) for the zonal and meridional comparisons at

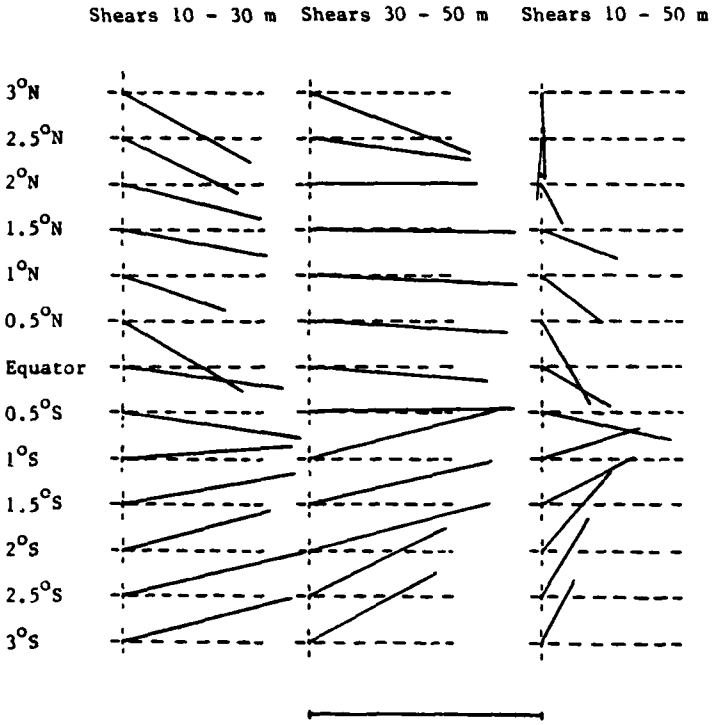

Fig. 5. Inner correlations in the complex plane between shear at 10 and 30 m, 30 and 50 m, and 10 and 50 m depth at each latitude. The phase indicates the turning of the deeper shear with respect to the shallower shear. The bar at the bottom of the figure represents a correlation of magnitude one.

10 m. At 30 m the correlations were 0.51 and 0.43 for the zonal and meridional components, and were significant at the 95% and 90% confidence levels respectively. The data in Fig. 6 seem to occupy mainly the first and third quadrants, although their distribution in those quadrants is rather diffuse; this indicates that with a constant value for A_v, the model can give a proper description of the direction of the shear, but its magnitude is poorly determined.

A notable improvement in the shear modeling was obtained when the value for A_v was calculated using eq.(1). The correlation coefficients from the comparisons in the zonal and meridional components increased to 0.74 and 0.72 respectively at 10 m, and to 0.59 and 0.46 at 30 m (Fig. 7).

To evaluate the effect of the wind speed on the model performance, the shear was calculated for different wind ranges and compared with the observations (Table 1). Only the shear above the depth of the mixed layer was used, so the number of samples decreased with depth. The correlations increased at higher wind speed, although the differences were not statistically significant. However, the regularity of this behaviour at all depths indicates that the model performs better at high wind speeds. An important pattern was that the higher the wind speed, the greater the depth where the correlations were still significant. This depth was

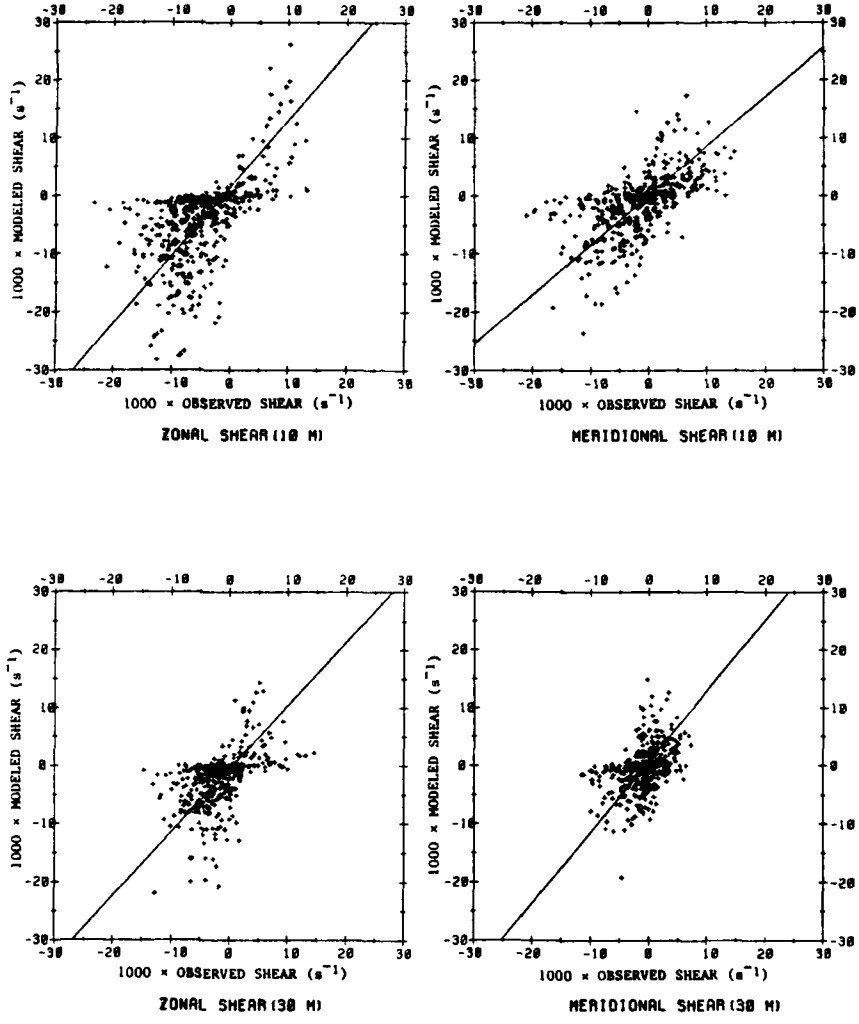

Fig. 6. Comparisons between modeled and observed shear for the zonal and meridional components at 10 and 30 m depth. A constant value of A_v = 35 cm^2/s was used in the modeling.

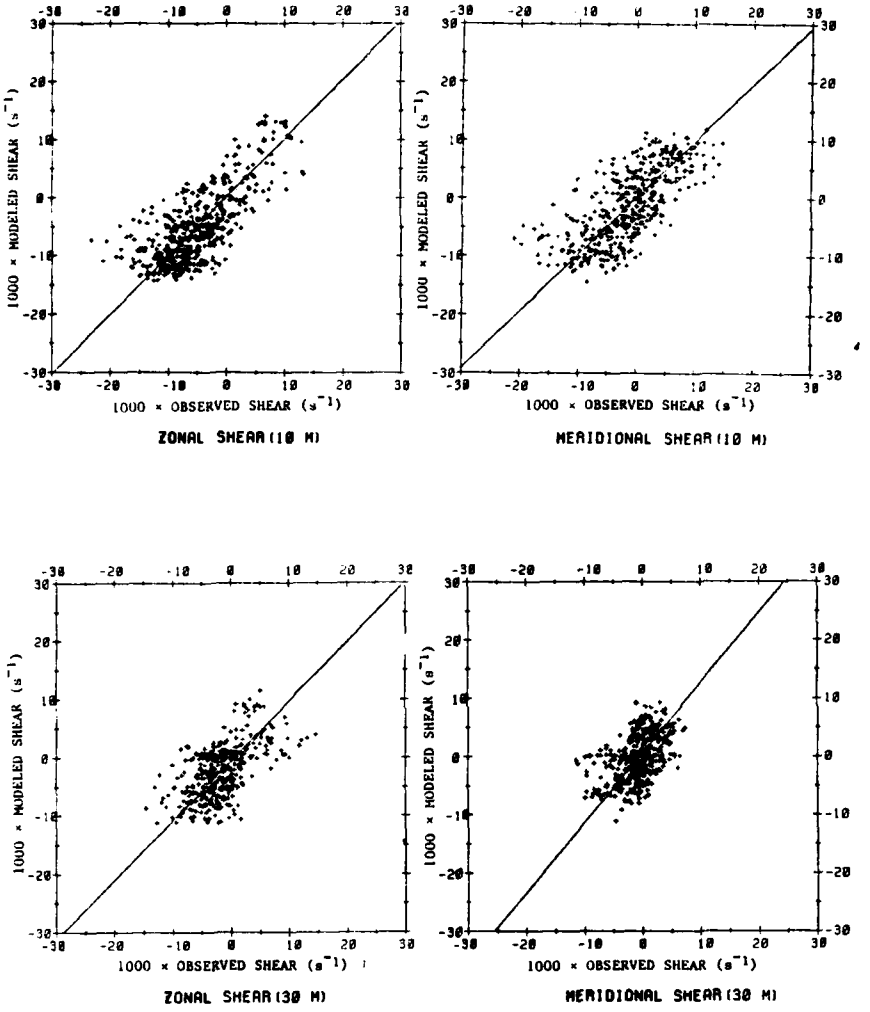

Fig. 7. Comparisons between modeled and observed shear for the zonal and meridional components at 10 and 30 m depth. A_v values depending on the wind speed were used in the modeling (eq.(1) in the text).

Table 1. Correlation coefficients between modeled and observed shears at different depths and wind ranges. The coefficients in parenthesis are not significant at the 95% confidence level. N is the number of data pairs.

Depth (m)	Component	Wind speed (m/s)		
		0.4 - 3	3 - 6	6 - 9
10	Zonal	0.55	0.76	0.83
	Meridional	0.61	0.74	0.78
	N	107	202	131
30	Zonal	(0.22)	0.62	0.71
	Meridional	(0.09)	0.48	0.62
	N	88	175	109
50	Zonal	(0.11)	(0.47)	0.63
	Meridional	(-0.06)	(0.30)	0.57
	N	75	150	90
70	Zonal	(-0.03)	(0.37)	0.59
	Meridional	(-0.03)	(0.21)	(0.43)
	N	66	111	66
	Ekman depth at 2° lat. (m)	∿ 10	∿ 30	∿45

comparable to the depth of the Ekman layer at 2°, using a value for A_v given by eq.(2). This suggests that the applicability of the model is limited to an Ekman depth proportional to the wind speed.

The model was tested for sensitivity to the mixed layer depth criterion. Four criteria were used: a constant depth of 50 m, the depth where the temperature difference from the surface was greater than 1°C, the depth where the vertical temperature gradient was greater than 0.05°C/m, and the 28°C isotherm depth (Table 2). No significant difference was obtained among the various criteria for h, although the temperature gradient criterion gave slightly better correlations than the constant depth.

5. *DISCUSSION AND CONCLUSIONS*

The present study has several serious limitations:

(1) The vertical resolution of the Pegasus allows us to look at the upper ocean shear only on scales of 20 m or more.

Table 2. Correlation coefficients between modeled and observed shears at 10 and 30 m depth, using different mixed layer depth criteria in the modeling. All the coefficients are significant at the 95% confidence level. N is the number of data pairs.

Depth (m)	Component	Mixed layer depth criteria			
		Constant 50 m	T_0-T_1 > 1°C	$T_{1-1}-T_1$ >.05°C/m	28°C depth
10	Zonal	0.71	0.79	0.79	0.75
	Meridional	0.76	0.75	0.75	0.76
	N	369	330	333	315
30	Zonal	0.52	0.64	0.64	0.52
	Meridional	0.55	0.53	0.53	0.51
	N	369	276	284	285

(2) The study was done with the standard version of the Pegasus data set which was not optimized for looking at small-scale shear, and in which adjacent points are not statistically independent.

(3) The surface drift velocity is heavily weighted in the analysis but, as was pointed out by Pierre Flament during this workshop, it may have been contaminated by wave rectification.

(4) The role of density stratification in the upper ocean has not been addressed.

(5) Finally, although the temporal sampling was better than in any previous series of current profiles, it was still inadequate to permit a fully time dependent rather than a quasi-steady model, and it yields statistical results that are far less robust than one would like.

In spite of these limitations, we have reached important conclusions. The surface shear in the central equatorial Pacific is correlated with the local wind in direction, but not in magnitude. This implies that the vertical eddy viscosity coefficient is proportional to the square of the wind speed, or to the wind stress. With this variable eddy viscosity coefficient, Stommel's (1960) Equatorial Undercurrent model predicts mixed layer shears that compare well with observations. The downwind flow on the equator and the rotation by the Coriolis force off the equator as predicted by the model are seen in the observations. The model is insensitive to the mixed layer depth parameter. The depth to which the model applies increases with the wind speed and is comparable to the Ekman depth at 2° off the equator.

AKNOWLEDGMENTS

This research was funded by the National Science Foundation under grant OCE83-14486 of the PEQUOD program. During the completion of this research one author (F S-M) was partially supported by a CONACYT fellowship from the government of Mexico. JIMAR Contribution Number 134. Hawaii Institute of Geophysics Contribution Number 1876.

REFERENCES

Davis, R. E., 1976: Predictability of sea surface temperature and sea level pressure anomalies of the North Pacific. J. Phys. Oceanogr., 6, 249-266.

____, 1977: Techniques for statistical analysis and prediction of geophysical fluid systems. Geophys. Astrophys. Fluid Dyn., 8, 245-277.

Donguy, J., G. Eldin, G. Meyers, A. Morliere and J. P. Rebert, 1984: A Thermal Interpretation of a change in Equatorial Western Pacific Circulation. Trop. Ocean-Atmos. Newslett., No. 24, 9-10.

Firing, E., R. Lukas, J. Sadler and K. Wyrtki, 1983: Equatorial Undercurrent Disappears During 1982-1983 El Niño. Science, 222, 1121-1123.

Hisard, P., J. Merle and B. Voituriez, 1970: The Equatorial Undercurrent at 170°E in March and April 1967. J. Mar. Res., 28, 281-303.

Large, W. G. and S. Pond, 1982: Sensible and Latent Heat Flux Measurements over the Ocean. J. Phys. Oceanogr., 12, 464-482.

Leetmaa, A. and D. Wilson, 1985: Characteristics of Near Surface Circulation Patterns in the Eastern Equatorial Pacific. Prog. Oceanog., 14, 339-352.

Mooers, C. N. K., 1973: A Technique for the cross spectrum analysis of pairs of complex-valued time series, with emphasis on properties of polarized components and rotational invariants. Deep-Sea Res., 20, 1129-1141.

Spain, P. F., D. L. Dorson, and H. T. Rossby, 1981: Pegasus: a simple, acoustically tracked velocity profiler. Deep-Sea Res., 28A, 1553-1567.

Stommel, H., 1960: Wind-drift near the Equator. Deep-Sea Res., 6, 298-302.

Wyrtki, K., E. Firing, D. Halpern, R. Knox, G. J. McNally, W. C. Patzert, E. D. Stroup, B. A. Taft and R. Williams, 1981: The Hawaii to Tahiti Shuttle Experiment. Science, 211, 22-28.

MIXED-LAYER FRONTS IN THE CALIFORNIA CURRENT

Pierre Flament

Woods Hole Oceanographic Institution
Woods Hole Massachusetts 02543

ABSTRACT

Observations of the structure of the mixed-layer in regions of large horizontal shear are presented. Cyclonic shears of order f were found to be associated with strong surface convergences. Several possible driving mechanisms are proposed and scaled.

1. INTRODUCTION

The summer-time mesoscale flow off Central and Northern California consists of narrow seaward baroclinic jets emanating from the coastal upwelling region, embedded in a field of cyclonic and anti-cyclonic eddies. These jets transport cold coastal water offshore, and appear as cold filaments on satellite infrared images. Some typical scales of the jets are: width 20 to 50 km, surface velocity 0.5 to 0.8 m/s, velocity e-folding depth 150 m, total flow 0.5 to $2{\cdot}10^6 m^3/s$ and alongshore spacing 50 to 500 km. These features have been discussed by Davis (1985), Flament et al. (1985), Kosro and Huyer (1986) and Rienecker et al. (1985).

The surface layer processes associated with the jets are asymmetric: at the anticyclonic boundary, the transition from cold to warm water is often spread over 20 km, whereas the cyclonic boundary corresponds to a front generally sharper than the 1-km resolution of the infrared images. This asymmetry seems to be an ubiquitous characteristic of the filaments and has been qualitatively observed in all the images analyzed.

A series of cruises was organized from 1982 to 1985 to study the small-scale structure of the filaments and the mechanisms maintaining the sharpness of the cyclonic front despite turbulent diffusion. The results of these cruises have been presented in details by Flament et al. (1985) and Flament (1986), and are summarized in section 2. Several possible frontogenetic mechanisms are discussed in section 3.

2. OBSERVATIONS OF THE FRONTAL STRUCTURE

The filament rooted near Point Arena was studied in 1982. A 10 m/s northwesterly wind prevailed during this experiment, deepening the surface mixed-layer to 35 m. The width of the sharp front was 350 m. It extended only to the bottom of the mixed-layer: there was no corresponding thermal front in the thermocline. The fronts observed in the satellite images were thus shallower than the velocity field.

Two results suggested that a strong cross-frontal convergence was responsible for the sharp front. In a sequence of satellite images, a "lucky streak" was observed to coalesce with the front. The cross-isotherm convergence was 18 cm/s over a distance of 20 km. Thermohaline layers were found to originate at the front and extend ~20 km into the thermocline underneath the anticyclonic region, consistent with a subduction of the denser frontal waters presumably forced by the convergence. Similar subducted layers were observed near Point Conception in 1983.

However, it was not possible to estimate the rate of divergence in the along-isotherm direction from the satellite images, and thus to distinguish between convergence ($\nabla \cdot u \neq 0$) and confluence ($\partial_x u \neq 0$ with $\nabla \cdot u = 0$). The subducted layers were the only indirect evidence suggesting that $\nabla \cdot u \neq 0$.

In July 1985, the hypothesis $\nabla \cdot u \neq 0$ at the sharp front was tested by deploying clusters of surface drifters at several positions across the filament rooted near Point Sur. This experiment was conducted during a period of light wind (<2 m/s), following a 10 m/s northwesterly wind event which lasted two days.

In the anticyclonic region, the flow was non-divergent within the sampling errors and the shear was -0.3 f ($f = 9 \cdot 10^{-5}$ s^{-1} is the planetary vorticity). At the cyclonic front, the flow was discontinuous at the 1-km resolution of the cluster. The shear was larger than 4.5 f and persisted for at least one week. It was associated with a cross-frontal surface convergence of 6 cm/s, visible as a 20 m wide accumulation of debris of seaweeds commonly found on the shelf. Thermohaline layers were again found to originate at the front and to extend under the anticyclonic region. The vertical scale of the layers was smallest near the front. However, a simple interpretation in terms of subduction was not possible, perhaps because a well-developed surface mixed-layer was lacking.

The convergence at the cyclonic front is a robust finding of this work: it has been consistently observed remotely from satellite images, in situ using clusters of drifters, and by the accumulation of kelp. The associated water subduction is more complicated to infer when there are many water types in presence, although thermohaline intrusions are clearly associated with the fronts.

3. POSSIBLE MECHANISMS DRIVING THE CONVERGENCE

Since the fronts were generally confined to the mixed-layer and were shallower than 35 m, it is tempting to interpret the convergence in terms of mixed-layer processes. Several possible ones discussed and scaled below could cause the convergence. A jet $U(y) < 0$ flowing westward will be assumed.

1. The simplest interpretation is a difference in the turbulent layer thickness H across the jet. Variations of H are likely because the mixed-layers on either side of the front have different deepening histories and because the rate of deepening is affected by the local vorticity (Klein and LeSaos, 1986). Assuming slab mixed-layers, the cross-frontal Ekman velocity v_e is

$$v_e = -\frac{\tau_x}{\rho f H(y)} \tag{1}$$

where τ_x is the x-component of the wind stress. A surface convergence is induced where $\partial_y H$ and τ_x have opposite signs. For a 10 m/s wind, an initial 10% change of H induces a convergence of only 0.5 cm/s at the latitude of our experiments. This process seems to require unreasonable mixed-layer depth variations to account for the observed convergence.

2. A convergence of the Ekman transport can also be caused by the horizontal shear, through the non-linear terms of the momentum balance (Niiler, 1969; Stern, 1975; Flament, 1983). The cross-frontal Ekman velocity

$$v_e = -\frac{\tau_x}{\rho(f - \partial_y U)H} \tag{2}$$

is decreased on the cyclonic side and enhanced on the anticyclonic side. Since a shear of order f exists at the cyclonic front, this coupling results in large variations of v_e across the jet, and, for a wind with an eastward component, the most frequent in the region studied, in a convergence along the axis of the jet. For the vorticities found during the 1985 experiment, the anticyclonic and cyclonic regions would converge at 9 cm/s with a 10 m/s wind. This mechanism should be tested by correlating the frontal gradients with the wind direction in existing infrared images archives.

3. The marine atmospheric boundary layer is modified when advected across a temperature front and a change of the drag coefficient results (Businger and Shaw, 1984). This can also create an Ekman convergence. For a mixed boundary layer of height h initially in thermal equilibrium with the water, the e-folding distance for recovering equilibrium is h/k where $k = 1.2 \cdot 10^{-3}$ is the sensible heat exchange coefficient (Friehe and Schmitt, 1976). For $h = 200$m, this distance is 170 km, an order of magnitude larger than the width of the filaments: this process does not seem important in the present case (see also Hanson, 1987).

4. Refraction of surface waves by the shear is another candidate for driving the convergence. Such sharp refractions have been observed off California by Sheres et al. (1985). A relevant theory on the effect of surface waves on mean flows is found in Garrett (1976). For waves propagating at a small angle with the axis of the jet, the dominant effect is a near-surface stress oriented to the right of the wave ray when the shear is cyclonic, and given approximately by

$$F = \frac{E_o \partial_y U}{c_o} \tag{3}$$

in which E_o and c_o are the energy density and the phase speed of the waves. The stress induced by a typical westerly swell of 6 s period and 1 m amplitude refracted by the cyclonic shear found in 1985 is 0.2 Pa, to be compared with a wind stress of 0.15 Pa for 10 m/s wind. A convergence at the southern edge of the cyclonic region and a divergence on the axis of the jet result.

5. The convergence may simply be a frictional effect on the quasi-geostrophic flow $U(y)$. Assuming an exponential velocity profile of e-folding depth D = 150m, the frictionally driven secondary circulation is

$$V = \frac{K_v U}{D^2 f} \tag{4}$$

where K_v is the vertical eddy viscosity. A convergence towards the southern edge of the cyclonic front results. For a typical mixed-layer eddy viscosity $K_v = 0.1\text{m}^2/\text{s}$, the convergence corresponding to the shear observed in 1985 would be 2 cm/s over a scale of 1 km. This process is also consistent with the lack of front below the mixed-layer, since the vertical eddy viscosity is much smaller there.

All these processes may contribute to the convergence, some may be more important when the wind is strong (the 1982 experiment), other may dominate when the wind is weak (the 1985 experiment) and the data presently available is not sufficient to single out any. A parallel shear flow has been assumed here; other effects may be play a role when the streamlines of the mean flow are curved. Further work is clearly needed to understand the dynamics of mixed layers in regions of strong horizontal shear.

ACKNOWLEDGMENTS

This work was done in collaboration with L. Armi and was funded by the Office of Naval Research. The author would like to thank Jerome Smith at SIO and Bob Hall at SAIC for helpful discussions on the driving processes, and the University of Hawaii for inviting him to this workshop.

REFERENCES

Businger, J.A. and W.J. Shaw, 1984: "The response of the marine boundary layer to mesoscale variations in sea-surface temperature," *Dynamics of Atmospheres and Oceans*, *8*, 267-281.

Davis, R.E., 1985: "Drifter observations of coastal surface currents during CODE: the method and descriptive view," *J. Geophys. Res.*, *90*, 4741-4755.

Flament, P., 1983: "Some three-dimensional aspects of coastal upwelling," in *Baroclinic instability and ocean fronts, notes of the summer study program in geophysical fluid dynamics, Tech. Rep. WHOI-83-41*, ed. M. Stern, Wood's Hole Oceanographic Institution, 286-297.

Flament, P., L. Armi, and L. Washburn, 1985: "The evolving structure of an upwelling filament," *J. Geophys. Res.*, *90*, 11765-11778.

Flament, P., 1986: "Finestructure and subduction associated with upwelling filaments," PhD Dissertation, University of California San Diego.

Friehe, C.A. and K.F. Schmitt, 1976: "Parameterization of air-sea interface fluxes of sensible heat and moisture by bulk aerodynamic formulas," *J. Phys. Oceanog.*, *6*, 801-809.

Garrett, C., 1976: "Generation of Langmuir circulation by surface waves: a feedback mechanism," *J. Mar. Res.*, *43*, 117-130.

Hanson, H.P., 1987: "Response of marine atmospheric boundary layer height to sea-surface temperature changes: mixed-layer theory," *J. Geophys. Res.*, *92*. (in press)

Klein, P. and J.P. LeSaos, 1986: "Influence of a quasi-geostrophic flow on the deepening of the wind-mixed layer," *Geophys. Res. Let.*, *13*, 452-455.

Kosro, P.M. and A. Huyer, 1986: "CTD and velocity surveys of seaward jets off Northern California," *J. Geophys. Res.*, *91*, 7680-7690.

Niiler, P.P., 1969: "On the Ekman divergence in an oceanic jet," *J. Geophys. Res.*, *74*, 7048-7051.

Rienecker, M., C.N.K. Mooers, D.E. Hagan, and A.R. Robinson, 1985: "A cool anomaly off Northern California: an investigation using IR imagery and in situ data," *J. Geophys. Res.*, *90*, 4807-4818.

Sheres, D., K.E. Kenyon, R.L. Bernstein, and R.C. Beardsley, 1985: "Large horizontal velocity shears in the ocean obtained from images of refracting swell and in-situ moored current data," *J. Geophys. Res.*, *90*, 4943-4950.

Stern, M.E., 1975: *Ocean circulation physics*, Academic Press, New York.

HORIZONTAL SCALES OF WIND FORCED INERTIAL MOTIONS

Eric A. D'Asaro

Applied Physics Laboratory and School of Oceanography, College of Ocean and Fishery Sciences, University of Washington, Seattle, Washington 98105

ABSTRACT

Wind forced upper ocean inertial motions are simulated using a theory appropriate for regions of low oceanic mesoscale activity with the goal of identifying the causes of horizontal variability in inertial currents. Mixed layer inertial currents are modeled as a uniform slab forced by the wind stress. The subsequent evolution of these currents and their propagation below the mixed layer is analyzed using a perturbation analysis of the linearized equations. The resulting equations allow only near-inertial frequency dynamics and suppress other classes of motion.

Realistic wind fields are generated from Seasat scatterometer data by horizontally advecting the measured fields over the simulated ocean at a constant speed. The scatterometer data appear to have sufficient resolution to make such simulations, although there is considerable uncertainty about their absolute precision. The models predict scales similar to those observed. The horizontal scales of the simulated inertial currents are set by the advection speed and the horizontal scales of the applied wind stress field. Typically, both scales are important, indicating that the complexities of realistic wind fields are needed for realistic models of wind forced inertial motions — even for wind features such as fronts which appear to be two-dimensional on the synoptic scale.

INTRODUCTION

Near-inertial oscillations are an important velocity component in the upper ocean, commonly contributing half or more of the kinetic energy and a somewhat smaller fraction of the 10 m shear (D'Asaro, 1985a). They play a key role in theories of mixed layer deepening (Niiler and Kraus, 1977; Price, 1981) and have been observationally linked with patches of enhanced mixing (Kunze and Lueck, 1986; Gregg et. al., 1986). Under some circumstances they may be sufficiently nonlinear to generate wave-forced and Stokes flows of several centimeters per second (Price, 1983; White, 1986).

Recent years have seen considerable work on the theory of near-inertial motions, particularly those forced by storms (Price, 1983; Gill, 1984; Greatbatch, 1984; Kundu, 1986). One result of these studies is that, although some of the characteristics of these motions are determined by the stratification, the evolution rate, amplitude, and horizontal structure depend on

the wind stress field. In particular, the horizontal scale of the inertial motions is crucial in determining the rate at which inertial motions transfer energy from the directly forced motions in the mixed layer into the deeper ocean. Because these scales are set by the wind, realistic models of wind forced inertial motions will require realistic wind stress fields. The above theoretical work, however, considered only highly idealized wind fields such as circular hurricanes (Price, 1983; Greatbatch, 1984), two-dimensional fronts (D'Asaro, 1985a; Kundu, 1986), and sinusoidal storms (Gill, 1984). This is because measurements of two-dimensional, time-dependent wind stress fields with a spatial and temporal resolution sufficient to drive these models are not available. A possible exception are wind field measurements by the Seasat microwave scatterometer, which have a 50 km resolution. In this paper upper ocean inertial motions will be simulated using a linear model driven by the Seasat wind fields. The goals are to determine the resulting horizontal scales and compare these with oceanic observations and to assess the suitability of scatterometer winds for use in upper ocean modeling.

A LINEAR MODEL OF INERTIAL FREQUENCY DYNAMICS

Consider the linear, Boussinesq, f-plane, hydrostatic equations for a flat bottomed ocean with a buoyancy frequency $N(z)$ and forced by a wind stress τ which is modeled by a body force with a depth distribution $Z(z)$:

$$u_t - fv = -P_x + \frac{\tau_x}{\rho_0 H} Z(z) \tag{1}$$

$$v_t + fu = -P_y + \frac{\tau_y}{\rho_0 H} Z(z) \tag{2}$$

$$N^2 w = -P_{zt} \tag{3}$$

$$u_x + v_y + w_z = 0 \tag{4}$$

where the reference density ρ_0 has been absorbed into the pressure. Previous studies have shown distinctly different responses for the barotropic and baroclinic modes (Gill, 1984). We are interested in the baroclinic response in this study and will therefore use rigid lid boundary conditions

$$w(0) = w(-B) = 0 \quad . \tag{5}$$

Equations (3)-(5) can be combined to form

$$P_t = I \nabla_H \cdot \mathbf{u} \tag{6}$$

where $\nabla_H \cdot \mathbf{u} = u_x + v_y$.

$$I = (1-M)\int_{-B}^{z} dz' N^2(z') \int_{-B}^{z} dz'' \tag{7}$$

is an integral operator that combines eqs. (3) and (4), and

$$M = \frac{1}{B}\int_{-B}^{z} dz \tag{8}$$

is an integral operator required by (5).

Following Gill (1984), the wind stress will be distributed uniformly over a mixed layer of depth H so that

$$Z(z) = -\frac{H}{B} + \begin{cases} 1 & z > -H \\ 0 & z < -H \end{cases} \tag{9}$$

where the first term ensures that $MZ = 0$ so that there is no projection upon the barotropic mode.

Assuming velocity, vertical, horizontal, and time scales V, D, L, and f^{-1} respectively, the nondimensional forms of eqs. (1), (2), and (6) are

$$u'_{t'} = v' - \varepsilon P'_{x'} + T_x Z(z') \tag{10}$$

$$v'_{t'} = -u' - \varepsilon P'_{y'} + T_y Z(z') \tag{11}$$

$$P'_{t'} = I' \nabla'_H \cdot \mathbf{u}' \ , \tag{12}$$

where

$$\varepsilon = \frac{g\,\Delta\rho D}{\rho_0 f^2 L^2} \tag{13}$$

$$\frac{g\,\Delta\rho}{\rho_0} = \int_{-B}^{0} N^2 dz \tag{14}$$

and $\mathbf{T} = \tau/(\rho_0 HVf)$. The prime denotes dimensionless variables. I and P are nondimensionalized by $g\,\Delta\rho Z/\rho_0$ and $fLU\varepsilon$, respectively. Combining (10) and (11)

$$U'_{t'} + iU' = -\varepsilon(P'_{x'} + iP'_{y'}) + FZ'(z') \tag{15}$$

$$P'_{t'} = \frac{1}{2} l' \left[U'_{x'} + U'^{*}_{x'} - i \left(U'_{y'} - U'^{*}_{y'} \right) \right] \tag{16}$$

where $U = u' + iv'$, $F = T_x + iT_y$, and * denotes complex conjugation. The use of this complex number technique can, at times, result in wrong answers. It does not do so in any of the results presented here and is used for the sake of clarifying the exposition.

For $\varepsilon = 0$, eq. (15) describes the behavior of a slab mixed layer forced by a horizontally uniform wind stress. Many investigators (see Pollard, 1980; D'Asaro, 1985a) have found this to be a useful model of the generation of mixed layer inertial currents. For inertial motions of finite, but large, horizontal scale, a small ε approximation may be appropriate. We will derive an asymptotic approximation to (15) and (16) that is valid for small ε using the method of multiple scales (Kervorkian and Cole, 1981). This is inspired by Hasselman (1970) and also expands upon some results in D'Asaro (1985a). We expand U and P in a perturbation expansion

$$U = U_0(t'', \tau'') + \varepsilon U_1(t'', \tau'') + \cdots , \tag{17}$$

where $t'' = t'(1 + O(\varepsilon^2))$ and $\tau'' = \varepsilon t'$ are "fast" and "slow" time variables. The equations are expanded in orders of ε with the τ'' equation chosen so as to eliminate resonance. The resulting solution to order ε is

$$U = \left[\tilde{U}_F(t'') Z'(z') + \tilde{U}(\tau'', z') \right] e^{-it''} + \varepsilon U_1(z, \tau'') e^{it''} + \varepsilon U_G I Z'(z') . \tag{18}$$

The complex inertial amplitude (in brackets) is the sum of a directly forced component $\tilde{U}_F$ and a component $\tilde{U}$ due to the inviscid evolution of previously forced motions.

The directly forced motions, described by (15) with $\varepsilon = 0$, can be divided into Ekman-type motions

$$U_E = -iFZ'(z') \tag{19}$$

and a residual $\tilde{U}_F$ described by

$$\frac{\partial' \tilde{U}_F}{\partial t''} = i \frac{\partial' F}{\partial t''} e^{it''} . \tag{20}$$

$\tilde{U}_F$ describes the time dependent part of the solution and is thus of interest here. The dynamics of the free part of the solution $\tilde{U}$ are described by

$$\frac{\partial \tilde{U}}{\partial \tau''} = -\frac{1}{2} i l' \nabla'^2 \left[\tilde{U} + \tilde{U}_F Z'(z') \right] . \tag{21}$$

In addition, there are several order ε terms. Evolving inertial motions are slightly

anisotropic. This is described by a component U_1 which rotates in a direction opposite to pure inertial currents and is given by

$$U_1 = \frac{1}{4}I'\left[\frac{\partial^2}{\partial x^2} - \frac{\partial^2}{\partial y^2} + 2i\frac{\partial^2}{\partial xy}\right](\tilde{U}^* + \tilde{U}_F\, {}^*Z'(z')) \quad . \tag{22}$$

The wind forcing also generates order ε motions U_G described by

$$\frac{\partial U_G}{\partial t''} + iU_G = I\left[\frac{\partial'}{\partial x} + i\frac{\partial'}{\partial x}\right]\left[\nabla'_H \cdot \mathbf{T} + \int_0^{t''} \hat{\mathbf{z}} \cdot \nabla' \times \mathbf{T}\, dt\right] \quad , \tag{23}$$

which represent the noninertial and geostrophic forced motions. These are not of interest here.

The dimensional forms of (18), (20), (21), and (22) are

$$U = \left[\tilde{U}_F(t)Z(z) + \tilde{U}(t,z)\right]e^{-ift} + U_1 e^{ift} + U_G \tag{24}$$

$$\frac{\partial \tilde{U}_F}{\partial t} = ie^{ift}\frac{\partial}{\partial t}\frac{(\tau_x + i\tau_y)}{\rho_0 H} \tag{25}$$

$$\tilde{U}_t = -\frac{i}{2f}I\nabla^2(\tilde{U} + \tilde{U}_F Z). \tag{26}$$

$$U_1 = \frac{1}{4f}I\left[\frac{\partial^2}{\partial x^2} - \frac{\partial^2}{\partial y^2} + 2i\frac{\partial^2}{\partial xy}\right](\tilde{U}^* + \tilde{U}^*_F Z) \quad , \tag{27}$$

respectively.

Equations (24)-(27) describe the evolution of the velocity field for $\varepsilon \ll 1$. They are valid as long as U varies on a time scale that is long compared with f^{-1}. These equations allow only mean and inertial motions, as defined by (24). Higher frequency internal wave motions have been filtered from the equations of motions by the perturbation analysis. The evolution equation (26) is only first order in time, as opposed to the full equations, (1)-(4), which are second order in time. They are thus simpler to analyze and can be numerically integrated with larger time steps.

APPLICATION TO STORM RESPONSE

D'Asaro (1985b) computed $\tilde{U}_F$ from a large number of long term wind records. He found that inertial motions are forced (i.e., $\tilde{U}_F$ changes) only intermittently, so that the concept of

energetic "storms," each of which produces a large response in the ocean, separated by long periods of "calm," is a useful idealization for upper ocean inertial motions. The goal of this study is to simulate the inertial motions initially generated by one such "storm" in the mixed layer and thermocline. The subsequent evolution of these motions, although it can be modeled using these equations, is a more ambitious project which is currently under way.

The ocean is initially assumed at rest, $\tilde{U} = 0$, and $\tilde{U}_F$ is computed from the wind stress field $\tau(x, y, t)$. The evolution of the wave field for small times is computed from (26),

$$\tilde{U} = \tilde{U}_F(t)Z(z) - \left[\frac{i}{2f}\int_0^t \nabla_H^2 \tilde{U}_F(t)dt\right] IZ(z) \quad . \tag{28}$$

Assuming that $\tilde{U}_F$ is nearly constant except for a brief period of forcing at $t = 0$, this simplifies to

$$\tilde{U} = \tilde{U}_F(t)Z(z) - ft\left[\frac{i}{2f^2}\nabla_H^2 \tilde{U}_F(0)\right] IZ(z) \quad . \tag{29}$$

The two terms in (29) have a different depth dependence. The depth structure is illustrated in Fig. 1 assuming

$$N^2(z) = \begin{cases} 0 & z > -H \\ N_0^2 e^{(z+H)/b} & z < -H \end{cases} \tag{30}$$

with $H = 50\,\text{m}$, $b = 1000\,\text{m}$, $N_0 = 5\times10^{-3}\,\text{s}^{-1}$ (3 cph) and $B = 5000\,\text{m}$. $Z(z)$ (Fig. 1b, solid) is large only in the mixed layer and is very small ($O(H/B)$) beneath. $IZ(z)$ (Fig. 1b, dashed) has a maximum value in the mixed layer and is continuous across the mixed layer base. Since this is a baroclinic flow, IZ is large and of opposite sign in the deep ocean, with a zero at mid-depth.

At $t = 0$ the inertial motions are described by $Z(z)$ and are thus concentrated in the mixed layer. A characteristic profile of inertial currents at a finite time is shown in Fig. 1c by assuming the bracketed term in (29) is equal to $e^{0.53\,i}\tilde{U}_F$. Inertial motions are now present both in the mixed layer and in the deeper ocean. Equation (29) therefore describes the "propagation" of inertial motions from the mixed layer into the thermocline.

Several characteristics of the velocity profiles (Fig. 1c) are notable. The inertial velocity is uniform across the mixed layer, jumps sharply across the mixed layer base, and then decays with depth in the thermocline, resulting in a velocity maximum beneath the mixed layer base. The thickness of this maximum is set by the stratification. For stratifications that include a thin seasonal thermocline, the velocity maximum is thinner and thus more distinct than that in Fig. 1c. Examples of this pattern for various stratifications can be seen in Rubenstein (1983), Gill (1984), D'Asaro (1985a), and Kundu (1986). It should be noted that since

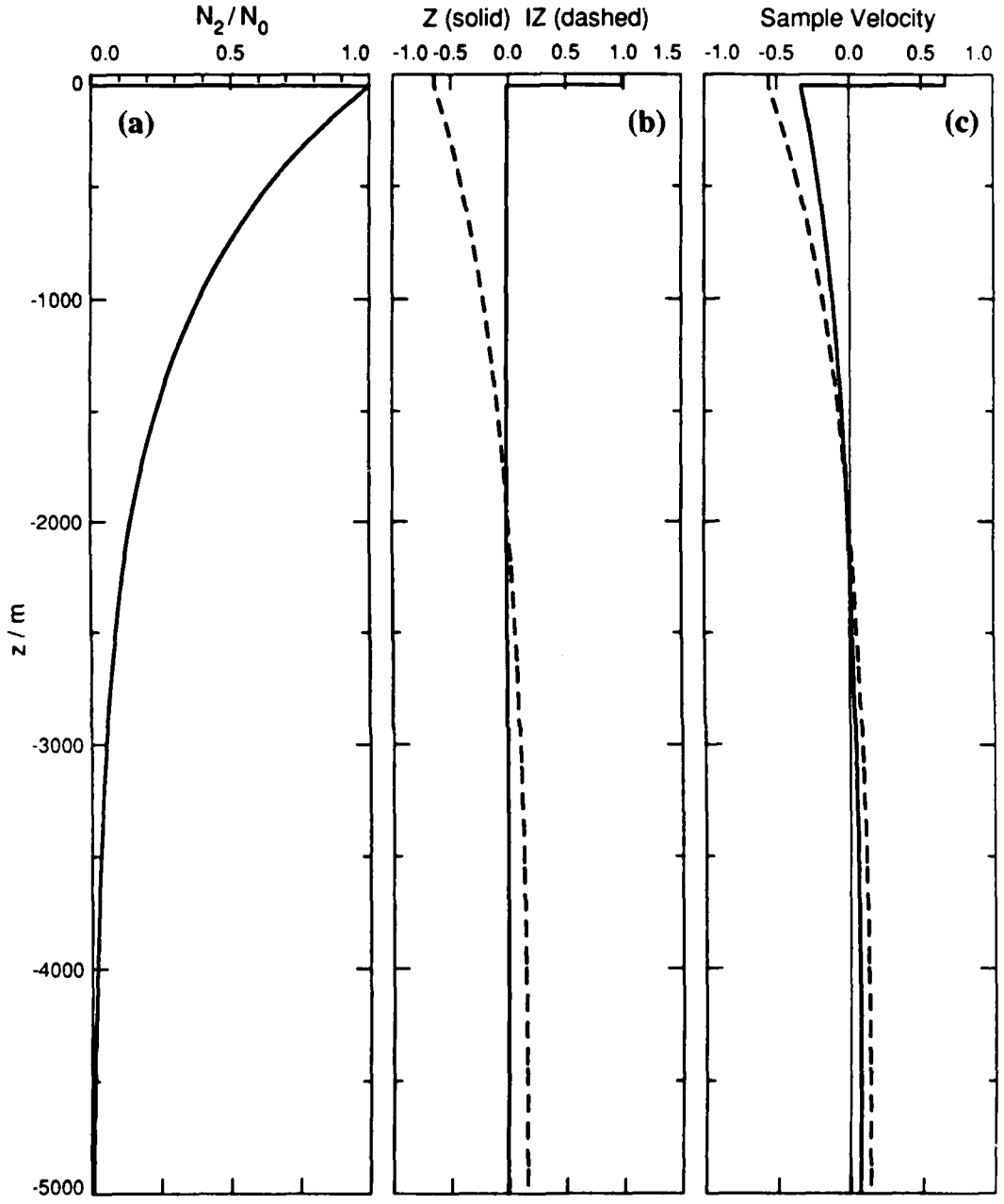

Fig. 1. Vertical structure of simulated wind forced inertial motions assuming N^2 profile shown in a). b) Vertical structure of motions directly forced by the wind (Z, solid) and of their initial evolution (IZ, dashed). c) A sample velocity profile with components $Z+\sin(0.53)IZ$ (solid) and $\cos(0.53)IZ$ (dashed).

IZ has no discontinuity across the mixed layer base, the shear at the mixed layer base is unchanged by the dynamics and in the time scales considered here.

The rate of energy transfer can be estimated from (29) by computing the total energy below the mixed layer

$$E_{therm} = \int_{-B}^{-H} \frac{1}{2} |\tilde{U}|^2 = \frac{1}{4} b |\tilde{U}_0|^2 , \tag{31}$$

where

$$\tilde{U}_0 = ift\, L_I^2 \nabla_H^2 \tilde{U}_F \tag{32}$$

is the value of $\tilde{U}$ immediately below the mixed layer base. L_I is a horizontal length scale set by the stratification

$$L_I^2 = \frac{HbN_0^2}{2f^2} \tag{33}$$

with a value of about 7 km for the above parameters. Equations (31)-(33) assume $H \ll b \ll B$ for simplicity. A more general expression, valid under this same approximation, is

$$L_I^2 = \frac{Hg\Delta\rho}{2\rho_0 f^2} , \tag{34}$$

where $\Delta\rho$ is the change in density across the thermocline. Notice that the energy in the thermocline increases quadratically with time, as has been found by other investigators (Price, 1983; Gill, 1984).

One measure of the rate of energy transfer is the time t_{trans} for the thermocline energy (31) to equal the energy $\frac{1}{2}H |\tilde{U}_F|^2$ initially in the mixed layer:

$$f\, t_{trans} = \left[\frac{2H}{b}\right]^{1/2} \frac{1}{L_I^2 k_F^2} \tag{35}$$

where

$$k_F^2 = \frac{|\nabla_H^2 \tilde{U}_F|}{|\tilde{U}_F|} \tag{36}$$

is a characteristic horizontal wavenumber. Note that t_{trans} depends strongly on the horizontal scale of the flow, specifically the scale associated with $\nabla^2 \tilde{U}$.

AN ADVECTIVE HYPOTHESIS

The above model requires a two-dimensional, time varying wind stress field. The required temporal resolution is clearly of order f^{-1}. The required spatial resolution can be estimated from observational estimates of the time for mixed layer inertial currents to decay, which are in the range of 2-20 days (Pollard and Millard, 1970; Pollard, 1980). Equating this time to t_{trans} in (36) yields k_F^{-1} in the range of 50-175 km, which is comparable to the few existing observations (D'Asaro, 1985a; Kundu and Thompson, 1985). Time varying wind fields with this resolution have not been measured over the ocean.

The problem can be simplified by assuming that the dominant cause of temporal variability is the advection of spatial structure — or equivalently, that on the forcing time scale of a few f^{-1}, storms move unchanged across the ocean. Similar assumptions are commonly made in the analysis of meteorological data on these spatial scales (Bond and Fleagle, 1985), which may provide a partial justification. The utility of this assumption is that simulations can now be made using a single, high resolution spatial wind field, such as is available from the Seasat scatterometer. Assuming an advection speed C in the +x direction, the wind stress field can be written

$$\tau(x,y,t) = \tau(x - Ct, y, 0) \quad . \tag{37}$$

Away from the regions of forcing and to first order in ε, $U = (\tilde{U} + \tilde{U}_F)\, e^{-i(\omega t - k_A x)}$ so that

$$\nabla^2 U = -k_A^2 U + \frac{\partial^2}{\partial y^2} U \tag{38}$$

$$= -(k_A^2 + k_y^2)\, U = k_F^2 U \tag{39}$$

where $k_A = f/C$ is an advective wavenumber and k_y is a characteristic wavenumber perpendicular to the advection direction. Relations (38) and (39) also apply to $\tilde{U}$. For the theory to be valid, $k_A^2 L_I^2 \ll 1$. Equivalently, storms must move fast enough that $C \gg L_I f \approx 0.7\ \mathrm{m\ s^{-1}}$, a condition that is easily met by most mid-latitude storms.

SCALES OF INERTIAL MOTIONS

In the above model, wind stress variations in the advection (x) and cross-advection (y) directions play fundamentally different roles. The x variations act as time variations and thus generate inertial motions as described by (25). The resulting inertial motions have an x wavenumber spectrum that is narrow band with a peak wavenumber near k_A. Accordingly,

the amplitude of the inertial motions depends on the variance of the wind stress in this band. The y variations in wind stress act to generate y variations in the inertial currents. The resulting y wavenumber spectrum of inertial currents reflects all the scales of the wind field and is thus broad band.

The wavenumber spectrum of the wind field over the ocean is typically red with an approximate k^{-2} shape (Freilich and Chelton, 1986) and a correlation scale of many hundred kilometers. The spectrum of the wind stress field should be similar. The equation (25) relating the directly forced inertial currents, U_F to the wind stress contains no spatial derivatives. The y wavenumber spectrum of $\tilde{U}_F$ should therefore be roughly the same as that of the wind stress (i.e., k^{-2}) as should their y coherence lengths.

The thermocline inertial currents $\tilde{U}_0$ depend on $\nabla^2\tilde{U}_E$ as given by (32). The y wavenumber spectrum of $\tilde{U}_0$ will thus be the sum of $-k_A^2 U_F$, with a spectrum of approximately k^{-2}, and $\partial^2\tilde{U}_0/\partial y^2$ with a spectrum of approximately k^2. Unless the wind stress is redder than k^{-5}, which seems unlikely given the numerous observations of small-scale atmospheric variability (Houze and Hobbs, 1982), this argument predicts a blue y wavenumber spectrum for U_0 and thus indeterminately large values for k_y, k_F, U_0, and t_{trans}^{-1}. Such a result violates the assumptions of the theory, which requires slow evolution of the inertial motions and therefore is valid only for wavenumbers such that $L_I^2 k_y^2 \ll 1$. Thus the wind stress fields that drive this model must not contain wavenumbers higher than this limit. Practically, this is not a problem, since measurements of wind stress fields with 10 km resolution are currently nonexistent. Conceptually, however, it means that all the predictions of this theory apply to spatially averaged variables and that the evolution rates predicted here are a function of the averaging scale. Small horizontal scales will evolve faster than large ones, and the coherence scales of the field will be a function of time. A full study of this problem requires a time stepping model, which is beyond the scope of this paper. Within the above limitations, it is still clear that the inertial motions can be diagnosed using a wind field with a known finite resolution. This is the approach taken here.

The above considerations indicate that the relative magnitude of k_y and k_A is an important parameter of inertial current models. If $k_A \gg k_y$ the dynamics becomes two-dimensional, and only one wavenumber, k_A, is important. In this case, the details of the wind field are not important in determining the structure and evolution rates of wind forced inertial motions. U_F and U_0 are, for example, always 90° out of phase. If $k_y \geq k_A$ the details of the wind stress become important and a broad band of spatial scales enters the dynamics. The relative phase of U_F and U_0, for example, now depends on the local value of $\nabla^2 U_F$. One goal of the following simulations is to determine the importance of k_y for realistic wind fields. This will require a wind stress field with a resolution sufficient to resolve cross-advection scales smaller than k_A^{-1}. The Seasat scatterometer winds have a resolution of 50 km, which compares favorably with a value of $k_A \approx (100\,\text{km})^{-1}$ for a typical advection speed of $10\,\text{m s}^{-1}$.

SIMULATION TECHNIQUES

Wind stress fields were computed using data from the Seasat scatterometer (Brown, 1986) supplied by the Jet Propulsion Laboratory. Estimates of the 10 m wind were edited for attenuation, and one of the four possible directions was chosen as described by Levy and Brown (1986). These were converted to estimates of surface wind stress using the formula of Large and Pond (1981) with no correction for boundary layer stratification. This results in a slightly irregular, gappy array of surface stress estimates with a spacing of about 50 km, such as that shown in Fig. 2a.

The above model requires a smooth estimate of $\tau(x,y)$ so that (25) can be evaluated. In addition, some smoothing is required to reduce noise in the wind estimates. Two-dimensional smoothing splines (Wahba, 1984) were used to accomplish both tasks. These fit a smooth function $f(x,y)$ with continuous first derivatives to n data points $f_i(x_i,y_i)$ to minimize

$$\frac{1}{n}\sum_{i=1}^{n}(f_i - f(x_i,y_i))^2 + \lambda^2 J(f)\ , \tag{40}$$

where $J(f)$ is an isotropic sum of second derivatives of f that measures its smoothness. This criterion is isotropic, unlike that for bicubic splines, and therefore imposes no asymmetries on the fitted function. The relative balance between the smoothness of the fit and the closeness of the surface to the data is controlled by the parameter λ. A value of $\lambda = 1000$ m is used here. This value yields an rms difference between the raw and smoothed stress fields somewhat larger than the official error estimates for the scatterometer (1.6 m s^{-1} in wind speed and 16° in direction (Born et al., 1982)). Typically about 20-30% of the stress field variance was removed by this method. The two components of τ were independently smoothed using this technique. An example of the resulting wind stress field is shown in Fig. 2b.

The wind fields from two Seasat passes over the eastern North Pacific on September 11, 1978, are used here. These were chosen because they cover the low and cold front of a strong cyclone and because the same data have been previously analyzed for their meteorological content (McMurdie and Katsaros, 1985). Each section of data used was small enough so that the advection speed was approximately constant and large enough to encompass a well-defined portion of the storm.

For each wind stress field and advection vector C, $\tilde{U}_F$ was computed using (25) and (37) along paths through the data parallel to C and ending at $t = 0$. The value of f corresponding to the final point was used throughout. The value of $\nabla^2 U_F$ was estimated by evaluating U_F on a 25 km grid and fitting a quadratic surface to all points within a 50 km radius of each grid point. Estimates of U_0, k_F, and t_{trans} were computed at $t = 0$ using $L_I = 7$ km.

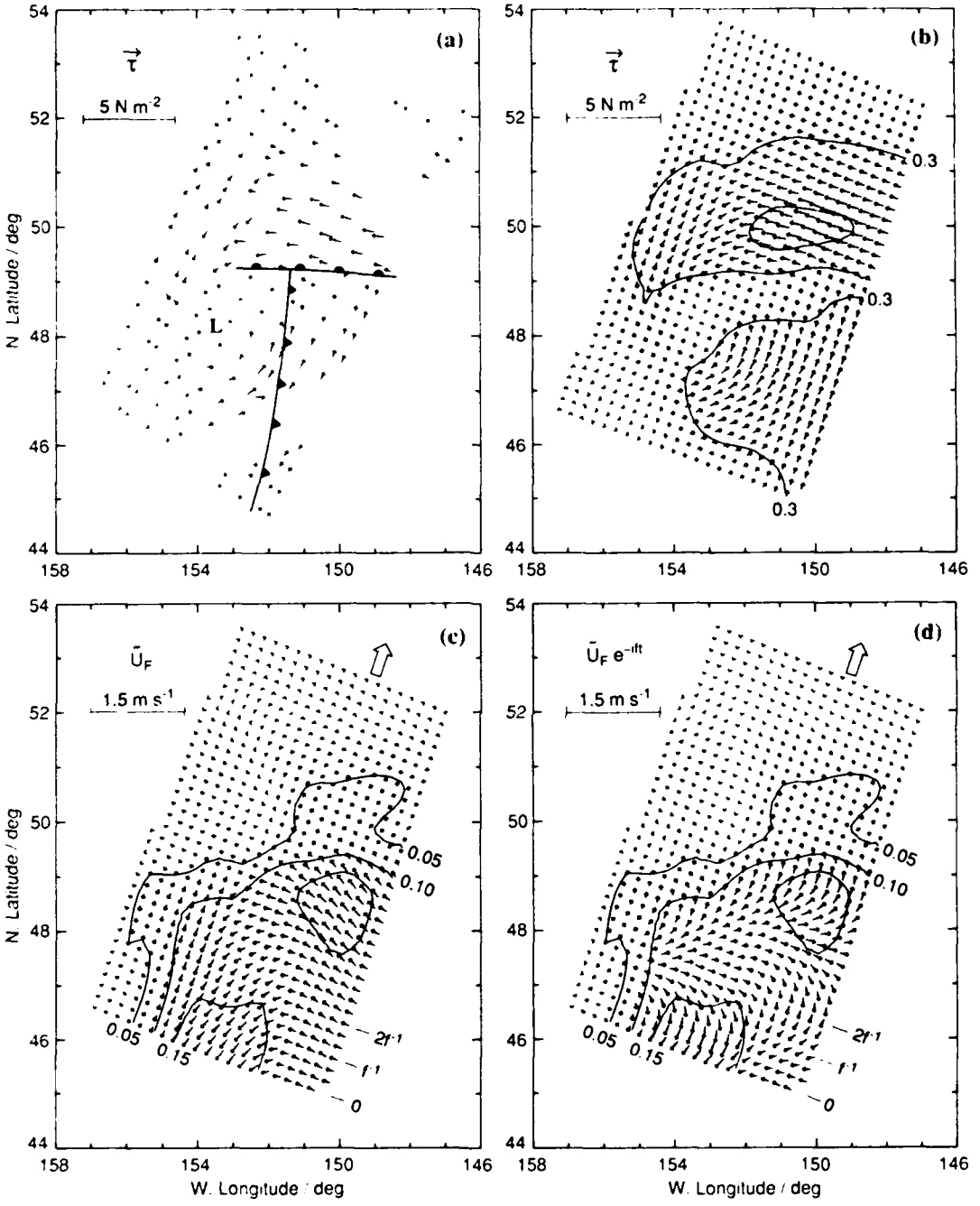

Fig. 2. Simulation using Seasat scatterometer winds from 900Z, Sept. 11, 1978.
a) Dealiased surface stress vectors. Front and low locations are indicated.
b) Smoothed wind stress field sampled on a 25 km grid with superimposed contours of wind stress magnitude. c) Complex inertial amplitude of wind forced motions, $\tilde{U}_F$. Advection direction and corresponding time axis are indicated. d) Inertial currents corresponding to c).

RESULTS

Response to a Low

Figures 2 and 3 show the simulated inertial response to a Seasat wind field measured at 900Z, September 11, 1978. The stress field (Fig. 2a, 2b) shows a well-defined cyclone with the strongest winds in the northeast and southeast quadrants. Warm and cold fronts from McMurdie (1983) have been drawn in Fig. 2a. As expected, the wind stress varies on a scale of several hundred kilometers.

Mixed layer inertial currents are generated by advecting this stress pattern in the direction indicated in Fig. 2c. The resulting field of data can be interpreted either as a space-time map, with the time scale given on the right-hand side of the data or as a true spatial pattern, bearing in mind that f is constant in the advection direction. The variation of the complex inertial amplitude U_F is shown in Fig. 2c; the corresponding currents $U_F e^{-ift}$ are shown in Fig. 2d.

In Fig. 2c,d, inertial currents are generated by the sharp changes in wind stress associated with the two wind stress maxima. The strongest inertial amplitudes occur on the right-hand side of the cyclone, because the winds are strongest in this region and because the turning of the winds corresponds to the turning of inertial currents and thus evokes a resonant response (Price, 1981). As expected, the inertial currents show two spatial scales, rotation with a wavenumber k_A, here about 75 km, and a variation of $\tilde{U}_F$ in the cross-advection direction with a scale of several hundred kilometers, approximately the same scale as that of the wind stress.

The cross-advection scales are shown more clearly in Fig. 3, which shows a number of variables at $t = 0$. $\tilde{U}_F$ (Fig. 3a) varies on a scale of many hundred kilometers, as discussed above. In contrast, the evolving part of the inertial motions, $\tilde{U}_0$ (Fig. 3b), shows two scales, as expected from (39). On the scale of several hundred kilometers, $i\tilde{U}_0$ mimics the behavior of $\tilde{U}_F$. For example at 300 km, the imaginary part of $\tilde{U}_F$ (dashed) is minimum, as is the real part of $\tilde{U}_0$ (solid). This is because of the k_A^2 term in (39). In addition, $\tilde{U}_0$ varies with a wavelength of about 150 km. This is caused by the wind stress variations in the cross-advection direction associated with the cyclone. As expected, the most energetic wavenumber is near the Nyquist wavenumber for the scatterometer data. Figure 3c plots both the simulated energy transfer time t_{trans} and a horizontal line representing its value assuming $k_y = 0$. The energy transfer rate varies spatially owing to the variations of k_y and is typically 25% below the two-dimensional estimate. Wind stress fluctuations in the cross-advection direction are an important, but not dominant, factor in this case; the two-dimensional approximation will be useful, but not accurate.

Effect of Advection Speed

Figures 4 and 5 show the effect of decreasing the advection speed from the observed 8.4 m s^{-1} to 4.0 m s^{-1}, corresponding to a decrease in k_A from about 85 km to about 40 km. Since there is, in general, less variance in the wind stress at smaller scales, we would expect the inertial amplitudes to be decreased. A comparison of Figs. 2 and 4 shows this to be the

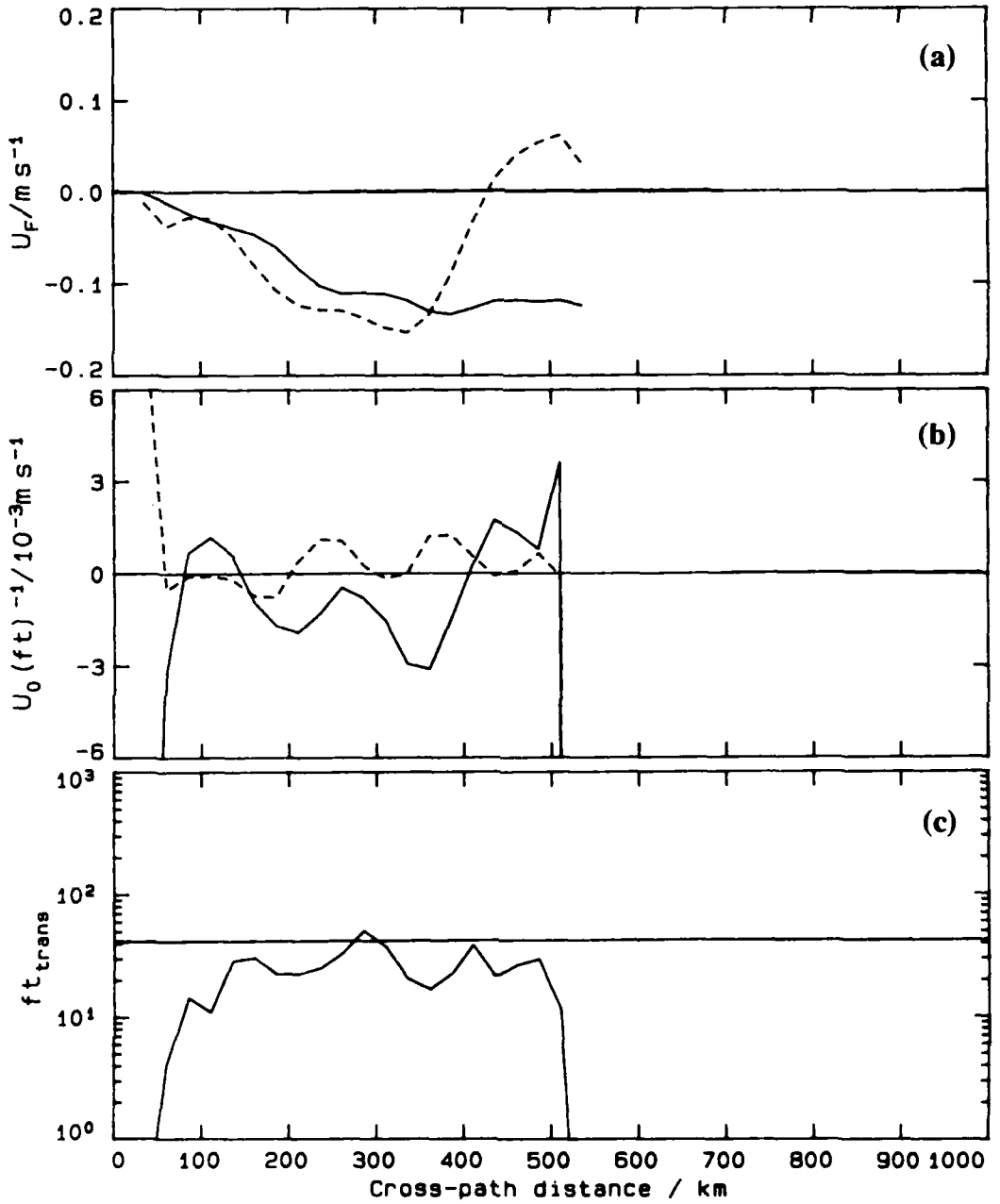

Fig. 3. Simulated quantities at $t = 0$ for Fig. 2. a) Real (solid) and imaginary (dashed) components of U_F. b) Same but for U_0, the thermocline inertial currents. c) Time for energy to be transferred from mixed layer to thermocline. Solid line indicates two-dimensional approximation.

case. The biggest change, however, is a concentration of the inertial motions into a small region. At this location the two wind maxima are separated by about one wavelength, $2\pi k_A^{-1}$, resulting in a coherent forcing of the inertial motions. In general, we would expect that a change in advection speed would increase k_A while k_y would remain roughly the same, thus decreasing t_{trans} by about a factor of 4 and increasing the accuracy of the two-dimensional approximation. Comparing Figs. 3c and 5c, we note that t_{trans} decreases as expected but its deviation from the two-dimensional value is about the same. The concentration of inertial motions into a small region has increased the small-scale variability of the inertial motions more than simple scaling argument would suggest. Mid-latitude storms, it would appear, are difficult to characterize with simple spectral arguments.

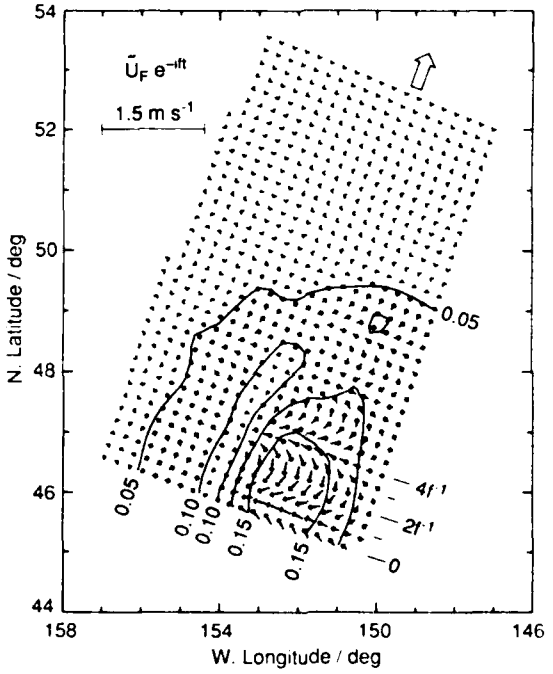

Fig. 4. Same as 2d) but with slower advection speed.

Response to a Cold Front

Figures 6 and 7 show the simulated response to the cold front associated with the same storm. The Seasat wind stresses (Fig. 6a) shift sharply from northeast to northwest at the front, which is drawn to coincide with the location of the wind shift. The strongest winds (Fig. 6b) occur near the front and on the edge of the associated low. Inertial currents are generated primarily by the frontal wind shift (Fig. 6c). This storm advects quickly (17.8 m s^{-1}) so that the advective wavenumber is small, $k_A \approx (180\,\text{km})^{-1}$. The decay time due to k_A alone is long, approximately $200f^{-1}$ (Fig. 7c). Accordingly, k_y is mostly much larger than k_A, and t_{trans} is commonly a factor of 3 less than the two-dimensional value. The two-dimensional approximation would not be appropriate in this case.

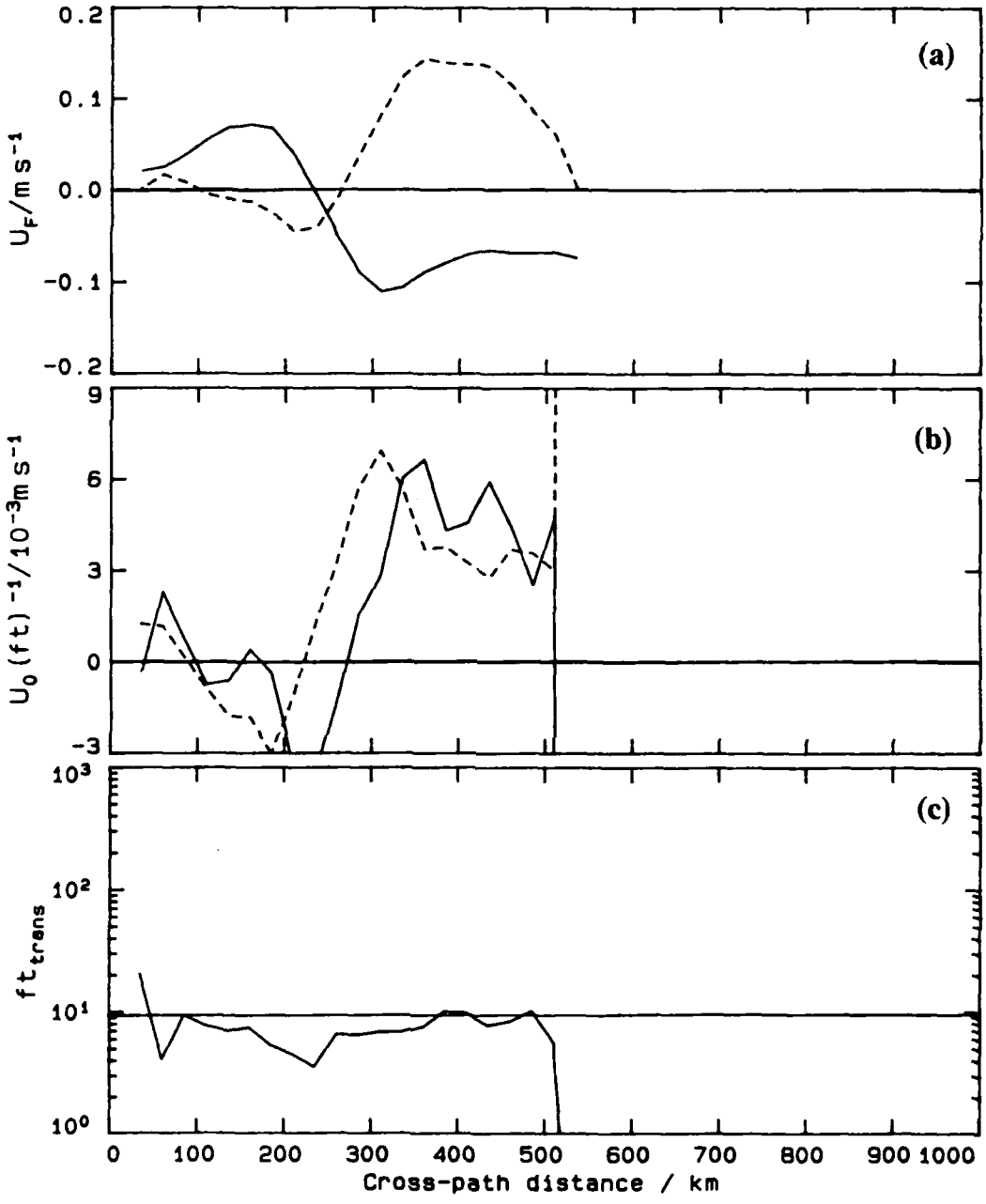

Fig. 5. Simulated quantities at $t = 0$ for Fig. 4.

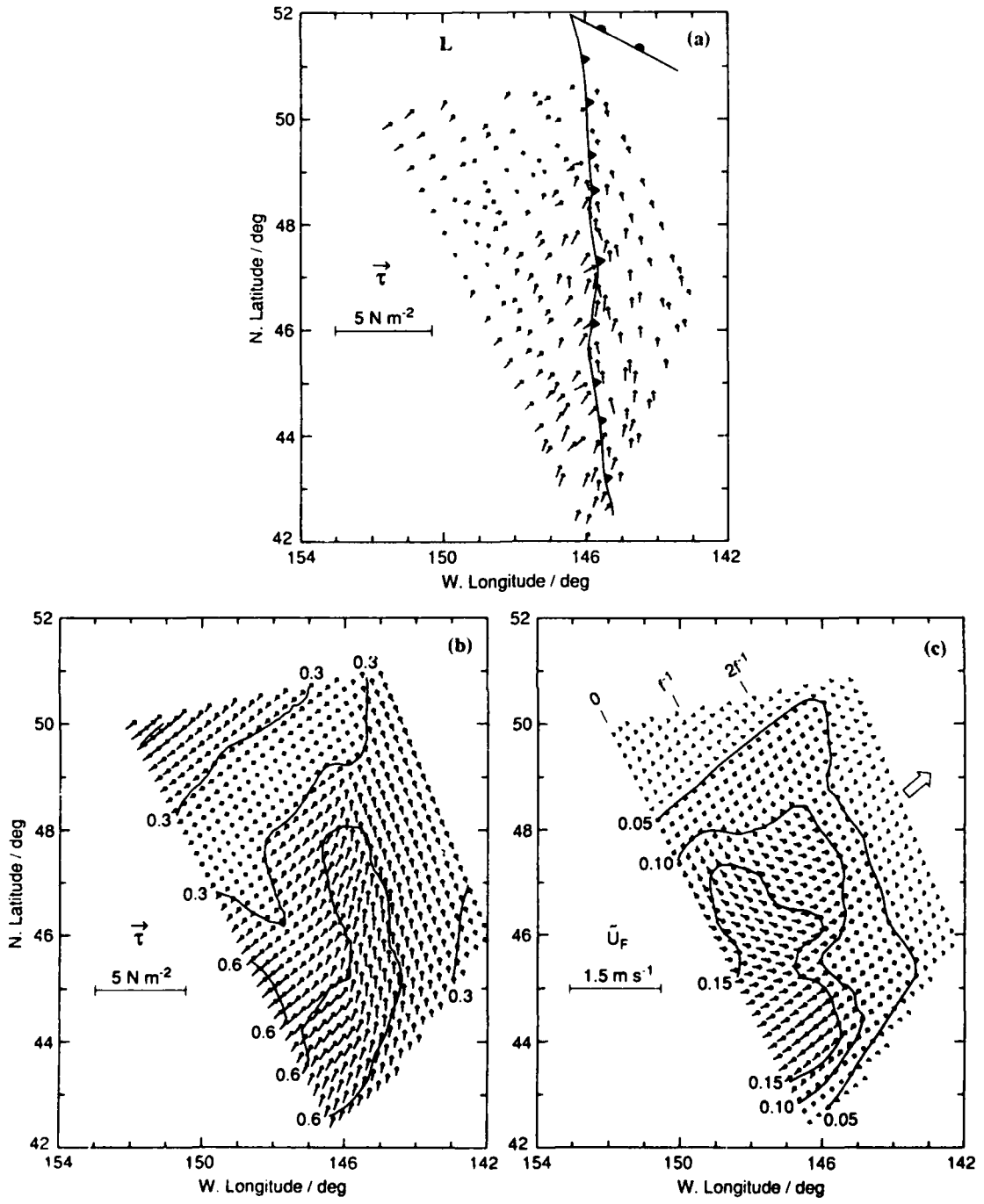

Fig. 6. Simulation of response to a cold front using Seasat scatterometer winds from 1840Z, Sept. 11, 1978. a)-c) same as Fig. 2.

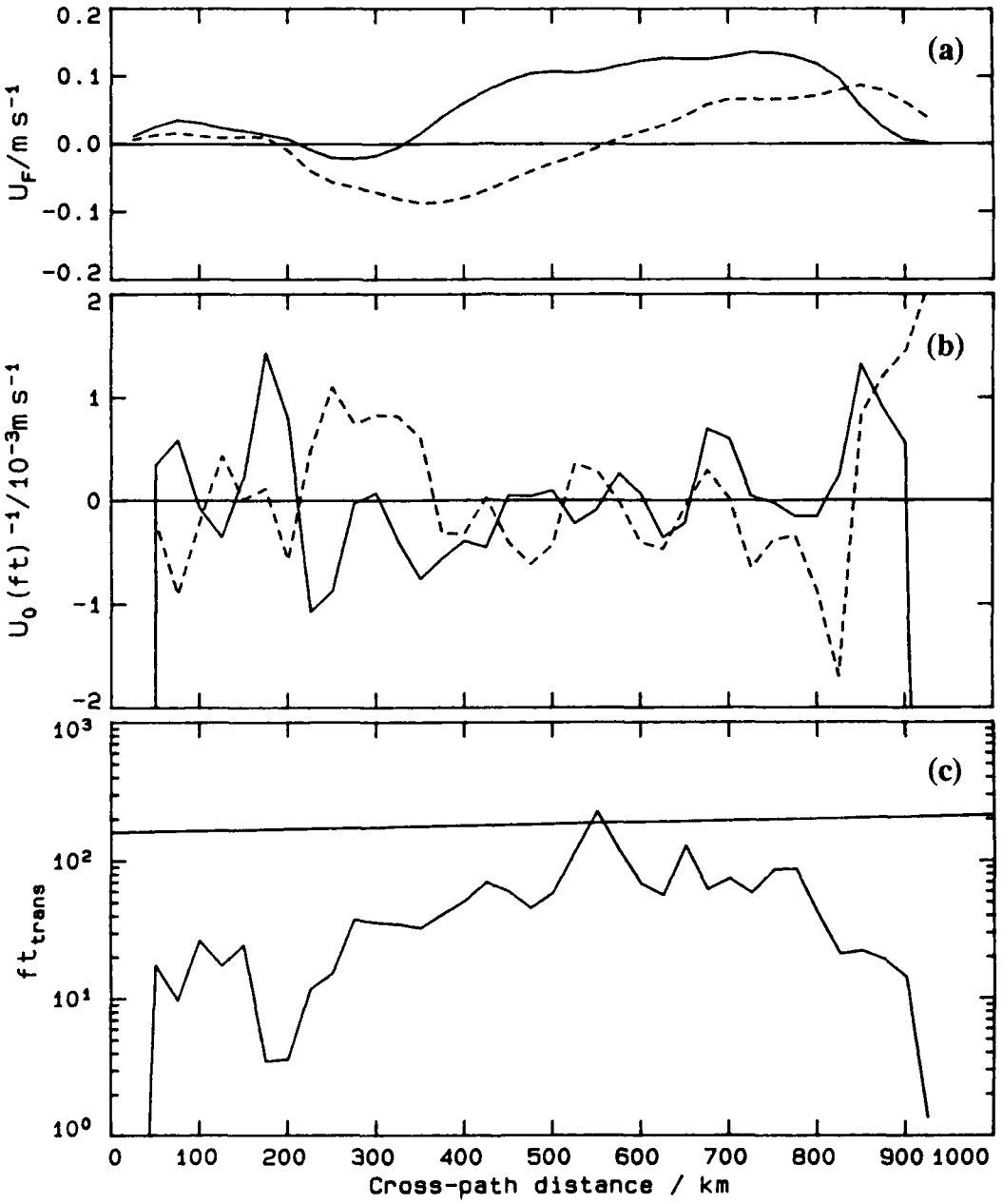

Fig. 7. Simulated quantities at $t = 0$ for Fig. 6.

On a typical weather map a cold front appears to be two-dimensional. Such a map has a resolution of a few hundred kilometers. These data suggest that significant deviations from two-dimensionality exist on the smaller scales relevant to the generation of inertial motions. If the advective speed of the frontal case is decreased to match that of the low case, so that k_A is the same, the decay rate also becomes the same. Thus the intensity of the cross-advection variations is about the same for the two cases. The frontal case appears to be no more two-dimensional than the low case.

Scatterometer Errors

The above analysis uses smoothed versions of the scatterometer data. The amplitude of the small scale wind variations that determine k_y depends on the degree of smoothing applied. Here the amount of variance removed is comparable to the official estimates of scatterometer accuracy. The scatterometer, however, is known to be less accurate in regions of precipitation and unsteady winds (Brown, 1986), exactly the conditions under which it is being used here. The errors may therefore be higher than average, although a quantification of the amount of extra error and its nature is not available. A second source of error can be seen in Fig. 6a, in which the frontal line zigzags as it passes obliquely through the lines of data. This is an aliasing effect due to a mismatch of the scatterometer footprint and its spatial resolution. Finally, the ocean is driven by wind stress not wind. Currently the ability of the scatterometer to measure wind stress is poorly known and the ad hoc scheme used here for computing stress from scatterometer wind is subject to an unknown error. Because of these errors, the work done here must be regarded as qualitative. Until the errors are better understood, it will be difficult to do quantitative work on the spatial scales of interest here using scatterometer data.

CONCLUSIONS

Wind forced near-inertial motions necessarily reflect the characteristics of the wind field with which they are forced. The limited simulations done here are encouraging in that they produce inertial currents with spatial scales and evolution rates comparable to those observed. They indicate that, in general, the two-dimensional approximation in which the advective scale C/f dominates (Kundu, 1986) is not appropriate, since the wind field itself usually contributes scales smaller than this. Realistic models of mid-latitude near-inertial motions will probably have to use realistic wind stress fields with a spatial resolution of at least C/f. Satellite scatterometry appears to be the only method of obtaining data on these scales. Considerable work on the interpretation of scatterometer measurements in terms of surface wind stress will be needed, however, before quantitative simulations of inertial motions are possible.

ACKNOWLEDGMENTS

Scatterometer data for this work was dealiased and edited by Gad Levy. Brad Bell provided the two-dimensional spline algorithms and educated me as to their meaning. Kraig Winters helped keep the perturbation analysis of the equations of motion mathematically correct. This work was supported by the Office of Naval Research under Contract N00014-84-C-0111.

REFERENCES

Bond, N.A., and R.G. Fleagle, 1985: Structure of a cold front over the ocean. Quart. J. R. Met. Soc., 111, 739-759.

Born, G.H., D.N. Held, D.B. Lame, R.G. Lipes, D.R. Montgomery, P.J. Rygh, and J.F. Scott, 1982: Seasat data utilization project report. Report D-36, Jet Propulsion Laboratory, Pasadena, California.

Brown, R.A., 1986: On satellite scatterometer capabilities in air-sea interaction. J. Geophys. Res., 91, 2221-2232.

D'Asaro, E.A., 1985a: Upper ocean temperature structure, inertial currents, and Richardson numbers observed during strong meteorological forcing. J. Phys. Oceanogr., 15, 943-962.

D'Asaro, E.A., 1985b: The energy flux from the wind to near-inertial motions in the surface mixed layer. J. Phys. Oceanogr., 15, 1043-1059.

Freilich, M.H., and D.B. Chelton, 1986: Wavenumber spectra of Pacific winds measured by the Seasat scatterometer. J. Phys. Oceanogr., 16, 741-757.

Gill, A., 1984: On the behavior of internal waves in the wakes of storms. J. Phys. Oceanogr., 14, 1129-1151.

Greatbatch, R.J., 1984: On the response of the ocean to a moving storm: Parameters and scales. J. Phys. Oceanogr., 14, 59-78.

Gregg, M.C., E.A. D'Asaro, T.J. Shay, and N. Larson, 1986: Observations of persistent mixing and near-inertial internal waves. J. Phys. Oceanogr., 16, 856-885.

Hasselman, K., 1970: Wave-driven inertial oscillations. Geophys. Fluid Dyn., 1, 463-502.

Houze, R.A. Jr., and P.V. Hobbs, 1982: Organization and structure of precipitating cloud systems. Adv. Geophys., 24, 225-315.

Kervorkian, J., and J.D. Cole, 1981: Perturbation Methods in Applied Mathematics. Springer-Verlag, New York.

Kundu, P.K., and R.E. Thompson, 1985: Inertial oscillations due to a moving front. J. Phys. Oceanogr., 15, 1076-1084.

Kundu, P.K., 1986: A two-dimensional model of inertial oscillations generated by a propagating wind field. J. Phys. Oceanogr., 16, 1399-1411.

Kunze, E., and R. Lueck, 1986: Velocity profiles in a warm-core ring. J. Phys. Oceanogr., 16, 991-995.

Large, W.G., and S. Pond, 1981: Open ocean momentum flux measurements in moderate to strong winds. J. Phys. Oceanogr., 11, 324-336.

Levy, G., and R.A. Brown, 1986: A simple, objective analysis scheme for scatterometer data. J. Geophys. Res., 91, 5153-5158.

McMurdie, L.A., 1983: Seasat scanning multichannel microwave radiometer (SMMR) observation of North Pacific cyclones. M.S. thesis, U. Washington, Seattle, WA.

McMurdie, L.A., and K.B. Katsaros, 1985: Atmospheric water distribution in a midlatitude cyclone observed by the Seasat scanning multichannel microwave radiometer. Mon. Weather Rev., 113, 584-598.

Niiler, P.P., and E.B. Kraus, 1977: One-dimensional models of the upper ocean. Modelling and Prediction of the Upper Layers of the Ocean. E.B. Kraus, Ed., Pergamon Press, 143-172.

Pollard, R.T., and R.C. Millard, 1970: Comparison between observed and simulated wind-generated oscillations. Deep-Sea Res., 17, 813-821.

Pollard, R.T., 1980: Properties of near-surface inertial oscillations. J. Phys. Oceanogr., 10, 385-398.

Price, J.F., 1981: Upper ocean response to a hurricane. J. Phys. Oceanogr., 11, 153-175.

Price, J.F., 1983: Internal wave wake of a moving storm. Part I: Scales, energy budget and observations. J. Phys. Oceanogr., 13, 949-965.

Rubenstein, D.M., 1983: Vertical dispersion of inertial waves in the upper ocean. J. Geophys. Res., 88, 4368-4380.

Wahba, G., 1984: Surface fitting with scattered noisy data on Euclidean d-space and on the sphere. Rocky Mountain Journal of Mathematics, 14, 281-298.

White, W.B., 1986: Vertical Reynolds stress divergence in the upper ocean associated with linear wind-driven, near-inertial waves of finite amplitude. J. Phys. Oceanogr., 16, 1190-1203.

SUBDUCTION

Benoit Cushman-Roisin
Department of Oceanography
The Florida State University, Tallahassee, Florida 32306-3048

ABSTRACT

Subduction, or the escape of fluid from the mixed layer, and its counterpart, entrainment of underlying stratum, are processes that couple the dynamics of both the mixed layer and the ocean interior. However, it is customary for mixed-layer dynamicists to take the state of the ocean interior for granted, while large-scale circulation theorists have a record for brushing aside the mixed layer as a mere converter of surface wind stress into vertical Ekman pumping. As the recent progress in the theory of large-scale ocean circulation has revealed the crucial role played by subduction in maintaining the permanent thermocline, and as the corresponding models become increasingly refined, the process of subduction deserves timely consideration.

The purpose of the present introductory analysis is to elucidate the kinematics and dynamics of subduction (and of its twin process, entrainment) by inductive reasoning through a series of increasingly more comprehensive models. Some likely pitfalls (e.g. the common belief that the rate of subduction is the Ekman pumping velocity) are identified, and several relevant dimensionless numbers are noted.

Particular attention is directed toward seasonal variations of the mid-latitude mixed layer, which control the intermittency, amount, density and potential vorticity of the subducted waters.

INTRODUCTION

Definition of subduction

Because subduction is such a new buzz word in physical and chemical oceanography, a definition seems prerequisite to any further discussion. Because of its generality, I propose the following definition: Subduction is the process by which mixed-layer convergence and/or retreat leave formerly turbulent fluid to become part of the underlying stratum.

Note that this definition does not make a distinction between diurnal and seasonal mixed layers, nor does it specify the underlying stratum except that it be markedly less turbulent than the mixed layer. Subduction from the diurnal wind-mixed layer during nighttime restratification can thus feed the seasonal thermocline, while

subduction induced by the retreat of the winter convective layer imparts fluid for the permanent thermocline and the large-scale circulation. Note also that no distinction is made between ventilation and subduction. In a layered model (as that of Luyten et al., 1983), ventilation is the fluid flow from the mixed layer into a layer of the stratum while subduction is the submersion of that layer under the next lighter one. But, for the continuously stratified ocean, this distinction is superfluous, and ventilation and subduction are equivalent.

Definition of subduction rate

As for many physical concepts, the same word can be used both to describe a process and to quantify it. The considerations developed later on make it natural to choose the following definition:

The subduction rate is the flux of volume of subducted fluid per unit horizontal area. It is therefore expressed in meters per second. This rate is chosen as negative if the flux is in the direction of subduction and positive if the flux is in the direction of entrainment.

Although the subduction rate connotes the idea of a vertical velocity, it is not a vertical velocity as the next considerations demonstrate.

VERTICAL VELOCITIES AND VOLUME FLUXES

The vertical excursion of the mixed-layer base, the vertical velocity of the fluid at that level, the Ekman pumping, and the subduction rate all seem to be related but are obviously not equivalent. A clarification is therefore most helpful.

As sketched on Figure 1, consider a vertically homogeneous mixed layer and, inside it, an infinitesimal fluid column of unit horizontal cross section. Since incompressibility of seawater is negligible, the mass budget of this fluid element can be stated as a volume budget. Leaving fluid comprises evaporation at the surface (Ev), lateral outflow and subduction through the mixed-layer base (Su, if Su < 0). Entering fluid includes precipitation at the surface (Pr), lateral inflow and entrainment (Su, if Su > 0). The net difference between inflows and outflows goes into storage or deepening of the mixed layer ($\partial h/\partial t$). The volume budget is therefore

$$\frac{\partial h}{\partial t} + \frac{\partial (hu)}{\partial x} + \frac{\partial (hv)}{\partial y} = Su + Pr - Ev. \qquad (1)$$

Precipitation minus evaporation is considerably less than the other fluxes (less than a meter per year versus several tens of meters per year), and the term Pr-Ev is heretofore neglected. Note that writing simply Su (and not Su multiplied by the cosine of a projecting angle) on the right of (1) required that the subduction rate be measured per unit horizontal area. This justifies the careful definition of the subduction rate in the previous section.

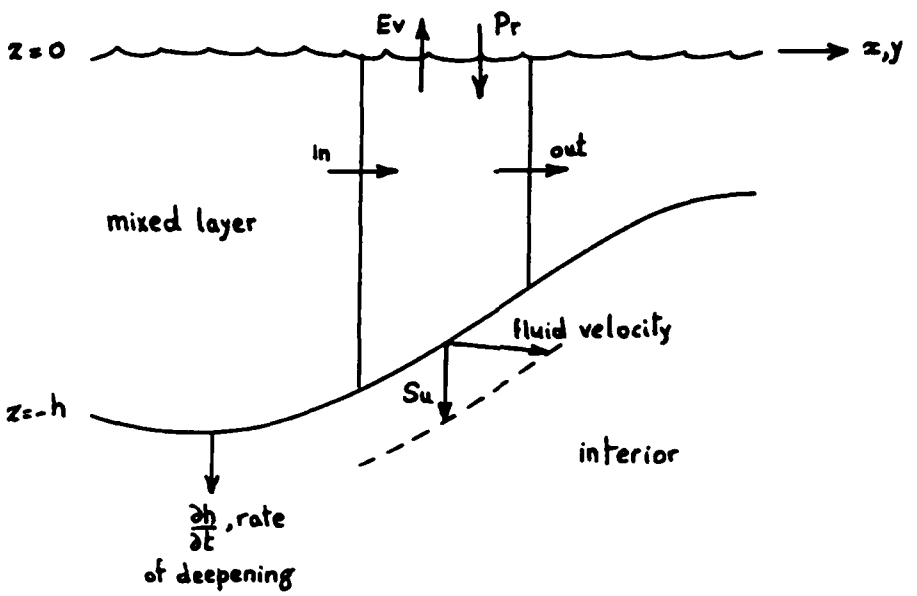

Figure 1. Sketch of the principal velocities and volume fluxes.

The vertical velocity of the fluid at the base of the mixed layer is given by

$$w = -\left[\frac{\partial h}{\partial t} + u\frac{\partial h}{\partial x} + v\frac{\partial h}{\partial y}\right] + Su. \tag{2}$$

The bracketed quantity would be the vertical velocity in the absence of subduction or entrainment (fluid flowing along the mixed-layer base, z = -h), while the last term would be the vertical velocity if the mixed-layer base were horizontal and stationary. There is thus a relation between vertical velocity (w), mixed-layer deepening ($\partial h/\partial t$) and subduction rate (Su). Combining (1) and (2), the subduction rate can be eliminated to obtain

$$w = h\left(\frac{\partial u}{\partial x} + \frac{\partial v}{\partial y}\right). \tag{3}$$

If one now makes the assumption that the horizontal velocity (u,v) in the mixed layer is only the Ekman drift ($\tau^y/\rho_0 fh$, $-\tau^x/\rho_0 fh$), the former relation (1) for Su becomes

$$Su = \frac{\partial h}{\partial t} + Ek, \tag{4}$$

where $Ek = \partial(\tau^y/\rho_0 f)/\partial x - \partial(\tau^x/\rho_0 f)/\partial y$ is the Ekman pumping. Averaging over a mixed-layer cycle (a day or a year), one finally obtains

$$\overline{Su} = \overline{Ek}, \tag{5}$$

where an overbar denotes a suitable time average. It is therefore concluded that the subduction rate is in general not the Ekman pumping, and that it is the Ekman pumping only if (i) precipitation and evaporation rates are negligible, (ii) the mixed-layer flow is very close to being the Ekman drift, and (iii) a time average is performed over the mixed-layer cycle.

Although a time average of relation (4), which is linear, is straightforward, it must be kept in mind that other quantities such as density and potential vorticity will not in general be linearly related to mixed-layer variables and, therefore, that the time averages of these quantities over a mixed-layer cycle will not be equal to the same quantities calculated from a time-averaged mixed-layer model. This is a very important problem, which motivates the careful evaluation of the time-dependent models presented in the subsequent sections.
The assumption of a mixed-layer flow dominated by Ekman dynamics is widely used in large-scale oceanography studies and thus deserves some consideration. In a low Rossby-number regime, relative acceleration and nonlinear advection can be safely neglected but a geostrophic current can be important. Let us write

$$\rho_0 f v = -\frac{\partial p}{\partial x} + \frac{\tau^x}{h}, \quad \rho_0 f u = -\frac{\partial p}{\partial y} + \frac{\tau^y}{h},$$

where $f = f_0 + \beta y$ varies with latitude and p is the mixed-layer pressure comprising the pressure in the underlying flow field (dynamic topography) and the pressure distribution resulting from an uneven mixed-layer base. The divergence terms of (1) now become

$$\frac{\partial}{\partial x}(hu) + \frac{\partial}{\partial y}(hv) = Ek + J\left(\frac{p}{\rho_0}, \frac{h}{f}\right), \tag{6}$$

where $J(a,b) = a_x b_y - a_y b_x$ is the Jacobian operator. The last term is new and can be split into two parts: the Jacobian of the pressure p with the mixed-layer depth h, which is not zero if the isolines of p do not follow those of h, and the Jacobian of the pressure p with the Coriolis factor f. Separating among these two contributions and implementing (6) in (1) to evaluate the various contributions to subduction, one finds

$$Su = \frac{\partial h}{\partial t} + Ek + \frac{1}{\rho_0 f} J(p,h) - \frac{\beta h}{\rho_0 f^2}\frac{\partial p}{\partial x}. \tag{7}$$

Physically, the four terms can be interpreted as follows: the first term represents the subduction caused by mixed-layer retreat; the second, subduction by Ekman pumping injection; the third, subduction resulting from convergence of a geostrophic flow squeezed into a shallower mixed layer; and the fourth, subduction caused by a decelerating poleward geostrophic flow on a beta plane. Orders of magnitude for these various contributions can be estimated with the following typical numbers:

variations of h ~ 50 m in 500 km and in one year,
Ek ~ 30 meters per year,
geostrophic flow ~ 1 cm/s,
$f \sim 10^{-4} s^{-1}$, $\beta \sim 2\ 10^{-11} m^{-1} s^{-1}$ at mid latitudes.

One finds, in meters per second,

$$\frac{\partial h}{\partial t} \sim 10^{-6}, \quad Ek \sim 10^{-6}, \quad \frac{1}{\rho_0 f} J(p,h) \sim 10^{-6}, \quad \frac{\beta h}{\rho_0 f^2} \frac{\partial p}{\partial x} \sim 2 \cdot 10^{-7}.$$

In conclusion, it must be recognized that geostrophic currents in the mixed layer can contribute to subduction as much as the Ekman pumping does, and that the neglect of convergence of geostrophic currents in the mixed layer is but a regrettable assumption of modelling convenience.

DEPTH-TIME MODEL

In addition to the important distinctions reviewed in the preceding sections, complexity arises because subduction is an intermittent process. Indeed, mixed layers are extremely variable in time, to the point of being classified by the length of their cycles (diurnal mixed layer and seasonal thermocline). Here, attention will be restricted to seasonal variations, for the author is concerned with the input of waters into the permanent thermocline.

A portion of the waters left behind as the mixed layer retreats (typically, from March to August) may not have penetrated sufficiently deeply by the time the mixed layer deepens again (typically, from September to February), and so may be recaptured to participate once more in the mixing process. Intermittency thus arises, for only a portion of the annual cycle is producing subduction and, moreover, only a portion of this subduction phase is not in vain. To determine the amount and type of subducted waters, it is therefore imperative to distinguish clearly between the following three phases: effective subduction (waters are subducted that will not be recaptured), temporary subduction (waters are subducted that will be recaptured), and entrainment (recapture of previously subducted waters).

To go further, it is most helpful to base our considerations on a simple example. Take the case of Stommel (1979): location 25°N-35°W in the central North Atlantic and its vicinity (the so-called Beta Triangle). There, the mixed layer has an annual cycle with a maximum depth of 100 meters that is reached around March 1. After summer restratification, the mixed layer is absent (depth = 0). At the same location, the vertical velocity, evaluated by the beta-spiral method, falls between -1.0 and $-1.5\ 10^{-6}$ m/s. The Ekman pumping is downward, and its annual average is estimated around $0.94\text{-}0.98\ 10^{-6}$ m/s. Therefore, a plausible value for the vertical velocity in the interior is 1×10^{-6} m/s or 30 meters per year, in the

downward direction. A simple model can then be devised with the mixed-layer depth following $h(t) = 50 + 50 \cos(2\pi t)$ and a parcel's trajectory in the geostrophic interior following $z(t) = z_0 - 30t$, where the depth unit is the meter, time is counted in years ($t = 0$ is March 1, $t = 1$ is March 1 one year later), and z_0 is a constant that varies from parcel to parcel depending on its depth and time of origin.

Here, the seasonal variation in the vertical velocity is neglected, and so are the lateral variations in the mixed-layer properties and interior flow. Relaxation of some of these simplifications is the object of the next two sections, and the simple depth-time model is meant only as an illustrative support for key ideas and as a first step of an inductive approach.

Figure 2 displays the relevant curves in the depth-time framework: the sine curve represents the mixed-layer depth while the sloping straight lines are various trajectories of the interior flow. One such trajectory is particular: it is the one that is tangent to the sine curve, in the vicinity of $t = 0$. Another similar trajectory is tangent in the vicinity of $t = 1$. Each trajectory corresponds to the same particular parcel, but at a one-year interval. The corresponding parcel is the last one to penetrate into the interior for that year by successfully escaping the mixed-layer deepening in late winter. The subsequent parcels will indeed be recaptured. The time t_0 (or t_0+1), where tangency occurs, is the time of year when the mixed layer ceases to recapture previously subducted waters and when effective subduction begins. For the expressions stated above, the curves are tangent at $t_0 = -0.015$ ($t_0+1 = 0.985$), that is day 359 of the year or February 22. The mixed-layer depth is then 99.8 meters, almost its maximum value. Therefore, February 22 is the time of year when active subduction starts, although the mixed layer still deepens until March 1, but at a rate slower than the downwelling rate of the interior. From February 22 until March 1, the mixed layer is no longer able to overtake descending parcels.

The parcel whose trajectory hugs the mixed-layer curve at t_0+1 has $z_0 = -70.23$ and its trajectory is $z(t) = -70.23 - 30t$. Tracing this trajectory backward brings it to the mixed-layer curve at time $t_1 = 0.166$, that is day 61 of the year or April 30. This is the time of year when that last parcel to make it successfully into the interior is subducted. After April 30, the mixed layer continues to retreat, but the parcels that it releases will be recaptured the following fall or winter. Therefore, April 30 is the time of year when effective subduction ends and temporary subduction begins. The period of active subduction thus lasts over two months of the year, from February 22 to April 30, that is late winter and early spring. Subduction cannot be said to be as intermittent as the shutter of a camera.

Finally, the time t_2, when the difference between $|z(t)|$ of our particular parcel and $h(t)$ is the largest, is the time of year when temporary subduction ends and when recapture of previously subducted waters begins. The separation between the two curves represents the amount of water that has been subducted in vain. Numbers provide: $t_2 = 0.515$, day 188 or September 4, and $|z(t_2)| - h(t_2) = 85.5$ meters.

Overall, through the year, 30 meters of water have been effectively subducted from February 22 to April 30, and 85.5 meters have been subducted from April 30 to September 4 but only to be remixed during the period from September 4 to February 22. The efficiency of subduction can be evaluated both in time and in volume:

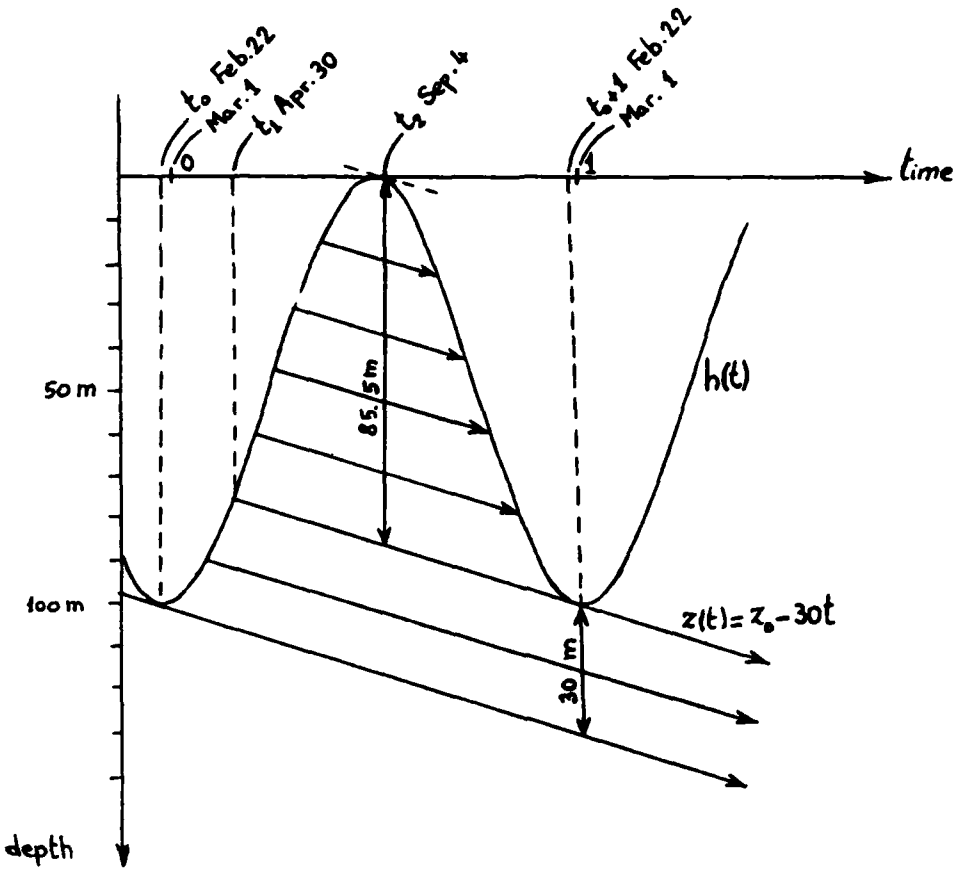

Figure 2. Schematic diagram of subduction according to a simple depth–time model

$$\text{Efficiency in time} = \frac{\text{duration of effective subduction}}{\text{duration of subduction}} = \frac{t_1-t_0}{t_2-t_0} = 34\%, \tag{8}$$

$$\text{Efficiency in volume} = \frac{\text{volume effectively subducted per year}}{\text{total volume subducted per year}}$$

$$= \frac{30\text{m}}{30\text{m}+85.5\text{m}} = 26\% \tag{9}$$

In conclusion, subduction is not as efficient as an engineer would expect from one of his/her machines, but is not as stroboscopic as one oceanographer could have anticipated.

Various cases can now be explored. Figure 3 depicts the subduction scenarios in three cases: weak downward flow, large downward flow, and upward flow. In the first case, subduction is very brief and inefficient; in the second case, it occurs throughout

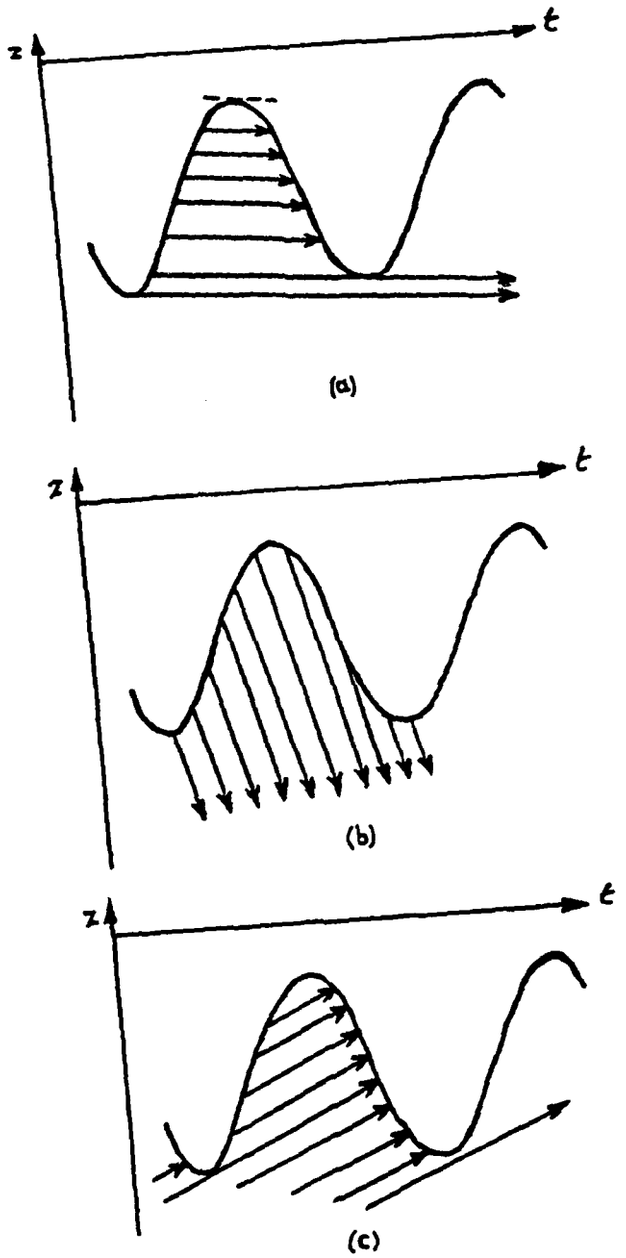

Figure 3. Various subduction regimes. (a) Interior vertical velocity downward and small; efficiency of subduction is low. (b) Interior vertical velocity downward and large; effective subduction occurs continuously. (c) Interior vertical velocity upward and not too large; no effective subduction occurs, but temporary subduction takes place.

the seasonal cycle; and in the third case, although there is no effective subduction, there remains the possibility of temporary subduction. From this range of possibilities, two important factors emerge: (i) the sign of the vertical velocity in the interior (remember, it is not necessarily the Ekman-pumping rate!), and (ii) the ratio of vertical velocity to maximum rate of deepening. The sign controls the existence of effective subduction (positive velocity means no effective subduction), while the ratio controls the efficiency of subduction (ratio less than unity means only partly efficient subduction, ratio greater than unity means 100% efficiency). From the orders of magnitude provided in the previous sections, one notices that the ratio will in general be in the vicinity of unity.

LATITUDE–DEPTH–TIME MODEL

Although illustrative, the above model has serious shortcomings. Perhaps chief of all is its prescription for the density profile in the interior. Indeed, the density varies in the mixed layer with the seasons so that the annual batch of subducted waters is somewhat stratified, but the same layering repeats year after year, and denser waters will top lighter waters. Therefore, under the above scenario, vertical mixing must occur, and the net effect is the formation of a homogeneous water column in the interior. This certainly is not the case for the ocean, and the model must be extended.

Vertical stratification can be explained (Luyten et al., 1983) by the higher latitudes of origin of the deeper waters. In the Subtropical Gyre where the Ekman pumping is downward, the meridional velocity is equatorward. Therefore, the deeper the water, the longer its sinking travel, the higher the latitude of its point of subduction, and, as the density in the mixed layer increases with latitude, the greater its density.

In consequence, if one wishes to elucidate the density profile, and hence the potential–vorticity input in the interior of the ocean, one must include latitudinal variations and a meridional velocity. Mathematically, the variables now become the mixed–layer depth h(y,t), the meridional velocity v(y,z,t), and the vertical velocity w(y,z,t), where y is the poleward coordinate. In the open ocean where Sverdrup dynamics are a fair approximation, the vorticity balance requires $\beta v = f\partial w/\partial z$ (f is the Coriolis parameter and ß its meridional gradient). The trajectory of a parcel in the geostrophic interior must now be constructed from the following equations:

$$\frac{dy}{dt} = v(y,z,t), \frac{dz}{dt} = Ek - v(y,-h,t)\frac{\partial h}{\partial y} - \frac{\beta}{f}\int_{z}^{-h} v(y,z',t)dz', \tag{10}$$

with the following initial conditions $y = y_0$, $z = -h(y_0,t_0)$ at $t = t_0$. [In (10), the vertical velocity at the base of the mixed layer was obtained from (2) and (4).] As one can immediately notice, the problem has become quite complex.

Again, we now choose a simple example to illustrate a few basic concepts. Let us take a mixed layer whose depth varies in time but not in space

$$h(t) = 50 + 30\cos(2\pi t), \tag{11}$$

and meridional-velocity and Ekman-pumping distributions that vary with latitude but not time

$$v(y) = y \quad , \quad Ek(y) = 4.2\ y. \tag{12}$$

Here, time is measured in years (t = 0 is March 1), y in degrees of latitude (y = 0 is 45°N), h in meters, v in degrees of latitude per year, and w in meters per year. [In this unit system, f = 3200 + 67y per year.] This example is thought to mimic the northern part of the Subtropical Gyre (from 30°N to 45°N, $-15<y<0$) where the Ekman pumping is downward and the meridional velocity southward, and the southern part of the Subpolar Gyre (from 45°N to 60°N, $0<y<15$) where the Ekman pumping is upward and the meridional velocity northward.

From expressions (4), (11) and (12), one can immediately determine the rate of subduction:

$$Su = \frac{\partial h}{\partial t} + Ek = -60\pi sin(2\pi t) + 4.2y. \tag{13}$$

Units are meters per year. In a latitude-time plot (Figure 4), the curve Su = 0 is the truncated sine curve $y = 45 \sin(2\pi t)$. Subduction ($Su<0$) occurs mostly, but not exclusively, during mixed-layer retreat ($0<t<0.5$), even in the northern part of the model where the Ekman pumping is directed upward. This is because the mixed layer retreats faster than the upwelling rate (see Figure 3c).

Interior trajectories are obtained from

$$y = y_0 \exp(t - t_0)$$

where y_0 and t_0 are the latitude and time of subduction, and from the numerical integration of

$$\frac{dz}{dt} = \left[4.2 + \frac{67(z + 50 + 30cos(2\pi t))}{3200 + 67y}\right] y, \tag{14a}$$

$$z(t_0) = -50 - 30cos(2\pi t_0). \tag{14b}$$

The complete set of all trajectories is doubly infinite (at a given time, both y and z can be varied), and cannot be plotted without clutter. Only particular trajectories will thus be constructed, those which delimit bodies of deep, temporarily subducted, and effectively subducted waters. We know from the previous model that these particular trajectories are those which graze the mixed-layer base.

In the southern half of the domain (from 30°N to 45°N), a marginal trajectory, that of a last parcel barely escaping recapture by the deepening mixed layer, is one that is tangent to the mixed-layer base at the time when the latter is near its deepest point

AD-A188 148 DYNAMICS OF THE OCEANIC SURFACE MIXED LAYER PROCEEDINGS 1/4
OF 'AHA HULIKO'A (U) HAWAII INST OF GEOPHYSICS
HONOLULU P MULLER ET AL 1987 N000014-87-G-0091

UNCLASSIFIED F/G 8/3 NL

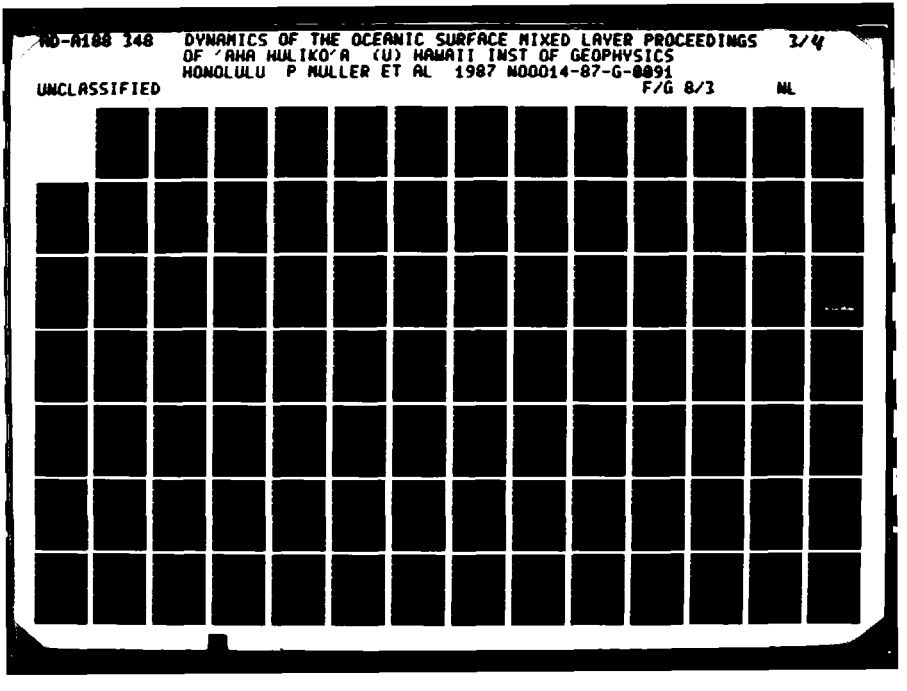

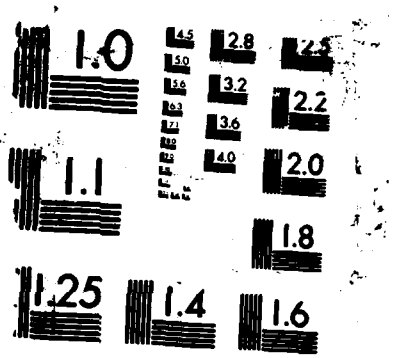

MICROCOPY RESOLUTION TEST CHART

(see previous model). Marginal trajectories thus pass at latitudes and times where subduction vanishes (Su=0) passing from positive (end of recapture) to negative (start of subduction). With that branch of the Su=0 curve of Figure 4 as a set of 'initial' conditions, trajectories were integrated backward in time until their previous intersection with the mixed-layer base. These trajectories are plotted on the latitude-time graph of Figure 5, where the intersections with the mixed-layer base are marked with stars. The set of these marginal trajectories defines a curved surface in the three-dimensional (y,z,t) space, lying at all times beneath the mixed-layer base. Sandwiched between that surface and the mixed-layer base are temporarily subducted waters, while under this surface flow the effectively subducted waters.

In the northern half of the domain (from 45°N to 60°N), a marginal trajectory, that of a last parcel rising from the deep and barely missing capture by the mixed layer that year, is one that is tangent to the mixed-layer base at the time when the latter is starting to retreat (see Figure 3c). Marginal trajectories of this kind thus pass at latitudes and times where subduction vanishes (Su=0) passing from positive (end of recapture) to negative (start of subduction). With that branch of Su=0 curve of

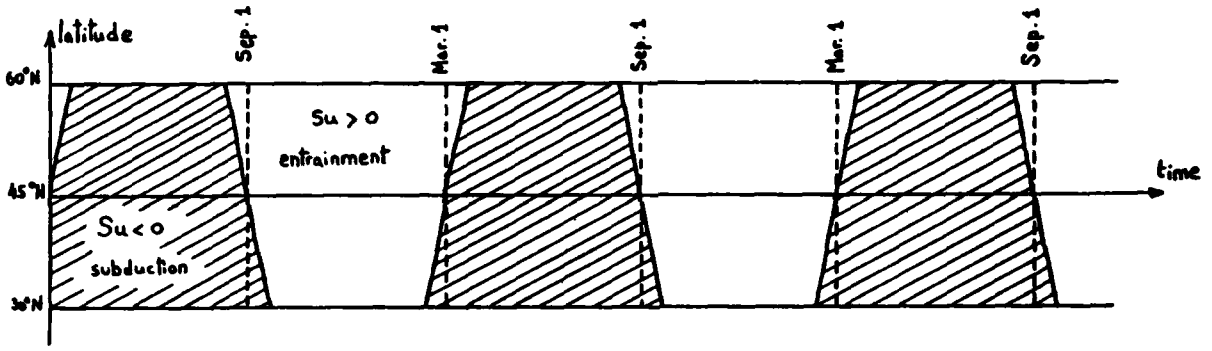

Figure 4. Latitude-time graph showing locations and times when subduction and entrainment occur.

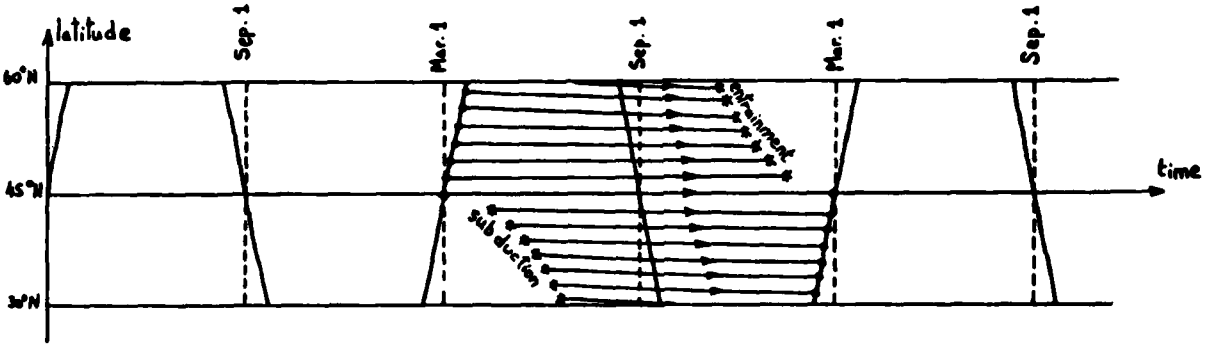

Figure 5. Latitude-time projection of trajectories that graze at one time the base of the mixed layer. Grazing points are marked with heavy dots, while previous or future intersections with the mixed-layer base are marked with stars.

Figure 4 as a set of initial conditions, trajectories were integrated forward in time until their intersection with the mixed-layer base the following winter. These trajectories are also plotted on the latitude-time graph of Figure 5, and, again, the stars mark the intersections with the mixed-layer base. The new curved surface in the three-dimensional (y,z,t) space now separates the lower waters rising from the deep, which will be captured the following winter, from the upper, temporarily subducted waters.

Figure 6 recapitulates the action taking place at the base of the mixed layer. Altogether, four processes occur: permanent subduction, temporary subduction, entrainment of previously subducted waters, and entrainment of deep, upwelling waters. Only up to three process can take place at a given location.
The above analysis sheds light on the data required for separate models of the mixed layer and interior circulation. A mixed-layer model requires data on the deep waters and their rate of upwelling; an interior-circulation model requires information on the variability of the mixed-layer base and on the characteristics of the effectively subducted waters.

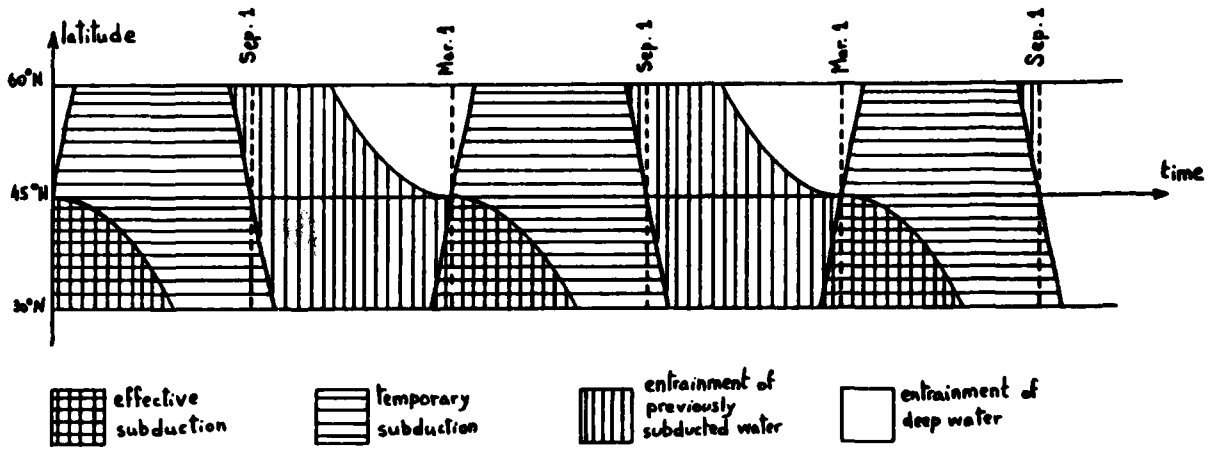

Figure 6. Recapitulation of the various subduction and entrainment regimes in the latitude-depth-time model.

The above analysis also brings up a critical parameter. If the meridional velocity is on the order of V, the meridional excursion of a parcel in a year is on the order of VT (T=one year). But, over that meridional span, the Ekman pumping changes by an amount on the order of VTdEk/dy. If that change is about as large as the Ekman pumping itself, knowing where the parcel originates really matters. Therefore, a critical dimensionless number is the ratio

$$\frac{VT}{Ek}\frac{dEk}{dy}, \tag{15}$$

where V is the magnitude of the interior meridional velocity, Ek is the magnitude of the Ekman pumping, and T is one year. If this ratio is on the order one, latitudinal variations are crucial. For the large-scale circulation numbers quoted earlier, it is found that the ratio is about one-third. Hence, the scenario effective subduction/temporary subduction/entrainment is sensitive to meridional gradients. In other words, determining what does the mixed layer entrain and what does the interior circulation receive requires proper treatment of meridional variations.

LONGITUDE-LATITUDE-DEPTH-TIME MODEL

In the actual ocean, zonal variations can also be important. With the addition of a fourth variable, graphical exploration becomes useless, but no new process is anticipated, the situation being only more intricate in space and time. A new critical ratio, however, now appears. It is

$$\frac{UT}{Ek}\frac{dEk}{dx}, \tag{16}$$

modelled after the previous one, where U is the magnitude of the zonal interior flow and x is the zonal coordinate. If this number is on the order of unity, zonal variations ought to be retained. Such can be the case in the northeast Atlantic Ocean, where the zero-Ekman-pumping line tilts appreciably from southwest to northeast.

DENSITY AND POTENTIAL-VORTICITY

A major question in the theory of large-scale circulation and of the main thermocline is the determination of the density and potential vorticity which are injected into the geostrophic interior. This question is now considered.

At a given location in the interior, the density is subject to fluctuations due to the intermittency of subduction and the seasonal variability of the subducted waters. But, if a requirement is met between interior flow, mixed-layer depth and mixed-layer density, the interior density will not vary in time. Our objective is now to establish this requirement and to determine how close actual ocean conditions come to satisfying it. For that purpose, let us assume that the interior flow (u,v,w) is steady and spatially uniform and that the mixed-layer characteristics are given in terms of its depth, $h(x,y,t)$, and density, $\rho(x,y,t)$.

An interior trajectory obeys $x = x_0+u(t-t_0)$, $y = y_0+v(t-t_0)$, $z = -h(x_0,y_0,t_0) + w(t-t_0)$ where (x_0,y_0) is the location where the parcel was subducted, and t_0 is the time when subduction took place. The density at the point (x,y,z) in the interior at any time, t, is equal to the mixed-layer density at subduction time, $\rho(x_0,y_0,t_0)$, because the interior flow conserves density. For this density to be constant in time, one must have $\partial\rho(x_0,y_0,t_0)/\partial t = 0$ or

$$\frac{\partial\rho}{\partial x}\frac{\partial x_0}{\partial t} + \frac{\partial\rho}{\partial y}\frac{\partial y_0}{\partial t} + \frac{\partial\rho}{\partial t}\frac{\partial t_0}{\partial t} = 0. \tag{17}$$

As time is varied at the fixed location (x,y,z), the coordinates of the trajectory satisfy

$$0 = \frac{\partial x_0}{\partial t} + u - u\frac{\partial t_0}{\partial t},\ 0 = \frac{\partial y_0}{\partial t} + v - v\frac{\partial t_0}{\partial t}, \tag{18a,b}$$

$$0 = -\frac{\partial h}{\partial x}\frac{\partial x_0}{\partial t} - \frac{\partial h}{\partial y}\frac{\partial y_0}{\partial t} - \frac{\partial h}{\partial t}\frac{\partial t_0}{\partial t} + w - w\frac{\partial t_0}{\partial t}. \tag{18c}$$

Elimination of $\partial x_0/\partial t$ and $\partial y_0/\partial t$ with (18a) and (18b) transforms (17) and (18c) into

$$\left(\frac{\partial \rho}{\partial t} + u\frac{\partial \rho}{\partial x} + v\frac{\partial \rho}{\partial y}\right)\frac{\partial t_0}{\partial t} = u\frac{\partial \rho}{\partial x} + v\frac{\partial \rho}{\partial y},$$

$$\left(\frac{\partial h}{\partial t} + u\frac{\partial h}{\partial x} + v\frac{\partial h}{\partial y} + w\right)\frac{\partial t_0}{\partial t} = u\frac{\partial h}{\partial x} + v\frac{\partial h}{\partial y} + w.$$

These last two equations for $\partial t_0/\partial t$ are compatible only if

$$\left(u\frac{\partial h}{\partial x} + v\frac{\partial h}{\partial y} + w\right)\frac{\partial \rho}{\partial t} = \left(u\frac{\partial \rho}{\partial x} + v\frac{\partial \rho}{\partial y}\right)\frac{\partial h}{\partial t}. \tag{19}$$

This is the requirement between the interior flow (u,v,w) and the mixed-layer characteristics (h,ρ). If we take the liberty to approximate the ocean conditions to understand better what (19) holds, we can neglect the zonal variations in front of the meridional variations and note that the density varies meridionally substantially more than the mixed-layer depth. Requirement (19) then becomes a balance between its two prominent terms:

$$w\frac{\partial \rho}{\partial t} \simeq v\frac{\partial \rho}{\partial y}\frac{\partial h}{\partial t}. \tag{20}$$

In a northern-hemisphere Subtropical Gyre where the interior flow is southward and downward (v and w negative), effective subduction takes place during mixed-layer retreat ($\partial h/\partial t$ negative), which is also the time of year when the mixed-layer temperature rises ($\partial \rho/\partial t$ negative). Balance (20) requires $\partial \rho/\partial y$ positive as a necessary condition for a constant density in the interior. This is the case in the ocean, where density increases northward. Physically, the situation is as follows: the waters passing at a given location and depth in the interior, have been subducted at different times; the more recent waters have been deposited somewhat north of that location when the mixed layer was deep and winter-cold; the older waters must come from further north where the mixed layer is colder but have been subducted when the mixed layer was not as deep. If the signs of the quantities in (20) favor a balance, it still remains to check the magnitudes of the various terms. For $w \simeq 10^{-6}$ m/s

(30m/year), $v \simeq 10^{-2}$m/s, $\partial\rho/\partial t$ = 0.6 sigma units in half a year, $\partial\rho/\partial y$ = 0.6 sigma units in 10° latitude, and $\partial h/\partial t$ = 100 meters in half a year, the ratio of the left-hand side of (20) over the right-hand side is approximately unity. Therefore, it turns out that the Subtropical Gyre in the ocean is naturally satisfying the requirement for a steady interior.

The next question is how to establish the potential-vorticity input function for the interior flow in terms of the mixed-layer variable. In a large-scale flow, the potential vorticity is simply PV = $-f\partial\rho_I/\partial z$, where ρ_I is the interior density. To evaluate the vertical gradient of density in the interior, let us first take a first parcel subducted at location (x,y) and time t; it was released at depth z = -h(x,y,t) and with a density $\rho(x,y,t)$. During the interval of time Δt immediately following subduction, it sinks to depth $z+\Delta z = -h(x,y,t) + w\Delta t$ while it migrates laterally to the location ($x+\Delta x = x+u\Delta t$, $y+\Delta y = y+v\Delta\tau$). At that location and at that time, the mixed layer has depth $h(x+\Delta x,y+\Delta y,t+\Delta t)$ and released a new parcel of density $\rho(x+\Delta x,y+\Delta y,t+\Delta t)$, just above our previous parcel. If the time interval, Δt, is infinitesimal, the vertical density gradient can be evaluated as follows

$$\frac{\partial \rho_I}{\partial z} = \frac{\rho(x+\Delta x, y+\Delta y, t+\Delta t) - \rho(x,y,t)}{-h(x+\Delta x, y+\Delta y, t+\Delta t) + h(x,y,t) - w\Delta t}$$

$$= -\frac{\rho_t \Delta t + \rho_x \Delta x + \rho_y \Delta y}{h_t \Delta t + h_x \Delta x + h_y \Delta y + w\Delta t} \tag{21}$$

and the potential vorticity is found to be

$$PV = f\frac{\rho_t + u\rho_x + v\rho_y}{h_t + uh_x + vh_y + w} = \frac{f}{Su}(\rho_t + u\rho_x + v\rho_y). \tag{22}$$

The reader is reminded that, in expression (22), h and ρ are the mixed-layer variables while u,v and w are the velocity components in the interior. Finally, if requirement (19) for a steady interior is met, then expression (22) simplifies to

$$PV = f\frac{\rho_t}{h_t}. \tag{23}$$

CONCLUSIONS

Although the above considerations have not provided an exhaustive treatment of subduction, several key questions were clarified. First, the common belief that the rate of subduction equals the rate of Ekman pumping was proven not to hold true, even after a suitable average over the mixed-layer cycle. The differences between rate of mixed-layer deepening, Ekman pumping, fluid vertical velocity, and rate of subduction have been clarified in the text.

Second, the intermittency of seasonal subduction was investigated with a hierarchy of models. It was found that subduction can be effective (permanent) or only temporary, and that effective subduction can take place over several months, as the mixed layer retreats. Critical dimensionless numbers were identified: (i) the ratio of interior vertical velocity over the maximum deepening rate, which controls the efficiency of subduction and hence the characteristics of the subducted waters, (ii) the ratio of meridional displacement during one year over the meridional distance over which the Ekman pumping changes appreciably, and (iii) the analogous ratio in the zonal direction. These last two numbers indicate the importance of lateral variations in subduction.

Third, it was found that the Subtropical-Gyre regions of the oceans, where subduction controls the permanent thermocline, naturally lead to a constant density field thanks to a competition by which seasonal intermittency of subduction negates variability in the subducted waters. Finally, a formula was constructed to determine the potential-vorticity injection into the interior in terms of the interior velocity flow at the base of the mixed layer and the mixed-layer depth and density.

ACKNOWLEDGEMENTS

The author is grateful to Dr. Peter Muller for the opportunity to discuss the above work with the participants of the fourth 'Aha Huliko'a Hawaiian Winter Workshop. Support for this research was provided by the Office of Naval Research.

REFERENCES

Luyten, J.R., J. Pedlosky, and H. Stommel, 1983: The ventilated thermocline. J. Phys. Oceanogr., 13, 292-309.

Stommel, H., 1979: Determination of water mass properties of water pumped down from the Ekman layer to the geostrophic flow below. Proc. Natl. Acad. Sci. USA, 76, 3051-3055.

WIND FORCING AND OBSERVED OCEANIC WAVENUMBER SPECTRA

Charles C. Eriksen

School of Oceanography, WB-10
University of Washington, Seattle, WA 98195

ABSTRACT

If internal waves are forced by wind stress applied as a body force (uniform vertical gradient of stress) in a surface layer, their spectrum has the vertical wavenumber shape of the Garrett-Munk internal wave spectrum. Bandwidth and high wavenumber shape are functions of the layer thickness and shape, respectively. Conversely, if the Garrett-Munk wavenumber shape is determined by wind forced waves at near-inertial frequencies, then the observed shape implies that the vertical gradient of stress from the surface is nearly uniform and cuts off sharply at a depth comparable to observed seasonal thermocline depths.

INTRODUCTION

Models of wind driven ocean circulation commonly use one of two methods to prescribe how wind stress drives the ocean. The more common method is to prescribe surface stress and assume that small scale processes can be parameterized by a given (normally uniform) eddy viscosity. The stress then vanishes exponentially with depth with a scale small compared to the ocean depth. Vertical velocities at the base of this frictional layer are independent of the form of friction, arise simply from any divergence pattern of transports within the layer, and drive the deeper circulation. This is the familiar construct of Ekman theory. The other choice, more common for equatorial models where the Ekman decay scale becomes singularly large, is to assume that wind stress acts as a body force distributed over some upper layer. As in the Ekman theory, stress is imagined to vanish beneath some (normally shallow) depth. Rather than specify a vertical velocity at this depth, the (normally uniform) body force is projected onto the available free modes of ocean oscillation (one barotropic plus an infinite number of baroclinic modes). This is the construct of Lighthill (1969) applied to the problem of generating a low-latitude western boundary current (the Somali current). As pointed out by Knox and Anderson (1985), the Lighthill approach is merely an alternate parameterization of small scale frictional processes to that chosen six decades earlier by Ekman. The key aspect shared by both models is that wind stress is applied completely to a near-surface layer of the ocean.

The details of how wind stress is applied to the upper ocean have implications for the character of response to time dependent forcing. For wind systems which move relatively rapidly compared to wave speeds of free baroclinic modes, oceanic response is largely at near-inertial frequencies. The amplitude of each mode excited depends on how the mode projects onto the forcing. It turns out that the vertical wavenumber shape of forced internal waves depends not on the spectrum of forcing but on how the vertical distribution of stress projects onto the modes.

The vertical wavenumber shape of observed internal wave spectra tends to -2 at high wavenumbers, as observed by many profile measurements of horizontal current components and/or temperature. At low wavenumber, the spectrum has not been measured directly but has been inferred from coherence measurements at different separations. The kinematic model fit of Garrett and Munk (GM 81) chooses a wavenumber shape $(n^2 + n_*^2)^{-1}$ where n is vertical mode number and n_* is a measure of wavenumber bandwidth (Munk, 1981). The transition vertical mode (or equivalent vertical wavenumber) scale n_* has been inferred from coherences to be 3. The GM model assumes that wavenumber spectral shape is independent of frequency, a notion which is challenged by upper ocean measurements (Pinkel, 1985). The profiles upon which the GM wavenumber shape is based are dominated by contributions to the joint frequency-wavenumber spectrum near the inertial frequency. This fact has been exploited to infer near-inertial fluxes from sequences of profiles rather coarsely spaced in time (see D'Asaro and Perkins, 1984, and others cited therein).

Explanations of the observed internal wave spectrum are incomplete. Rather complex theories of wave interaction, scattering, and turbulence in stratified media have been invoked to explain the GM spectrum (Müller et al., 1986). The wave interaction models find the GM shape to be in equilibrium but do not explain the shape of the most energetic part of the spectrum. "The transfers within the energetic low-frequency, low-wavenumber region are weak and not dominated by any particular process (McComas and Müller, 1981a)". They do not explain, either, the total energy level or the wavenumber bandwidth n_* (McComas and Müller, 1981b; Müller et al., 1986). An alternative model will be used here to explain the wavenumber shape.

The internal wave wavenumber shape at near-inertial frequencies can be a consequence of forcing. We adopt the view that the near-inertial part of the internal wave spectrum is dominated by response to wind forcing, consisting of a number of overlapping wakes to traveling stress patterns. Near-inertial waves can be generated efficiently by sharp changes in wind stress, as demonstrated by D'Asaro (1985) and others. Atmospheric wind systems often take the form of fronts which travel at speeds greater than the free wave speeds of all but near-inertial internal modes. The internal wave wake behind a particular front may last for several days during which time other fronts may pass a given site. Energy is continually being added to the ocean by the wind stress jump across each

front, but because the source translates, the energy density at a fixed site behind the front is invariant. Forcing by traveling wind systems predisposes the near-inertial part of the oceanic internal wave spectrum to have a particular vertical wavenumber shape.

INTERNAL WAVE GENERATION BY WIND STRESS

The linearized perturbation equations for a stratified f-plane resting ocean of uniform depth D can be written, using conventional notation, as:

$$u_t - fv = -p_x + \tau^x(y,y,t)Z(z) \tag{1a}$$

$$v_t + fu = -p_y + \tau^y(x,y,t)Z(z) \tag{1b}$$

$$N^2 w = -p_{zt} \tag{1c}$$

$$u_x + v_y + w_z = 0 \tag{1d}$$

following McCreary (1985) where wind stress τ is given at the surface and its vertical gradient is specified by Z(z). The form of Z(z) is crucial to the vertical wavenumber spectrum of forced wave response. For completeness, we specify that the vertical integral of Z(z) over the total depth D be unity. If $G_n'(z)$ is the vertical structure function for horizontal current components u and v and reduced pressure p and $G_n(z)$ that for vertical velocity w, then the equations (1) reduce when projected on these modes to:

$$u_{nt} - fv_n + c_n p_{nx} = \tau_n^x \tag{2a}$$

$$v_{nt} + fu_n + c_n p_{ny} = \tau_n^y \tag{2b}$$

$$u_{nx} + v_{ny} + p_{nt}/c_n = 0 \tag{2c}$$

where n is the vertical mode number corresponding to eigenvalues c_n of the vertical structure equation

$$G_n''(z) + \frac{N^2(z)}{c_n^2} G_n(z) = 0 \tag{3}$$

These modes are the barotropic (n=0) and baroclinic ($\geq$1) free modes of the flat-bottom ocean considered. The equations (2) express the components of velocity and pressure associated with each mode n. Forcing takes the form

$$\tau_n = \frac{\tau \int_{-D}^{0} Z(z) G_n'(z)\,dz}{\int_{-D}^{0} G_n'^2(z)\,dz} \qquad (4)$$

where τ_n is called the coupling coefficient linking wind stress τ (= τ^x or τ^y) to the horizontal structure equations for a particular vertical mode. Without loss of generality, the vertical modes $G_n'(z)$ can be normalized so that their mean square value averaged vertically is unity (so that the denominator in (4) is D).

The common choice for distributing stress in a surface layer of thickness h is to prescribe $Z(z) = h^{-1}$. If this surface layer is identified with the mixed layer depth (or is even shallower than the mixed layer), the equation (3) becomes

$$G_n''(z) = 0 \quad \text{for} \quad -h < z \leq 0 \qquad (5)$$

since N(z) = 0 for (at least) the layer in which stress is distributed. Typically h is identified with the mixed layer depth. Then $G_n'(z)$ = constant = $G_n'(0)$ over the interval $-h < z \leq 0$. This implies the coupling coefficients τ_n are:

$$\tau_n = \frac{\tau}{D} G_n'(0) \qquad (6)$$

Notice that the depth of the layer depth h over which stress is distributed does not appear explicitly. This is because the vertical structure functions $G_n'(z)$ are constant over this depth range.

Some simple examples of different distributions Z(z) are illustrative. For convenience, consider an ocean of uniform stratifiction N without a mixed surface layer. The functions $G_n'(z) = \sqrt{2}\cos(n\pi z/D)$ satisfy the normalization chosen above. The coupling coefficients take the form of a discrete cosine transform given by

$$\tau_n = \frac{\tau\sqrt{2}}{D} \int_{-D}^{0} Z(z) \cos(n\pi z/D)\,dz \qquad (7)$$

Now if stress is concentrated as a delta function at the surface $Z(z) = \delta(0)$, then τ_n is independent of n. That is, it has a white

spectrum. If, however, stress is distributed uniformly over depth h as in the example of the previous paragraph, then τ_n is proportional to $\mathrm{sinc}(n\pi h/D)$ where $\mathrm{sinc}(x)$ is the interpolating function $\sin(\pi x)/\pi x$. Finally, if stress is distributed as a ramp $Z(z) = 2(z/h+1)/h$ within the layer h and vanishes outside, then the coupling coefficients decay more steeply with vertical mode number n ($\tau_n \alpha \mathrm{sinc}^2(n\pi h/D)$). As these examples show, the distribution of stress gradient Z(z) determines the functional dependence of the coupling coefficients τ_n on mode number n. The layer thickness h relative to the total depth D determines the wavenumber bandwidth upon which forcing projects.

The form of Z(z) for real oceanic situations is uncertain and is even time and location dependent, since storms and heating modify mixed layer depth. Instead of a cosine transform, the projection of Z(z) onto the vertical modes of the vertical structure equation for non-uniform stratification determines the relative excitation of motions of different scales. The constant N examples do provide some intuition: sharp transitions in Z(z) imply energetic high wavenumber portions of the response spectrum.

To go from the coupling coefficients τ_n to the internal wave response spectrum requires solution of equations (2). These have been solved for various idealized geometries (open ocean, coastal equatorial) and forcings (stationary, traveling, irrotational, vortical, etc.). The general properties are that the most efficiently excited waves are those which are most closely matched by the wind in structure and scale; that is, nearly resonant. An illustrative case is the idealization of a moving atmospheric front to a moving line source of stress divergence. Kundu and Thomson (1985) demonstrate that the solution is composed of the available vertical modes, each with its own horizontal structure, traveling at the speed of the front. Waves whose minimum phase speed c_n exceeds the speed of the front (typically the barotropic mode) are excited as evanescent waves. Those with minimum phase speeds c_n slower than the frontal speed are excited as standing oscillations moving with the front. The most strongly excited waves are those modes for which c_n is near the translation speed U and the coupling coefficient is high. From their solutions, the average energy per unity horizontal area of each mode can be calculated as:

$$E_n = \frac{\rho_o}{2} \tau_n^2 \frac{D}{f^2(1 - c_n^2/U^2)} = \frac{\rho}{2} \left(\frac{G_n'(0)\tau}{D}\right)^2 \frac{D}{f^2(1 - c_n^2/U^2)} \qquad (8)$$

where τ is the stress jump across the front in the direction of its travel. (This calculation assumes Z(z) is a constant and non-zero only over a depth at most as deep as the surface mixed layer.) The two dependences of vertical mode number n are in the coupling coefficient

(e.g., $G_n'(0)^2$) and resonance with the forcing $(1 - c_n^2/U^2)^{-1}$. For a fast moving front ($U >> c_n$, $n \geq 1$, where $c_1 \sim 3$ m/s), the baroclinic modes are far from resonance so that the dependence on n of the internal wave spectrum enters only through the factors $G_n'(0)^2$. Examples of this behavior are given below.

A stratification appropriate to comparing forced vertical wavenumber spectra with the GM spectrum is the profile used by Garrett and Munk to calculate model vertical structure functions. It is a rough approximation to the stratification found at many oceanic locations: an exponential thermocline capped by a mixed layer. Garrett and Munk use:

$$N(z) = 0 \qquad -h < z < 0 \tag{9}$$

$$N_o e^{(z+h)/b} \qquad -D \leq z < -h$$

where N_o = 3 cph and b = 1300 m. For illustration, we use D = 5 km and h = 50, 100, or 200 m. The vertical structure functions $G_n'(z)$ for this profile are analytic (Bessel functions) but can be calculated numerically for ease. Completeness implies that

$$\frac{h}{D} \sum_{n=0}^{\infty} G_n'(0)^2 = 1 \tag{10}$$

so that $hD^{-1}G_n'(0)^2$ is the relative contribution each mode makes to the total spectrum of response (neglecting any resonances, i.e., $U>>c_1>c_2>c_3...$). That is, $hD^{-1}G_n'(0)^2$ gives the vertical wavenumber spectral shape of internal waves forced by fast-moving wind systems. Plots of this quantity are given in Figure 1 for three different choices of h/D, as labeled. Solid circles are drawn to highlight the values for n=1 to 10. As expected for the case of $Z(z) = h^{-1}$ for $-h < z < 0$ and zero otherwise, the forced spectra all asymptote to n^{-2} decay for high enough n. Also as expected, the transition mode number is inversely proportional to h/D.

The heavy curve labeled GM81 drawn in Figure 1 is $(n^2+n_*^2)^{-1}$ with n_*=3 normalized by its sum from n=1 to 100 (instead of infinity). It is, of course, the Garrett-Munk vertical wavenumber shape inferred from observed internal wave statistics. The curves $hD^{-1}G_n'(0)^2$ are remarkably similar to GM81. In particular, the curves labeled h/d = 0.02 and 0.04 are within

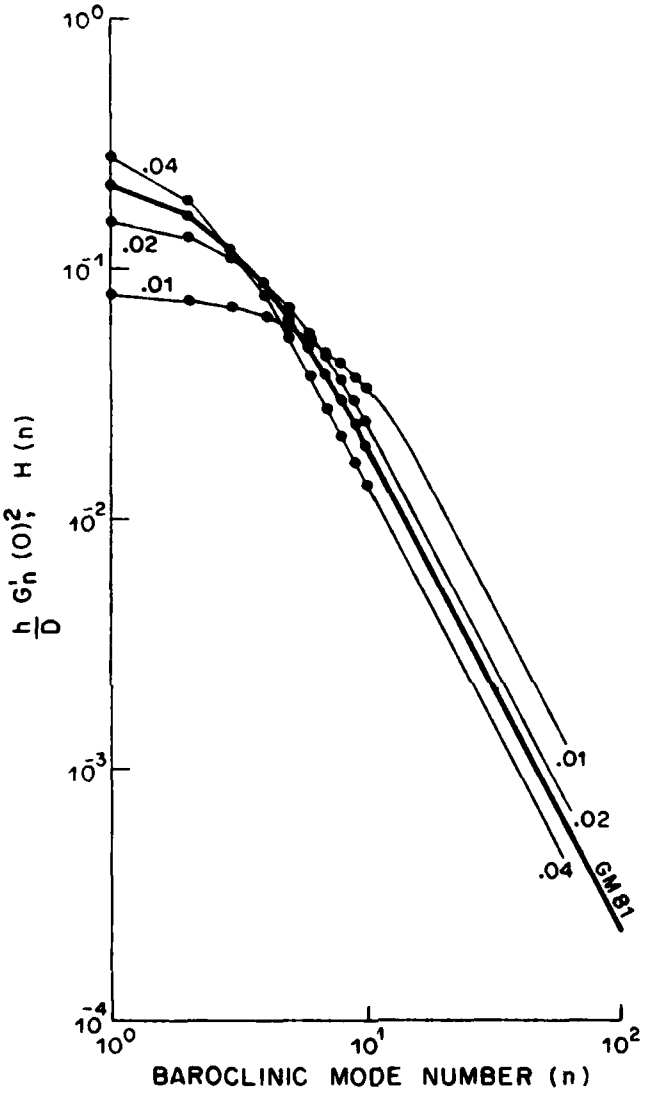

Fig. 1. Relative energy of baroclinic modes excited by wind stress applied as a uniform body force in a layer of depth h to an ocean of depth D with an exponential N(z) profile. Light curves marked 0.01, 0.02, and 0.04 correspond to h/D. Heavy curve is the Garrett-Munk vertical wavenumber shape (GM81). All curves are normalized to have the same (unit) energy. Evaluations for the first ten modes are marked with circles.

25% of GM81 for all but the lowest baroclinic mode (where the differences are less than 40%). These ratios imply depths of frictional influence of 100 and 200 m in a 5000 m deep ocean, respectively.

DISCUSSION

The close similarity of the model forced spectra and GM81 suggests that the oceanic internal wave spectrum at near-inertial frequencies is predisposed to its shape by wind-forced waves. The GM81 wavenumber shape is based on wavenumber spectra and coherence as a function of separation rather than on direct measurements of the joint frequency-wavenumber spectrum of internal waves. As such, it is dominated by contributions near the inertial frequency, since this part of the joint frequency-wavenumber spectrum is most energetic. The interaction theories which find GM81 to be in equilibrium do not explain the spectral shape in the neighborhood of this most energetic part of the spectrum (the lowest octave or two in frequency and wavenumbers not larger than the bandwidth). Forcing by traveling wind systems may provide an explanation for this part of the spectrum.

The spectral levels obtained from the wind-forced model are reasonable, given jumps in stress τ across model fronts of 1-5 dynes/cm^2 and frontal translation speeds U ~ O(10 m/s) where deep ocean low baroclinic mode speeds are O(1 m/s). Curiously, the energy in any particular mode is independent of the depth h over which stress is absorbed by the ocean (see equation (8)), but the total wave energy is proportional to $\tau^2 h^{-1} f^{-2}$ (which can be seen by summing (8) together with (10)). More complicated wind systems will yield different constants of proportionality, but the basic features of the model results must be preserved. These are that 1) energy density of a particular baroclininc mode should be independent of the stress layer depth, 2) total energy should be inversely proportional to stress layer depth, 3) bandwidth should be a monotonically decreasing function of stress layer depth, and 4) both energy density of a particular mode and the total energy should be proportional to stress squared (roughly wind speed to the fourth power!).

If the forced wave explanation of the near-inertial, low wavenumber portion of the internal wave spectrum is correct, the form of the spectrum has profound implications for the distribution of stress gradient from wind in the upper ocean. As the examples of the previous section demonstrate, concentrating the stress gradient as a delta function at the surface or as a linear ramp down from the surface gives vertical wavenumber spectral shapes which disagree strongly with those observed. A constant stress gradient confined to a shallow surface layer gives a spectral shape which agrees with the observed shape. Justification for this constant gradient stress layer model has been lacking in the past. If the forced wave model is correct, it implies that stress vertical divergence truly is nearly uniform throughout a shallow layer and cuts off sharply. As long as the transition zone between the region of nearly

uniform stress divergence (of depth h) and the deep interior with vanishing stress divergence is small (compared to h), wind forcing will excite waves whose spectrum asymptote to a -2 slope in vertical wavenumber.

REFERENCES

D'Asaro, E.A., 1985: The energy flux from the wind to near-inertial motions in the surface mixed layer. J. Phys. Oceanogr., 15, 1043-1059.

D'Asaro, E.A. and H. Perkins, 1984: A near-inertial wave spectrum for the Sargasso Sea in late summer. J. Phys. Oceanogr., 14, 489-505.

Knox, R.A. and D.L.T. Anderson, 1985: Recent advances in the study of the low-latitude ocean circulation. Progr. Oceanogr., 14, 259-318.

Kundu, P.K. and R.E. Thomson, 1985: Inertial oscillations due to a moving front. J. Phys. Oceanogr., 15, 1076-1084.

Lighthill, M.J., 1969: Dynamic response of the Indian Ocean to the onset of the Southwest Monsoon. Phil. Trans. R. Soc. London, A265, 45-93.

McComas, C.H. and P. Müller, 1981a: Time scales of resonant interaction among oceanic internal waves. J. Phys. Oceanogr., 11. 139-147.

McComas, C.H. and P. Müller, 1981b: The dynamic balance of internal waves. J. Phys. Oceanogr., 11, 970-986.

McCreary, J.P. Jr., 1985: Modeling equatorial ocean circulation. Ann. Rev., Fluid Mech., 17, 359-409.

Müller, P., G. Holloway, F. Henyey and N. Pomphrey, 1986: Nonlinear interactions among internal gravity waves. Rev. Geophys., 24, 493-536.

Munk, W.H., 1981: A survey of internal waves and small-scale processes. In Evolution of Physical Oceanography, edited by B.A. Warren and C. Wunsch, pp. 264-291, MIT Press, Cambridge, MA.

Pinkel, R., 1985: A wavenumber-frequency spectrum of upper ocean shear. J. Phys. Oceanogr., 15, 1453-1469.

ENERGY AND MOMENTUM FLUXES THROUGH THE SEA SURFACE

Gerbrand Komen

Royal Netherlands Meteorological Institute KNMI, De Bilt, The Netherlands

ABSTRACT

We use recent progress in our understanding of the energy and momentum balance in wind driven surface waves, to give a new estimate for the energy and momentum flux to and from the waves.

INTRODUCTION

It is generally assumed that to a given wind speed and stratification, there corresponds a definite turbulent transport of momentum and mechanical energy downward through the lowest part of the atmospheric boundary layer over sea. A large fraction of these fluxes (nearly 100% in fully rough flow) is used to grow the surface waves. However, this energy can not be retained by the waves, and a sizable fraction is passed on to the underlying ocean, quasi-instantaneously. The processes by which this dissipation takes place are insufficiently understood, but whitecapping seems to be a dominant mechanism.

The momentum flux in particular, tends to be dominated by what is happening at high frequencies, i.e. with the short waves. Therefore, in the past, people have tried to calculate these fluxes on the basis of empirical estimates of spectral levels at high frequency (see e.g. Huang, 1986) or by other means (Mitsuyasu, 1985 and Donelan, 1979). Recently, our understanding of the energy and momentum balance in the energy containing range of the spectrum has increased greatly (Komen et al, 1984; Hasselmann et al, 1987). Therefore, we are now in a better position to give flux estimates over the full spectral range.

After a short review of the recent progress we will estimate fluxes throughout the wave spectrum: at high frequencies from a simple "tail"-parametrization, but at lower frequencies from the physical balance, between sources and sinks in the energy and momentum budget of the surface waves.

Denoting momentum fluxes by τ and energy fluxes by Φ, we can formally write

$$\tau_a = \tau_{aw} + \tau_{ao} \,, \quad \tau_o = \tau_{wo} + \tau_{ao} \tag{1a}$$

$$\Phi_a = \Phi_{aw} + \Phi_{ao} \,, \quad \Phi_o = \Phi_{wo} + \Phi_{ao} \tag{1b}$$

Here τ_a is the momentum flux downward through the atmospheric boundary layer; τ_{aw} is the momentum flux going into waves, whereas τ_{ao} is the difference, creating such things as the drift current at the surface; τ_o is the total momentum flux into the ocean, τ_{wo} from the waves and τ_{ao} directly from the atmosphere. The same conventions apply to Φ. One should note that there is an important difference between energy and momentum fluxes. The momentum flux in the lower part of the atmospheric boundary layer is thought of as being constant over some height range, forces being absent. The energy flux is affected by viscous dissipation at every height. In this note we will concentrate on τ_a, τ_{aw}, τ_{wo}, Φ_{aw}, Φ_{wo}. As mentioned above we believe that

$$\tau_{ao} \ll \tau_a \ , \quad \Phi_{ao} \ll \Phi_a \tag{2}$$

in realistic situations, but we have not actually checked this in any way. More detailed investigations of the physical microscale aspects have recently been made by Chalikov (1986) and Hsu et al. (1982).

THE ENERGY BALANCE IN OCEAN WAVES

There is strong interest in ocean wave prediction, and the equation describing the evolution of ocean waves has been known for over 25 years now (Hasselmann, 1960). Yet, only recently have wave researchers been able to actually compute the wave spectrum from first principles, starting from this equation.

We denote the variance wavenumber spectrum by $F(\underline{k}\ ;\ \underline{x}\ ,\ t)$ with $\underline{k}$ the wave vector, and $\underline{x}$ and t place and time. It is normalized as

$$\int_{-\infty}^{+\infty} F(\underline{k})\, d\underline{k} = \int_0^{\infty} k dk \int_0^{2\pi} d\theta\, F(k, \theta) = \langle \eta^2 \rangle \tag{3}$$

with η the surface elevation. It satisfies the following equation

$$\frac{\partial F}{\partial t} + \underline{\nabla} c_g F = S = S_{in} + S_{nl} + S_{ds} \tag{4}$$

This says that when you consider the spectral level for a given frequency and direction, it does not change if you move with the appropriate group velocity $\underline{c_g}$ except for the effect of the source terms S. They represent energy gain due to wind (S_{in}), weakly nonlinear resonant interactions among different wave components (S_{nl}) and energy loss due to dissipation (S_{ds}).

S_{in} has been estimated theoretically by several authors. The idea is that turbulent shear flow with a free internal boundary is unstable. The first successful calculation was done by Miles (1957). Later his methods have been refined. In addition, growth rates have been carefully measured (Snyder et al, 1981).

The weakly nonlinear resonant interactions have been calculated from first principles by Hasselmann (1961). This same author has also given an expression for the dissipation source term S_{ds}, based on an estimate of the whitecapping contribution (Hasselmann, 1974).

Even with all of these tools available, it was not so easy to make a wave prediction model based on the integration of (4). In fact, all of the models participating in the so-called Sea Wave Modelling Project (SWAMP, 1985) had to make some additional simplifying assumptions about the spectral shape and/or the evolution of spectral parameters. This led to contradictory results, especially in complex non-stationary situations with rapidly turning winds and wind-sea/swell transitions.

To overcome these problems an international group of wave researchers decided to jointly develop a wave model based on direct integration of eq. (4). This group, the WAM (= Wave Modelling) group has made considerable progress. A first version of the model has been run successfully on the CRAY-XMP/48 of the European Centre for Medium Range Weather Forecasts in Reading, U.K. It has been installed in both a regional and a global version, and it has been applied in both hind- and forecasting modes. (Komen, 1986). A full account of the model is in preparation (Hasselmann et al, 1987).

For the present application it is important to give the source terms of the WAM model. The wind input is taken as

$$S_{in} = \gamma_{in} F$$

$$\frac{\gamma_{in}}{\omega} = 0.25\, \varepsilon \max \left(28 \frac{u_*}{c} \cos\phi - 1,\ 0\right) \qquad (5)$$

Here $\omega = 2\pi = (gk)^{\frac{1}{2}}$ for gravity waves, $g = 9.8\ m/s^2$ being gravitational acceleration, ε is the ratio of the density of air and seawater, u_* is the friction velocity in the air, c is the phase velocity ($c = \omega/k$) and ϕ is the angle between wind and waves. The nonlinear transfer, which conserves overall energy and momentum, but moves it from one wavenumber to another, is calculated numerically in the so-called discrete interaction approximation, (Hasselmann et al, 1985). The dissipation, finally, is taken as

$$S_{ds} = -\gamma_{ds} F$$

$$\frac{\gamma_{ds}}{\omega} = 1.59\, (\omega/\bar{\omega})\, \hat{\alpha}^2 \qquad (6)$$

$$\hat{\alpha} = \frac{\langle \eta^2 \rangle \bar{\omega}^4}{g^2}$$

which is quasi-linear in the spectrum, $\langle \eta^2 \rangle$ and the mean angular frequency $\bar{\omega}$ expressing global properties of the spectrum.

FLUXES VERSUS SOURCE TERMS

Ocean waves carry energy and momentum, which can be expressed in terms of the variance spectrum

$$E = \rho_w \int_{-\infty}^{+\infty} \frac{\omega^2}{k} F(\underline{k})\, d\underline{k} \tag{7a}$$

$$\underline{P} = \rho_w \int_{-\infty}^{+\infty} \frac{\omega \underline{k}}{k} F(\underline{k})\, d\underline{k} \tag{7b}$$

Here E is energy, $\underline{P}$ momentum and ρ_w the density of water. For ω we now read the more general expression $\omega = (gk + Tk^3)^{\frac{1}{2}}$, with T surface tension, which is also valid at very high frequencies when capillary effects become important. For the longer waves ($k^2 << g/T$) this reduces to the deep water gravity wave dispersion relation, for which the factor $\rho\omega^2/k$ reduces to the familiar ρg, translating variance spectrum into energy spectrum. An easy way of memorizing (7) is by observing that the energy spectrum can be written as ωA, with A the action density, and the momentum spectrum similarly as $\underline{k}A$.

Anyway, from (4) and (7) it follows that the fluxes from the atmosphere to the waves and from the waves to the ocean can be written as

$$\underline{\tau}_{aw} = \rho_w \int d\underline{k}\ \frac{\omega \underline{k}}{k} S_{in} \tag{8a}$$

$$\underline{\tau}_{wo} = -\rho_w \int d\underline{k}\ \frac{\omega \underline{k}}{k} S_{ds} \tag{8b}$$

$$\Phi_{aw} = \rho_w \int d\underline{k}\ \frac{\omega^2}{k} S_{in} \tag{8c}$$

$$\Phi_{wo} = -\rho_w \int d\underline{k}\ \frac{\omega^2}{k} S_{ds} \tag{8d}$$

It is important to realize that the integrals extend over all wave numbers. Therefore, we will now first investigate the high wavenumber behaviour of the integrands.

THE SHORT WAVE CONTRIBUTION

Crucial for an estimate of the convergence of the integrals (8) is the short wave behaviour of the spectral density. There has been a lot of discussion as to whether this was f^{-4} or f^{-5}. Before joining this discussion one should always clearly state what frequency range one is referring too. Originally, Phillips (1958) considered wave spectral levels between say 3 times the peak frequency and 1 Hz. The JONSWAP tail-fit was made between 1.3 and 2 times the peak frequency. In his early paper Phillips proposed an f^{-5} tail, on the presumption that the limiting spectral level is determined by hydrodynamic processes alone. On dimensional grounds one then obtains for the frequency-directional variance spectrum:

$$G(f,\theta) = \frac{\alpha_p g^2}{(2\pi)^4 f^5} I(\theta) \tag{9}$$

with the directional distribution $I(\theta)$ still to be specified. In k-space this corresponds with a wavenumber spectrum ($Gdf = F\,kdk$)

$$F(k,\theta) = \frac{\alpha_P}{2k^4} I(\theta) \tag{10}$$

Later Toba (1973) suggested that the saturation level was not independent from the friction velocity and that in fact

$$G(f,\theta) = \frac{\alpha_T g u_*}{(2\pi)^4 f^4} I(\theta) \tag{11}$$

should be more appropriate. This idea was endorsed by Phillips (1985). Experimental data favour both. At not too high frequency Birch and Ewing (1986) observed f^{-4}; at higher frequencies they found f^{-5}. A crude estimate of the transition frequency/wavenumber was given by Peter Janssen (private communication), who obtained

$$k_{tr} = \frac{g}{u_*^2} \left(\frac{\alpha_P}{\alpha_T}\right)^2 \tag{12}$$

With typical values for the α's ($\alpha_P = 0.01$, $\alpha_T = 0.1$) the corresponding transition frequency is within the dynamic range of the WAM model. Therefore, in the following, we will consider WAM model spectra up to the transition frequency. Above, we will assume the f^{-5} tail.

We will now proceed by estimating the high frequency contribution to the momentum-flux from the atmosphere to the waves. Before doing this, however, we should point out that the wind input source term, eq. 5, is not applicable in the high frequency range. In fact, Plant (1982) presented a compilation of wave growth measurements, which turned out to be described by a quadratic u_*/c dependence,

$$\frac{\gamma_{in}}{\omega} = A \left(\frac{u_*}{c}\right)^2 \cos\phi \quad , \quad A = 0.04 \pm 0.02 \tag{13}$$

This fit is valid for growing waves and extends towards the highest frequencies. At lower frequencies it has to be merged with (5). So we split τ_{aw} in a high and a low frequency contribution

$$\tau_{aw} = \tau_{aw}^l + \tau_{aw}^h \tag{14}$$

τ_{aw}^l will be considered below. Here we compute τ_{aw}^h as

$$\tau_{aw}^h = \rho_w \int_{k_{tr}}^{\infty} \frac{\omega k}{k} A\omega \left(\frac{u_*}{c}\right)^2 \cos\phi \times \frac{\alpha_P}{2k^4} I(\theta) k\,dk\,d\theta \tag{15}$$

Taking the X-axis in the wind direction one finds $\underline{\tau} = (\tau, o)$ with

$$\tau_{aw}^{h} = \tfrac{1}{2} A \rho_w \alpha_p u_*^2 \int_{k_{tr}}^{\infty} \frac{dk}{k} \int d\theta \; I(\theta)\cos^2\theta \tag{16}$$

The k-integral is divergent. Fortunately, the theory considered so far is incomplete at very high frequencies. There, viscosity damps the waves. Therefore, we introduce as an ultra-violet cutoff the wavenumber at which viscosity begins to dominate. This is at

$$\omega_v = \frac{Au_*^2}{4\nu_w} \tag{17}$$

with ν_w the viscosity of water. Not much is known about the angular distribution. To be specific we will assume a $\cos^2\theta$ distribution ($I(\theta) = (2/\pi)\cos^2\theta$). This then yields

$$\tau_{aw}^{h} = \frac{3}{8} \rho_w \alpha_p \, Au_*^2 \ln (k_v/k_{tr}) \tag{18}$$

The pseudo-divergence, resulting in a $\ln k_v$ factor stresses the importance of the short wave contribution.

The energy can be dealt within a similar way. Performing similar manipulations one obtains

$$\Phi_{aw}^{h} = \frac{4}{3\pi} \rho_w \alpha_p A u_*^2 \int_{k_{tr}}^{k_v} \frac{\omega}{k^2} \, dk$$

$$\omega = (gk + Tk^3)^{\frac{1}{2}} \tag{19}$$

This integral would also diverge for $k_v = \infty$, but here the divergence only appears in the ultra capillary limit. In the gravity range the integrand behaves as $k^{-3/2}$. Eq. (19) was evaluated by splitting the integration range in 3 parts: $(k_{tr}, k_o/3)$, $(k_o/3, 3k_o)$ and $(3k_o, k_v)$ where $k_o = (g/T)^{\frac{1}{2}}$ is the wavenumber at which gravity and surface tension effects are equally important. In the first interval the waves are approximated as pure gravity, in the middle range the integral was computed numerically, and in the last interval the capillary limit was taken. Using $k_{tr} < k_o$ I obtained

$$\Phi_{aw}^{h} = \frac{4}{3\pi} \rho_w \alpha_p \, Au_*^2 \left\{ \frac{2g}{\omega_{tr}} + 2.41 \, (\omega_o/k_o) + 2\, T^{\frac{1}{2}} \left[k_v^{\frac{1}{2}} - (3k_o)^{\frac{1}{2}} \right] \right\} \tag{20}$$

Because of the smallness of T ($7.2\ 10^{-5}$ $m^3\ s^{-2}$) the last term is rather small. We will illustrate this by considering a friction velocity of 0.85 m/s. This

value roughly corresponds to a windspeed of 20 m/s. It will be used as a reference in all numerical estimates to follow. We find

$$k_{tr} = 0.14 \quad , \quad k_o = 369 \quad \text{and} \quad k_v = 8360 \quad m^{-1}$$

and

$$\tau_{aw}^h = 1.19 \text{ Pa} \tag{21a}$$

$$\phi_{aw}^h = 0.12 \, (16.7 + 0.56 + 0.98)$$

$$= 2.2 \text{ W/m}^2 \tag{21b}$$

It is interesting to note that τ_{aw}^h exceeds $\tau_a = \rho_a u_*^2$ by 40%. We will discuss this result below, after the estimate of the low frequency contribution. So far we have only considered fluxes from the atmosphere to the waves. To estimate the fluxes from the waves to the ocean we would have to use (8b) and (8d) for high frequencies. Unfortunately, S_{ds} is not known there. Therefore, we will use the fact that at high frequencies there is a balance between the source terms

$$- \int_{k_{tr}}^{k_v} \frac{\omega^2}{k} S_{ds} \, d\underline{k} = \int_{k_{tr}}^{k_v} \frac{\omega^2}{k} (S_{in} + S_{nl}) \, d\underline{k} =$$

$$= \int_{k_{tr}}^{k_v} \frac{\omega^2}{k} S_{in} d\underline{k} - \int_{o}^{k_{tr}} \frac{\omega^2}{k} S_{nl} \, d\underline{k} \tag{22}$$

The second line follows because the nonlinear transfer conserves energy. A similar expression holds for the momentum flux. Below we will give a numerical estimate of (22).

LONG WAVE CONTRIBUTION

We have calculated long wave contributions by using results of the WAM model. This is a relatively straightforward calculation, because, once you run the model, you have spectra and source terms every time step in every grid point. It should be emphasized that in general the fluxes depend on local wind speed as well as on details of the spectral shape, which are determined by the geometry of the basin and by the time history of the windfield. A full analysis was outside the scope of this note. We have only analyzed fetch limited growth, in which a constant windfield blows off-shore, perpendicular to a straight coast, and in which the stationary response is considered. The results are given in table 1 for two different fetches, one in which the waves are still actively growing (X = 50 km, H_s = 4 m) and one in which saturation is being approached (X = 500 km, H_s = 7.5 m)

Table 1 Modelled fluxes of energy Φ and momentum τ into (aw) and from (wo) the energy containing waves ($k<k_{tr}$, eq. (12)) at two different fetches. Φ_{nl} and τ_{nl} denote the nonlinear transfer from long waves to short waves as modelled with the discrete interaction approximation. ($u_* = 0.85$ m/s).

X(km)	Φ^l_{aw}	Φ^l_{wo}	Φ_{nl}	τ^l_{aw}	τ^l_{wo}	τ_{nl}
	(W/m^2)				(Pa)	
50	1.5	0.6	0.1	0.13	0.04	0.02
500	2.4	1.7	0.7	0.19	0.10	0.09

At the shorter fetch the energy and momentum excess makes the waves grow. In the steady state the excess is advected away, making the waves higher at longer fetch. At the longer fetch there is a balance between energy gain and energy loss.

DISCUSSION

First of all let us combine the results of the previous two sections. We then obtain the following picture

Table 2. Modelled energy fluxes (W/m^2) to (aw) and from (wo) the waves, l denotes long waves, h indicates the short wave contribution ($u_* = 0.85$ m/s).

X(km)	Φ^l_{aw}	Φ^h_{aw}	Φ_{aw}	Φ^l_{wo}	Φ^h_{wo}	Φ_{wo}
50	1.5	2.2	3.7	0.6	2.3	2.9
500	2.4	2.2	4.6	1.7	2.9	4.6

Table 3. Modelled momentum fluxes (Pa). The meaning of sub and superscripts is as in table 2.

X(km)	τ^l_{aw}	τ^h_{aw}	τ_{aw}	τ^l_{wo}	τ^h_{wo}	τ_{wo}
50	0.13	1.19	1.32	0.04	1.21	1.25
500	0.19	1.19	1.38	0.10	1.28	1.38

In the tables Φ^h_{wo} and τ^h_{wo} have been calculated using (22).

A few remarks can be made:

(i) Both energy and momentum flux to and from the waves increase with fetch.

This is because the level in the tail was fixed, and for larger fetch more wave components take part in the transfer. The dissipation increases more strongly then the input, a necessary condition for reaching equilibrium.

(ii) The momentum fluxes are dominated by high frequency contributions, much more than the energy fluxes.

(iii) There is something "wrong" with the magnitude of τ_{aw}. For example at X = 500 km we have

$$\tau_{aw} = 1.7 \times \tau_a$$

implying that the waves would receive more momentum then the boundary layer provides. We distinguish two possibilities

a. Our estimate is correct. This is possible when a deceleration extracts momentum from the lowest part of the atmospheric boundary layer. Although τ_a is defined as the momentum flux at the lower boundary of the boundary layer, it will be measured in practice at, say, 10 m height. Over land the flux is then constant down to the surface. Over waves this might be different. In fact it could be that over sea the flux to short waves is suppressed as has been suggested by Janssen (1982) (see also Chalikov, 1986).

b. Our estimate is wrong. One should note that the high frequency contribution alone already exceeds τ_a, so this is suspect. One should realize that our knowledge of source terms and spectra at high frequencies in the field is still fragmentary. Plant's constant is A = 0.04 ± 0.02, which implies a 50% error in our estimate of τ_a. Also the spectral level was taken as in (10) with α_p = 0.01, which also is only true to a certain accuracy. One of the weakest assumptions was the $\cos^2\theta$ angular distribution at high frequency. There are indications, also in the WAM model, that this might be considerably flatter. (An explanation of this is perhaps found in the behavior of the nonlinear transfer at high frequencies). This could reduce our estimate by a factor of 2 or 3.

CONCLUSION

Although our understanding of the energy balance in wind driven ocean waves has improved greatly, our ability for estimating energy and momentum fluxes to and from the waves is still limited. For the energy flux from waves generated by a wind of about 20 m/s ($u_* = 0.85$ m/s) we typically find a few W/m^2. This is large compared to the fluxes currently studied inside the mixed layer, so one wonders what happens to this energy. Part will go into mean motion, an other part will dissipate, but the rest will certainly penetrate as turbulence. How this exactly happens is a challenge for mixed layer modelers.

The momentum flux through the energy containing waves is relatively small. When we estimated the total flux we made a number of assumptions about source

terms and spectral shapes at high frequencies. These require further confirmation. Our answer came out slightly larger than what would have been considered acceptable. The discrepancy can be easily explained for instance by a flat angular distribution; it could also hint at something we don't understand about the lowest meter or so of the atmospheric boundary layer over sea.

Acknowledgement: I would like to thank Peter Janssen for discussions and ideas. The WAM Project was supported by NATO grant 523/85.

REFERENCES

Birch, K.G., and J.A. Ewing, 1986: Observations of wind waves on a reservoir. IOS-report no. 234. 37 p.

Chalikov, D.V., 1986: Numerical simulation of the boundary layer above waves. Bound.-Layer Meteor. 34, 63-98.

Donelan, M., 1979: On the fraction of wind momentum retained by waves. Marine forecasting, Elsevier Oceanographic Series, 25, 141-160.

Hasselmann, K., 1960: Grundgleichungen der Seegangsvorhersage. Schiffstechnik, 7, 191-195.

Hasselmann, K., 1961: On the nonlinear energy transfer in a gravity-wave spectrum. J. Fluid Mech. 12, 481-500.

Hasselmann, K., 1974: On the spectral dissipation of ocean waves due to whitecapping, Bound.-Layer Meteor. 6, 107-127.

Hasselmann, S., K. Hasselmann, J.H. Allender and T.P. Barnett, 1985: Computations and parameterizations of the nonlinear energy transfer in a gravity-wave spectrum. Part II. Parameterizations of the nonlinear transfer for application in wave models. J. Phys. Oceanogr. 15, 1378-1391.

Hasselmann, S., K. Hasselmann, P.A.E.M. Janssen, G.J. Komen, L. Bertotti, A. Guillaume, V.C. Cardone, J.A. Greenwood, M. Reistad, J.A. Ewing, 1987: The WAM-model- a third generation ocean wave prediction model. In preparation.

Hsu, C.T., H.W. Wu, E.Y. Hsu and R.L. Street, 1982: Momentum and energy transfer in wind generation of waves. J. Phys. Oceanogr. 12, 929-951.

Huang, N.E., 1986: An estimate of the influence of breaking waves on the dynamics of the upper ocean, Wave Dynamics and Radio Probing of the Ocean Surface, Phillips and Hasselmann, eds. Plenum, 295-313.

Janssen, P.A.E.M., 1982: Quasilinear approximation for the spectrum of wind-generated water waves. J. Fluid Mech. 117, 493-506.

Komen, G.J., S. Hasselmann and K. Hasselmann, 1984: On the existence of a fully developed wind-sea spectrum. J. Phys. Oceanogr. 14, 1271-1285.

Miles, J.W., 1957: On the generation of surface waves by shear flow. J. Fluid Mech. 3, 185-204.

Mitsuyasu, H., 1985: A note on the momentum transfer from wind to waves. J. Geophys. Res. 90, 3343-3345.

Phillips, O.M., 1958: The equilibrium range in a spectrum of wind generated ocean waves. J. Fluid Mech. 4, 426-434.

Phillips, O.M., 1985: Spectral and statistical properties of the equilibrium range in wind-generated gravity waves. J. Fluid Mech. 156, 505-531.

Plant, W.J., 1982: A relationship between wind stress and wave slope. J. Geophys. Res. 87, 1961-1967.

Snyder, R.L., F.W. Dobson, J.A. Elliot and R.B. Long, 1981: Array measurements of atmospheric pressure fluctuations above surface gravity waves. J. Fluid Mech. 102, 1-59.

SWAMP group: J.H. Allender, T.P. Barnett, L. Bertotti, J. Bruinsma, V.J. Cardone, L. Cavaleri, J. Ephraums, B. Golding, A. Greenwood, J. Guddal, H. Günther, K. Hasselmann, S. Hasselmann, P. Joseph, S. Kawai, G.J. Komen, L. Lawson, H. Linné, R.B. Long, M. Lybanon, E. Maeland, W. Rosenthal, Y. Toba, T. Uji and W. de Voogt, 1985: Sea wave modelling project (SWAMP). An intercomparison study of wind wave prediction models, Part 1: Principle results and conclusions in Ocean Wave Modelling Plenum Press 1-156.

Toba, Y., 1973: Local balance in the air-sea boundary process III. On the spectrum of wind waves, J. Oceanogr. Soc. Jpn. 29, 209-220.

HAMILTONIAN DESCRIPTION OF THE INTERACTION OF SURFACE WAVES WITH MIXED-LAYER CURRENTS

Frank S. Henyey and Jon Wright

Center for Studies of Nonlinear Dynamics, La Jolla Institute, La Jolla, California 92037

ABSTRACT

The Hamiltonian for the dynamics of water motion with a free surface is constructed by combining the irrotational flow surface Hamiltonian and the interior rotational flow Hamiltonian. This Hamiltonian is then specialized to the effect of a depth-dependent current on small-amplitude surface waves. The dispersion relation and an associated variational principle are presented. The modification of the gravity-capillary group velocity by a wind-drift layer is remarkable.

INTRODUCTION

Ocean surface waves are an important driving mechanism for the mixed layer. Significant momentum and energy fluxes enter the mixed layer from the waves. In turn, the mixed layer acts back on the waves; its currents refract the waves, modifying their spectrum, and thereby modifying the energy and momentum fluxes to the mixed layer. The theory of Langmuir circulation is an outstanding example of such a feedback.

If the characteristic scales of the variation of the currents exceed a wavelength/4π in the vertical or about half a wavelength in the horizontal, the effect of the current on the wave is well described as a simple advection. (This is not to say that the consequences of advection are simple; Langmuir circulation could result from such advection.) It is often the case that this requirement is not met. The waves of interest may have wavelengths on the order of 4π times characteristic depths of currents. This paper describes an appropriate formulation for this case. This problem has been studied from other points of view; see Peregrine (1976) and Smith (1986).

There are a number of applications of the interactions of depth-dependent currents with waves. Not all of these involve what is usually thought of as mixed layer processes. Applications include Langmuir circulation, effects of currents on the evolution of the wave spectrum, wind-drift layer, wind-wave coupling, SAR observations of internal waves and other currents, and giant waves focussed by the ocean currents. All scales of waves are affected by depth-dependent currents, so these applications extend from centimeter to kilometer waves.

This paper does not discuss any application in detail, but is concerned with the general framework. It is becoming more widely appreciated that there are many advantages in a Hamiltonian description of the dynamics of fluid systems. We present a Hamiltonian for water motion involving both surface waves and rotational (vorticity-containing) subsurface flows.

THE HAMILTONIAN

The Hamiltonian is a function which allows equations of motion to be deduced. It exists whenever viscosity or other loss processes can be neglected. (Losses can be appended perturbatively, however.) Its value is the energy. The energy must be expressed in terms of canonical variables. An expression for the energy is usually readily available, so the harder part of providing a Hamiltonian is to identify the canonical variables. These variables come in conjugate pairs, generically named p_j , q_j. We have

$$H\left(p_j, q_j\right) = E \tag{1}$$

where H is the Hamiltonian and E is the energy. Hamilton's equations of motion follow from the canonical variational principle

$$\delta \int \left[\sum_j p_j \dot{q}_j - H\left(p_j, q_j\right) \right] dt = 0 \tag{2}$$

The statement that this principle is canonical means that p_j and q_j are to be varied independently, unlike Lagrange's variational principle which involves only the q_j's. The task of the Hamiltonian constructor is to find the p , q pairs and to express the energy in terms of them.

The Hamiltonian for pure surface waves, with only irrotational subsurface motion, is well known. It has been rediscovered several times. The first paper we are aware of is Zakharov (1968). Miles (1981) gives a review of the history. The canonical pairs are the surface elevation

$$q_j = \zeta(x, y) \tag{3}$$

and the velocity potential at the surface

$$p_j = \phi_s(x, y) = \phi\left(x, y, z = \zeta(x, y)\right) \tag{4}$$

The index j is to be thought of as a label for the point (x, y) giving the horizontal coordinates of the surface. The velocity is

$$\vec{v} = \nabla \phi \tag{5}$$

with

$$\nabla^2 \phi = 0 \tag{6}$$

And the energy (Hamiltonian) is

$$H\left[\zeta,\phi_s\right] = \int dx\,dy\left[\rho\int^{\zeta}\frac{v^2}{2}\,dz + \rho g\,\zeta^2/2\right] \tag{7}$$

For now, we have left out surface tension. Later in the paper it will be included.

The Hamiltonian is also well known for rotational interior flow with no free boundaries. The canonical variables are Clebsch's potentials

$$p_j = \beta(x,y,z) \tag{8}$$

$$q_j = \alpha(x,y,z) \tag{9}$$

where j labels the point in space, and α,β are defined by the expression for the velocity

$$\vec{v} = \nabla\phi + \alpha\nabla\beta \tag{10}$$

The physical interpretation of this expression is described in Lamb (1932) p. 248. The potential ϕ is to be thought of as a functional of α,β given by

$$\nabla^2\phi + \nabla\cdot(\alpha\nabla\beta) = \nabla\cdot\vec{v} = 0 \tag{11}$$

or, alternatively, as a free variable without a conjugate partner, in the variational principle eq. (2), in which case eq. (11) follows. The energy is

$$H = \int dx\,dy\,dz\,\rho v^2/2 \tag{12}$$

In this paper we ignore stratification and the Earth's rotation. If we wished to include these effects, we would use Henyey's (1983) generalization of Clebsch's representation.

In order to construct the Hamiltonian for our problem, we must properly combine these two well-known theories. By experience, we know it is easy to write down incorrect combinations. We think that we should have been able to proceed deductively, but we actually found the correct combination by guesswork. Our result is a variational equation very similar to eq. (2), but it is not exactly a Hamiltonian in the usual sense, as described below. We slightly rewrite Clebsch's expression for the velocity by redefining ϕ (adding $\alpha\beta$ to the old ϕ) to get

$$\vec{v} = \nabla\phi - \beta\nabla\alpha \tag{13}$$

We use the step function at the surface

$$\theta = \theta(\zeta - z) = \begin{cases} 1 \text{ in the water} \\ 0 \text{ outside} \end{cases} \tag{14}$$

and its derivative, Dirac's delta function

$$\theta' = \delta(\zeta - z) \ . \tag{15}$$

The variational principle is

$$\delta \int L \, dx \, dy \, dz \, dt \ = 0 \tag{16}$$

where

$$L = \beta \dot{\alpha} \theta + \phi \dot{\zeta} \theta' - \frac{v^2}{2} \theta - g \frac{\zeta^2}{2} \theta' \tag{17}$$

The last two terms integrate to the energy. This is not exactly a canonical variational principle because the dynamical variable ζ appears in the θ and θ' of the first two terms.

As with the Clebsch case, ϕ in the interior can either be considered a functional of the other variables, or, more conveniently, as a free variable. The variable ζ is understood as independent of the the vertical coordinate z, while α, β, ϕ depend on all three coordinates. By variation with respect to all variables, we obtain the equations of motion

$$\dot{\alpha} + \vec{v} \cdot \nabla \alpha = 0 \tag{18}$$

$$\dot{\beta} + \vec{v} \cdot \nabla \beta = 0 \tag{19}$$

$$\nabla \cdot \vec{v} = 0 \tag{20}$$

$$\dot{\zeta} + \vec{v}_s \cdot \nabla \zeta = \vec{v}_s \cdot \hat{z} \tag{21}$$

$$\beta_s \dot{\alpha}_s - \dot{\phi}_s - \frac{v_s^2}{2} - g \zeta = 0 \tag{22}$$

The subscript s means evaluated on the surface; e.g., $\alpha_s(x,y) = \alpha\big(x,y,\zeta(x,y)\big)$.

This set of equations is very general. The surface waves and the interior flow are arbitrarily nonlinear, and the relative scales are arbitrary. For many purposes (but not all), this generality only amounts to an unnecessary complication.

WAVES ON A CURRENT

Often, the horizontal scales of the currents are larger (a factor of two suffices) than those of the waves. In that case, short waves asymptotics can usually be used. To keep the discussion simple, and as the most important case, we assume that the surface waves can be treated linearly. We could handle moderate nonlinearities of the surface waves by themselves, using Whitham's method [Whitham (1974)].

For any linear wave system in the short-wavelength limit which has a Hamiltonian, there is a quadratic Hamiltonian such that

$$H = A\,\omega \tag{23}$$

where A is a conserved wave action and ω is the frequency. The wave momentum is given by the wave number

$$\vec{p} = A\vec{k} \tag{24}$$

The variational principle, in this limit, is

$$\delta \int dt \left[\vec{k}\cdot\vec{x} - \omega(\vec{x},\vec{k}) \right] \tag{25}$$

where $\vec{x}$ is the center of action of a packet of the waves. The dispersion relation expresses the frequency in terms of the wave number and position. The position dependence arises, in our problem, by the (slow) horizontal dependence of the current. These results can be found, for example, in the work of Whitham (1974).

We are concerned with the case in which we cannot consider the currents as arbitrarily uniform with depth. Therefore, there does not exist a Lagrangian frame. We cannot, for this problem, use the restriction of Whitham's theory described by Bretherton and Garrett (1969). The frequency cannot be written as an intrinsic frequency depending only on wave number and a Doppler shift by a wave number-independent velocity. For the group velocity, we must use

$$\vec{v}_g = \partial\omega(\vec{x},\vec{k})/\partial\vec{k} \tag{26}$$

The dispersion relation follows from linearizing eqs. (18)–(22) about a state with a depth-dependent flow. The equations that result are not new. They are, for example, in Peregrine (1976). They are conveniently expressed in terms of a depth-dependent "intrinsic frequency"

$$\sigma(z) \equiv \omega - \vec{k}\cdot\vec{U}(z) \tag{27}$$

Then the excess of pressure over hydrostatic pressure obeys the equation

$$P''(z) - \frac{2\sigma'(z)}{\sigma(z)}P'(z) - k^2 P(z) = 0 \tag{28}$$

where

$$\sigma(0)P(0) = g\,P'(0)/\sigma(0) \tag{29}$$

and an appropriate boundary condition at the bottom; in deep water

$$P(-\infty) = 0 \tag{30}$$

Unless ω in eq. (27) is chosen properly, eqs. (28)–(30) have only the trivial solution $P = 0$. Thus, this system is very much like an eigenvalue problem. An approximate solution is

$$\omega \approx \sqrt{gk} + \vec{U}\left(z = 1/(2k)\right)\cdot\vec{k}\ , \tag{31}$$

with improvements [Smith (1986)] possible. For waves interacting with larger waves rather than currents, g is replaced by an effective g including the surface acceleration, and the advection $\vec{U}$ is evaluated exactly on the surface, not at a depth of $1/(2k)$ [Henyey et al. (1987)]. The equations of motion for wave packets involve all the partial derivatives of $\omega(\vec{x},\vec{k})$. Knowing only eqs. (28)–(30), and having the desire to do better than (31) or its improvements, calculating such derivatives requires solving the eigenvalue-like system at a set of values of $\vec{x},\vec{k}$, and taking differences.

Given the variational formulation, however, this procedure can be simplified. The general variational principle (16) induces a variational principle for the eigenvalue-like problem. As is familiar in eigenvalue problems (the "Hellmann-Feynman theorem"), this variational principle allows one to reduce the calculation of derivatives of ω to quadratures involving the unperturbed function (in our own case, the unperturbed pressure). The eigenvalue-like system need be solved only once at a $(\vec{k},\vec{x})$ point, and derivatives can be easily obtained.

One reduces the variational principle by ignoring horizontal dependence (due to the short-wavelength assumption) and Taylor-series expanding, retaining only quadratic terms (due to the linearity assumption). One assumes a fixed wave number and constrains the variables to be in the proper relationship as given by eqs. (18)–(22); in our problem we constrain all variables to be expressed in terms of the pressure. The pressure is related to the velocity potential by

$$P(z) = \sigma(z)\phi(z) \tag{32}$$

which is obtained by taking the time derivative of eq. (10), inserting eqs. (18)–(20), and comparing to Euler's equation. This is an application of a mathematical theorem, that if a variational problem is constrained by conditions true at an extremum, the extremum remains the same. On doing these manipulations and including surface tension γ, we find

$$0 = \delta \int dz \left[\frac{1}{2} \left[\frac{P'(z)}{\sigma(z)} \right]^2 + \frac{1}{2} \left[\frac{k P(z)}{\sigma(z)} \right]^2 - \frac{P(z)P'(z)}{g + \gamma k^2} \right] \tag{33}$$

The equivalences of this to eqs. (28)–(30) can easily be verified. We believe that this variational formulation is new.

In order to take derivatives, we abbreviate eq. (33) as

$$0 = \delta S / \delta P \tag{34}$$

For any solution P, another solution is a constant times P. The only way this can happen is

$$S = 0 \tag{35}$$

on the solution. Differentiating eq. (35) (with respect to any variable) we get

$$\int dz \left[\frac{\delta S}{\delta P(z)} d P(z) + \frac{\delta S}{\delta \sigma(z)} \left[d\omega - d\left(\vec{k} \cdot \vec{U}(z) \right) \right] \right] + \frac{\delta S}{\delta k} dk = 0 \tag{36}$$

By eq. (34), the first term is zero, so we do not have to evaluate $d P(z)$, which is hard. The remaining terms only involve easily evaluated explicit derivatives. We can solve for $d\omega$, the desired derivative. The result is

$$\vec{v}_g = \frac{\partial \omega}{\partial \vec{k}} = \frac{\int dz \left[\left\{ \frac{(P'(z))^2}{\sigma^3(z)} + \frac{(k P(z))^2}{\sigma^3(z)} \right\} \vec{U}(z) + \frac{\vec{k} P^2(z)}{\sigma^2(z)} + \frac{2\gamma \vec{k}}{(g + \gamma k^2)^2} P(z)P'(z) \right]}{\int \left[\frac{(P'(z))^2}{\sigma^3(z)} + \frac{(kP(z))^2}{\sigma^3(z)} \right] dz} \tag{37}$$

If there is a slow horizontal (x) variation in U, the spatial variation in frequency also follows from 36:

$$-\frac{dk_x}{dt} = \frac{\partial\omega}{\partial x} = \frac{\vec{k}\cdot\int \frac{\partial\vec{U}}{\partial x}(z,x)\left\{\frac{(P'(z))^2}{\sigma^3(z)} + \frac{(k\,P(z))^2}{\sigma^3(z)}\right\}dz}{\int\left\{\frac{(P'(z))^2}{\sigma^3(z)} + \frac{(k\,P(z))^2}{\sigma^3(z)}\right\}} \tag{38}$$

and the corresponding expression for $-dk_y/dt$.

WIND DRIFT LAYER

We have carried out the calculation outlined above for the case of a thin wind-drift layer. We assume $\vec{U}(z) = \hat{x}U_0 e^{-|z|/d}$. Since a wind drift layer is very thin, we have included capillarity in the dispersion relation. In figure 1 we compare the group velocity (for a wave in the $\hat{x}$ direction) for $U_0 =$ 40cm/s, $d =$ 8 mm with that of a uniform current of 40cm/s. Instead of the minimum at $\lambda =$ 4.4cm (Lamb, (1932) p. 460), there is a broad minimum at much larger wavelengths.

The resonant four-wave interaction, in the weak interaction limit, transfers energy at a rate proportional to $1/(\partial v_g/\partial k)$. We have not yet evaluated the four-wave coupling with the current present. If we assume that the wind-drift layer does not significantly reduce the coupling, then transfer rates will greatly increase with the layer present, since $\partial v_g/\partial k$ is so small. The nonlinear transfer of energy in the moderately short wavelength part of the spectrum may have been grossly underestimated in the past by not including this effect.

SUMMARY

Problems involving the interaction between surface waves and currents can be usefully treated in the Hamiltonian framework. The Hamiltonian function is the energy expressed in terms of Clebsch's variables for the current, and the surfaces elevation and velocity potential for the surface waves. There is a variational principle associated with the Hamiltonian. Approximations and special cases are properly handled by using this variational principle. As an example, we have presented evidence that the four-wave resonant interaction is greatly enhanced for short waves due to the presence of a wind-drift layer.

ACKNOWLEDGMENTS

This work was supported in part by the Office of Naval Research by DARPA and in part by independent research funds of the La Jolla Institute.

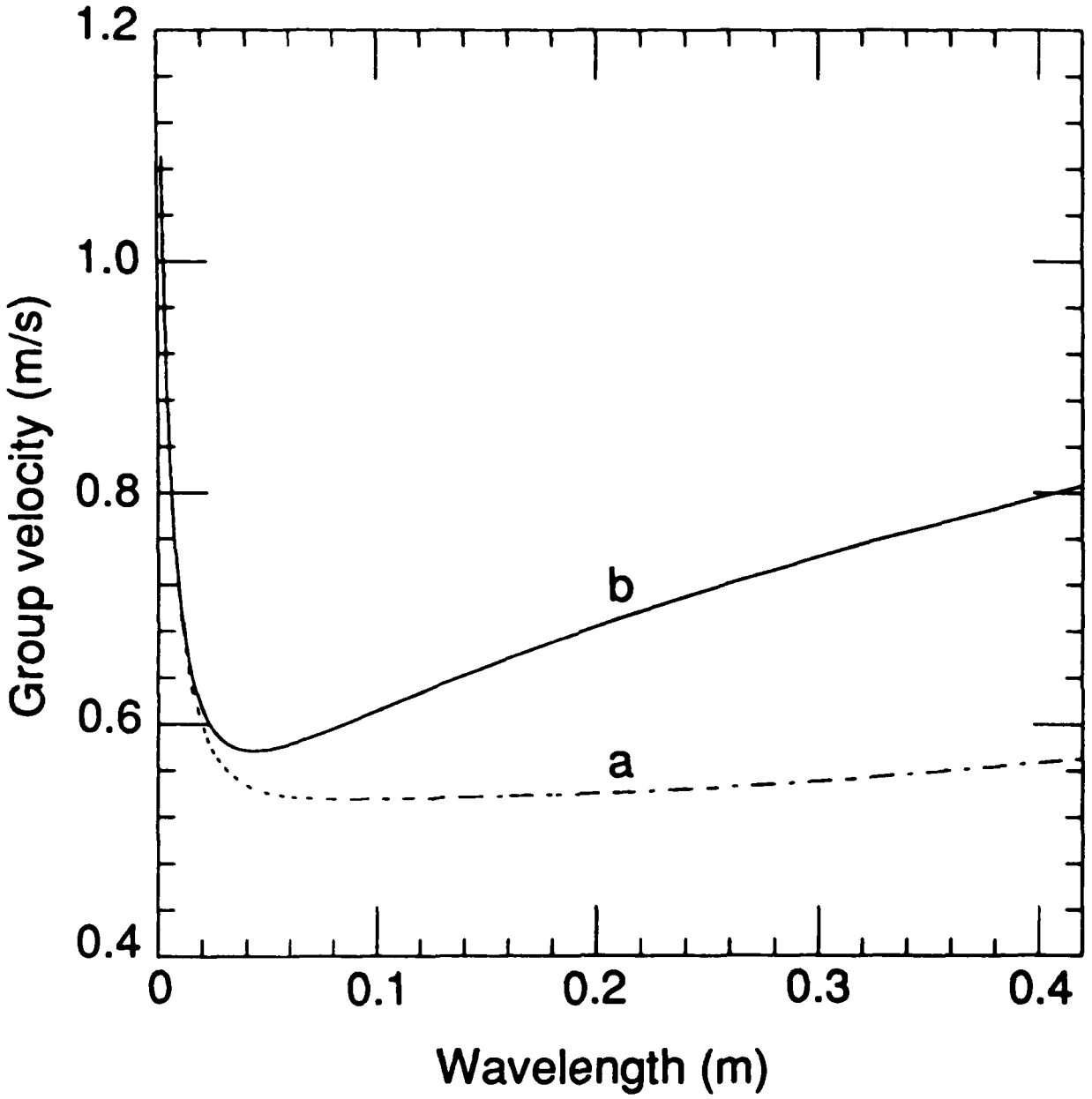

Fig. 1. Curve a is the group velocity for a wave moving in the direction of a current $U = U_0 e^{-|z|/d}$ with $U_0 = 0.4$m/sec and $d = 0.008$m. Curve b is the usual no current group velocity boosted by 0.4m/sec. The extremely flat curve for the group velocity should lead to considerably enhanced transport between different waves.

REFERENCES

Bretherton, F. and C. Garrett, 1969: "Wavetrains in Inhomogeneous Moving Media," *Proc. Roy. Soc.* **A302**, 529.

Henyey, F.S., 1983: "Hamiltonian Description of Stratified Fluid Dynamics," *Phys. Fluids*, **26**, 40-47.

Henyey, F.S., D.B. Creamer, K.B. Dysthe, R.L. Schult and J.A. Wright, 1987: "The Energy and Action of Small Waves Riding on Large Waves," submitted to *J. Fluid Mech.*

Lamb, H., 1932: *Hydrodynamics*, 6th ed., Cambridge University Press.

Miles, J.W., 1981: "Hamiltonian Formulations for Surface Waves," *Appl. Sci. Res.*, **37**, 103-110.

Peregrine, D.H., 1976: *Adv. Appl. Mech.*, *"Interaction of Water Waves and Currents,"* **16**, 10-117.

Smith, J., 1986: "Short Surface Waves with Growth and Dissipation," *J. Geophys. Res.*, **91**, 2616-2632.

Whitham, G.B., 1974: *Linear and Nonlinear Waves*, John Wiley and Sons, New York.

Zakharov, V.E., 1968: "Stability of Periodic Waves of Finite Amplitude on the Surface of a Deep Fluid," *J. Appl. Mech. Tech.*, **9**, 190.

RADIATIVE PROCESSES AFFECTING OCEAN MIXED-LAYER HEAT CONTENT AND THEIR MONITORING FROM SATELLITE

Catherine Gautier

California Space Institute A-021
Scripps Institution of Oceanography
La Jolla, California 92093

ABSTRACT

Radiation flux observations (satellite and surface) from various studies are examined to assess their possible roles in modifying the ocean's mixed-layer heat content. Several processes are investigated. First, observations indicate that the magnitude and extent of SST diurnal warming events (changes of up to 3 °C), which affect air-sea heat fluxes, can be effectively monitored by satellite. Second, although still not well understood, a mechanism is suggested that would involve convective lines in upper ocean turbulent mixing generation. This mechanism has a strong diurnal variability, resulting in nighttime cooling in bursts concurrent with wind stress bursts, and might generate bursts of turbulent mixing. Third, mixing's effect on photosynthesis and the potential influence of phytoplankton distribution on mixing and thermal stratification are discussed. Lastly, several satellite methods for computing net surface radiation flux are reviewed and assessed.

1. INTRODUCTION

The radiation flux across the air-sea interface, one component of the ocean surface heat flux, plays an important role in modifying the upper ocean heat content. The effects of radiation fluxes on the ocean vary geographically, from the tropics to mid-latitudes, and temporally, on diurnal to seasonal cycles.

For this paper I have selected three processes through which radiation fluxes may play a role in modifying the mixed-layer heat content. Though some of the selected processes have been studied for many years, they are looked upon here from different perspectives and their importance to global studies: 1) their large extent (e.g., diurnal warming of SST); 2) their potential influence on other physical processes (e.g., oceanic turbulent mixing); and 3) their connection to biological processes (e.g., phytoplankton growth). In addition to these processes, I examine the status of net (shortwave + longwave) surface radiation flux global monitoring from satellite observations because of radiation's importance to the surface heat budget and its role in global scale processes.

2. SOME RADIATIVE PROCESSES AFFECTING MIXED-LAYER HEAT CONTENT

a. SST Diurnal Warming and Turbulent Heat Flux Enhancement

In light wind and cloudfree conditions, increases of up to 3 °C in sea surface temperature can take place diurnally as a result of solar heating of a thin ocean surface layer. Under these conditions ocean surface heating by solar radiation is maximum, and because of light winds and surface heating, oceanic vertical mixing and ocean surface waves are reduced. Strong thermal stratification is also established as solar radiation is absorbed by the thin surface layer (few centimeters to a meter, Price et al., 1986).

Diurnal warmings of a few degrees centigrade are observed during summer at mid-latitudes and throughout the year in the tropics. It has been shown that differences between daytime and nighttime satellite-derived sea surface temperatures can provide a first estimate of these warming events (Fig. 1, from Stramma et al., 1986). Furthermore, spatial information obtained from satellites can provide the magnitude of their extent (Cornillon and Stramma, 1985). Together these studies have shown that in mid-latitudes temperature differences between the surface and the mixed-layer of 1 to 2 °C can extend over regions of 10 degrees latitude by 10 degrees longitude (10^6 km^2) during summer. At one location during the LOTUS experiment an average monthly temperature difference of 0.4 °C was observed between the surface and 0.6 m.

These diurnal warmings are important in climate studies because they can induce changes in the turbulent sensible and latent heat fluxes from the ocean to the atmosphere and, as a consequence, in the upper ocean heat content. Since turbulent heat fluxes affect a thin ocean surface layer, which can have a much higher temperature than the first few meters of upper ocean, cooling of more than 5 w/m^2 can occur over these few meters on a monthly basis from turbulent heat flux increases (Cornillon and Stramma, 1985). Additionally, surface cooling of about the same magnitude can take place through longwave radiation flux. The overall cooling can be much larger on a daily time scale for which surface temperature changes of 1 to 2 °C are frequent.

No assessment of this overall effect has yet been made for the tropical regions but it can be expected that in the equatorial Pacific band (3 °N to 3 °S), which is cloudfree most of the year and where winds are often light, sea surface temperature diurnal warmings will extend over large areas. The magnitude of these warmings can be studied in part from satellite observations by using either day-versus-night temperature differences obtained from the Advanced Very High Resolution Radiometer (AVHRR) or daily temperature evolutions obtained from the VISSR Atmospheric Sounder (VAS) (Bates and Smith, 1985).

b. Convective Lines and Ocean Turbulent Processes in Equatorial Regions

The role convective lines might play in upper ocean turbulent mixing is discussed here; yet it remains a controversial issue in the absence of more comprehensive observations. It is suggested here, however, because of revealing observations made during the first intensive TROPIC HEAT experiment. At that time, observations of turbulent mixing (e.g., Moum et al., 1986) indicated that mixing was strongly modulated on a diurnal scale and occurred principally at night. Furthermore, these observations revealed that turbulence occurred in bursts separated by a few hours (Fig 2, from Park et al., 1985), and that the mixing seemed to be generated in the near surface layer and to propagate deeper, below the mixed-layer.

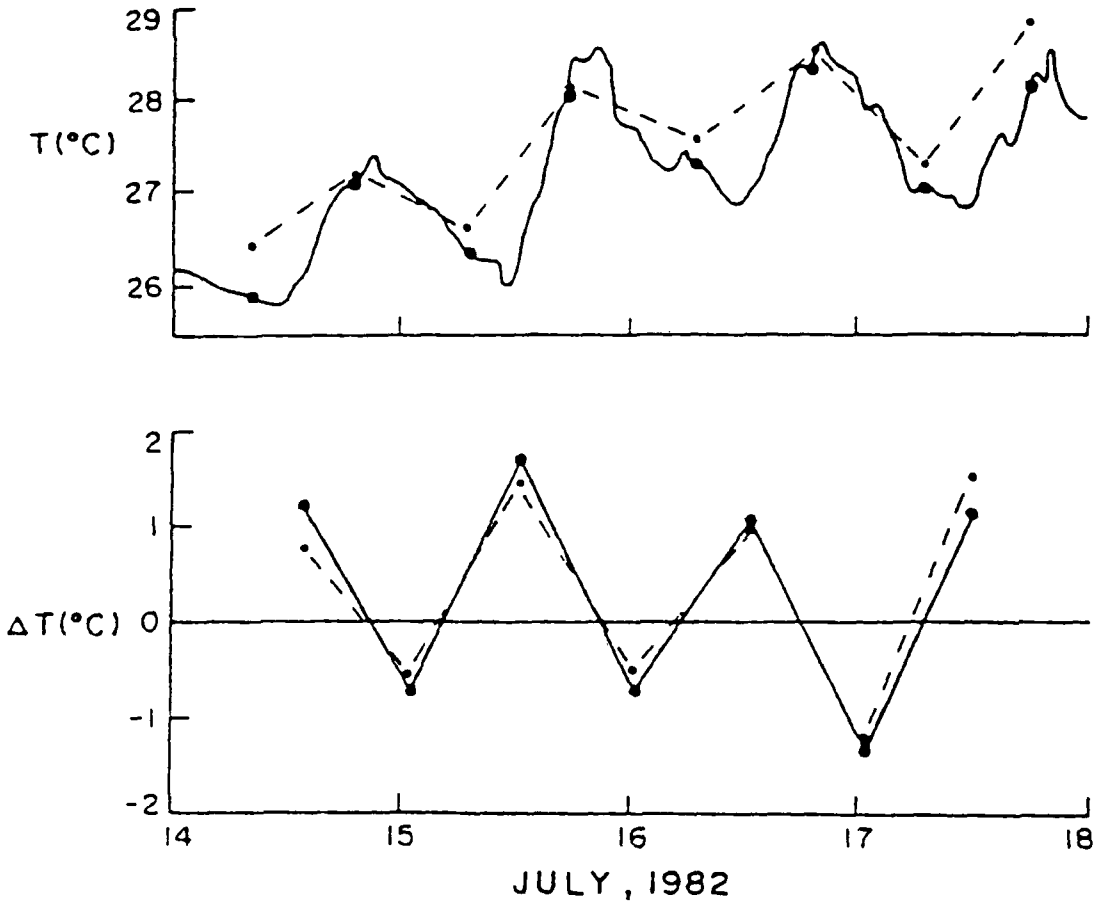

Figure 1. SST at 34 °N, 70 °W for the period 14-18 July 1982 (upper curves) and the day-night temperature differences (lower curves) from satellite data (dashed line) and in situ measurements at 0.6 m depth (solid line). Time is GMT (subtract 0.21 for local solar). The dots on the upper curves represent temperatures at the time of the satellite pass. (Figure taken from Stramma et al., 1986).

In an attempt to clarify the source of the mixing, a possible generation mechanism at the surface was investigated. This mechanism should have strong diurnal variability and, because of the bursts, be modulated at a high frequency. Although surface wind stress is known to generate ocean turbulent mixing, it has very little diurnal variability. The largest diurnal signal is in the net surface heat flux and results from insolation variability. The high frequency variability could have many possible origins; here, however, the hypothesis selected for testing examines the relationship between this high frequency variability and the passage of convective lines, which are often observed in the equatorial regions.

This hypothesis can be better understood by looking at the schematics of convective lines presented in Fig 3. Convective lines of differing nature and intensity were observed and extensively studied in the tropical Atlantic during the GATE experiment (e.g., Mower et al., 1979). They are all found to have similar characteristics that are summarized in Fig 3. These lines are usually associated with an intense gust front and atmospheric convective cells with

strong updrafts and downdrafts. These vertical circulations induce near-surface pressure and vertical velocity gradients across the line, as well as increased turbulent surface heat fluxes behind the gust front in the downdraft region of the line as a result of descending cold (low static energy) air and dry (low moist static energy) air near the surface. Both small horizontal scale convective clouds (ahead) and more extended stratified clouds (behind) are associated with such lines. Thus, in summary, these lines are associated with small-scale pressure perturbations, increased surface wind stress in the gust front region, increased turbulent heat fluxes behind the gust front, and decreased net surface shortwave and longwave radiation fluxes, resulting from cloudiness. Overall, they induce rapid pressure changes, short bursts of increased wind stress, and ocean surface cooling.

Occurring during the day, while the net surface heat flux is generally directed from the atmosphere to the ocean, the convective line effect on the surface heat flux will be to decrease oceanic heating. Occurring at night, while the ocean surface is cooling, the convective line effect will be to increase the cooling in bursts concurrent with wind stress bursts. It is therefore reasonable to hypothesize that this short-lasting intensification of both surface wind stress and cooling, associated with a rapid pressure perturbation, might generate bursts of turbulent mixing, as those observed during the TROPIC HEAT field experiment.

The first step in this study was to verify that convective lines were present during the TROPIC HEAT first intensive period and that they indeed had the characteristics described above. Whereas cloud and precipitation observations were not reported during this experiment,

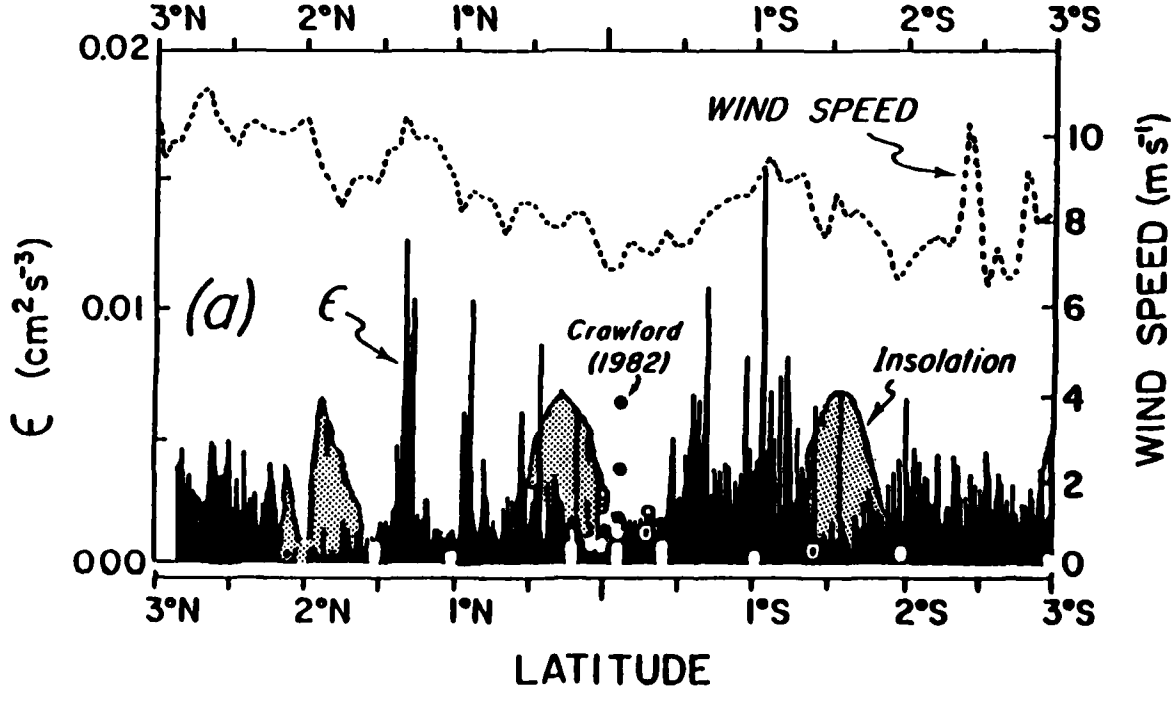

Figure 2. Measurements at 140 °W, from 3 °N to 3°S. This figure plots three parameters versus latitude: turbulent kinetic energy (black area), wind speed (dashed line), and insolation (shaded area). (Figure taken from Park et al., 1985).

radiative flux (both shortwave and longwave) measurements were made by Clayton Paulson aboard the R/V WECOMA and were used to determine the presence of convective cloud lines. Although turbulent surface flux measurements were not made during the experiment, we attempted to quantify the effects of the lines on the upper ocean by computing the wind stress and the net surface turbulent heat fluxes from the meteorological measurements using standard bulk formulae. The wind stress was obtained using a drag coefficient $C_D = 1.5 \times 10^{-3}$. The latent heat and sensible heat fluxes were obtained following standard bulk formulae and using the same coefficients for turbulent heat and moisture transfer. Although these coefficients have only a statistical meaning and have not been derived for these particular meteorologicial conditions, they are useful for providing quantitative information about the fluxes. The net heat flux is obtained as the sum of its four components: shortwave and longwave radiation, latent and sensible heat fluxes. To further test our hypothesis, we studied these fluxes only at night (i.e., shortwave radiation flux = 0), since it is assumed that night is the only time during which the presumed effect will take place. In this case, only the longwave measurements can be used to delineate the periods during which clouds are present.

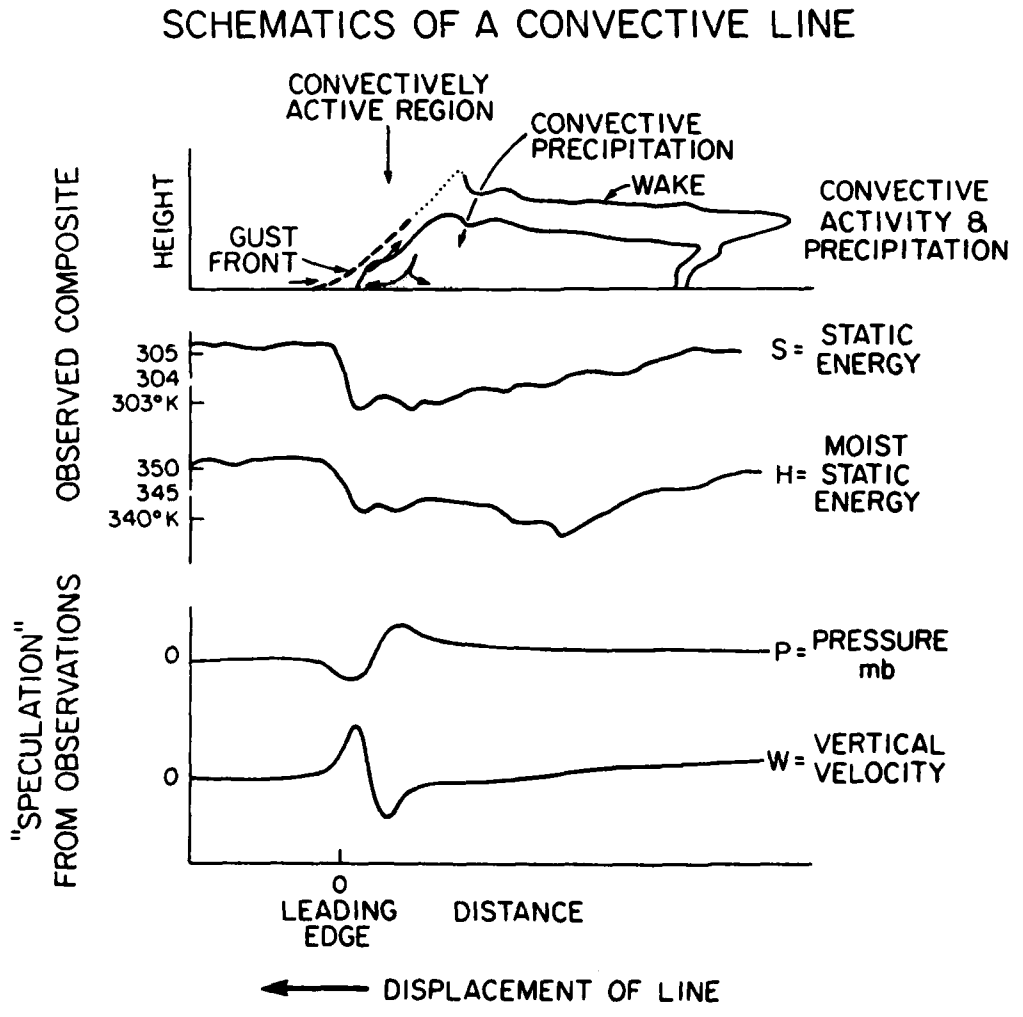

Figure 3. This figure summarizes the characteristics associated with a convective line. The top three curves (convective activity, static energy, and moist static energy) represent observed activity whereas the bottom two (pressure and vertical velocity) are speculations from observations.

A set of nighttime measurements, centered at about 2.4 °S on day 323, is presented in the following figures to demonstrate the fluxes associated with the passage of convective lines. The sign convention adopted for the cooling process is positive, and Fig 4a shows the evolution of the net longwave flux, i.e., LWN = LWU - LWD. The variability is relatively small (25 - 85 W/m^2) but not negligible, as it is often assumed. The reduction of LWN radiation indicates the presence of several convective lines, two larger ones around 2.3 and 2.7 °S. Between these two lines the atmosphere is clear and very dry (i.e., the largest LWN value of the set), as could be expected from the presence of near-surface convective scale downdrafts, which bring drier and cooler air from aloft near the surface.

The associated wind stress (Fig 4b) ranges from 0.05 to 0.22 N/m^2 and displays two large burst of wind associated with the two main convective lines and a small maximum in between. The maximum intensity of the main burst is occurring under some convective activity; the wind stress is still strong (but only about half its maximum value) in the clear and dry region.

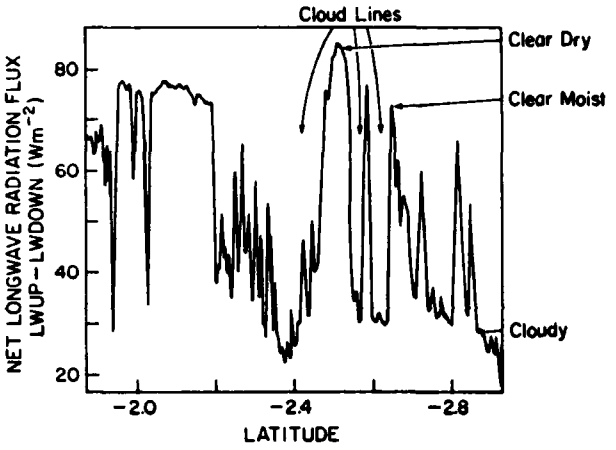

Figure 4a. Measurements of the net longwave radiation flux taken from the R/V WECOMA at 140 °W and from -1.9 °S to -2.9 °S. (Measurements are courtesy of Clayton Paulson).

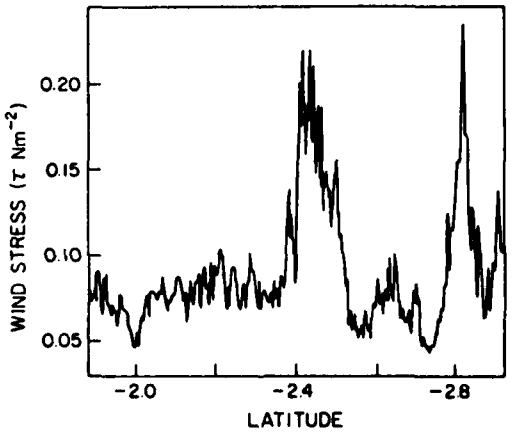

Figure 4b. Same R/V WECOMA track as Fig 4a but with the wind stress estimated from wind measurements.

The evolution of the latent heat flux (Fig 4c) reflects both the wind stress and the atmospheric moisture changes. It varies from 60 to 200 W/m^2 and displays two large increases associated with the wind stress bursts; a third one is associated with the secondary wind stress maximum, indicating that the atmospheric surface layer was relatively dry in between the two largest bursts. The sensible heat flux (not presented here) is very small and varies from -6 to +4.5 W/m^2.

The net heat flux (Fig 4d) varies from 120 to 255 W/m^2 and reflects the changes in both the net longwave and the latent heat flux. In clear and light wind conditions near (2.2 - 2.4 °S), the contribution of the two components is about the same. During the latent heat flux increases the net heat flux is dominated by the latent heat flux in the cloudy and partly cloudy conditions (small LWN), but the location of the maximum is driven by the LWN, i.e., it is located in the clearest and driest conditions. This suggests some care in making assumptions about the respective importance of the various heat flux components on the net heat flux.

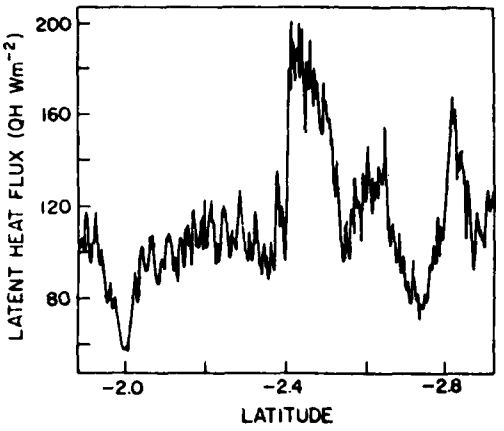

Figure 4c. Same R/V WECOMA track as Fig 4a but with the latent heat flux estimated from surface meteorological measurements.

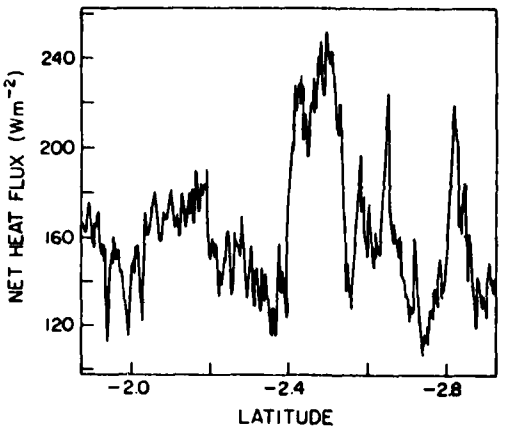

Figure 4d. Same R/V WECOMA track as Fig 4a but with the net heat flux estimated from surface meteorological measurements.

From the results just presented, it is clear that under cloudy conditions the variability of the net heat flux is driven principally by the latent heat flux variability. This would probably hold for daytime conditions too. Thus, while we have demonstrated that the presented convective line has the characteristics schematically presented in Fig 3, we have also found some important relationships between the two main components of the net heat flux. The two main modulators of the net heat flux are the wind and clouds; the wind affecting mostly the latent heat flux and the clouds affecting both the longwave and the shortwave (during the daytime) radiation fluxes. The correlation between wind changes and cloudiness is important for determining the net surface heat flux. The third important parameter is the near-surface moisture, which affects both the net longwave flux and the latent heat flux. Again, the effects of moisture changes on the net heat flux will depend on the wind and cloud conditions.

The next step in this study was to investigate a potential deterministic relationship between the surface (momentum and heat) fluxes and the nighttime ocean turbulence generation. For that we have used the turbulence data from the R/V WECOMA on its equatorial crossing already presented in Figure 2. The evolution of the total turbulent kinetic energy is plotted along with the wind stress and the net heat flux (Fig 5). Four consecutive days have been investigated: Julian Day 320 (Fig 5a), 321 (Fig 5b), 322 (Fig 5c) and 323 (Fig 5d). The largest bursts of turbulence are encountered in the near equatorial region, whereas the largest wind bursts occur away from the equatorial region. In some cases there is a high correlation between the main turbulence bursts and those of the wind stress and heat flux (Day 321, 1.5 °N), but this is not always the case (Day 321, 0.9 °N, Day 322, 0.6 °S and 1.1 °S). From these figures it is therefore quite difficult to draw any conclusion about the generation mechanism of the upper ocean turbulence through surface heat flux changes induced by the passage of convective cloud lines.

If this mechanism is indeed acting, the generation of the observed turbulence might take place away from the region where the turbulence was measured, and only a statistical study of the relationship between the density of the convective lines and the intensity of their associated surface fluxes and the magnitude of the ocean turbulence might provide a definitive answer. The important question is thus whether there is more convective line activity during periods of intense turbulence generation. This question can only be addressed using a larger data set than the one collected during the first TROPIC HEAT intensive field experiment. Convective line statistics can be studied from high resolution (1 km) infrared satellite data. These data need to be collected in conjunction with field experiments during which ocean turbulence and surface fluxes are measured. Geostationary infrared (nighttime) satellite data from the VAS instrument are collected on a routine basis, but their resolution is too coarse (8 km) for such a study. Although AVHRR data are routinely collected at a higher 4 km resolution, it is still insufficient for studying convective line statistics. The higher resolution Local Area Coverage (LAC) data, however, would be appropriate for such a study, but they are not routinely collected and must be specifically requested for experiments. In addition, because of storage limitations aboard NOAA satellites, only a few passes can be archived on board, and, as a consequence, day-night passes over the same region are difficult to obtain. The LAC AVHRR data, however, will be requested for the next TROPIC HEAT turbulence field experiment.

c. Solar Radiation, Turbulence, Phytoplankton, and Subsurface Heating

Recent research on the interaction among turbulence, solar radiation, and biota distribution has shown some interesting connections with and interactions between very small scale biophysical processes and large scale physical ones. Here I briefly present two processes: 1) the direct effects of mixing on photosynthesis; and 2) the potential influence of phytoplankton distribution on mixing and thermal stratification since they are both influenced by the net solar radiation flux.

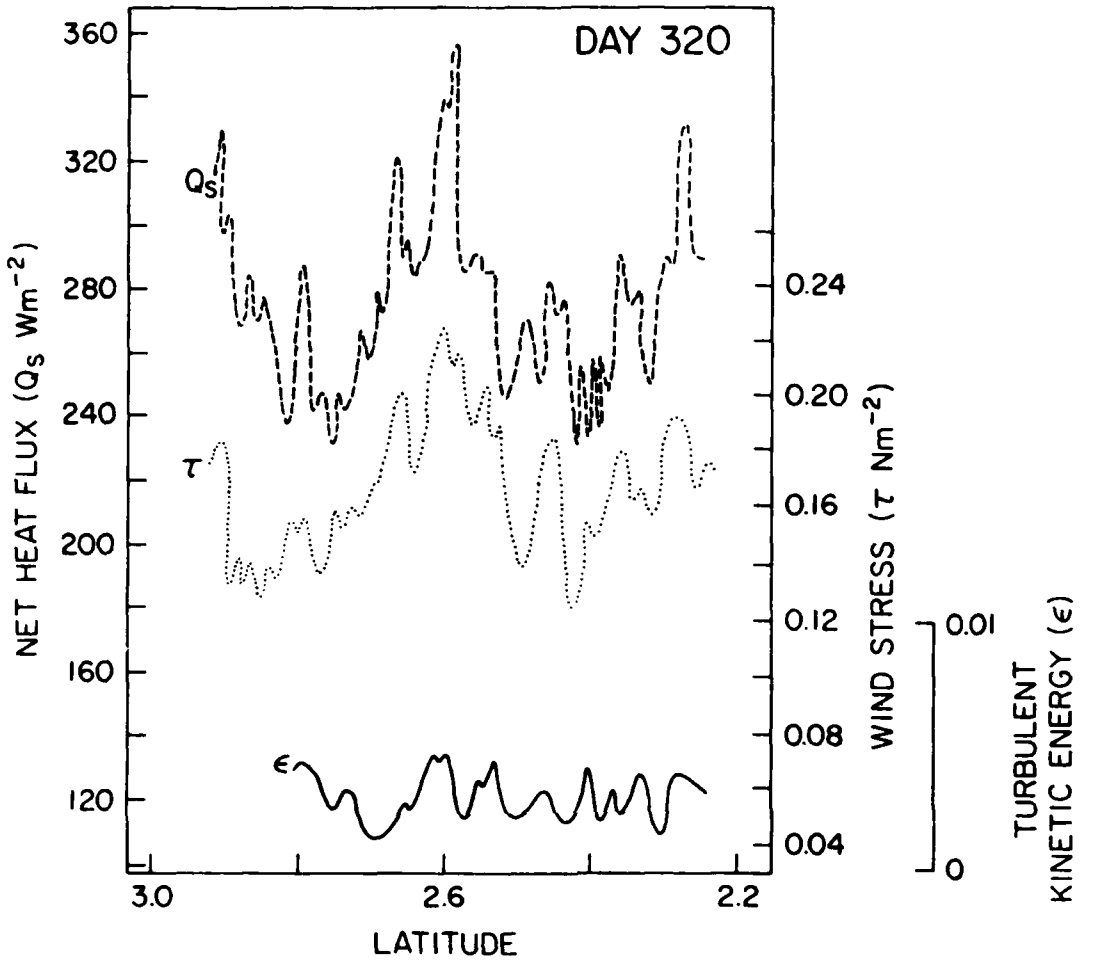

Figure 5a. This series of figures includes measurements taken from the R/V WECOMA at 140 ^{O}W and from 2.9 ^{O}N to 2.3 ^{O}S for four consecutive days (320, 321, 322, 323). They present the following parameters: net heat flux (dashed line), wind stress (dotted line), and turbulent kinetic energy (solid line). (Measurements are courtesy of Clayton Paulson).

Mixing's direct effects on photosynthesis by cycling organisms into the light field (solar radiation distribution) are still controversial. On the one hand, Gallegos and Platt (1982) showed that organisms can apparently adjust very quickly to light levels they are carried to by turbulence. On the other hand, Lewis et al., 1984, showed from contemporaneous measurements of vertical mixing and photosynthetic performance of algae that vertical mixing controls photosynthesis to a large degree. This conclusion is based on observations that indicate very little variation in potential photosynthetic rates (Pm) with depth and at high turbulent kinetic energy dissipation rates. Morever, higher values of Pm near the surface were found on days when energy dissipation rates were low. Algae populations were found to become physiologically more uniform throughout the mixing region as the ratio of turbulent kinetic energy dissipation increased. More research is being conducted to resolve this disagreement.

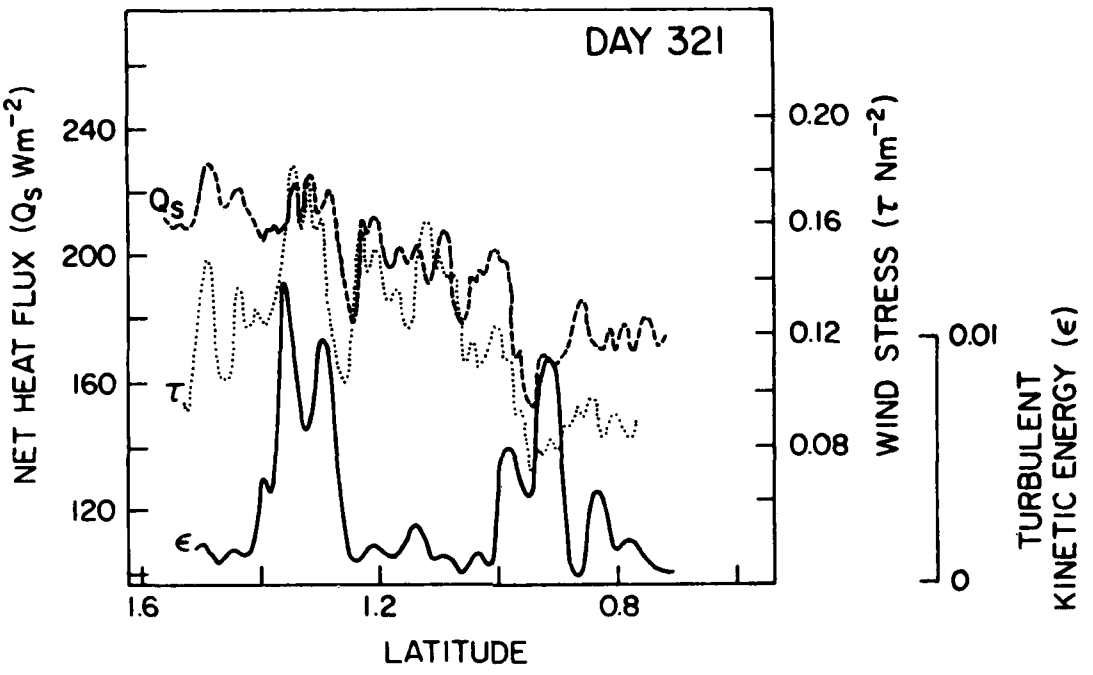

Figure 5b Similar figure as 5a--day 321.

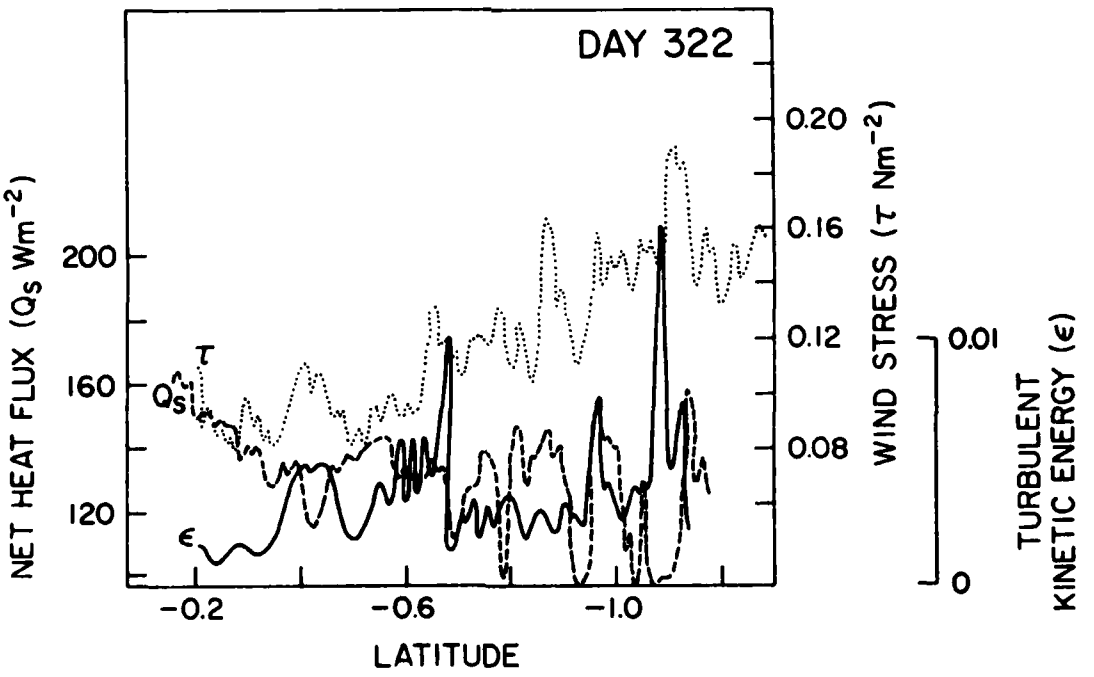

Figure 5c Similar figure as 5a--day 322.

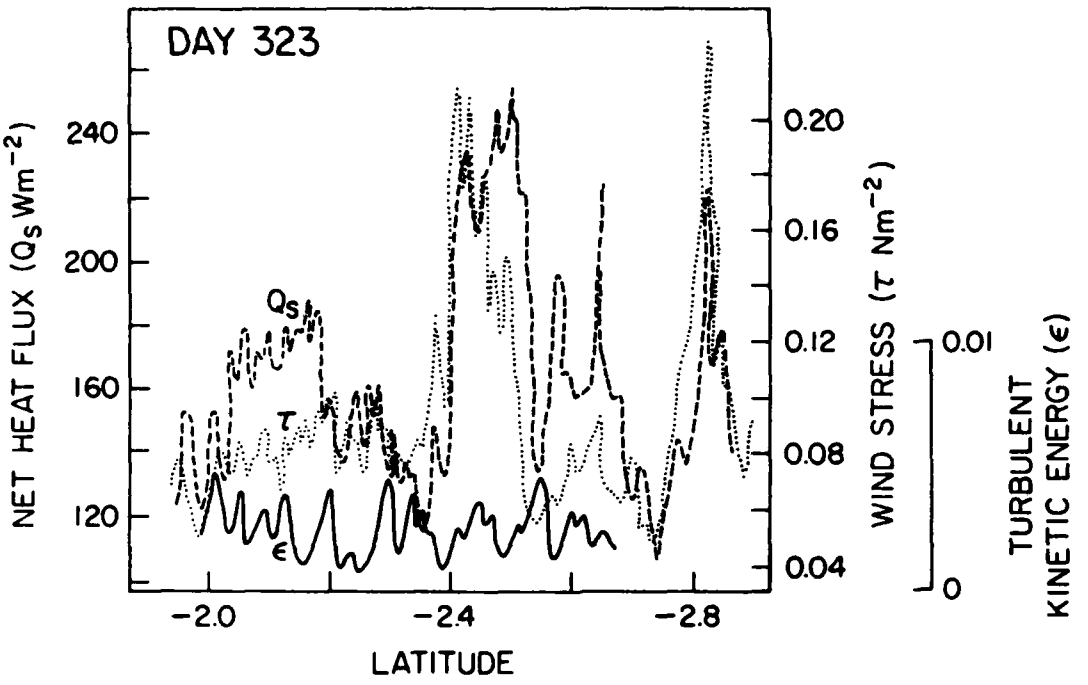

Figure 5d Similar figure as 5a--day 323.

The effects of chlorophyll depth distribution on oceanic heating is also a matter of speculation at the moment. Platt, Lewis, and collaborators and Woods and collaborators have recently discussed the influence of chlorophyll distribution on heating rates at depth and its potential effect on deepening seasonal thermoclines during early spring at mid-latitudes. Solar radiation absorption in the ocean's upper layers is strongly influenced by phytoplankton concentration; thus non-uniformities in the vertical chlorophyll/phytoplankton distributions will induce non-uniformities in absorption, and, as a result, variations in local heating. The importance of these subsurface heating variations on temperature profiles and vertical mixing will depend on the magnitude of local heating. The combination of optically clear water and an intense chlorophyll maximum layer relatively near the surface (i.e., where solar radiation is still present) permits an increased heating rate at depth (Lewis et al., 1983). Fig 6, taken from Lewis et al., 1983, illustrates this effect. In tropical regions where the water is optically clear and subsurface maxima of phytoplankton are found at depths, where irradiance is still about 15% of its surface value, computed heating rate profiles show a maximum at levels equivalent to upper regions of the phytoplankton maximum. Such subsurface heating can result in vertical transfer of heat through the base of the mixed layer and vertical mixing caused by thermal stratification. Both of these effects might be important to global heat budgets. In the future biological measurements should be included among the sets of measurements in ocean turbulence and surface meteorological parameters taken in equatorial regions.

3. NET SURFACE RADIATION FLUX FROM SATELLITE

Recent developments have taken place in methods for computing the two components of the net surface radiation flux, i.e., the shortwave and the longwave components from satellite visible and infrared radiances.

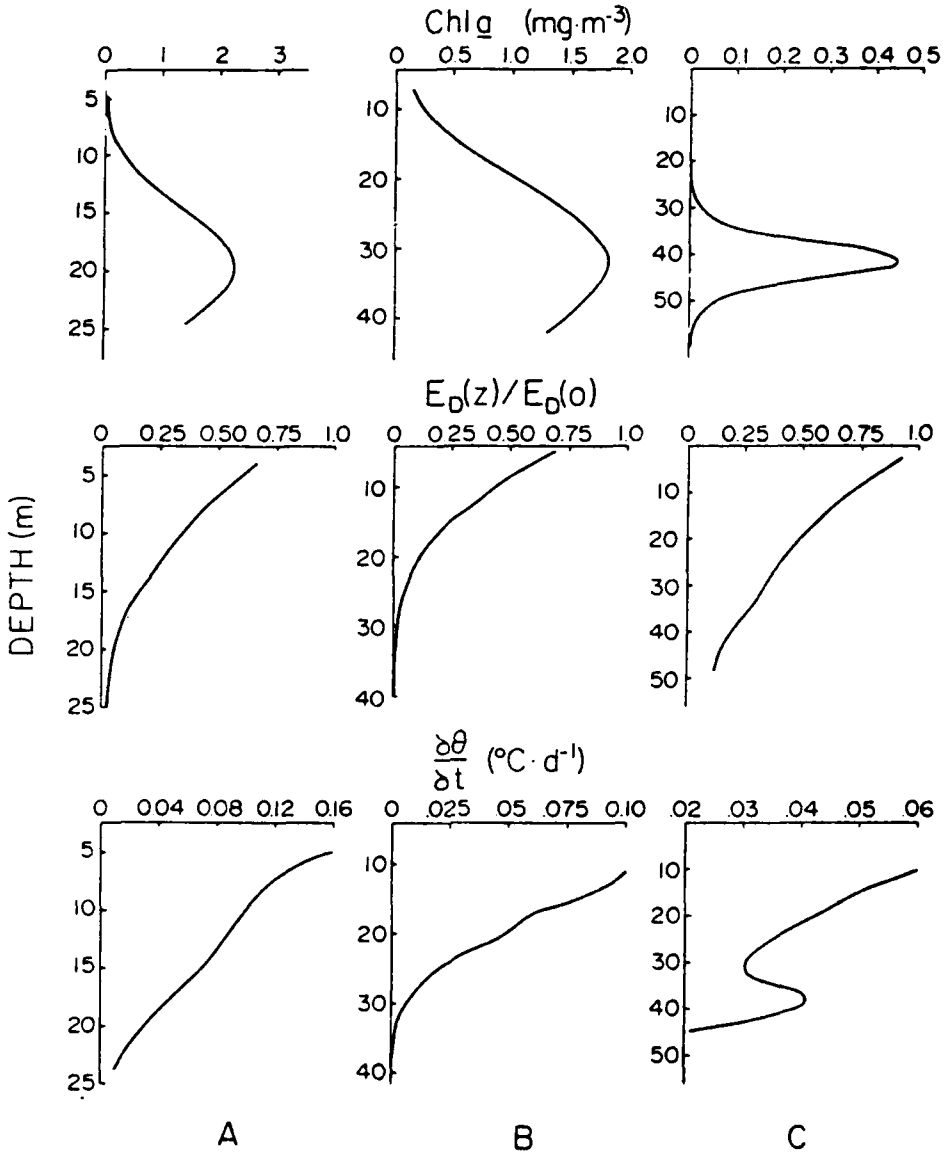

Figure 6 Computed values of the depth distribution of chlorophyll, irradiance, and heating rates for four different regions (A= coastal Southern California, B= Scotian Shelf, C= tropical Azores). (Figure taken from Lewis et al., 1983

The shortwave radiation part can now be derived routinely for mid-latitude and tropical oceanic regions (i.e, latitudes < 50 °) following a technique developed and refined by Gautier, Frouin, and collaborators. This technique has been amply validated and, in general, gives standard errors of about 10% of mean values (e.g., about 20 W/m^2 in the tropical regions). The technique of Gautier et al., 1980, is based on repeated visible brightness observations from geostationary satellite, which are interpreted in terms of cloud radiative properties. The success of this approach hinges on the fact that cloud reflectance information inferred from visible brightness is strongly related to total liquid water content of the observed column, which is itself strongly correlated to the surface shortwave radiation flux. As an example, Fig 7a shows comparisons of satellite-derived net shortwave radiation flux with surface measurements during MILDEX (Frouin et al., 1987). It indicates a standard error in the satellite-based method of 13 W/m^2. At higher latitudes the standard error is about the same, but it represents a larger percentage of the net solar radiation flux (~25-30% at 50 °N, Gautier and Katsaros, 1984)

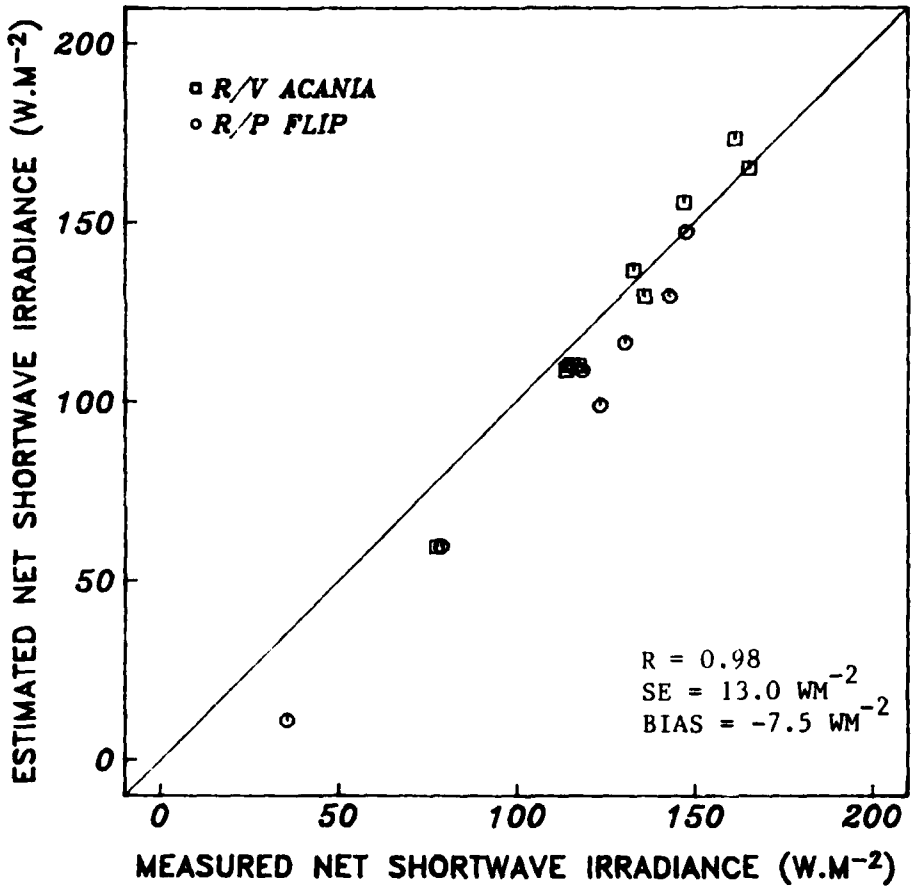

Figure 7a Comparison between satellite-derived net shortwave radiation flux and surface measurements taken during MILDEX. Statistics are included within the plot. (Figure taken from Frouin et al., 1987).

The longwave component of the net radiation flux at the surface, LWN = LWD - LWU (note different sign convention from earlier one), is more complex to derive, particularly in cloudy conditions for which the downwelling component (LWD) strongly depends upon information at and below cloud base and that cannot be directly inferred from satellite observations. Recently, however, methods have been developed based on approaches that either indirectly infer below-cloud information from satellite radiances or parameterize the cloud effects as a function of simple cloud parameters (e.g., cloud cover). In most cases, LWD in clear air conditions is obtained through radiative transfer computations using atmospheric profiles obtained from satellite infrared radiances.

Frouin et al., 1987, for instance, tested several approaches, ranging from complex physical descriptions of cloud and atmospheric parameters to highly parameterized descriptions of the cloud effects. They obtained their atmospheric temperature and humidity profiles from TIROS Vertical Sounder Data (TOVS) operational retrievals, which are spatially interpolated in case of complete cloudiness. In their most sophisticated method (A) cloud base altitude is deduced from cloud top altitude and liquid water content, assuming a liquid water content distribution within the clouds. Fig. 7b shows net longwave radiation estimation results using method A to compute the LWD, which are compared with surface measurements during MILDEX. It indicates a standard error of about 22 W/m^2 on values ranging from -20 to -100 W/m^2. Most of this error results from errors in estimating LWD.

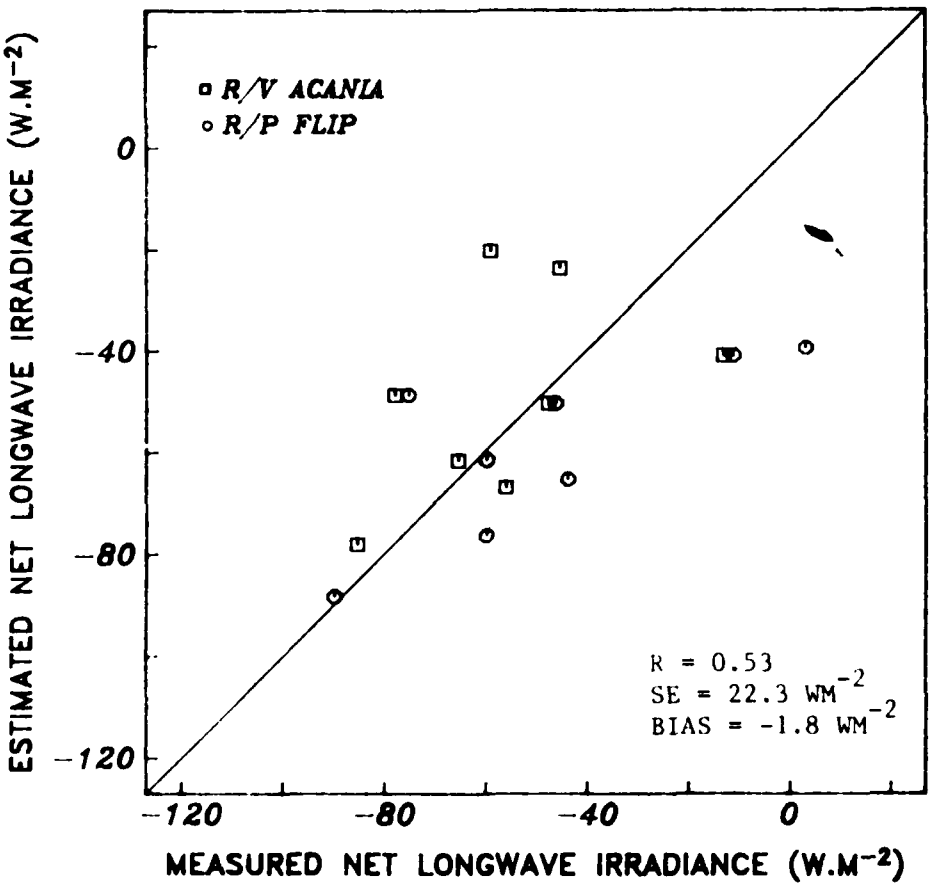

Figure 7b Comparison between satellite-derived net longwave radiation flux and surface measurements taken during MILDEX.

In the other methods they use a hierarchy of simplifying assumptions, which include directly relating the liquid water content to the cloud geometrical thickness (B), fixing the cloud geometrical thickness to its climatological value (C), and, finally, parameterizing the effects of clouds only as a function of fractional cloud coverage (D). A summary of the results obtained from and standard errors associated with all the methods is provided in Table 1. The standard error of the various methods are quite similar. The main conclusion from these results is that, in most cases, the largest errors are associated with the atmospheric profile retrievals in cloudy conditions. Thus, efforts are now devoted to improving atmospheric retrievals in cloudy conditions and to developing more physical and spatial interpolation schemes.

Table 1. Performance of the different satellite-based methods (r is correlation coefficient and Se is standard error).

	Comparison of Half-Hourly Averages of Downward Longwave Irradiance (104 pairs)				Comparison of Daily Averages of Downward Longwave Irradiance (16 pairs)			
Method	r (%)	Se (Wm^{-2})	Bias (Wm^{-2})	Slope	r (%)	Se (Wm^{-2})	Bias (Wm^{-2})	Slope
A	69	22.6	−6.5	0.53	73	18.0	−6.5	0.52
B	74	24.0	−13.3	0.54	76	20.8	−13.1	0.50
C	55	26.6	−4.3	0.46	59	20.6	−4.2	0.39
D	58	24.9	−1.2	0.45	53	21.7	−1.0	0.39

The net surface radiation flux is obtained by adding its two components. Fig 7c represents comparisons between the satellite estimated net surface radiation flux and surface measurements. The standard error of this comparison is about 32 W/m^2, which represents about 20% of the signal. This results from the fact that a large part of the standard errors in the shortwave and longwave radiation fluxes add up when computing the net radiation flux. For both components the largest errors are associated with cloud conditions, but these errors do not compensate one another in these conditions.

Fields of both the net solar shortwave irradiance (Fig 8a) and the net longwave irradiance (Fig 8b) were derived for MILDEX (Gautier and Frouin, 1986), and have the above stated standard errors. These two fields were added to describe the evolution of the net radiation flux during MILDEX (Fig 8c). The spatial variability of the net radiation flux reflects the variability of both its components. In very cloudy regions (net solar radiation flux minimum) the net radiation flux is negative because of the two components' low values. In this case the spatial

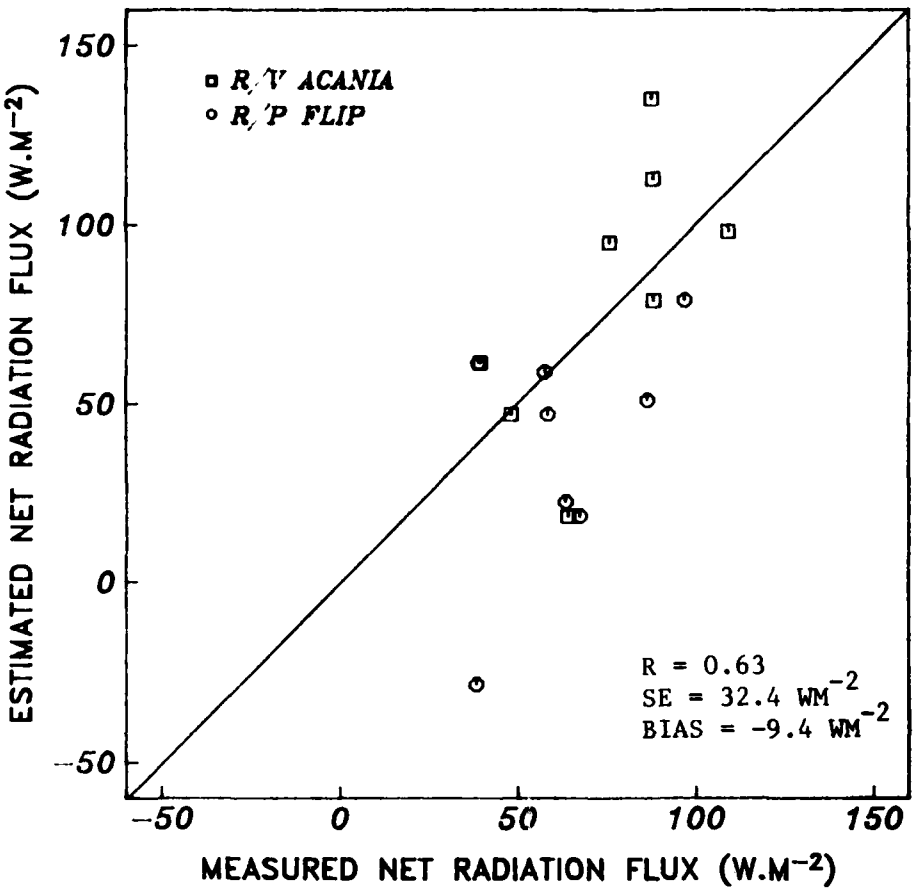

Figure 7c Comparison between satellite-derived net radiation flux and surface measurements taken during MILDEX.

variability of the net radiation flux is strongly modulated by the shortwave radiation flux. In clear conditions the net radiation flux is positive but reduced by the low values of the net longwave radiation flux. The region of maximum net radiation flux corresponds to a partly cloudy region where the net solar radiation flux is only marginally reduced by clouds and the net longwave radiation flux is, however, increased by the presence of clouds. Thus, the heating of the upper ocean mixed layer as a result of the net radiative flux in mid-latitudes probably takes place in regions which are not completely clear of clouds!

Fields of $SW_{\downarrow\uparrow}$, $LW_{\downarrow\uparrow}$, and F_{NET} (daily averages).

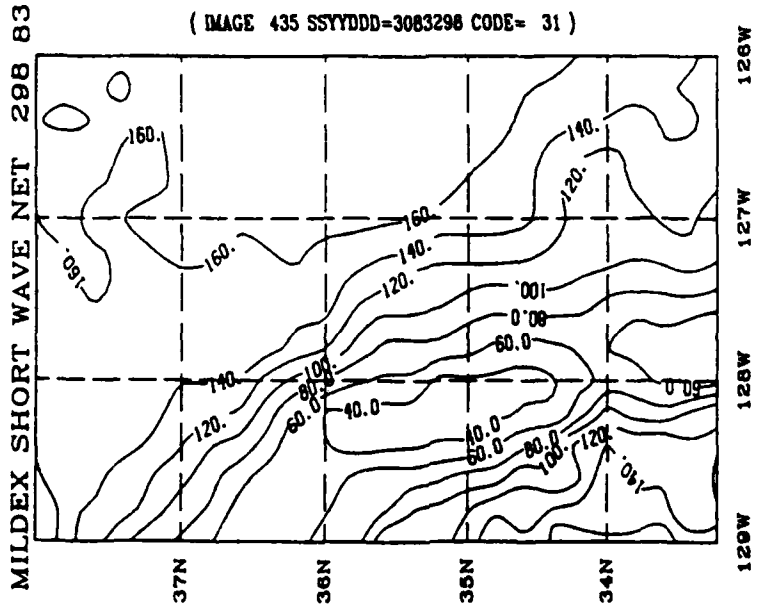

Figure 8a Net shortwave radiation field estimated from satellite during MILDEX.

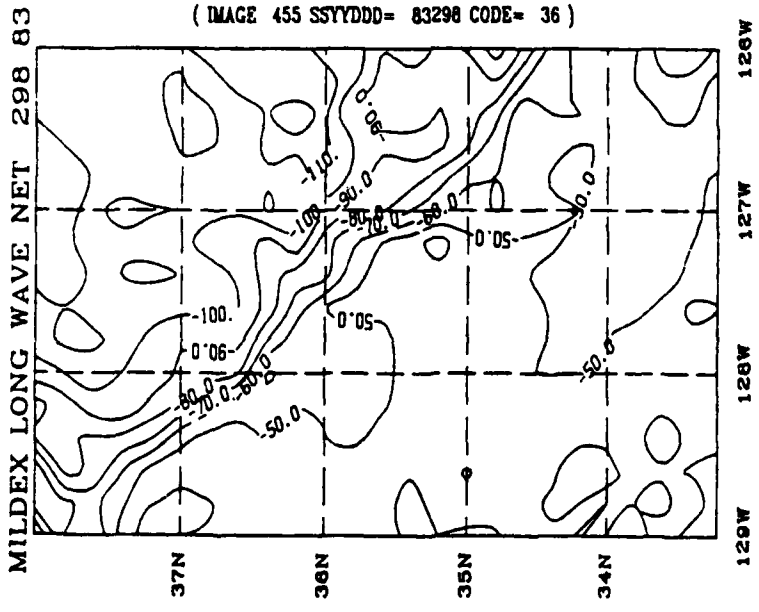

Figure 8b Net longwave radiation field estimated from satellite during MILDEX.

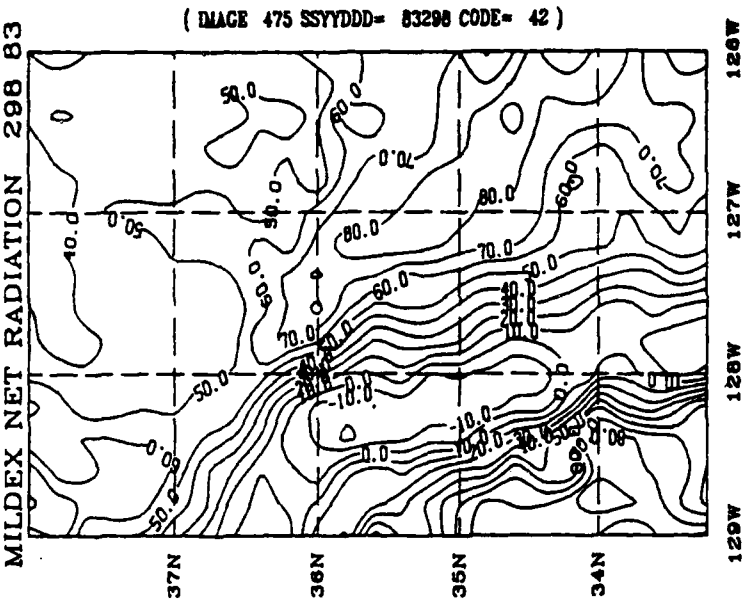

Figure 8c Net radiation field estimated from satellite during MILDEX.

Acknowledgments

This research has been supported by the National Science Foundation (grant NSF OCE82-14791) and the preparation of this document has been supported by the Office of Naval Research University Research Initiative (grant N00014-86-K0752).

I would like to thank Dr. Robert Frouin for his contribution to this research, Dr. C. Paulson for making his surface measurements available, and Dr. M. Lewis for pointing out to me the importance of oceanic biological processes and radiative process interactions. In addition, I want to thank Mr. Brian Bloomfield for his editing support.

References

Bates, J., and W.L. Smith, Sea surface temperatures from HIRS2/MSU, J. Geophys. Res., 90, 11,609-11,619, 1985.

Cornillon, P., and L. Stramma, The distribution of diurnal sea surface warming events in the western Sargasso Sea, J. Geophys. Res., 90, 11,811-11816, 1985.

Gallegos, C., and T. Platt, Phytoplankton production and water motion in surface mixed layers, Deep-Sea Res., 29, 65-76, 1982.

Frouin, R., C. Gautier, and Morcrette, Downward longwave irradiance at the ocean surface from satellite data: methodology and in-situ validation, (accepted for publication) J. Geophys. Res., 1987.

Gautier, C., and R. Frouin, Variability of the daily net (shortwave and longwave) radiative flux at the ocean surface during MILDEX, Proc.of 6th Conf. on Atmos. Rad., Williamsburg, VA, 4 pp., 1986.

Gautier, C., and K. Katsaros, Insolation during STREX part I: comparisons between surface measurements and satellite estimates, J. Geophys. Res., 89, 11,779-11788, 1984.

Gautier, C., G. Diak, and S. Masse, A simple physical model to estimate incident solar radiation at the surface from GOES satellite data, J. Appl. Meteor. (19, 8), 1005-1012, 1980.

Lewis, M. R., J. J. Cullen, and T. Platt, Phytoplankton and thermal structure in the upper ocean: consequences of nonuniformity in chlorophyll profile, J. Geophys. Res., 88, 2565-2570, 1983.

Lewis, M. R., E. P. W. Horne, J. J. Cullen, N. S. Oakey, and T. Platt, Turbulent motions may control phytoplankton photosynthesis in the upper ocean, Nature, 331, 49-50, 1984

Moum, J. N., D. R. Caldwell, C. A. Paulson, T. K. Chereskin, and L. A. Regier, Does ocean turbulence peak at the equator? J. Phys. Oceanogr., 16, 1991-1994, 1986.

Mower, R. N., G. L. Austin, A. K. Betts, C. Gautier, R. Grossman, J. Kelly, F. Marks, and D. W. Martin, A case study of GATE convective activity, Atmos. Ocean., 17, 46-59, 1979.

Park M.M. et al, Tropic heat 1984 rapid sampling vertical profiler observations, Col. of Ocean, Oregon State Univ., 85-21, 396 pp.,1985.

Price, J. F., R. A. Weller and R. Pinkel, Diurnal cycling: Observations and models of the upper ocean response to diurnal heating, cooling, and wind mixing, J. Geophys. Res., 91, 8411-8427, 1986.

Stramma, L., P. Cornillon, R. A. Weller, J. F. Price, and M. G. Briscoe, Large diurnal sea surface temperature variability: satellite and in situ measurements, J. Geophys. Res., 16, 827-837, 1986.

MONITORING OCEAN SURFACE LAYER PROCESSES

W. G. Large

National Center for Atmospheric Research
Boulder, Colorado 80307

ABSTRACT

The monitoring of several upper ocean processes over large spatial scales on monthly and longer time scales is discussed. The surface forcing functions of wind stress, heat flux, and freshwater flux are treated in terms of the potential roles that in situ observations, satellites, and atmospheric general circulation models might play in producing the most useful fields on a regular basis globally. Thermocline mixing and daily cycling are presented as examples of phenomena that, once understood from intensive regional studies, could be observed from a much wider perspective using relatively easily measured data. Specifically, episodic cooling, a symptom of intense thermocline mixing in the North Pacific during autumn, appears to occur over large regions of the Southern Hemisphere, depending on the annual cycle of wind forcing. Also, the daily cycle of equatorial oceanic turbulence seen in the short Tropic Heat study of 1984 appears to persist throughout the year over 20° of longitude. A similar cycle is not evident during heating season in the Sargasso Sea.

INTRODUCTION

Only a few of the parameters important to ocean surface layer processes are currently being monitored. One example is the vertical temperature profile from ship of opportunity XBT casts. Most of the others are summarized in the Climate Diagnostics Bulletin (CDB), distributed monthly by NOAA's Climate Analysis Center (CAC). In addition, the Australian Bureau of Meteorology's National Climate Center issues a Southern Hemisphere Climate Monitoring Bulletin (SHCMB) each month.

A large international effort is underway to take large numbers of XBT casts in most of the world's oceans, excepting the Arctic and Southern Oceans. From these casts, important parameters such as thermocline depth and heat content can be computed on a quasi-synoptic basis. In the Anomaly Dynamics Study, for example, such data and winds were used to test the Ekman pumping mechanism in the North Pacific (White et al., 1980). In a study of thermal variability in the Pacific from 20°S to 50°N, White et al. (1985) used 85000 XBT observations. Recently, the Tropical Oceans Global Atmosphere (TOGA) program has provided the impetus for a rapid expansion of the XBT network in all three equatorial oceans. In the Pacific an ambitious program calls

for sampling with 1 to 2° latitude and 10 to 20° longitude spacing on a monthly to seasonal time scale. An extensive program is planned initially for the Indian Ocean in order to establish its data base. An Atlantic XBT network is well on its way to becoming operational.

The oceanographic data in the CDB are particularly useful for following the generation and eastward propagation of Kelvin waves along the Pacific equator. These data include pan–Pacific sea level anomalies and Equatorial Pacific thermocline depth (depth of the 20°C isotherm from the XBT program), surface wind psuedo–stress vectors, and zonal wind indices. Interest in Equatorial Pacific wave processes stems from the focus of the TOGA program on ENSO (El Niño, Southern Oscillation) phenomena. Global fields in the CDB appear to be less concerned with specific processes. However, they do include several air–sea interaction parameters; namely, sea level pressure, sea surface temperature (SST), 850mb vector wind, and outgoing longwave radiation. The SHCMB deals primarily with meteorological variables, but it does include SST anomalies.

Of course equatorial waves and the surface forcing are not the only important processes that govern the upper ocean's structure. However, studies of other processes, such as mixing, diurnal cycling, Langmuir circulation, entrainment, and advection, have largely been confined to local, small scale, short duration, observational programs, such as JASIN, MILE, STREX, FASINEX, and Tropic Heat. In order to assess the overall impact of a particular process on the state of the upper ocean it is not enough to observe it in one of these programs. It is also necessary to determine both its frequency of occurrence and its global distribution. Such assessments are essential to the success of large scale oceanographic and climatic programs like WOCE (World Ocean Circulation Experiment) and TOGA.

Realistically it will not be possible to mount intensive process oriented experiments covering all seasons in more than a few regions of the world's oceans. Therefore, indirect methods, through indices or signatures involving more easily measured parameters, need to be developed and tested for monitoring important surface layer processes globally. In the case of the surface forcing functions and waves in the Equatorial Pacific, the situation appears to be relatively well in hand. The former will be discussed further in the next section. Generally, other processes are not being looked at in this way, but the following attempts to do so for a particular thermocline mixing process and for an aspect of diurnal cycling.

SURFACE FORCING FUNCTIONS

The ocean is forced by the surface fluxes of momentum (wind stress), $\vec{\tau}_0$, heat, Q_0, and freshwater, F_0. Global wind stress measurements are showing a great deal of promise, because of the advent of satellite techniques for both scalar (altimetry, radiometry) and vector (scatterometry) wind estimates, and because of the long term efforts to establish the parameterization :

$$\vec{\tau}_0 = \rho_a C_D U \vec{U}0 \tag{1}$$

where the drag coefficient C_D is a function of measurement height and stability, ρ_a is the air density and $\vec{U}$ is the wind velocity, with U its magnitude.

The surface heat flux into the ocean, Q_0 , is the balance between net solar heating SW, net longwave radiation LW, the latent heat flux H_L , and the sensible heat flux H_S:

$$Q_0 = SW + LW - H_L - H_S \cdot \tag{2}$$

The bulk transfer coefficients, C_E andC_T, in the formulae

$$H_L = \rho_w \Lambda E_0 = \Lambda C_E U(q_0 - q_a) \tag{3}$$

$$H_S = \rho_a c_p C_T U(T_0 - T_a), \tag{4}$$

where Λ is the latent heat of evaporation, ρ_w is the density of seawater, q_0 and q_a (T_0 and T_a) are the air humidities (temperatures) at the surface and measurement height, respectively, and c_p is the specific heat of air, are less well established than C_D . Nevertheless, suitable measurements of the mean quantities in (3) and (4) would give global estimates of H_L and H_S . The prospect of monitoring Q_0 globally has improved greatly, because of the recent development of techniques for estimating SW from satellite imagery (Gautier et al., 1980). Should present efforts to retrieve LW also prove fruitful, then it will become feasible to produce fields of Q_0 routinely.

The difference between the rates of evaporation, E_0 , and precipitation, P_0, is

$$F_0 = E_0 - P_0 \cdot \tag{5}$$

Although (3) parameterizes E_0, measurements of P_0, either from satellite or in situ, are unproven and may preclude using (5). However, the net divergence of moisture in a vertical column of the atmosphere is a direct measure of F_0 , that it may be possible to extract from an atmospheric general circulation model, such as those used at the major forecast centers, such as ECMWF (European Center for Medium Range Weather Forecasting) and NMC (the U.S. National Meteorological Center).

The problem of producing global fields of the forcing functions for WOCE is addressed in Large (1985). What emerges there and here is that should the following become available :

1) Standard bulk parameterizations (1), (3) and (4) with established uncertainties

2) Satellite SW and LW,

3) Satellite and in situ SST (T_0 and q_0),

4) Atmospheric GCM assimilation of bulk parameters, especially U, q_a, and T_a, and computation of F_0,

then useful estimates of the forcing functions could be produced routinely over all the world's oceans. Of course the accuracy would likely be better in the more well travelled and sampled northern hemisphere.

Should such an effort be undertaken, there would need to be a significant effort put into data communication and management. Figure 1 shows the present scheme used by NOAA to produce monthly SST maps. It uses data from voluntary observing ships (VOS) and select buoys as ground truth for satellite radiometric fields. Also shown are other potential sources of data that could be incorporated for a better product. The improvements possible include smaller spatial and shorter temporal resolution, greater accuracy, and a more geographically uniform reliability.

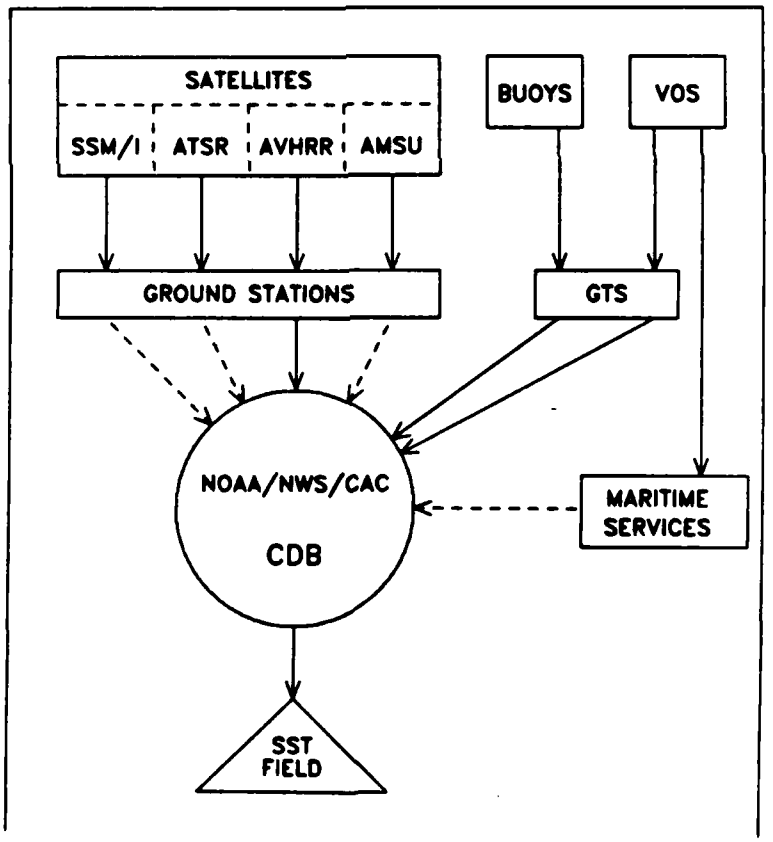

Fig. 1 Satellite and in-situ data flow of measurements relevant to producing sea surface temperature fields. Solid lines represent the flow used by CAC, and the dashed lines are potential augmentations.

Figure 2 shows the hypothetical data flow needed to produce surface wind stress fields. The most straightforward path is to produce the fields from satellite data alone. It is being pursued by NASA. Should this approach prove to be too unreliable it may be necessary to gather more of the available surface wind data together to produce the stress field as is being done for TOGA. Figure 3 illustrates the possible role of an atmospheric general circulation model. It is now being explored for the limited case of incorporating near-real-time satellite wind data (from ERS-1) into the surface analysis now performed at ECMWF before forecast runs. Such a scheme may exclude a great deal of data that arrives too late. The alternative that would make maximum use of all data is to run a delayed analysis. Since the result would not be of use to forecasts there are considerable political and economic problems with implementing such an operation. Therefore, it is first essential to establish that such an effort is needed and worthwhile.

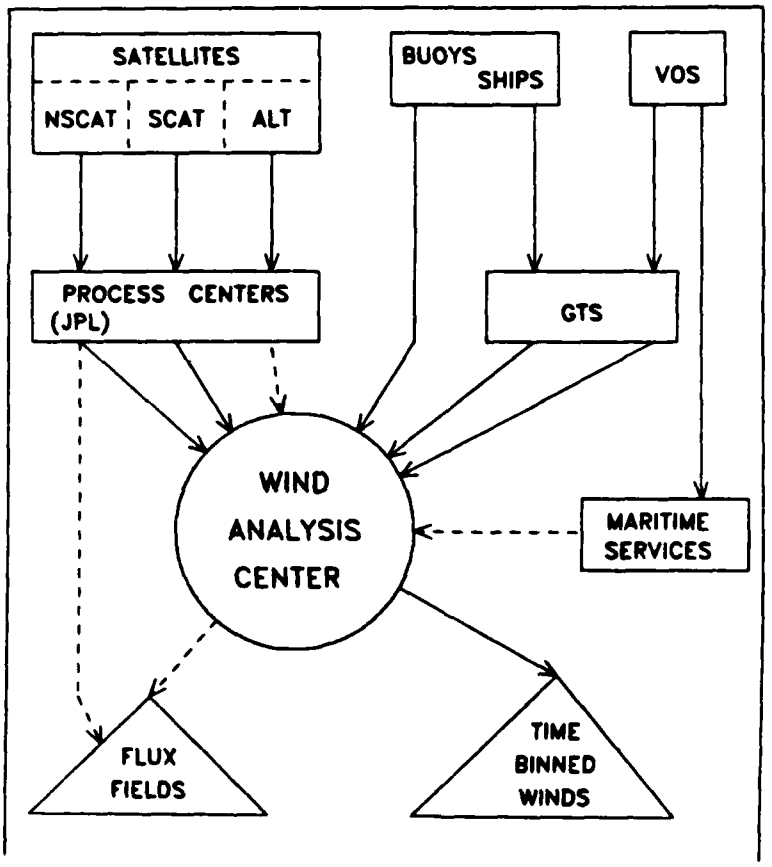

Fig. 2 Hypothetical data flow into a wind analysis center, where time binned wind fields as well as the wind stress field could be produced.

THERMOCLINE MIXING

One of the important discoveries of the Storm Transfer and Response Experiment (STREX) was that the episodic nature of the autumn SST cooling is indicative of intense vertical mixing in the seasonal thermocline, whereby cool thermocline water is exchanged with warm mixed layer water, without the mixed layer depth necessarily increasing as required for entrainment (Large et al., 1986). Furthermore, subsequent horizontal advection in the now locally warmer thermocline could be responsible for the ultimate removal of summertime mixed layer heat from the water column. This heat loss was estimated to be sufficient to account for the annual average imbalance between Q_0 and local heat storage observed by Tabata (1965).

The STREX scenario appears to be common over a large area of the Gulf of Alaska and is a major component of the annual heat budget. The question to be addressed here is: Are there any other ocean regions where similar physics are important and what are

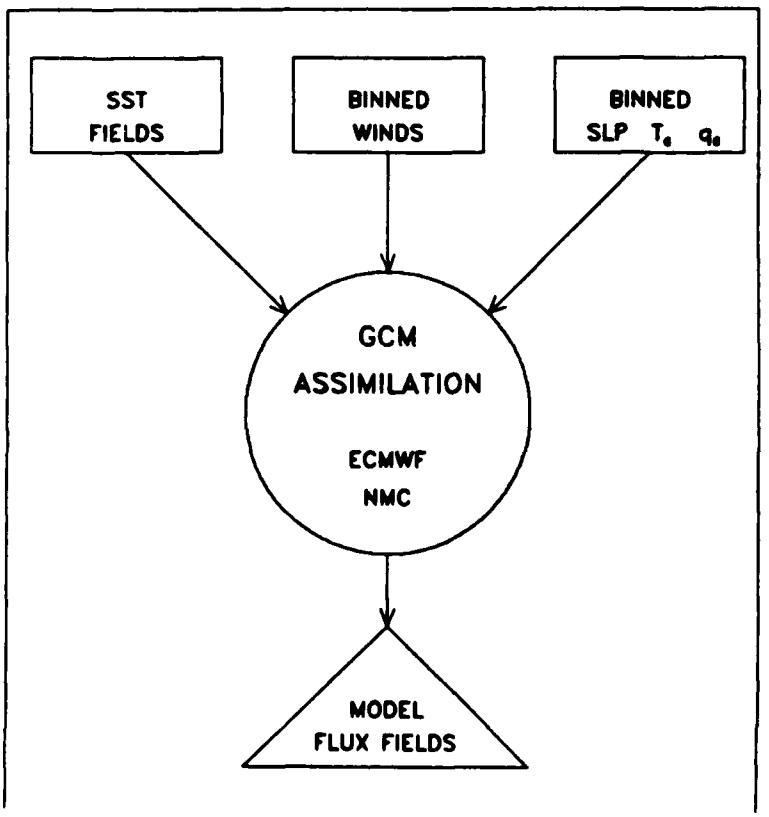

Fig. 3 Hypothetical data flow for assimilation and flux field production by an atmospheric general circulation model. Potential venues are the European Center for Medium-Range Wather Forecasting (ECMWF) and the U.S. National Meteorological Center (NMC).

the necessary conditions? First, it is necessary to develop quantitative measures of the episodic behavior of the autumn SST decrease in STREX. These measures can then be computed for all the 1979 southern hemisphere SST records from the FGGE drifting buoy array. Where these values are similar to those found in STREX it is probable that similar thermocline mixing also occurred.

The episodic nature of the STREX fall cooling is illustrated in Fig. 4, where the fraction of the net cooling over 50 days is plotted cumulatively against that fraction of the 50 days over which the cooling took place. Because of the brief intense cooling events, 80% of the ~3.0°C takes place in just 20% of the time and cooling occurs only 50% of the time. Solar heating and some negative H_L are occasionally sufficient (12% of the time) to produce some heating. A measure of the departure from uniform cooling is the area between the solid and dashed curves, A = 0.60.

Plots similar to Fig. 4 were produced for 120 FGGE buoys with a complete SST

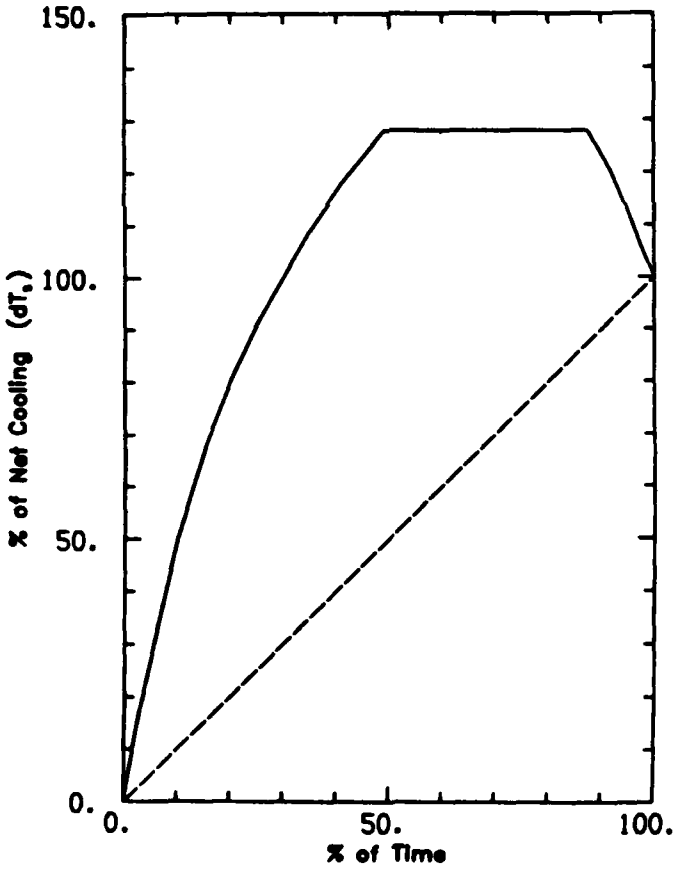

Fig. 4 Normalized cumulative sea surface temperature cooling curve from nine drifting buoys near Ocean Weather Station "PAPA" over 50 fall days of both 1980 and 1981.

record over the 60 autumn days from 16 April to 15 June, 1979. An example of the SST data from buoy 54602 is shown in Fig. 5 along with the sea level pressure at the buoy. Episodic cooling is evident and as in STREX it appears to be associated with some, but not all, of the storm conditions (low pressure). The SST records were smoothed by averaging over each 48-h period and excluding any period with fewer than two SST observations. The results from buoy 54602 (Fig. 6) are very similar to the STREX experience, implying that in this area (40–45°S, 160–170°W) of the South Pacific Ocean, the mixed layer physics, including thermocline mixing, during the fall season is similar to that found in the North Pacific. The probability distribution (histogram) of "amount of cooling over two days" is very distinct for regions of episodic cooling. It is very non-Gaussian with a large standard deviation. There are also too many cases of values very much smaller (more negative) than the mean amount of cooling.

From the time series and histograms it was possible to associate some of the buoys with episodic cooling and these are plotted with solid circles and trajectories in Fig. 7. Other buoys do not seem to experience this mode of cooling and they are shown as open circles and dashed trajectories. Others, where it is unclear, have been omitted. At present this selection process is rather subjective and efforts are underway to find quantitative criteria by which to judge whether or not buoy SST time series is indicative of episodic cooling.

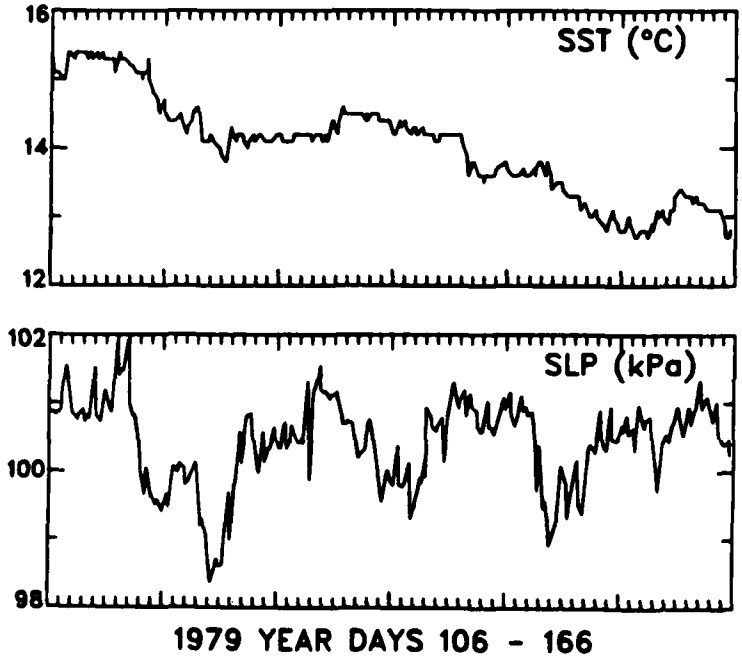

Fig. 5 Sea surface temperature (SST) and sea level pressure (SLP) at FGGE buoy 54602 (40–45° S, 160–170° W) from 16 April to 15 June 1979.

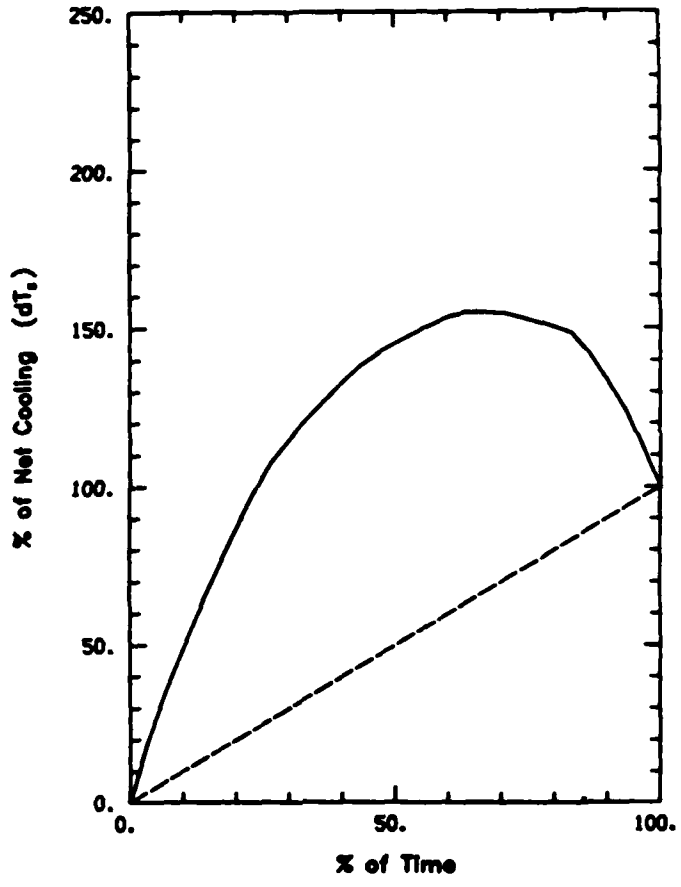

Fig. 6 Normalized cumulative sea surface temperature cooling curve at FGGE buoy 54602, from 16 April to 15 June 1979.

Figure 7 suggests that thermocline mixing occurred in two distinct regions: one in the South Pacific and the other in the South Atlantic. They both extend over most of the basins in longitude and are both bounded approximately by 35 and 45° south latitude. There does not appear to be a corresponding region in the Indian Ocean, nor is there any evidence of episodic cooling anywhere around the Southern Ocean, which includes the southern latitudes corresponding to the STREX area (50°N).

The geographic distribution found in Fig. 7 appears to be governed by the summer and fall surface wind forcing. In order to have intense thermocline mixing cause episodic cooling, the summer winds need to have been weak enough for a shallow warm mixed layer to form over a strongly stratified seasonal thermocline, as is the case in the Gulf of Alaska. From Fig. 8a it is remarkable how closely the episodic cooling regions of both the Atlantic and Pacific correlate with the latitudes of low (<5 m/s) mean 1979 summer winds. Farther south the winds were very much stronger, probably preventing the establishment of a seasonal mixed layer and thermocline. Secondly, the autumn

winds must be very strong to generate sufficient inertial shear across the thermocline for it to go unstable and provide the energy for mixing. Although there is a large area of weak summer winds over the Indian Ocean (Fig. 8a), the autumn winds in this area appear too weak (Fig. 8b) for thermocline mixing. In contrast the areas of episodic cooling in Fig. 7 experienced an intensification from low to moderate (5–10 m/s) in the mean wind from summer to fall.

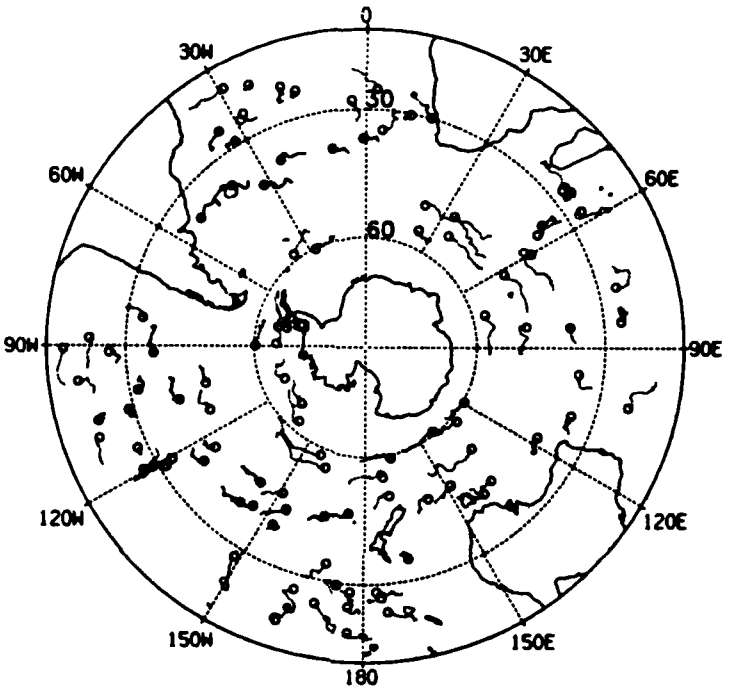

Fig. 7 Trajectories of 98 FGGE drifting buoys over the Austral autumn of 1979. Solid circles indicate the 16 April positions of buoys clearly displaying episodic cooling and the solid lines show their 60 day movement. Open circles and dashed trajectories represent buoys that do not seem to have experienced such cooling.

THE DIURNAL CYCLE

Renewed interest in the diurnal cycle of the upper ocean has been spawned by the Tropic Heat observation that near equatorial (Pacific) values of turbulent kinetic energy dissipation rate (and hence vertical mixing) are much larger at night than during the day (Chereskin et al., 1986). Also, the mid-latitude diurnal cycle has recently been intensely sampled and modelled (Price et al., 1986).

The upper ocean heat budgets during the day and at night are, respectively,

$$H_t^D = SW - L^D - A^D - R^D \text{ , and} \tag{6}$$

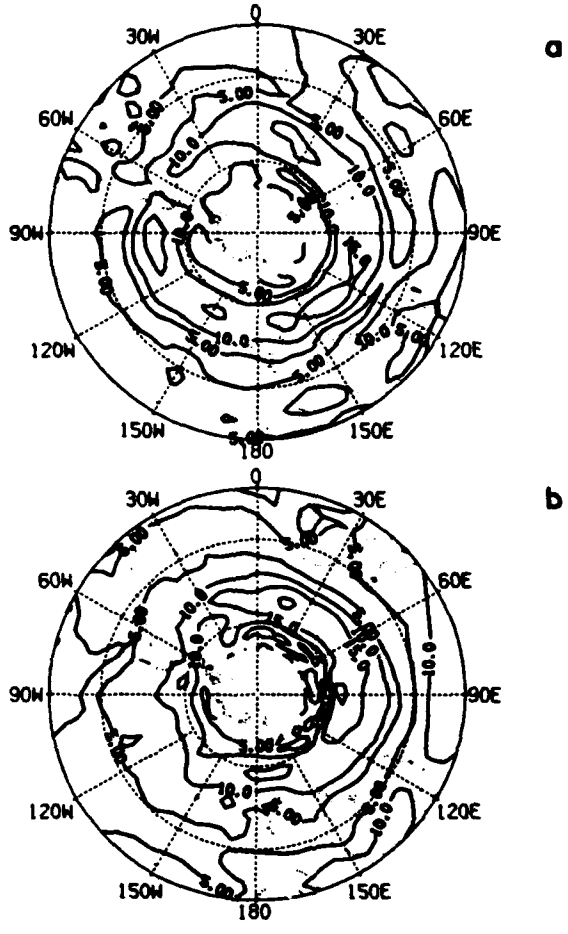

Fig. 8 Mean geostrophic surface wind speed (m/s) in the southern hemisphere, a: January–February (summer) 1979 and b: April–May (autumn) 1979.

$$H_t^N = -\left(L^N + A^N + R^N\right), \tag{7}$$

where H_t is the average rate of change in heat content; $-L = LW - H_L - H_S$; A and R are, respectively, the net advection and turbulent cooling; and superscripts D and N refer to day and to night, respectively. Subtraction of (7) from (6) yields an expression for the night–to–day bias in the sum of the loss terms,

$$B = \Delta\left(L + A + R\right) = \left(H_t^D - H_t^N\right) - SW \cdot \tag{8}$$

Imawaki et al. (1987) demonstrate that in the eastern Equatorial Pacific there is no night–to–day bias in either L or A, and so they were able to reduce (8) to a measure of the bias in the turbulent cooling,

$$\Delta R = \left(H_t^D - H_t^N\right) - SW \tag{9}$$

$$\Delta H_t = \left(H_t^D - H_t^N\right) = \frac{\rho_w c_w}{\Delta t} \int_{-h}^{0} (2T(2) - T(1) - T(3))\, dz \tag{10}$$

where c_w is the water's specific heat, $\Delta t = 12$ hours, h is depth, and the ocean temperatures at sunrise, sunset, and sunrise the next day are T(1), T(2), and T(3), respectively. Thus, using only thermistor chain data and SW values from satellites, they were able to extend the conclusions of the Tropic Heat observations of dissipation rate made at 140°W. Their results from 125°W (Fig. 9) and 140°W indicate that the bias persists throughout the year at both longitudes. It is also evident at 1°S at 140°W.

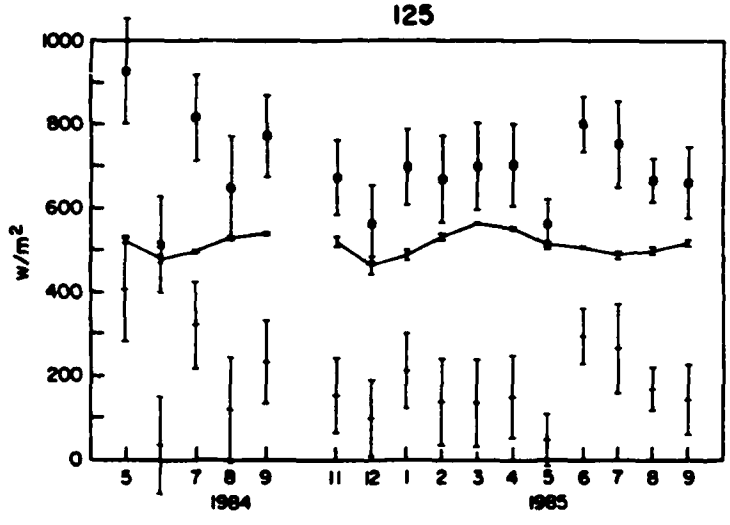

Fig. 9 Monthly mean estimates of ΔH_t (open circles), SW (solid line) and ΔR (crosses) from mooring data on the equator at 125° W. Abscissa is the month of 1984 and 1985 (from Imawaki et al., 1987.)

Observations of the diurnal cycle (34°N, 70°W) in the Sargasso Sea have been reported by Price et al. (1987). From April through August of 1983 there were also three thermistor chain drifting buoys in the vicinity. It is evident that days of strong solar heating and little wind display large diurnal variations in surface temperature. Observations of daytime temperature changes and of SW give the sum of the daytime loss terms in (6), $(L^D + A^D + R^D)$. Since there is no solar heating at night the measured heat content change must reflect the sum of the nighttime loss $(L^N + A^N + R^N)$. In contrast to the Equatorial Pacific, the tendency during the spring and summer in the Sargasso Sea appears to be for B in (8) to be negative.

Figure 10 shows the average profile from the drifting thermistor chains of

$$\Delta T_t(z) = \left(\Delta t^D\right)^{-1} \left(T(2) - T(1)\right) - \left(\Delta t^N\right)^{-1} \left(T(3) - T(2)\right) \qquad (11)$$

where Δt^D and Δt^N are the length of day and night, respectively. Only 120 buoy days, where the diurnal SST warming at a buoy was greater than the overall average (0.37°C), are included in the Fig. 10 average. The average SW over these days was likely greater than the average SW at LOTUS over all the days (435 W/m^2). Even so, when this SW value is used in (8) along with $\Delta H_t = 300$ W/m^2 from the profile in Fig. 10 to h = 10 m, a negative value of $B = -150$ W/m^2 , results. Further work is needed to determine if this result is significant relative to the uncertainties and if so, to isolate which of the loss terms is responsible for the bias.

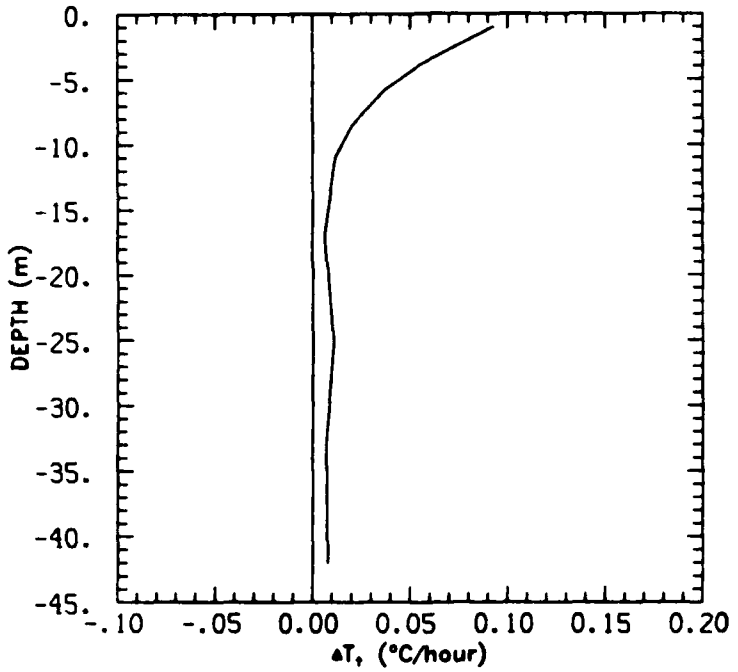

Fig. 10 Average profile from drifting thermistor chains of ΔT_t (11) over a total of 120 buoy days when the diurnal sea surface tempreature warming was greater than its overall average (0.37° C).

DISCUSSION

The advent of WOCE and TOGA has meant that more attention is being paid to the ocean basin and global scales than ever before. These programs require ocean data over very large scales, relatively frequently. It seems likely that fields of the

surface forcing functions will be produced routinely. However, a great deal of effort is still needed to obtain the necessary accuracies and coverage. Central to this activity are satellite observations whose value, although probably considerable, has yet to be fully demonstrated; however, their range of applications extends beyond the forcing functions.

Satellite altimetry promises to provide routine monitoring of global sea level; relative on its own and absolute in areas with sufficient supplementary data. Simulation experiments with eddy resolving ocean general circulation models indicate that TOPEX-like altimetric measurements will be extremely powerful in constraining models to behave properly. Even the lowest layers of a quasigeostrophic model feel the effects of the altimetric data, if properly assimilated, within a month or so (W. R. Holland, personal communication, 1987). Altimetry will also be able to track features of the turbulent mesoscale eddy field and of planetary waves.

Monitoring the upper ocean is particularly challenging, because of the numerous processes at work there, and its relatively rapid response to atmospheric forcing, which necessitates frequent sampling. Results from the foregoing examples of equatorial waves, thermocline mixing, and the daily turbulence cycle are encouraging and rewarding. It would be exciting and important if other upper ocean processes could be assessed globally using relatively easily obtained data. Some possible examples are subduction, Ekman advection, and Langmuir circulation.

REFERENCES

Chereskin, T.K., J.N. Moum, P.J. Stabeno, D.R. Caldwell, C.A. Paulson, L.A. Regier and D. Halpern, 1986:Fine-scale variability at 140°W in the Equatorial Pacific. J. Geophys. Res., **91**, C-11, 12887-12897.

Gautier, C., G. Diak and S. Masse, 1980: A simple physical model to estimate incident solar radiation at the surface from GOES satellite data. J. Appl. Meteor., **19**, 1005-1012.

Imawaki, S., P. Niiler, C. Gautier, D. Halpern, R. Knox, W. Large, D. Luther, J. McWilliams, J. Moum and C. Paulson, 1987: A new method for estimating the turbulent heat flux and the bottom of the daily mixed layer. In preparation.

Large, W.G. (ed), 1985: WOCE Global Air-Sea Interaction Fields. U.S. WOCE Technical Report No. 1, 36 pp.

Large, W.G., J.C. McWilliams and P.P. Niiler, 1986: Upper ocean thermal response to strong autumnal forcing of the Northeast Pacific. J. Phys. Oceanogr., **16**, 1524-1550.

Price, J.F., R.A. Weller and R. Pinkel, 1986: Duirnal cycling: Observations and models of the upper ocean response to diurnal heating, cooling, and wind mixing. J. Geophys. Res., **91**, C7, 8411-8427.

Tabata, S., 1965: Variability of oceanographic conditions at Ocean Station 'P' in the Northeast Pacific Ocean. Trans. Roy. Soc. Can., III, Series IV, 367–418.

White, W., R. Bernstein, G. McNally, S. Pazan and R. Dickson, 1980: The thermocline response to transient atmospheric forcing in the interior midlatitude North Pacific 1976–1978. J. Phys. Oceanogr., **10**, 372–384.

White, W.B., G.A. Meyers, J.R. Donguy and S.E. Pazan, 1985: Short-term climatic variability in the thermal structure of the Pacific Ocean during 1979–82. J. Phys. Oceanogr., **15**, 917–935.

SIMILARITY THEORIES AND MICROTURBULENCE IN THE ATMOSPHERIC MIXED LAYER

C. W. FAIRALL

Department of Meteorology, Pennsylvania State University, 505 Walker Building, University Park, Pennsylvania, 16802

ABSTRACT

The cloud-free, convective mixed-layer is the simplest and best understood atmospheric boundary layer regime. Many of the mean and turbulent properties can be well represented by similarity models based upon scaling in terms of the basic forcing processes (e.g., the surface and tropospheric interfacial fluxes). The boundary layer can be divided into three scaling height regimes which, historically, are described with different scaling models: the surface layer (Monin-Obukhov similarity), the mixed layer (top-down/bottom-up diffusion), and the inversion layer (Wyngaard-Lemone entrainment similarity). These models are known to be particularly successful when used to describe the small scale turbulence properties (dissipation rates and structure function parameters for velocity and passive scalars). Combined with these simple models, measurements of small scale turbulence can be used to infer surface fluxes, entrainment rate, and flux profiles.

INTRODUCTION

Compared to the ocean, the atmospheric boundary layer (ABL) has been extensively investigated and, in many ways, is considered to be better understood. This understanding has developed from a combination of information sources: (1) laboratory models (e.g., Willis and Deardorff, 1974; Deardorff and Willis,1982), (2) three-dimensional, primitive equation large eddy simulations (e.g., Deardorff, 1974; Deardorff, 1980; Moeng, 1984),and (3) atmospheric measurements with aircraft and tethered balloons (e.g., Lenschow, 1973; Kaimal et al., 1976; Lenschow et al., 1980; Brost et al., 1982; Nicholls, 1984). Remote sensors are just beginning to make major contributions to knowledge about atmospheric boundary layers. An interesting example from Brost et al. (1982) is shown in Fig. 1, where aircraft measured profiles of the various terms of the budget equations for the turbulent kinetic energy (TKE) and vertical velocity variance are given. All terms are measured except the pressure terms which are inferred as an imbalance.

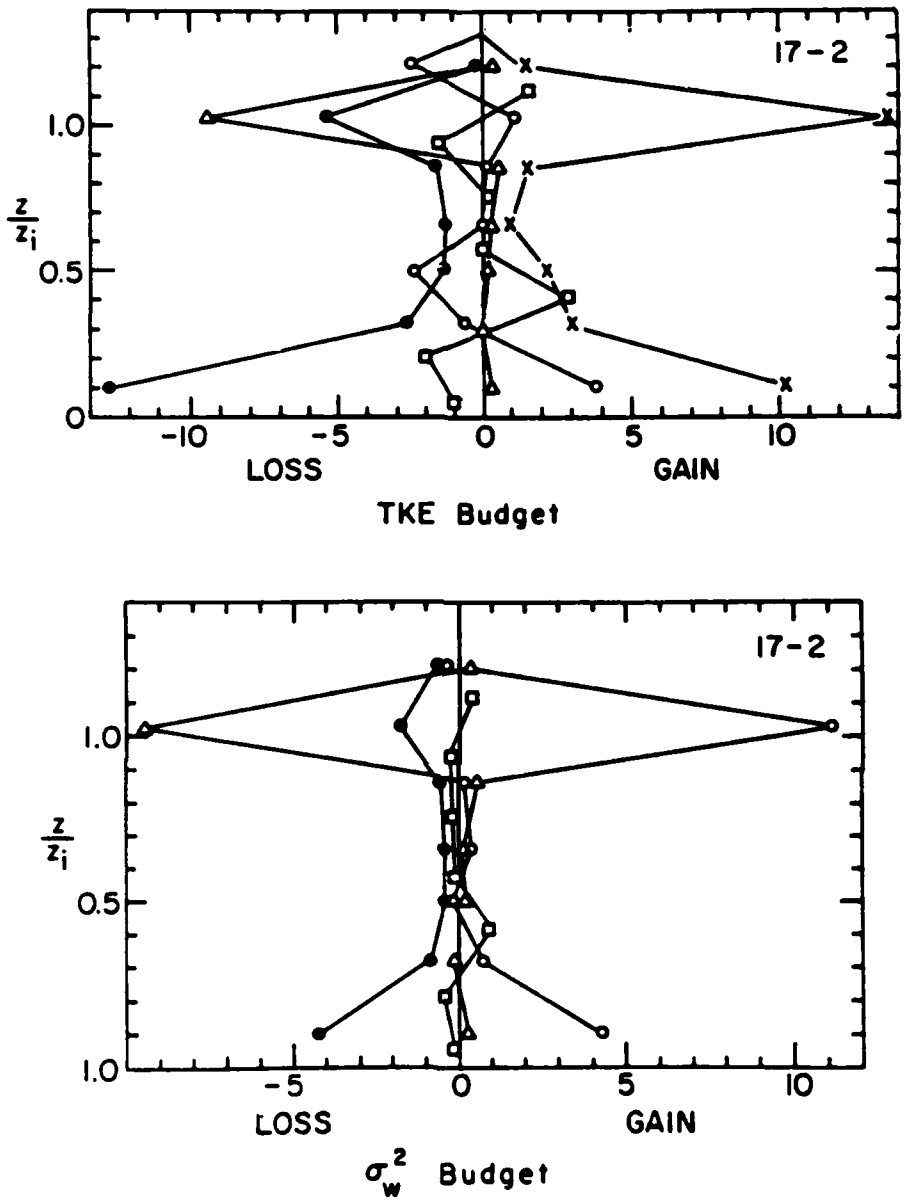

Fig. 1. Terms of the TKE budget (upper) and one-half the vertical velocity variance (lower) normalized by $\kappa z_i / u_*^3$. For the upper panel the terms are: dissipation (solid circles); shear production (crosses); buoyant production (open triangles); turbulent transport (open squares); and pressure transport (open circles). For the lower panel the terms are: $\epsilon/3$ (solid circles); buoyant production (open triangles); turbulent transport (open squares); and pressure scrambling (open circles).

Given this vast store of information, it is of interest to ponder the present 'state of understanding' of the ABL. I admit that the word understanding is rather subjective and that my own opinions may not be universally held. Given the complexity of ABL dynamics, it is natural to classify the conditions under dynamical regimes (see Table 1).

Table 1. An evaluation of the present 'state of understanding' for several typical ABL regimes.

Regime	Understanding
Cloudfree, convective	good
Cloudfree, shear driven	not good
Stratocumulus	not good
Tradewind cumulus	not good
Stable	poor
Broken cloud	poor
Mesoscale forcing	poor

One index of our understanding is the existence of simplified conceptual models and useful scaling laws or parameterizations. By this measure, the cloudfree, convective ABL is clearly the best understood regime. It is also closely analogous to the convective regime in the oceanic mixed layer; and the simple scaling laws may be applicable to both the ocean and the atmosphere. Some evidence for this viewpoint is given in Fig. 2, where profiles of the dimensionless rate of dissipation of TKE, ϵ/Jo, are remarkably similar in the ocean and the atmosphere (Jo is the surface buoyancy flux). This paper will present a summary of similarity models developed to describe the ABL. Following these introductory comments are sections on general background, surface flux scaling, entrainment scaling, and top-down/bottom-up diffusion.

BACKGROUND

Microturbulence Variables

The primary small scale turbulence variables of interest to meteorologists are the standard dissipation rates: ϵ (for TKE), χ_T (temperature variance), and χ_q (specific humidity variance). These variables represent the viscous/diffusive loss terms in the TKE or variance budget equations. The dissipations are related to the inertial subrange variables known as the structure function parameters,

$$C_x^2 = \langle (X(r)-X(r+d))^2 \rangle / d^{2/3} \qquad (1)$$

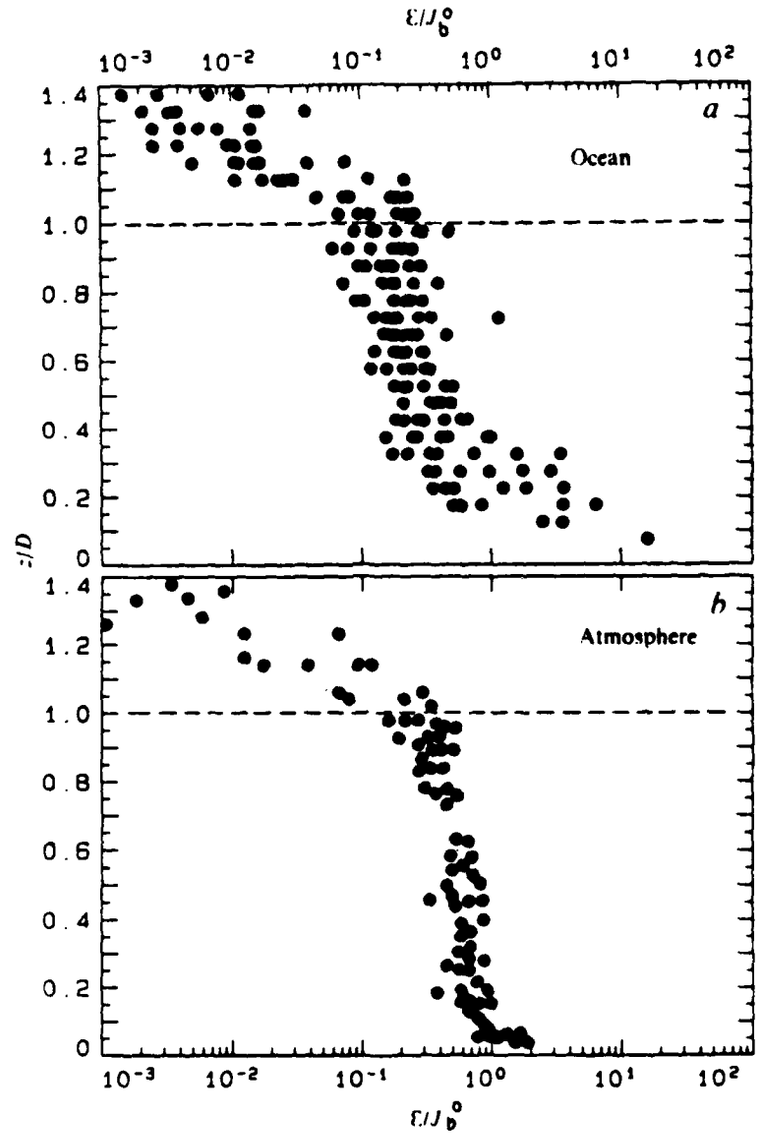

Fig. 2. Rate of dissipation of TKE (ϵ) scaled by the surface buoyancy flux (J_b^o) as a function of height (or depth) scaled by the mixed layer depth (D). The upper panel is from the ocean and the lower from the atmosphere (Shay and Gregg, 1984).

where X(r) represents the value of the variable X (X=u for velocity, T for temperature, and q for specific humidity) at the position r and X(r+d) is the value of X at a position a distance d from r. The brackets (<>) signify the standard ensemble average. In the inertial subrange of isotropic turbulence, the 1-dimensional variance spectral density, S_x, is given by the Kolmogorov -5/3 law:

$$S_x = 0.25\ C_x^2\ k^{-5/3} \qquad (2)$$

where k is the wavenumber magnitude. The structure function parameters and dissipations are related by the Corrsin's equation,

$$C_x^2 = 4\ \beta_x\ \chi_x\ \epsilon^{-1/3} \qquad (3)$$

where β_x is the Kolmogorov constant (β_u=0.5 and β_T=β_q=0.4) for the variable X. Note that for velocity, this implies that C_u^2=2 $\epsilon^{2/3}$. Incidently, the value 0.25 in eq.(1) is a mathematical constant while the β_x are empirically determined by measurement (e.g., Champagne et al., 1977).

The microturbulence variables are important for several reasons. The dissipation is important in dynamics and the inertial-dissipation method is useful for estimating surface fluxes over the ocean. In regions where gradient production is approximately balanced by dissipation, the dissipation profile can be used to infer the flux profile. The structure functions are important in the realm of wave propagation (optical, acoustic and radar) and atmospheric dispersion.

Scaling Regimes

Scaling theories have their origins in dimensional analysis, where important variables of the problem are selected and other properties are calculated from dimensionally consistent combinations of those variables. The basic concept of similarity theory is that some selected dynamical property (e.g., ϵ), when normalized by the proper combination scaling variables, can be described by 'universal' function of the scaling variables. In other words, the flow of honey around a basketball is indistinguishable (i.e., 'similar') from the flow of helium around a BB when viewed scaled by diameter and when the flow velocity is adjusted so the Reynolds numbers are the same. Modern ABL similarity theories are now based on arguments about the relative variability (or lack of variability) and magnitude of the various terms in the mean and turbulent budget equations (see Fairall and Larsen, 1986, for examples). Since this is considered to be a more firm foundation than the dimensional analysis approach, the universal function of the scaling variables described above is often referred to as a semi-empirical function. The 'semi' supposedly imparts some increased credibility. In fact the functions must be determined by measurements but often the limiting forms of the functions can be determined by scaling arguments so that only one or two constant coefficients must be determined by fitting to real data.

In the ABL the similarity regimes are broken down by vertical scale. Historically, this process has proceeded from the ground up. Fig. 3 depicts a schematic of the typical mean structure of the ABL under convective, well-mixed conditions in a synoptic regime with sufficient subsidence to ensure a healthy capping inversion. Compared to the ABL, the overlying free troposphere is essentially nonturbulent. Table 2 contains a summary of scaling regimes that will be discussed.

Table 2. Summary of the hierarchy of ABL scaling models/regimes beginning at the surface and moving up to the inversion. The basic scaling parameters, the form of the dimensionless height (ξ), the vertical region of applicability, and an example of a parameterization are given. The symbols will be explained in the text. Scaling parameters for humidity (not shown) are similar to those for temperature.

Name	Scaling parameters	ξ	Height Region	Example
Monin-Obukhov	u_*, T_*, z, L	z/L	constant flux	$\epsilon = u_*^3/(\kappa z)\ f(\xi)$
Free Conv.	$\langle w'T' \rangle_o$	-	$z \gg -L$	$\epsilon = 0.5(g/T)\langle w'T' \rangle_o$
Mixed Layer	W_*, θ_*, z_i	z/z_i	$\xi > 0.1$	$\epsilon = W_*^3/z_i\ F(\xi)$
Top-dn Bot-up	W_*, θ_*, z_i, R_x	z/z_i	$\xi < 0.9$	$F(\xi) = f_b + Rf_{tb} + R^2 f_t$
Invers.	$We, \Delta\theta, \Delta u, \Gamma_T$	-	$z \sim z_i$	$\epsilon = \epsilon_c + \Delta u^2 \Gamma_T We/\Delta\theta$

SURFACE FLUX SCALING

Monin-Obukhov

Surface layer similarity theory is based on scaling parameters obtained from the surface fluxes (Wyngaard, 1973). The theory is considered valid in the region near the surface where various terms (particularly the gradients) in the TKE and scalar variance budget equations are considerably more dependent on height than the surface fluxes. Thus, the assumptions on which the theory is based are generally valid in the lowest 10% of the ABL. The basic scaling parameters are the friction velocity, u_*, and the temperature scaling parameter, T_*, given by

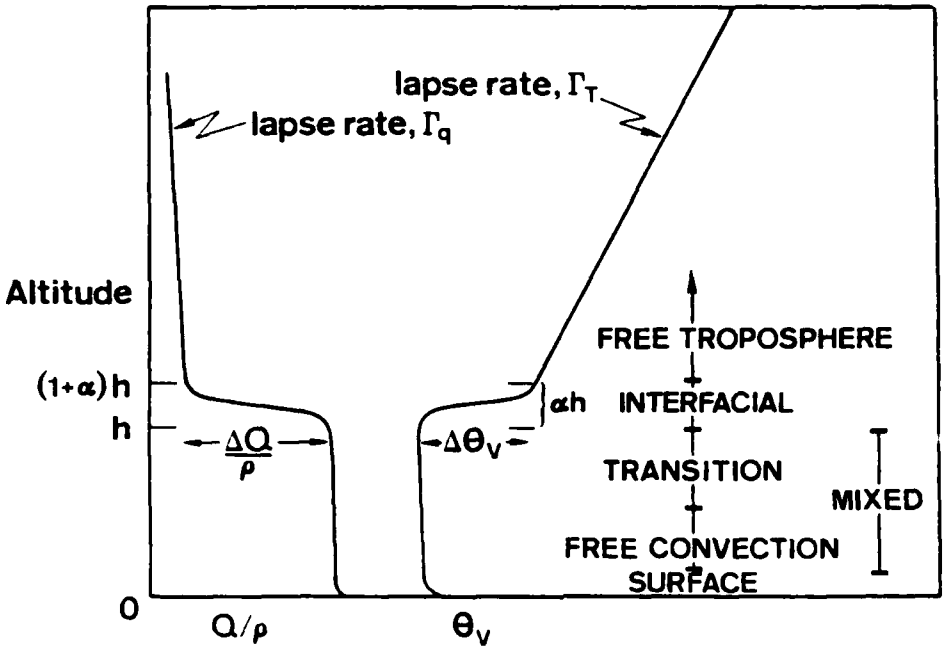

Fig. 3. Schematic of a typical convectively mixed ABL. The absolute humidity (Q) and virtual potential temperature (θ_v) are shown as a function of height where h is the height of the turbulent ABL.

$$u_* u_* = -\langle u'w' \rangle_o \tag{4a}$$

$$u_* T_* = -\langle T'w' \rangle_o \tag{4b}$$

where the primes denote turbulent fluctuations and the o denotes the surface value. The humidity equations will not be given since they can be obtained from the temperature equations by replacing T with q. According to M-O theory, the suitably non-dimensionalized variables are functions of the dimensionless height scale, ξ,

$$\xi = z/L = -\kappa(g/T)z\langle w'T' \rangle_o / u_*^3 \tag{5}$$

The standard meteorological convention is that heat flux is positive upward so that convective conditions are characterized by $\xi<0$. Consider as an example, the standard deviation of vertical velocity, σ_w, written

$$\sigma_w/u_* = f(\xi) \tag{6}$$

where $f(\xi)$ represents the semi-empirical dimensionless function.

The M-O forms for the microturbulence variables are

$$\epsilon\kappa z/u_*^3 = \Phi_\epsilon \tag{7a}$$

$$\chi_T \kappa z/(u_* T_*^2) = \Phi_\chi \tag{7b}$$

The dimensionless dissipation functions were initially measured in the famous Kansas experiment (Wyngaard and Cote, 1971; Wyngaard et al., 1971). For example,

$$\Phi_e = (1+0.5\ |\xi|^{2/3})^{3/2} \qquad (8)$$

under unstable ($\xi<0$) or convective conditions. Similarly, the dimensionless structure function parameters are given by

$$C_x^2 z^{2/3}/x_*^2 = f_x(\xi) \qquad (9)$$

and are shown in Fig. 4. Under unstable conditions, these are represented by the empirical formulae (Fairall and Larsen, 1986)

$$f_u(\xi) = 4.0\ (1+0.5\ |\xi|^{2/3}) \qquad (10a)$$

$$f_T(\xi) = 4.9\ (1-7.0\ \xi)^{(-2/3)} \qquad (10b)$$

$$f_q(\xi) = 0.7\ f_T(\xi) \qquad (10c)$$

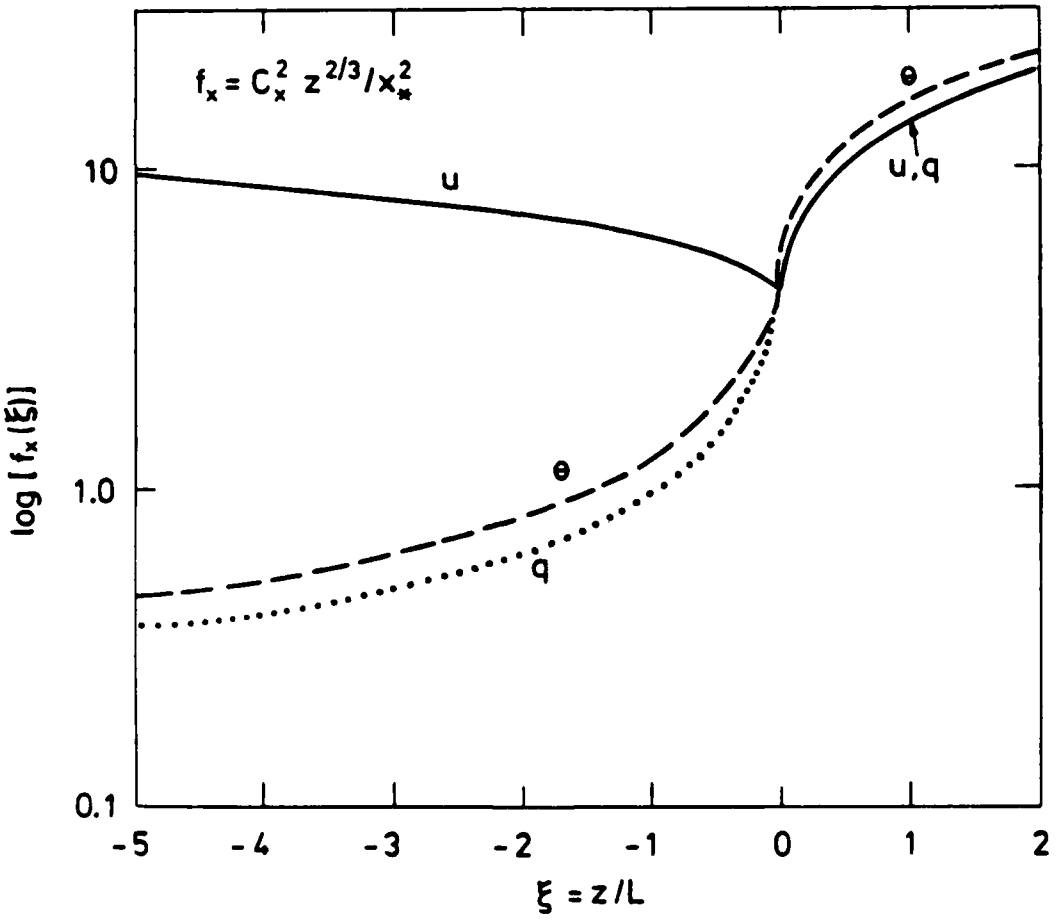

Fig. 4. Dimensionless structure function parameters (eqs.10) as a function of surface layer stability (ξ).

The empirical formulae for the dimensionless scalar variance dissipation functions can be obtained from eqs.(8) and (10) using the Corrsin relation given in eq.(3). Of course it is important to remember that these empirical formulae are only expected to be correct in an average sense and that any particular measurement (say a one hour average at a surface tower) can be expected to be in error by an amount associated with normal atmospheric variability and deviations from the assumptions of the theory (something on the order of 20% for the case sited above). The average accuracy of eqs. (8) and (10b) is illustrated by a series of aircraft profile data (Fairall et al., 1980) where 15 profiles have been normalized and averaged in bins of ζ (Fig. 5). The apparently poorer fit of the temperature struture data is believed to be caused by a failure of the isotropic assumption very near the surface (the temperature probe spacing was not much smaller than the altitude).

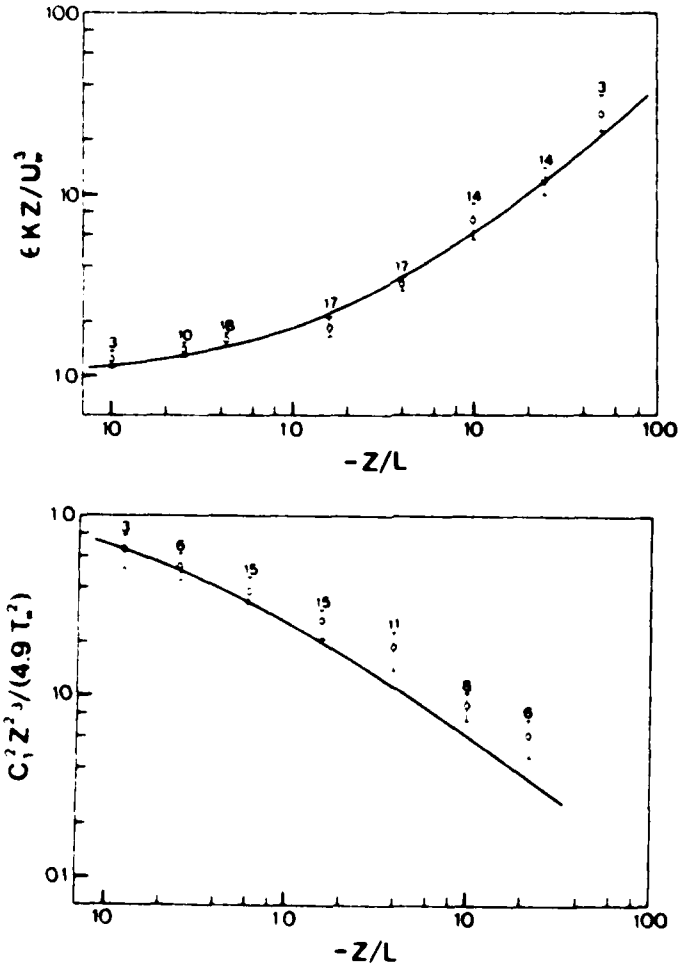

Fig. 5. Composites of aircraft measurements of ϵ and C_T^2 (non-dimensionalized) indicating the average fit of eqs.(10).

Free Convection

The mathematical form of the dimensionless functions as z/(-L) becomes large is referred to as the convective limit. This limit may be obtained by z becoming large at fixed L or by -L becoming small at fixed z. Physically, the convective limit is obtained when the buoyant production of TKE greatly exceeds the surface shear production (the two are equal when z=-L). Since the shear production due to the surface shear becomes unimportant, the friction velocity, u_*, is not a relevant scaling parameter in the convective limit. This means that T_* is also no longer relevant but is replaced as a scaling parameter by the surface buoyancy flux. The asymptotic behavior of the dimensionless functions is expressed as $f(\xi)\simeq\xi^m$ where m is a constant that is selected u_* to drop out of the scaling relation. For example, let us consider the relation for vertical velocity variance. As $-\xi$ becomes large, eq.(6) becomes

$$\sigma_w \simeq u_* \left[\kappa(g/T)z\langle w'T'\rangle_o/u_*^3\right]^m \qquad (11)$$

Clearly if m=1/3, then u_* will drop out of eq.(11) yielding

$$\sigma_w \simeq \left[\kappa(g/T)\langle w'T'\rangle_o z\right]^{1/3} \qquad (12)$$

This implies that σ_w increases as $z^{1/3}$ near the surface, which is consistent with observations (Wyngaard, 1973).

The forms of the dimensionless functions for the dissipation and structure functions [eqs.(8) and (10)] have been constructed to obtain the proper free convection limits. Thus, the structure function parameters have a $z^{-2/3}$ dependence very near the surface but approach a $z^{-4/3}$ behavior as z increases (see Fig. 6). Because the TKE has an additional source (buoyancy), the behavior for ϵ is quite different. Near the surface ϵ decreases as z^{-1} (which reflects the decrease in the shear production from the surface) but for large z, ϵ becomes independent of height,

$$\epsilon \simeq (0.5^{3/2}/\kappa)(g/T)\langle w'T'\rangle_o \qquad (13)$$

Note that eq.(13) implies $\epsilon/J_b^o\simeq$constant (recall the discussion concerning Fig. 2), where we used $J_b^o=(g/T)\langle w'T'\rangle_o$. These asymptotic behaviors are very consistently observed under convective conditions in the lower ABL (an example is given in Fig. 7).

Mixed-layer Scaling

The dynamics of the convective ABL are greatly influenced by the total depth, z_i, which determines the vertical scale of the largest eddies. Clearly, z_i is a natural choice for a length scale for mixed-layer scaling and it is natural to assume $\xi=z/z_i$ as the dimensionless length scale. The mixed layer velocity scale (usually called the convective mixing velocity) is easily obtained by writing eq.(12) in terms of ξ,

$$\sigma_w \simeq \left[(g/T)z_i\langle w'T'\rangle_o\right]^{1/3}(z/z_i)^{1/3} \qquad (14)$$

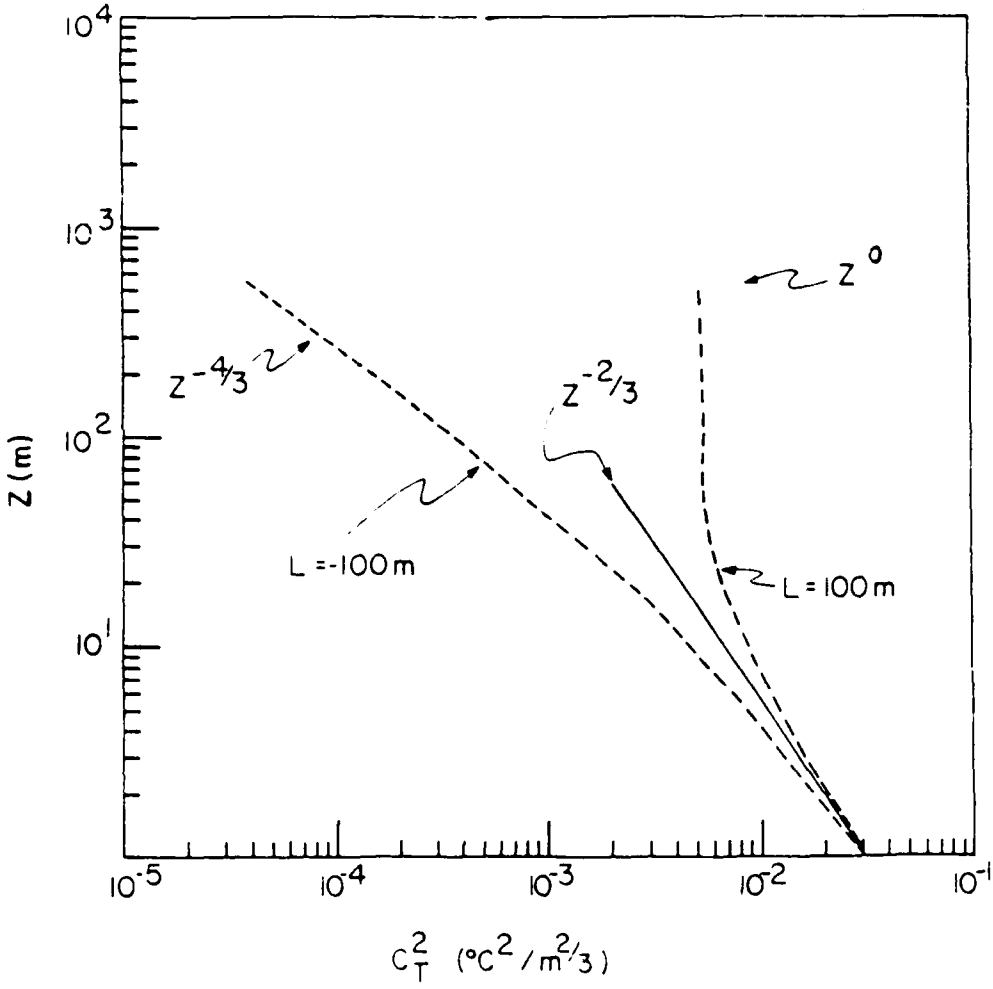

Fig. 6. Schematic representation of the altitude dependence of C_T^2 at fixed L for the asymptotic limits of surface layer scaling.

Following the philosophy expressed by eq.(6), the dimensionless vertical velocity standard deviation is

$$\sigma_w/W_* = f(z/z_i) \tag{15}$$

where the velocity scale is

$$W_*^3 = (g/T)\langle w'T'\rangle_o z_i \tag{16}$$

Similarly, the microturbulence parameters can be expressed in convective scaling,

$$\epsilon z_i/W_*^3 = F_e(\xi) \tag{17a}$$

$$C_T^2 z_i^{2/3}/\theta_*^2 = F_T(\xi) \tag{17b}$$

where $\theta_* = \langle w'T'\rangle_o/W_*$.

Failure of Surface Flux Based Scaling

The convective limit forms of eq.(17) are

$$F_{ef}(\xi) = \text{constant} \simeq 0.4 \qquad (18a)$$

$$F_{Tf}(\xi) = A_T \xi^{-4/3} \qquad (18b)$$

where A_T=2.7 is a constant obtained from eq.(10b). As described earlier (Fig. 2 and Fig. 7), the convective forms are often well followed in the lower ABL but deviations are usually observed in the upper ABL (particularly for the scalar structure function parameters). Further examples for C_T^2 are given in Fig. 8. The upper panel is from the classic convective regime of the so-called Minnesota experiment (Kaimal et al., 1976). Note that eq.(18b) is followed until ξ>0.5. The fact that the free convection form is not followed is, of itself, no cause for concern. Since $F(\xi)$ is an empirically determined function, we simply find the function that does fit the data. As long as our normalization collapses all conditions onto a single curve, the similarity hypothesis is valid. However, contrast the Minnesota data with several other field experiments (the lower panel in Fig. 8) where the deviations vary considerably.

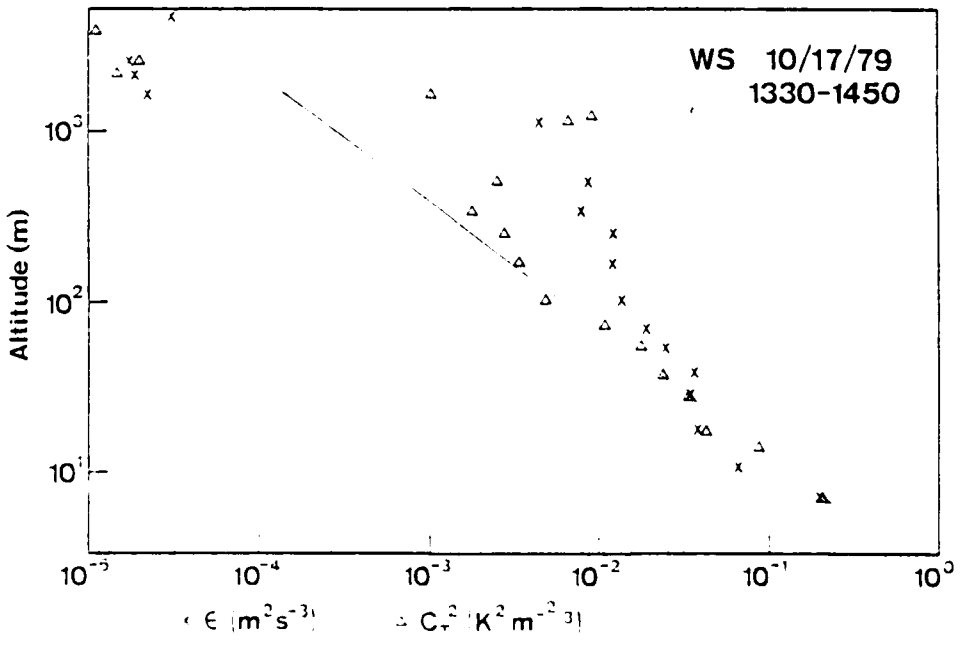

Fig. 7. An example of a profile of ϵ (X's) and C_T^2 (triangles). Note the deviations of the C_T^2 profile from the -4/3 altitude dependence in the upper mixed layer, the tendency of ϵ to approach a constant, and the dramatic decrease of both variables above the ABL.

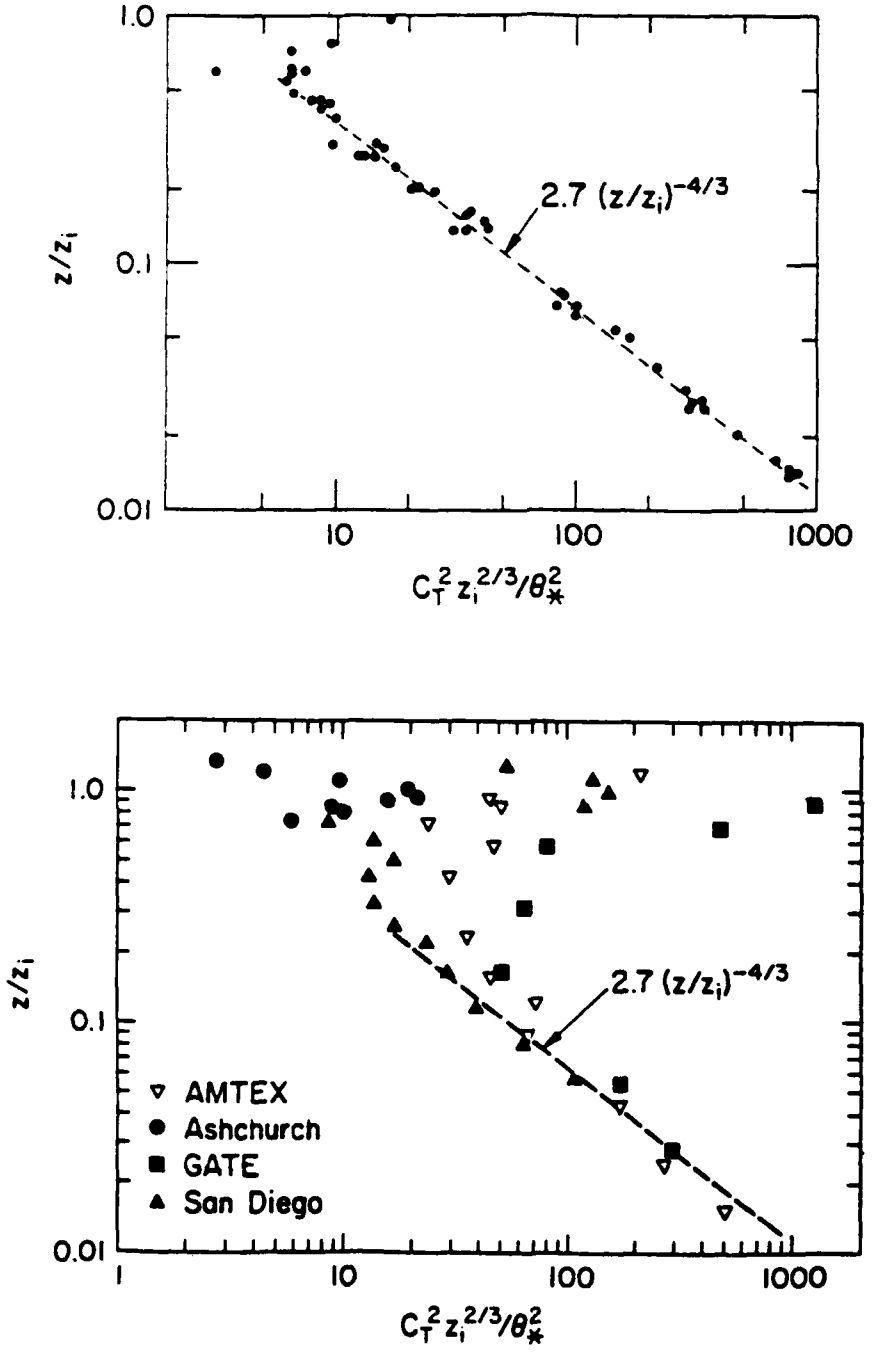

Fig. 8. Average normalized C_T^2 profiles from the Minnesota experiment (upper panel) and several other major field experiments (Wyngaard and LeMone, 1980). The lack of similarity for this scaling approach is apparent in the upper ABL.

Clearly there is no 'universal' function of the form $F(\xi)$. In order to construct a universal function we must consider at least one additional scaling parameter. Also, a careful examination of individual profiles shows that there are two separable deviations from the free convective forms: (1) a gradual increase in C_T^2 [relative to the value predicted by eq.(18b)] in the upper ABL and (2) a dramatic, spike-like increase confined to the interfacial region of the capping inversion. Both of these features are due to the entrainment process. The spike at the inversion is due to the large temperature variance created by mixing warm tropospheric air with cool ABL air at the interface. This behavior is described by the Wyngaard-LeMone interfacial entrainment model (Wyngaard and LeMone, 1980) which is described in the next section. The steady mixing and dissipation of the temperature variations as the recently entrained parcels are transported downward in the ABL lead to the smoother feature in the upper ABL. This behavior is described by top-down and bottom-up diffusion theory (Fairall, 1987).

THE ENTRAINMENT REGION

Background on Entrainment

Between the turbulent ABL and the nonturbulent free troposphere above is a transition or interfacial region characterized by rapid changes (or jumps) in the mean meteorological variables. Entrainment is the process whereby this boundary is eroded by the turbulent diffusive processes in the ABL. The erosion process creates a vertical flux in the interfacial region referred to as the entrainment flux, $\langle w'x' \rangle_i$, for the quantity X. This is illustrated in Fig. 9 where the upper panel shows a typical profile for the potential temperature and buoyancy flux and the lower panel shows mean and flux profiles for some unspecified quantity, X. Note that the buoyancy flux is negative in the entrainment region because the entrainment process transports warmer air downward and, therefore, consumes TKE. The entrainment flux is also represented as

$$\langle w'x' \rangle_i = -We\ \Delta X \qquad (19)$$

where We is the entrainment velocity and ΔX the increase [X_2-X_1 in Fig. 9] in X across the inversion. The rate of growth of the height of the inversion is

$$d(z_i)/dt = We+Ws \qquad (20)$$

where Ws is the subsidence velocity at $z=z_i$. Under cloud free, convective conditions the buoyancy flux in the entrainment region is typically about 20% of the surface value,

$$We_f = -0.2 \langle w'T' \rangle_o / \Delta\theta \qquad (21)$$

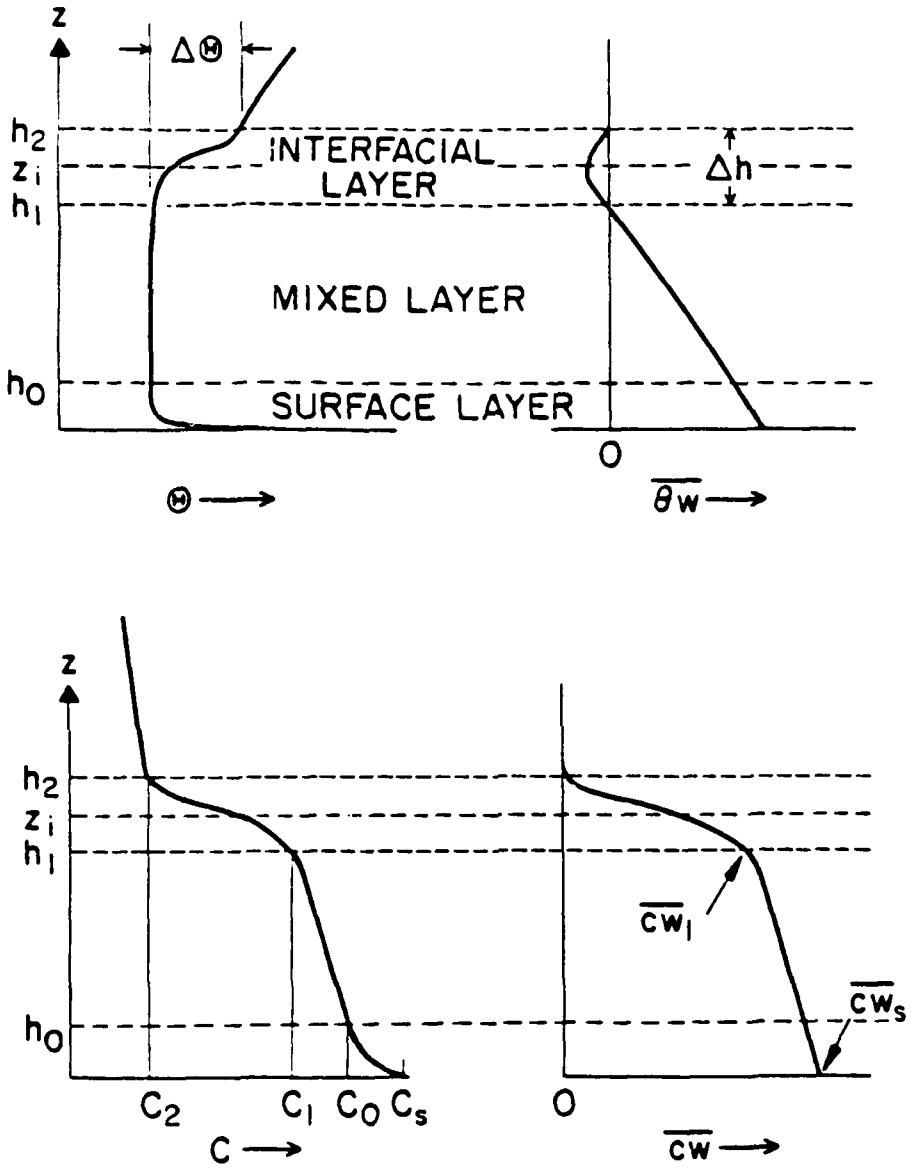

Fig. 9. Typical ABL structure for potential temperature (upper panel) and a conservative scalar (lower panel). The mean profile is on the left and the vertical flux profile is on the right.

Wyngaard-LeMone Scaling

Wyngaard and LeMone (1980) developed a scaling model for the scalar dissipations and structure function parameters in the interfacial region by considering the scalar variance budget equation

$$\partial\langle x'^2\rangle/\partial z = -2\langle w'x'\rangle\partial X/\partial z - \partial/\partial z(\langle w'x'^2\rangle) - \chi_x \qquad (22)$$

By considering only the average of the various terms of eq.(22) defined over the interfacial region, $\Delta z=h_2-h_1$, by

$$\bar{x} = (\Delta z)^{-1}\int x\, dz \qquad (23)$$

(where the integral is from h_1 to h_2), it can be shown that the scalar variance dissipation is approximately balanced by the gradient production term. Integrating by parts and assuming a cubic shape for the mean potential temperature profile in the interfacial region that matches the mean gradient of the lower free troposphere, Γ_T, yields

$$\bar{\chi}_x = (\Delta X)^2\Gamma_T We/\Delta\theta \qquad (24)$$

In the special case of $X=\theta$, the dissipation is about a factor of five smaller than indicated by eq.(24) because the temperature flux profile is zero at $z=h_1$ by definition (see Wyngaard and LeMone, 1980; Fairall, 1984).

The scalar structure function parameter can be evaluated using eq.(24) and the mean Corrsin relation [eq.(3)] where it is assumed that the average value of the TKE dissipation rate is one half the convective limit (ϵ_f)

$$\bar{\epsilon} = 0.5\ \epsilon_f = 0.2\ W_*^3/z_i \qquad (25a)$$

$$\bar{C}_x^2 z_i^{2/3}/(\Delta X)^2 = 2.3\ (\Gamma_T z_i/\Delta\theta)\ We/W_* \qquad (25b)$$

In the presence of inversion region velocity shear, a similar process can be followed (Fairall, 1984) to yield

$$\bar{\epsilon} = 3/2\ \epsilon_f - 1/2\ (g/T)We\Delta\theta + 1/2\ (\Delta U)^2\Gamma_T We/\Delta\theta \qquad (26)$$

If the velocity shear is zero and We is set to We_f, then eq.(26) will reduce to eq.(25a). Notice that if we define the dimensionless inversion layer thickness, $\alpha = \Delta z/z_i$, then eq.(25b) can be written in the natural interfacial scaling parameters

$$C_x^2(\Delta z)^{2/3}/(\Delta X)^2 = 2.3\alpha^{-1/3}S_T We/W_* \qquad (27)$$

The quantity $S_T=\Gamma_T\Delta z/\Delta\theta$ is the ratio of the stability of the free troposphere to the stability of the inversion. A representative atmospheric value is $\alpha^{1/3}\approx 0.6$.

TOP-DOWN AND BOTTOM-UP DIFFUSION

Background on ABL Diffusion

The concept of a mixed-layer is based on the observation that the mixing in the convective ABL is sufficiently strong to minimize the vertical gradients of the mean variables. This idea is often expressed in terms of an gradient diffusion coefficient, K,

$$\langle w'x' \rangle = -K \, \partial X/\partial z \qquad (28)$$

For a given value of the flux, the gradient will become very small if K becomes very large. Thus the vertical gradients in the mixed-layer are considered to be negligible or quite small. An important consequence of this assumption is that the flux becomes linearly dependent on height in the ABL (also true if the gradient is independent of time). Because convection is highly skewed (small, powerful updrafts but broadly diffuse downdrafts), the situation is more complicated than implied by the simple local gradient approach implied by eq.(28). Wyngaard and Brost (1984) have shown that the vertical diffusion of a passive, conservative scalar through the convective ABL can be considered as the superposition of top-down components driven by the scalar fluxes at the mixed-layer top and bottom-up components driven by fluxes at the bottom. This situation is depicted in Fig. 10 where a purely bottom-up (surface flux but no entrainment flux) configuration is shown in the left panel while the top-down configuration is shown in the right panel. An example of purely bottom-up diffusion could occur for evaporation from the ocean (finite surface flux) when the free tropospheric air had the same humidity as the ABL (no jump in q at the inversion). An example of purely top-down diffusion would occur with the dilution by entrainment of a completely nonreactive and insoluble gas (i.e., no deposition to the surface so the surface flux is zero) that was present in lower concentrations above the ABL.

The linear flux profile of the variable, X, is represented as the sum of two linear components

$$\langle w'x' \rangle = \langle w'x_t' \rangle + \langle w'x_b' \rangle = \langle w'x' \rangle_o (1-\xi) + \langle w'x' \rangle_i \xi \qquad (29)$$

In top-down/bottom-up notation, this is written

$$\langle w'x' \rangle = \langle w'x' \rangle_o [e_b(\xi) + R_x e_t(\xi)] \qquad (30)$$

where $e_b=(1-\xi)$, $e_t=\xi$ and $R_x=\langle w'x' \rangle_i / \langle w'x' \rangle_o$. The vertical gradient can be decomposed similarly as

$$\partial X/\partial z = \partial X_b/\partial z + \partial X_t/\partial z \qquad (31)$$

where the individual components are given by

$$\partial X_b/\partial z = -[\langle w'x' \rangle_o / (W_* z_i)] g_b(\xi) \qquad (32a)$$

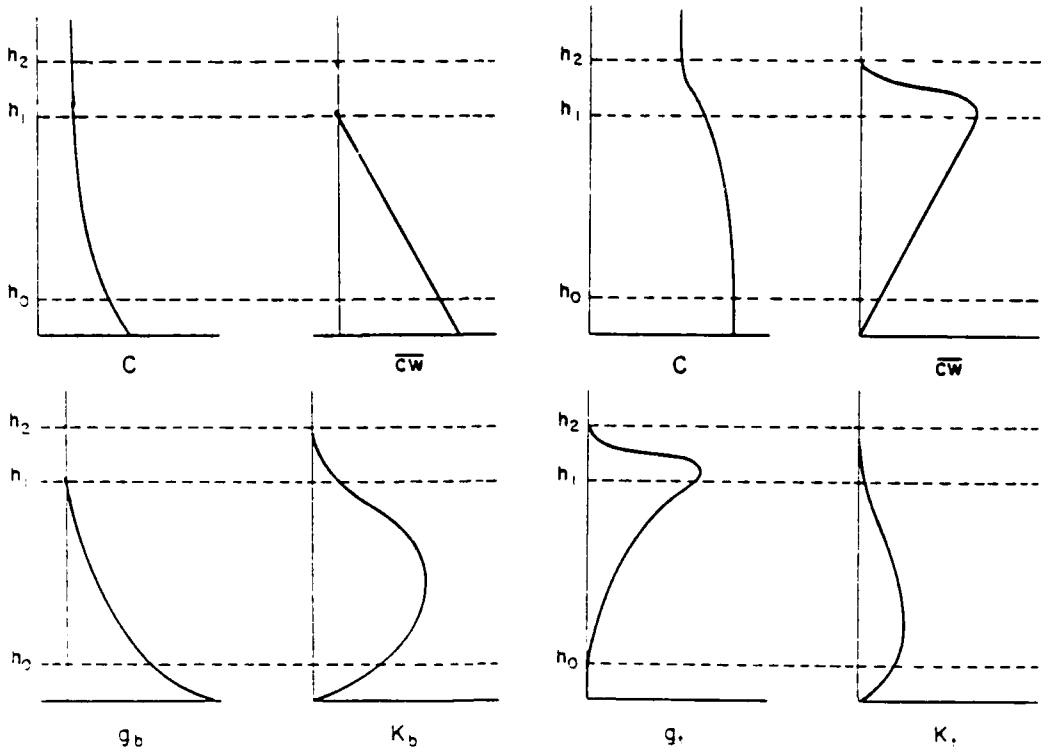

Fig. 10. Schematic representation of purely bottom-up up diffusion of a scalar with a surface source (leftmost grouping of panels) and purely top-down diffusion of a scalar with no surface source or loss (rightmost grouping of panels). The quantities shown are the mean scalar concentration, C, the vertical flux of C ($\langle c'w' \rangle$ in the notation used in this paper but indicated with an overbar in the figure), the dimensionless gradient function, g_b or g_t [eq.(32)], and the dimensionless gradient diffusion coefficient, k_b or k_t .

$$\partial X_t/\partial z = -[\langle w'x' \rangle_i/(W_* z_i)]g_t(\xi) \qquad (32b)$$

where $g_b=0.4\xi^{-3/2}$ and $g_t=0.7(1-\xi)^{-2}$ represent the empirical bottom-up and top-down dimensionless mixed-layer gradient functions in the notation of Moeng and Wyngaard (1984). The dimensionless total gradient is expressed

$$-(z_i/X_*)\partial X/\partial z = g_b(\xi) + R_x g_t(\xi) \qquad (33)$$

where $X_*=\langle w'x' \rangle_o/W_*$ as before. These functions were determined from so-called large eddy simulations (LES) where tracers were numerically introduced to simulate purely top-down or bottom-up diffusion.

From eqs.(30) and (33) we can show that the dimensionless gradient diffusion coefficients are the ratio of the flux and gradient functions

[i.e., $(K_b/W_* z_i)=e_b/g_b$], which are shown in Fig. 11. Notice that in most of the ABL the bottom-up diffusion coefficient is about 2.5 times greater than the top-down coefficient (again, a manifestation of the skewed nature of convection). This approach permits the slightly positive potential temperature gradient often observed in the upper half of the ABL without demanding a negative diffusion coefficient.

Scalar Variance

Moeng and Wyngaard (1984) applied the top-down/bottom-up formalism to fluctuations of scalars in the ABL by expanding on the standard Reynolds decomposition of variables:

$$x = X + x' \tag{34a}$$

$$x' = x_b' + x_t' \tag{34b}$$

where X represents the mean and x' the total fluctuation which is due to the superposition of top-down and bottom-up components. The total variance of X is

$$\langle x'^2 \rangle = \langle x_b'^2 \rangle + \langle x_t'^2 \rangle + 2\langle x_b' x_t' \rangle \tag{35}$$

which can be represented as

$$\sigma_x^2/X_*^2 = f_b(\xi) + 2R_x f_{tb}(\xi) + R_x^2 f_t(\xi) \tag{36}$$

Structure Function Parameters

The results for the scalar variance can be applied to the structure function parameters (Fairall, 1987). This yields expressions of the form

$$C_x^2 z_i^{2/3}/X_*^2 = A_x h_b(\xi) + 2R_x h_{tb}(\xi) + R_x^2 h_t(\xi) \tag{37}$$

where $A_T=2.7$ and $A_q=1.9$. The present estimates for these empirical functions are

$$h_b = 3.7\, \xi^{-2/3} (z_i/(-L))^{2/3} (1-7\, z/L)^{-2/3} \tag{38a}$$

$$h_{tb} = 6\, \xi^{-1/12} \tag{38b}$$

$$h_t = 12\, \xi^{-1/12} (1-\xi)^{-3/2} \tag{38c}$$

with the dimensionless entrainment rates being

$$R_T = -0.2\, [1+3.2(-L/z_i)] \tag{39a}$$

$$R_q = (\Delta q/\Delta\theta)(\theta_*/Q_*) R_T \tag{39b}$$

Similarly, the cospectral structure function parameter, C_{Tq}, can be written in top-down/bottom-up form (see Fairall, 1987).

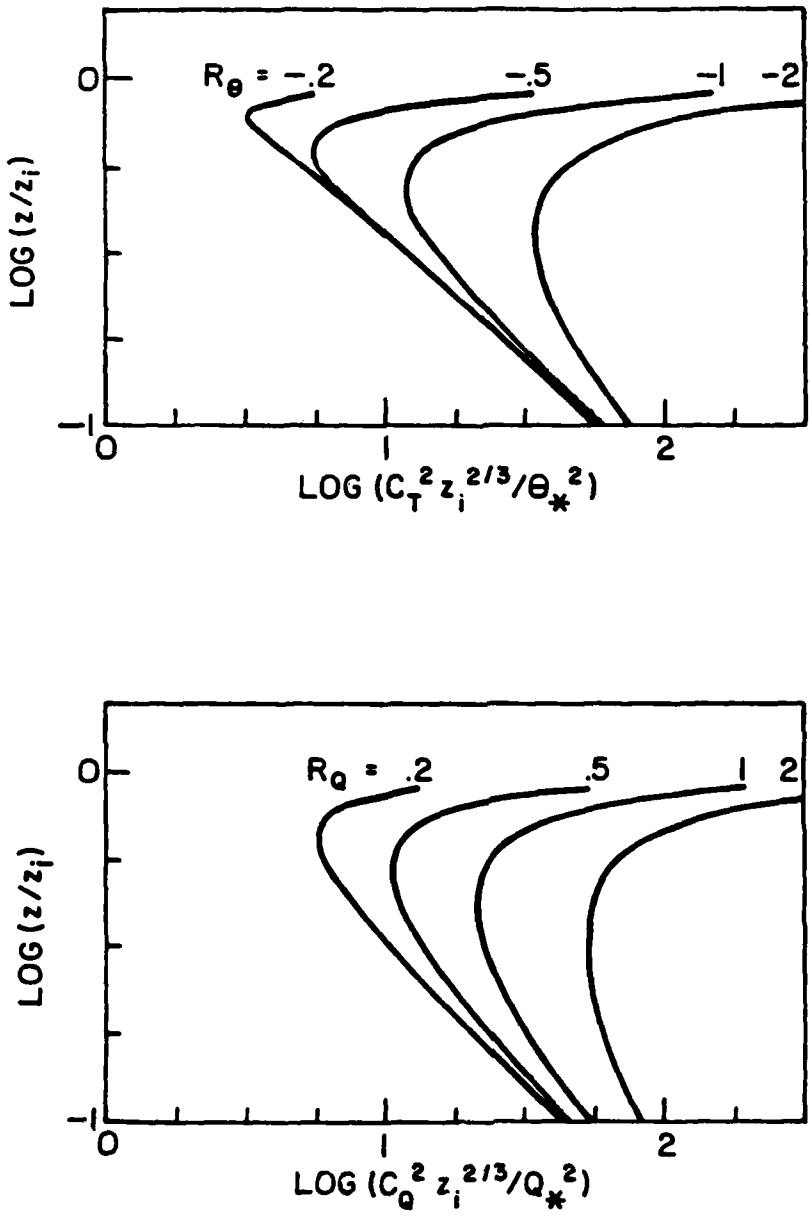

Fig. 12. Dimensionless scalar structure function parameters (temperature and humidity) based on a top-down/bottom-up diffusion model [eqs.(37)] for typical atmospheric values of the entrainment parameter, R_x.

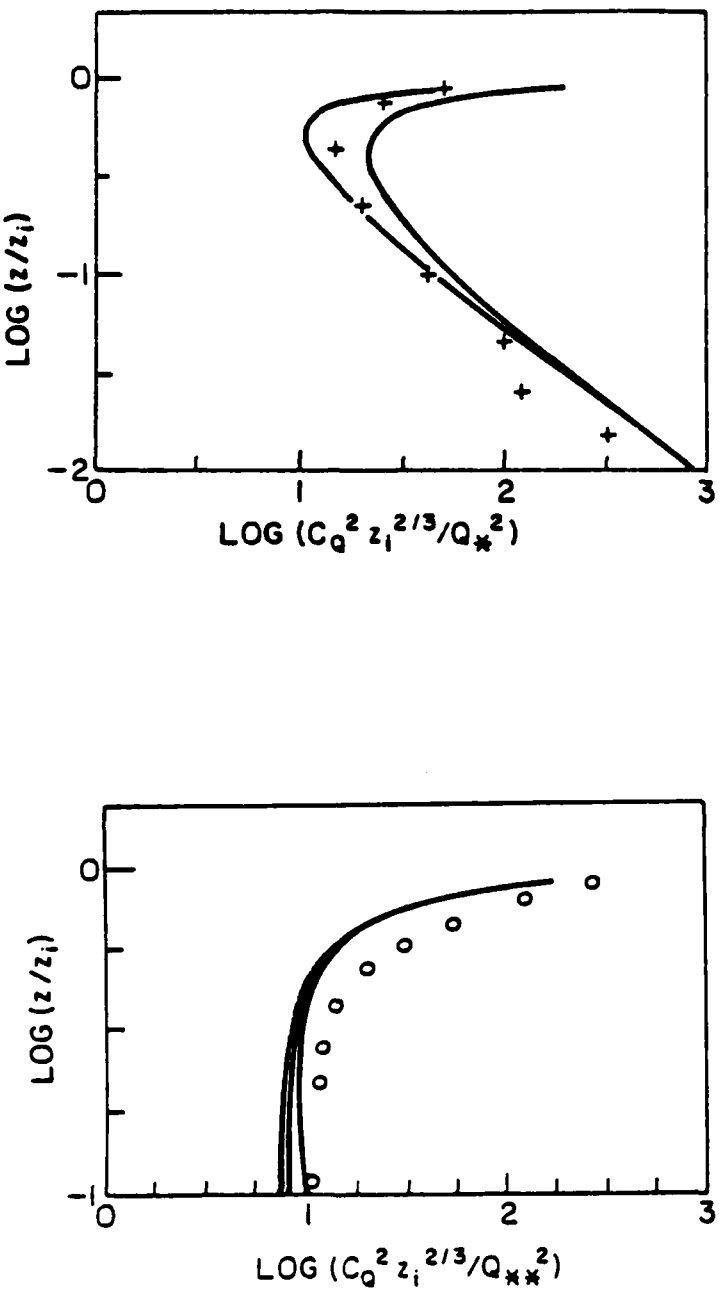

Fig. 13. Normalized profiles of humidity structure function parameter. In the upper panel, the crosses represent average atmospheric data from the AMTEX experiment (Wyngaard and LeMone, 1980). The solid lines are the top-down/bottom-up model equations for R_Q=0.5 and 1.0, values that are expected to bracket the AMTEX averages. In the lower panel, the open circles represent average aircraft measurements (Druilhet et al., 1983). The solid lines are from the model with R_Q=2, 5, 20, and 50. In this case, C_Q^2 is normalized by an inversion flux scaling parameter, $Q_{**}=R_Q Q_*$, because the surface flux was so small.

TKE Dissipation Rate

The top-down/bottom-up closure for ϵ has not been worked out to date, but the general form can be easily outlined. This is actually a bit risky because the momentum is not a passive, conservative scalar (although momentum is usually reasonably well-mixed). Another factor working against us in this regard is the conceptual difficulty involved in defining a tracer for velocity. We also do not, to date, have an analysis of LES information for velocity from the top-down and bottom-up point of view. At any rate, the dimensionless form of the TKE equation gives

$$\epsilon z_i / W_*^3 = M+B+T+P \qquad (40)$$

where the various terms are

Shear production: $M = -\langle u'w' \rangle \partial U/\partial z * z_i / W_*^3$

Buoyant production: $B = (g/T)\langle w'T' \rangle * z_i / W_*^3$

Turbulent transport: $T = -\partial(\langle w'e' \rangle)/\partial z * z_i / W_*^3$

Pressure transport: $P = -\partial(\langle w'p' \rangle/\rho)\partial z * z_i / W_*^3$

The dimensionless shear and buoyant terms are straightforwardly worked out in terms of existing functions,

$$M = u_*^4 / (W_*^4)[e_b g_b + R_u(e_b g_t + e_t g_b) + R_u^2 e_t g_t] \qquad (40a)$$

$$B = e_b + R_T e_t = 1 - \xi + R_T \xi \qquad (40b)$$

Notice that the shear term does not scale as the other terms but is multiplied by the factor

$$(u_*/W_*)^4 = (-L\kappa/z_i)^{4/3} \qquad (41)$$

The effect of surface shear on the dimensionless dissipation is given by the bottom-up term

$$M_b = 0.8(-L\kappa/z_i)^{4/3}(1-\xi)\xi^{-3/2} \qquad (42)$$

Without a detailed LES analysis, the turbulent and pressure terms can only be estimated from atmospheric measurements (which are of the top-down and bottom-up components combined) and educated guesses about their scaling forms.

CONCLUSION

The behavior of the classic microturbulence variables in the cloudfree, convective ABL are well described by scaling models based on using the interfacial fluxes (surface and inversion) to construct appropriate scaling parameters. This approach appears to be particularly successful for the small scale turbulence properties, which probably implies that the small scale diffusive processes are more locally determined and less subject to mesoscale modulation effects. If we think of Monin-Obukhov similarity as the near surface form of the bottom-up scaling, then the top-down and bottom-up scaling approach can account for the average behavior of the structure functions from the surface to within 10% of the top of the ABL. The implications of this success are not obvious, because of the restricted nature of the theory (cloudfree, convective, etc.). Certainly the scaling approach has been quite useful as a method of estimating surface fluxes (e.g., Fairall and Larsen). With the present trend toward the use of realtime processing combined with surface based remote sensors, the similarity models will be very useful when combined with clear-air radar or acoustic radar doppler systems where the backscatter is proportional to the scalar structure function parameters. In principle, this can result in 'intelligent' ABL profilers capable of producing not only mean velocity profiles but also estimates of surface fluxes, entrainment rates, optical properties, dispersion characteristics and short term forecasts of ABL evolution. With the continued growth in computing power, it may eventually be prudent to utilize much more complicated models (e.g., second order closure or LES)from the beginning. Even if this turns out to be true, the simple scaling models still provide a conceptual framework for thinking about the internal working of boundary layers.

ACKNOWLEDGMENTS

This work is supported by the Marine Meteorology section of the Office of Naval Research (contracts N00014-85-K-0250 and N00014-86-K-0688) and the Air Force Office of Scientific Research (contract AFOSR-86-0049). I am grateful to the Hawaii Institute of Geophysics and Department of Oceanography, University of Hawaii, for the invitation and the hospitality.

REFERENCES

Brost, R.A., J.C. Wyngaard and D.H. Lenschow, 1982: Marine stratocumulus layers. Part II: Turbulence budgets. J. Atmos. Sci. , 39 , 818-836.

Champagne, F.H., C.A. Friehe, J.C. LaRue and J.C. Wyngaard, 1977: Flux measurements, flux estimation techniques, and finescale turbulence measurements in the unstable surface layer over land. J. Atmos. Sci. , 34 , 515-530.

Deardorff, J.W., 1974: Three-dimensional numerical study of turbulence in an entraining mixed layer. Bound.-Layer Meteor. , 7 , 199-226.

Deardorff,J.W., 1980: Stratocumulus-capped mixed layers derived from a three-dimensional model. Bound.-Layer Meteor. , **18** , 495-527.

Deardorff, J.W. and G.E. Willis, 1982: Dependence of mixed-layer entrainment on shear stress and velocity jump. J. Fluid Mech. , **115** , 123-149.

Druilhet, A., J.P. Frangi, D. Guedalia, and J. Fontan, 1983: Experimental studies of the turbulence structure parameters of the convective boundary layer. J. Clim. Appl. Met. , **22** , 594-608.

Fairall, C.W., R. Markson, G.E. Schacher, and K.L. Davidson, 1980: An aircraft study of turbulence dissipation and temperature structure parameter in the unstable marine atmospheric boundary layer. Bound.-Layer Meteor. , **19** , 453-469.

Fairall, C.W., 1984: Wind shear enhancement of entrainment and refractive index structure parameter at the top of a turbulent mixed layer. J. Atmos. Sci. , **41** , 3472-3488.

Fairall, C.W. and S.E. Larsen, 1986. Inertial-dissipation methods and turbulent fluxes at the air-ocean interface. Bound.-Layer Meteor. , **34** , 287-301.

Fairall, C.W., 1987: A top-down and bottom-up diffusion model of C_T^2 and C_Q^2 in the entraining convective boundary layer. J. Atmos. Sci. , **44** , 1009-1017.

Kaimal, J.C., J.C. Wyngaard, D.A. Haugen, O.R. Cote, Y. Izumi, S.J. Caughey, and C.J. Readings, 1976: Turbulence structure in the convective boundary layer. J. Atmos. Sci. , **33** , 2152-2169.

Lenschow, D.H, 1973: Two examples of planetary boundary layer modification over the Great Lakes. J. Atmos. Sci. , **30** , 568-581.

Lenschow, D.H., J.C. Wyngaard, and W.T. Pennell, 1980: Mean-field and second-moment budgets in a baroclinic, convective boundary layer. J. Atmos. Sci. , **37** , 1313-1326.

Moeng, C.H., 1984: A large-eddy simulation model for the study of planetary boundary-layer turbulence. J. Atmos. Sci. , **41** , 2052-2062.

Moeng, C.H. and J.C. Wyngaard, 1984: Statistics of conservative scalars in the convective boundary layer. J. Atmos. Sci. , **41** , 3162-3169.

Nicholls, S., 1984: The dynamics of stratocumulus: aircraft observations and comparisons with a mixed layer model. Q.J.R. Meteorol. Soc. , **110** , 783-820.

Shay, T.J. and M.C. Gregg, 1984: Turbulence in an oceanic convective mixed layer. Nature , **310** , 282-285.

Willis, G.E. and J.W. Deardorff, 1974: A laboratory model of the unstable planetary boundary layer. J. Atmos. Sci. , **31** , 1297-1307.

Wyngaard, J.C., and O.R. Cote, 1971: The budgets of turbulent kinetic energy and temperature variances in the atmospheric surface layer. J. Atmos. Sci. , **28** , 190-201.

Wyngaard, J.C., Y. Izumi, and S.A. Collins, 1971: Behavior of the refractive index structure parameter near the ground. J. Opt. Soc. Amer. , **61** , 1646-1650.

Wyngaard, J.C., 1973: On surface-layer turbulence. Workshop on Micrometeorology , D.A. Haugen, Ed., Amer. Meteor. Soc., 101-149.

Wyngaard, J.C. and M.A. LeMone, 1980: Behavior of the refractive index structure parameter in the entraining convective boundary layer. J. Atmos. Sci. , **35** , 1573-1585.

Wyngaard, J.C. and R.A. Brost, 1984: Top-down and bottom-up diffusion of a scalar in the convective boundary layer. J. Atmos. Sci. , **41** , 102-112.

GLOBAL MIXED-LAYER NATURAL AND ANTHROPOGENIC FLUXES

Fred T. Mackenzie

Department of Oceanography and Hawaii Institute of Geophysics
University of Hawaii at Manoa, Honolulu, Hawaii 96822

ABSTRACT

The oceanic surface mixed layer is generally the initial reservoir for materials that enter the ocean from the land and atmosphere. In this paper a number of global biogeochemical cycles of dissolved constituents, gases and particulates are portrayed. Some brief comments are made concerning the role of the mixed layer in the cycling behavior in the ocean of the chemical species H, O, C, N, P, S, Ca, Si, and As, and of particulate materials. It is demonstrated that the open ocean mixed layer can undergo chemical changes induced by perturbations of processes and fluxes on land on a time scale of decades. These perturbations may result from natural causes or may be due to the industrial and agricultural activities of society.

INTRODUCTION

The purpose of this short contribution is to present some information on chemical fluxes across the air-sea interface, within the oceanic mixed layer, and to the abyssal realm. To accomplish this task, I take the methodological approach that portrays natural system material transport in terms of reservoirs (boxes), transfer paths, that is, processes and mechanisms of transport, and fluxes or rates of transfer. Simply, these types of models are called biogeochemical cycling models.

Obviously not all substances and their interactions with the mixed layer can be considered, but the cases presented are representative of a variety of situations. The biogeochemical cycles shown emphasize the various environments that the oceanic mixed layer interacts with, and the processes affecting the mixed layer. The cycles are derived primarily from publications of Mackenzie and co-authors (Garrels et al., 1973; Lantzy et al., 1979; Mackenzie et al., 1983; Lantzy and Mackenzie, 1987; Lerman et al., 1987). Reservoir and flux magnitudes are the interpretations of the authors; it should be emphasized that some of these magnitude estimates are the subject of considerable debate.

AD-A188 348 DYNAMICS OF THE OCEANIC SURFACE MIXED LAYER PROCEEDINGS 4/4
OF 'AHA HULIKO'A (U) HAWAII INST OF GEOPHYSICS
HONOLULU P MULLER ET AL 1987 N00014-87-G-0091

UNCLASSIFIED F/G 8/3 NL

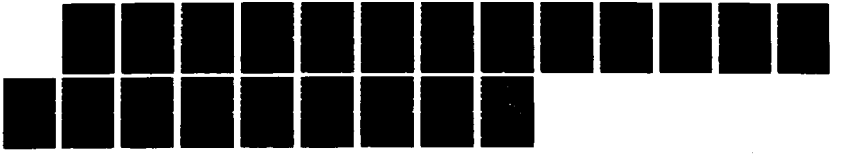

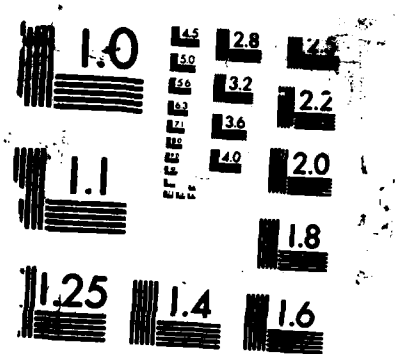

MICROCOPY RESOLUTION TEST CHART

METHODOLOGICAL APPROACH

Many natural chemical substances circulate through the environment and are important to the chemistry and biology of the earth. The circulation of a particular substance—as defined by its reservoirs, processes affecting it, and fluxes—is termed its biogeochemical cycle. Biogeochemical cycles vary in time and spatial scales. The long-term circulation of earth materials, the exogenic cycle, represents one extreme in which materials are transported through the atmosphere to the land and through the soils to streams that carry materials to the oceans. In the oceans, stream-borne solids, and some originally dissolved substances now part of solids, sink and become sea-floor sediments, and some substances are returned to the atmosphere. Oceanic residence times of dissolved substances vary from less than the mixing time of the ocean (1600 years) to 10^8 years. Reservoir sizes in the exogenic system can be huge; that of carbonate in sediments is 600×10^{20} grams.

On the other extreme are the biogeochemical cycles of substances in systems smaller than the global exogenic. In soils, rivers, and estuaries, for example, the circulation of a substance may be described in terms of reservoir sizes of less than tons and turnover times measured in days.

The concepts and principles related to modeling of biogeochemical cycles have been developed extensively elsewhere (e.g., Garrels and Mackenzie, 1971; Lerman et al., 1975; Mackenzie and Wollast, 1977; Holland, 1978; Lerman, 1979; Lasaga, 1981; Wollast, 1986). The mathematical treatment used is briefly discussed below with reference to Figure 1.

Figure 1 represents a system of three reservoirs with two-way fluxes between the reservoirs for substance i. For a closed system at steady state, the mass of substance i in each reservoir (M_i), and each flux of i (F_{ij}) between reservoirs are constant, and no material enters or departs the system; therefore

$$\sum_J F_{ij} = \sum_J F_{ji}. \qquad (i \neq j) \tag{1}$$

The fluxes are measured in units of mass time^{-1}, usually in terms of mols or grams year^{-1}, and commonly are taken as proportional to the reservoir mass from which the flux is emanating; that is

$$F_{ij} = k_{ij}M_i, \tag{2}$$

where k_{ij} is a rate constant with dimensions time^{-1} (usually year^{-1}). If a flux were second order, its magnitude is a function of both the mass of the source and receiving reservoirs,

$$F_{ij} = k_{ij}M_iM_j. \tag{3}$$

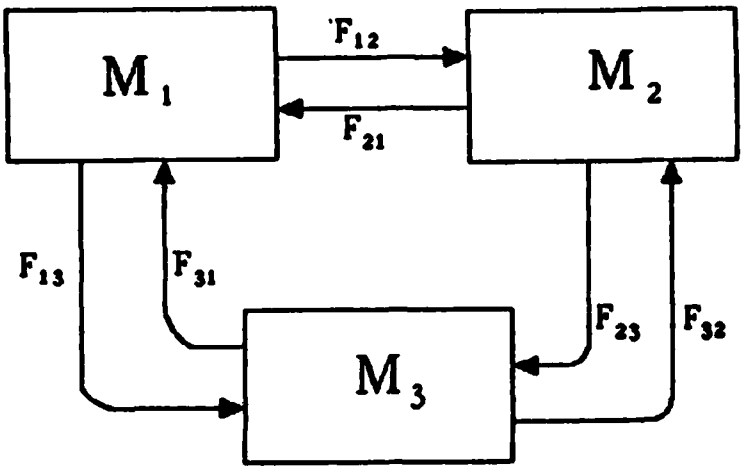

$$\frac{dM_1}{dt} = F_{21} - F_{31} - (F_{13} + F_{12})$$

$$= k_{21}M_2 + k_{31}M_3 - M_1(k_{12} + k_{13})$$

$$\frac{dM_2}{dt} = k_{12}M_1 + k_{32}M_3 - M_2(k_{21} + k_{23})$$

$$\frac{dM_3}{dt} = k_{13}M_1 + K_{23}M_2 - M_3(k_{31} + k_{32})$$

Figure 1. Schematic representation of a three-box model of the global biogeochemical cycle of substance i. M_i is mass of substance i in reservoirs 1, 2, and 3; F_{ij} are fluxes of i between reservoirs; and k_{ij} are rate constants.

The reciprocal of the rate constant k has been defined as the residence time, and for J fluxes of a substance i for a single reservoir with mass M_i.

$$\lambda_i = 1/k_{ij}. \tag{4}$$

From substitution of eq. (2) into eq. (1), we obtain

$$\sum_J k_{ij}M_j = M_i \sum_J k_{ij}. \qquad (i \neq j) \tag{5}$$

and at steady state

$$\sum_J k_{ji}M_j - M_i\sum_J k_{ij} = 0. \tag{6}$$

For a system in a transient state (one disturbed by a perturbation for example), the change of the mass of i in a reservoir with time is

$$dM_i/dt = \sum_j k_{ji} M_j - M_i \sum_j k_{ij}. \quad (7)$$

where $i \neq j$, and $i, j = 1 \ldots n$. This equation represents a series of n differential equations for a system with n number of reservoirs.

BIOGEOCHEMICAL CYCLES AND THE OCEANIC MIXED LAYER

In the following diagrams, the mixed layer of the global ocean is usually taken as the upper 100 m of the ocean. It is recognized that this definition is not necessarily in accord with that used by all oceanographers. The general conclusions drawn, however, are not affected significantly by the nature of the mixed layer, such as its changing depth with season in subtropical regions.

Oceanic Hydrologic Cycle

The oceanic hydrologic cycle is shown in Figure 2. In this figure the "mixed layer" is divided into nearshore and open-ocean environments, and fluxes of water are shown in units of 10^{16} l y^{-1}. In this model, residence times of H_2O in the nearshore and open-ocean mixed layer are about 11 and 17 years, respectively, whereas that of the deep ocean is 815 years. These residence times are consistent with a global upwelling rate of 4.5 m y^{-1}. The annual river input of H_2O to the nearshore realm represents the net imbalance between global oceanic evaporation and precipitation.

Chemical elements are transferred in the water cycle by currents and turbulence as dissolved species in the fluid, or as suspended particles carried by the fluid. If the concentration of an element in a flux involved in the hydrologic cycle is known, then its flux can be calculated as, e.g., concentration of element (g l^{-1}) x H_2O flux (l y^{-1}) = g y^{-1}. This type of calculation forms the basis for estimating many dissolved fluxes in the oceanic system.

Oceanic Terrigenous And Organic Carbon Cycles

Particulate materials in the oceanic mixed layer have two principal sources, exogenic and endogenic. Exogenic particulates are derived from the continents and transported to the ocean in the suspended and traction load of rivers, and enter the oceanic mixed layer as dust particles scavenged in oceanic rain or as dry deposition. Endogenic particulates are formed within the mixed layer primarily through biological processes that lead to the generation of inorganic skeletal and organic materials in organisms such as foraminifera, diatoms, pteropods, etc. Figure 3 illustrates the major fluxes associated with the transfer of terrigenous materials and organic matter represented by organic C in the ocean.

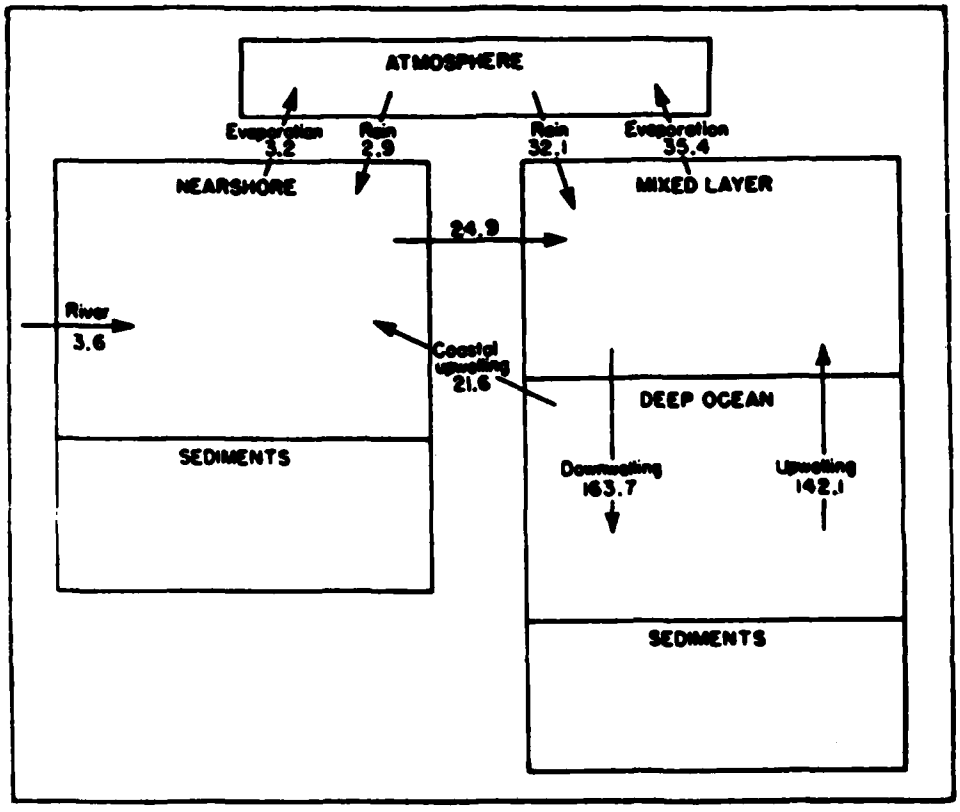

Figure 2. The oceanic hydrologic cycle. Fluxes are in units of 10^{16} l y^{-1}. Nearshore surface area and volume are 0.3×10^{14} m^2 and 0.3×10^{9} l, respectively. Mixed layer area and volume are 3.31×10^{14} m^2 and 3.31×10^{19} l.

The main flux of terrigenous materials to the oceanic mixed layer is via rivers. Most of this flux, 80-90%, is sedimented in the nearshore environment, but a small amount escapes to the deep ocean. Terrigenously derived dust particles settle on the surface ocean over most of its area. Both of these fluxes are not uniform over the ocean surface, and therefore the effect of these fluxes on the oceanic mixed layer is regional in nature. For example, the rivers of southeast Asia deliver 90% of the solids reaching the ocean annually. Dust storms originating in the Gobi and Saharan Deserts affect different regions of the oceans at different times because of the seasonality of these storms and the wind patterns transporting the dust. Once these terrigenous materials reach the mixed layer they may be chemically unreactive or they may adsorb or desorb chemical species.

In a portion of the mixed layer organic carbon is photosynthesized, and this reaction adds to the particulate burden of this region. These organic particles may be regenerated in the mixed layer by respiration-decay processes or pelletized and transported along with terrigenous

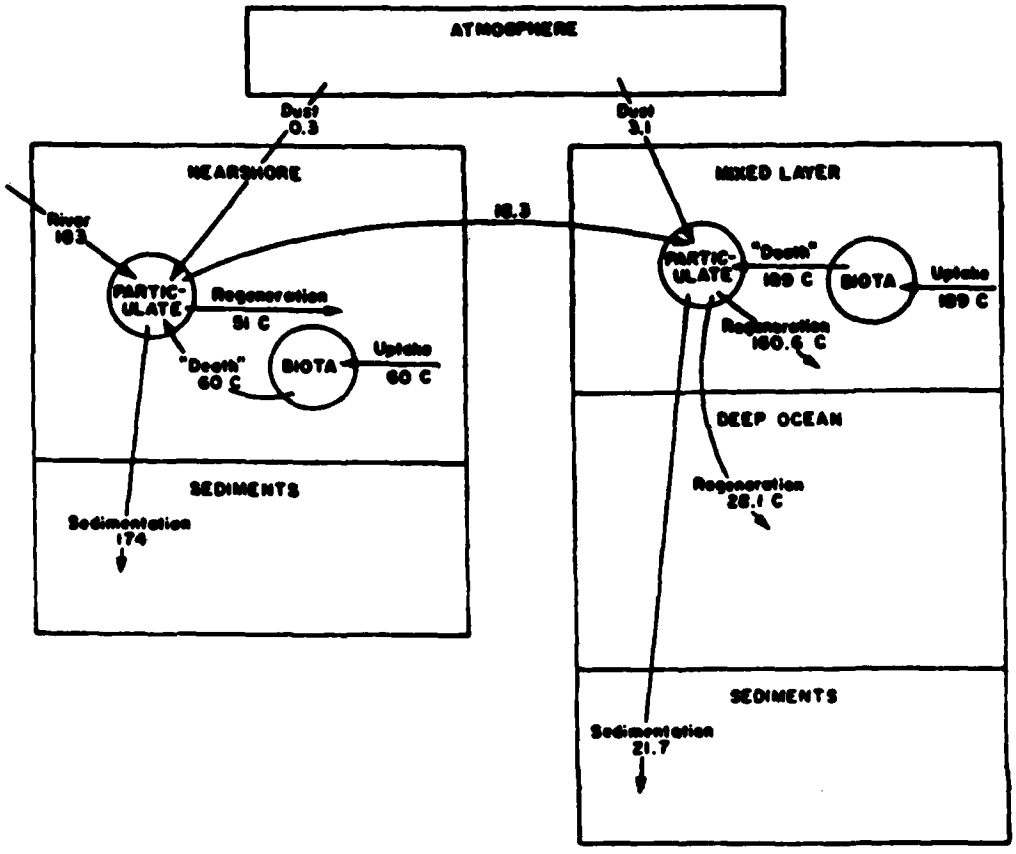

Figure 3. Oceanic terrigenous and organic carbon particulate cycles. Terrigenous fluxes are in units of 10^{14} g y^{-1}, and organic fluxes in units of 10^{14} g C y^{-1}. C refers to fluxes of organic carbon.

materials to the deep ocean. If the concentration of an element in terrigenous material reaching the ocean is known, its flux can be calculated as concentration of element (g g^{-1}) x terrigenous particulate flux (g y^{-1}).

In a similar way, if the organic C:element concentration ratio in marine biota is known then an approximation of the element flux can be made by multiplying the C/element x organic C flux. The important point is that the mixed layer, or part of it, is involved initially in the cycling of elements found in terrigenous materials and involved in the cycling of organic materials.

Ocean Skeletal Cycle

The cycling of skeletal $CaCO_3$ and SiO_2 in the nearshore and open ocean is shown in Figure 4. In the mixed layer $CaCO_3$ and SiO_2 are taken up in the tests and frustules of organisms. As shown for the open ocean mixed layer, these skeletal materials settle out of the mixed layer into

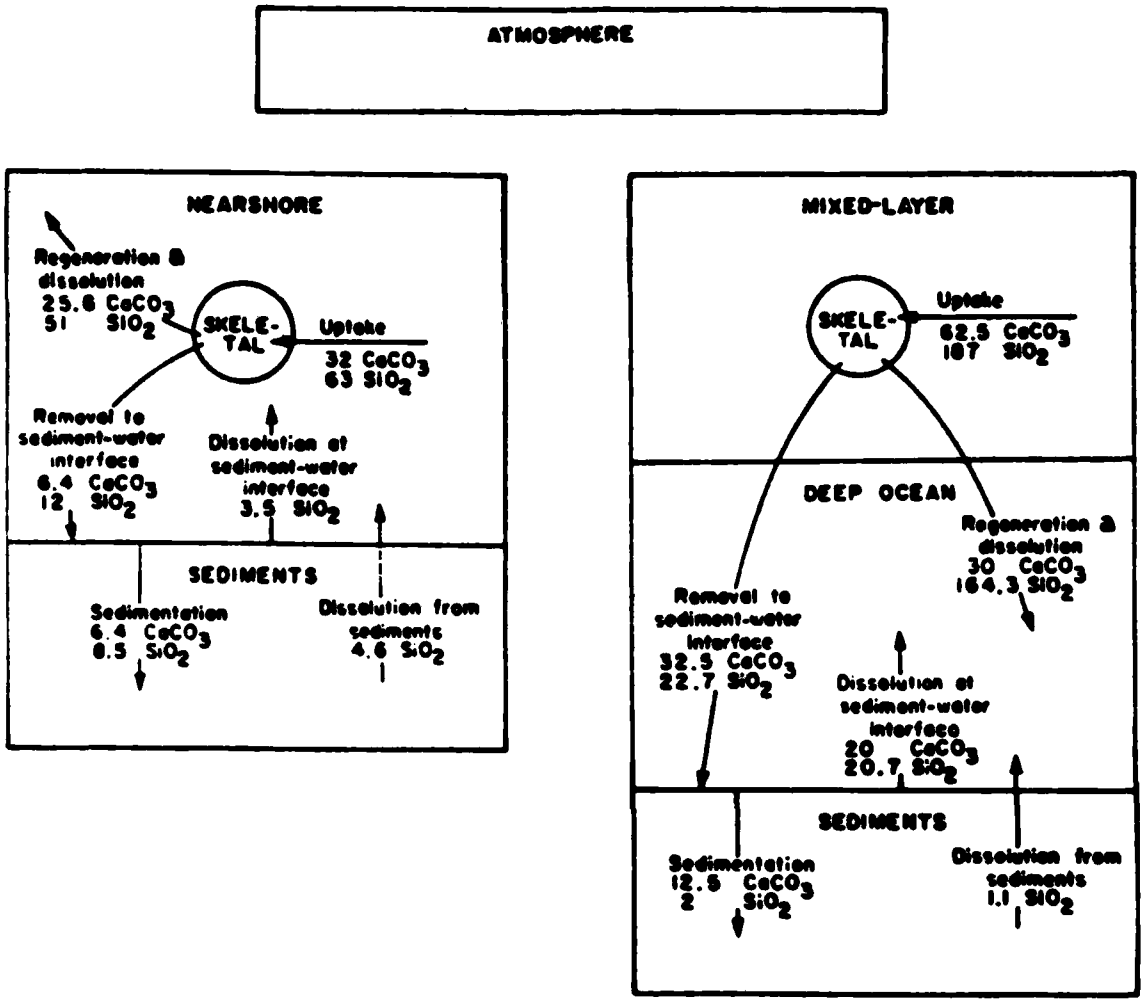

Figure 4. Oceanic cycle of skeletal $CaCO_3$ and SiO_2. Fluxes are in units of 10^{14} g y^{-1}.

the deep sea where they may dissolve en route to the bottom or at the sediment-water interface. Some $CaCO_3$ and SiO_2 accumulate in the sediments. The actual site of dissolution of the skeletons of pelagic organisms is very controversial today. Perhaps a significant portion of the skeletal SiO_2 actually is regenerated in the mixed layer and not the deep ocean. Much $CaCO_3$ may be dissolved at the sediment-water interface after deposition. As with organic matter, upwelling processes return dissolved constituents coming from dissolution of these components to the mixed layer.

C, N, P, S Global Biogeochemical Cycles

The global biogeochemical cycles of the elements that are critical to organic matter synthesis in the mixed layer—carbon, nitrogen, phosphorus

and sulfur—are shown in Figures 5-8. These are reasonably detailed representations of the global aspects of these cycles. Some fluxes between the oceanic reservoir and land via rivers and the atmosphere are emphasized below.

First some comments on organic production. Production in the mixed layer utilizes C derived principally from the atmosphere as CO_2, regenerated N as NH_4 or N biologically fixed from atmospheric N_2, or N transported via streams to the ocean principally as NO_3, regenerated P or phosphorus delivered to the ocean as PO_3 in streams, and sulfur introduced via the atmosphere and streams or regenerated in the ocean. In the global N cycle, the estimated magnitude of the regenerated oceanic N flux is shown as 320×10^{12} mol N y^{-1}. In the other cycles only the net global fluxes are portrayed. The generalized reaction for phytoplankton synthesis in the ocean is

$$106CO_2 + 16HNO_3 + H_3PO_4 + 138H_2O = (CH_2O)_{106}(NH_3)_{16}H_3PO_4 + 1220_2.$$

At this ratio of C:N:P, the regenerated C and P fluxes in the ocean would be about 2100×10^{12} and 20×10^{12} mol y^{-1} of C and P, respectively. Leakage of organic carbon out of the euphotic zone with its N, P, and S contents represents the flux that is now known as new production. This flux is probably on the scale of 0.1-1% of total production.

The mixed layer plays an important role in terms of inputs of chemicals to the global environment because of the industrial, agricultural, and other activities of society. Examples of these anthropogenic fluxes are shown in all four global cycles. For example, C, N, and S enter the atmosphere from fossil fuel burning. About 50% of the fossil fuel CO_2 flux dissolves in the ocean leading to an accumulation of C in the ocean reservoir. The initial environment of the ocean affected by this increased C flux is the mixed layer. The ability of the ocean to act as a sink of fossil fuel CO_2 depends on the rate of exchange of mixed layer waters with the deep ocean.

The nearshore mixed layer receives N and P fluxes from agricultural and industrial activities that lead to enhanced organic production in coastal waters. These fluxes are the principal cause of the eutrophication of some coastal marine waters.

Space does not permit further consideration of C, N, P, and S fluxes involving the oceanic mixed layer. Study of Figures 5-8 as an integrated whole can provide the reader with a more complete view of the interactions between the mixed layer and other environments in terms of element processes and fluxes.

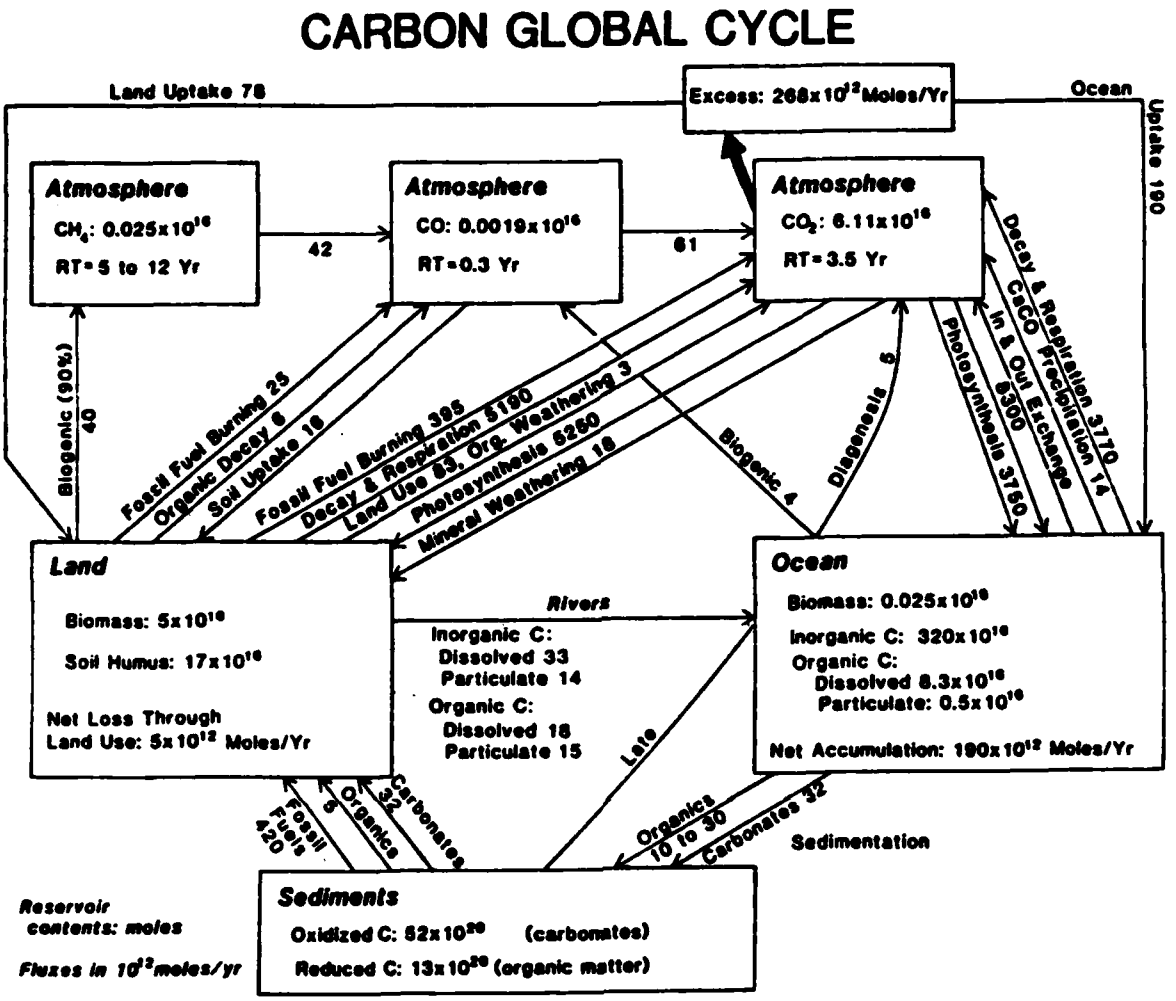

Figure 5. Global biogeochemical cycle of carbon. Reservoir masses are in units of mol C, and fluxes in units of 10^{12} mol C y^{-1}.

Carbon And Phosphorus Land-Mixed Layer Cycle

In Figures 9 and 10, detailed representations of the coupling between the global land and ocean biogeochemical cycles of C and P are shown. In both cycles the land and ocean reservoirs of Figures 5 and 7 have been subdivided into sub-reservoirs. The open ocean has been separated from the land by a coastal realm, and coastal waters and surface open ocean from the deep ocean. These representations of the C and P cycles are important to an understanding of element transfers from the land to the ocean and of the interactions between the coastal region and the open ocean.

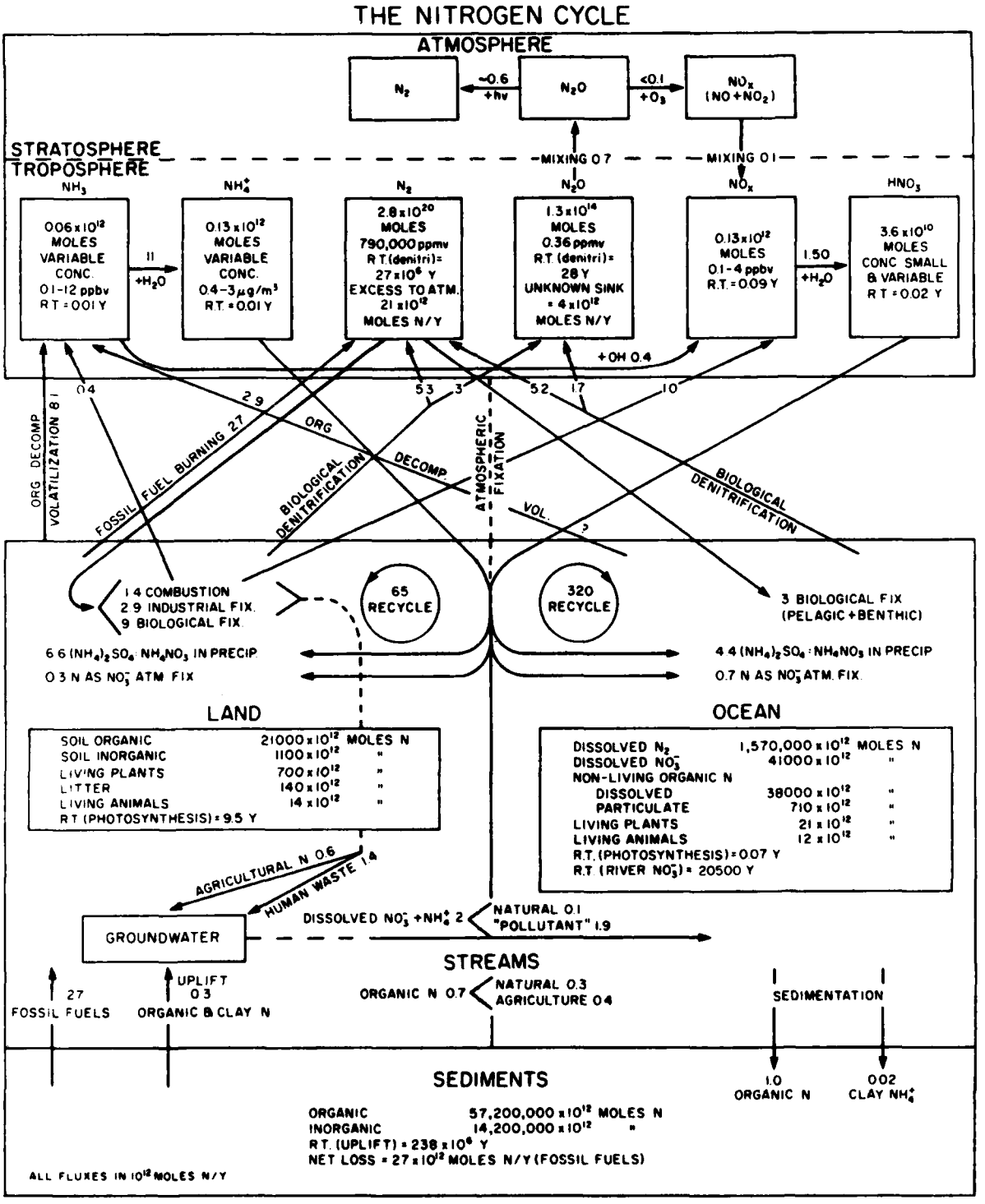

Figure 6. Global biogeochemical cycle of nitrogen. Fluxes are in units of 10^{12} mol N y^{-1}.

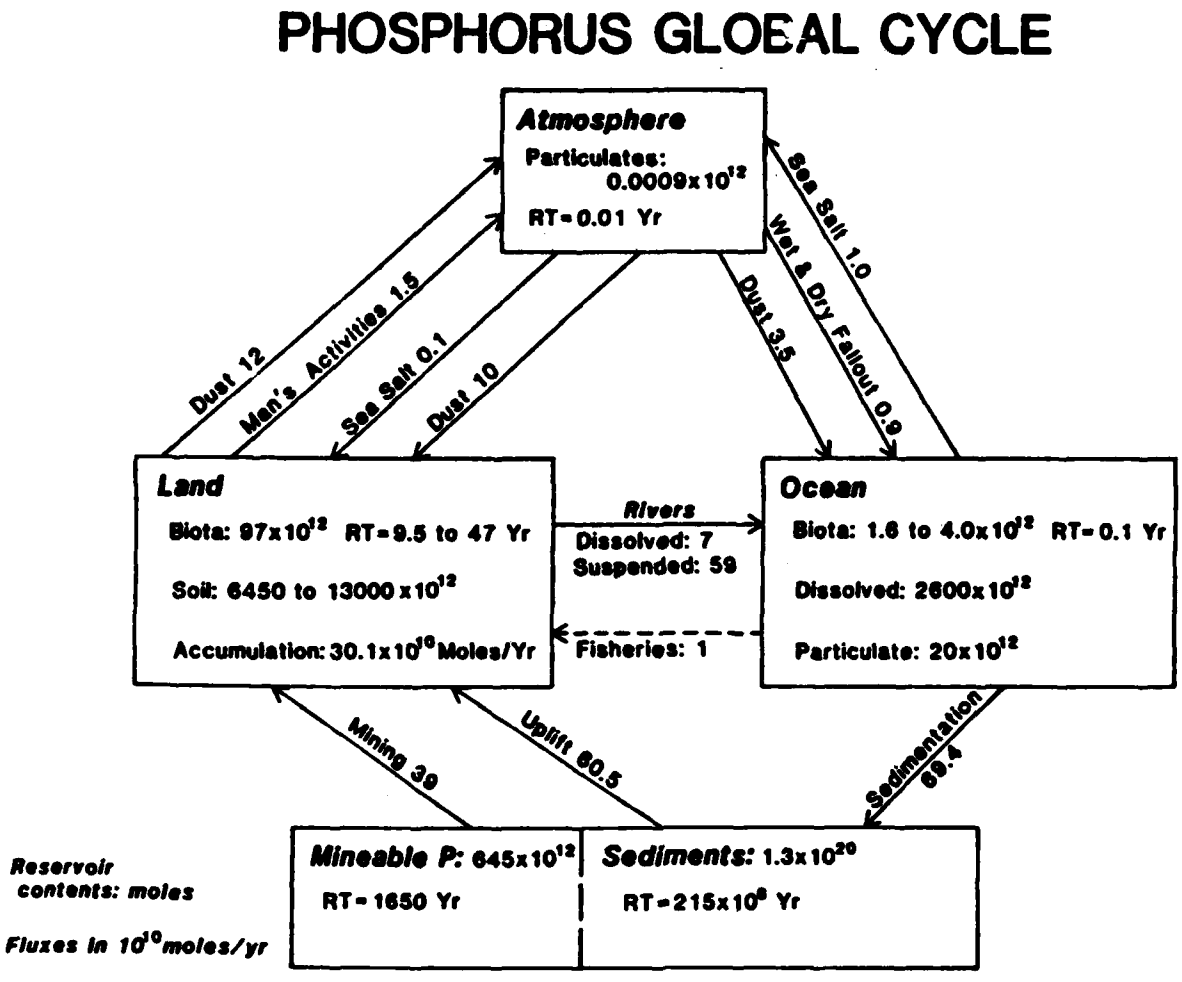

Figure 7. Global biogeochemical cycle of phosphorus. Reservoir masses are in units of mol P, and fluxes in units of 10^{10} mol P y^{-1}.

The C and P cycles portrayed are steady state cycles without anthropogenic fluxes. These cycles can be perturbed, and the results of a perturbation calculated using solutions of eq. (7). One of these perturbation scenarios is shown in Figure 11. This figure shows the changes with time in the masses of C and N in the major reservoirs affected, because of changes in weathering rate on land and terrestrial bioproductivity. In this model, the present continental weathering rate has been increased by 1.5 times today's rates given in Figures 9 and 10, and terrestrial productivity reduced by 25 percent.

It can be seen from Figure 11 that the coastal zone and the surface open ocean, plus other shallow-water reservoirs of C and P, gain these elements on a time scale of decades. The ultimate sources of these elements are the land reservoirs of humus and terrestrial biota. Notice that after the initial gain in C and P mass, the atmospheric C reservoir and several of

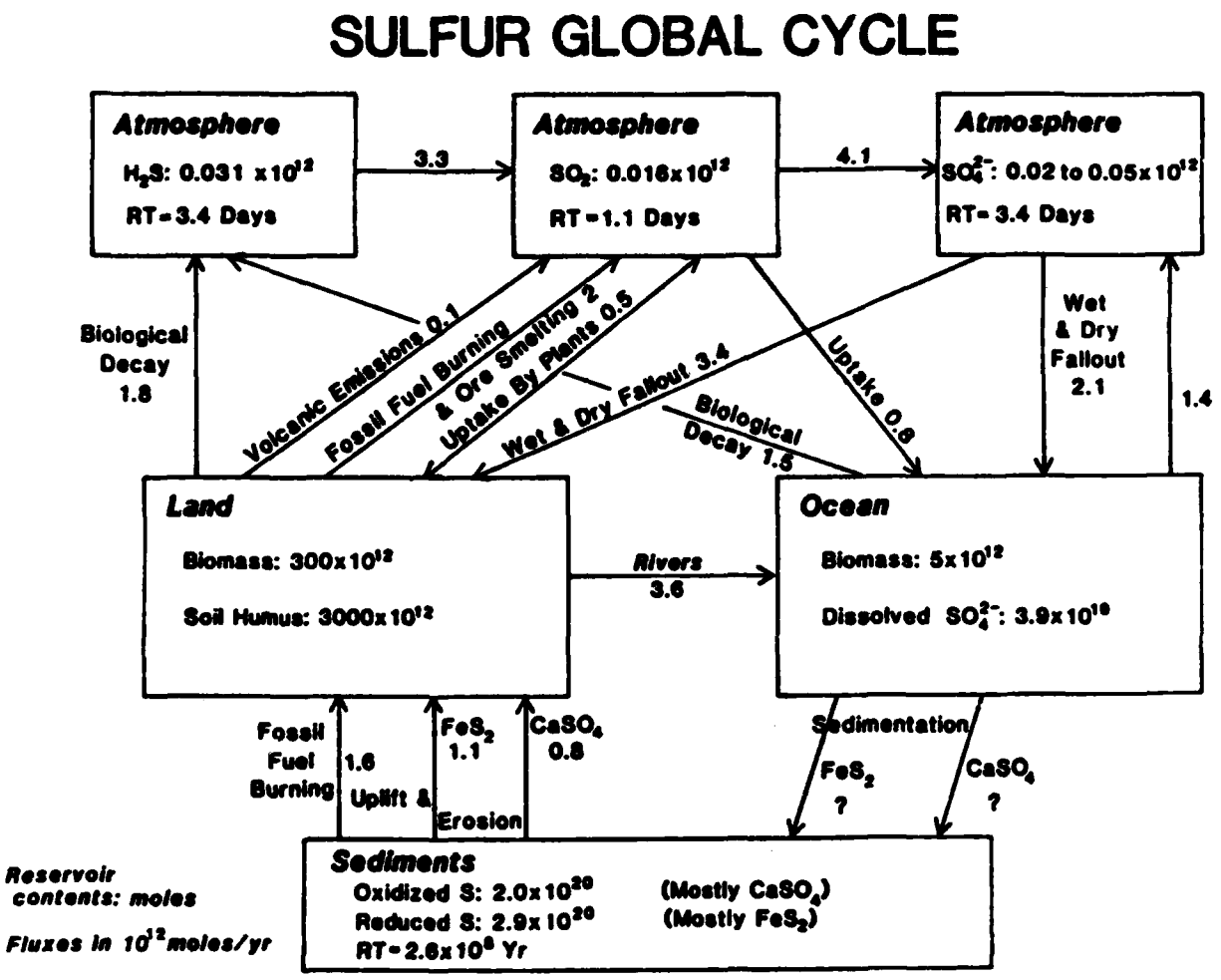

Figure 8. Global biogeochemical cycle of sulfur. Reservoir masses are in units of mol S, and fluxes in units of 10^{12} mol S y^{-1}.

the oceanic C and P reservoir masses decline. This result is due to transfer of these elements to other reservoirs—e.g., C as CO_2 from the atmosphere to the oceanic mixed layer, and C and P from coastal waters to the open ocean. The important point is that the chemistry of the mixed layer is affected on a time scale measured in decades both in the coastal and open ocean setting by changes on land.

This is not an unexpected result, but the modeling of these perturbations emphasizes how intimately connected the mixed layer is to other global reservoirs, and how quickly it may react to environmental changes even as far removed as those obtained on land. Considerations of global oceanic element fluxes must involve an assessment of the interactions between the mixed layer and the land via the coastal realm, as well as the atmosphere and deep ocean.

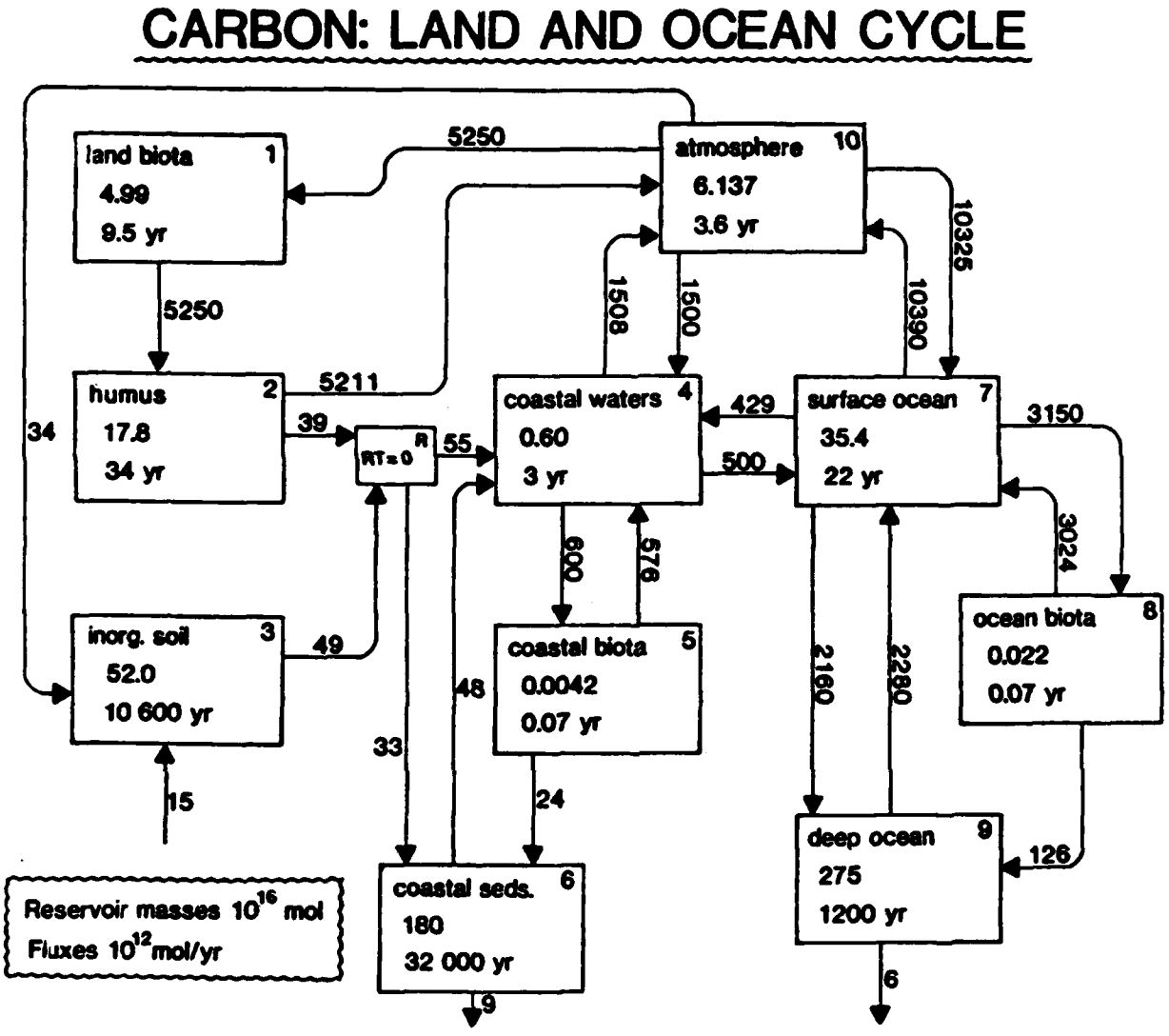

Figure 9. Global coupled land and ocean cycle of carbon. Reservoir masses are in units of 10^{16} mol C, and fluxes in units of 10^{12} mol C y^{-1}.

Global Oceanic Arsenic Biogeochemical Cycle

A detailed cycle of the oceanic arsenic cycle is portrayed in Figure 12. This cycle was selected as an example of a trace metal for which the mixed layer plays an important role in its cycling behavior. Arsenic is introduced into the mixed layer by rainfall, dust fallout, and river discharge. Arsenic is removed in the skeletal and organic components of marine biota. Terrigenous particulates may pass through the mixed layer without reaction or they may desorb arsenic.

Arsenic is an element that has been added to the environment by fossil fuel burning, mining, cement manufacturing, and ore smelting activities of

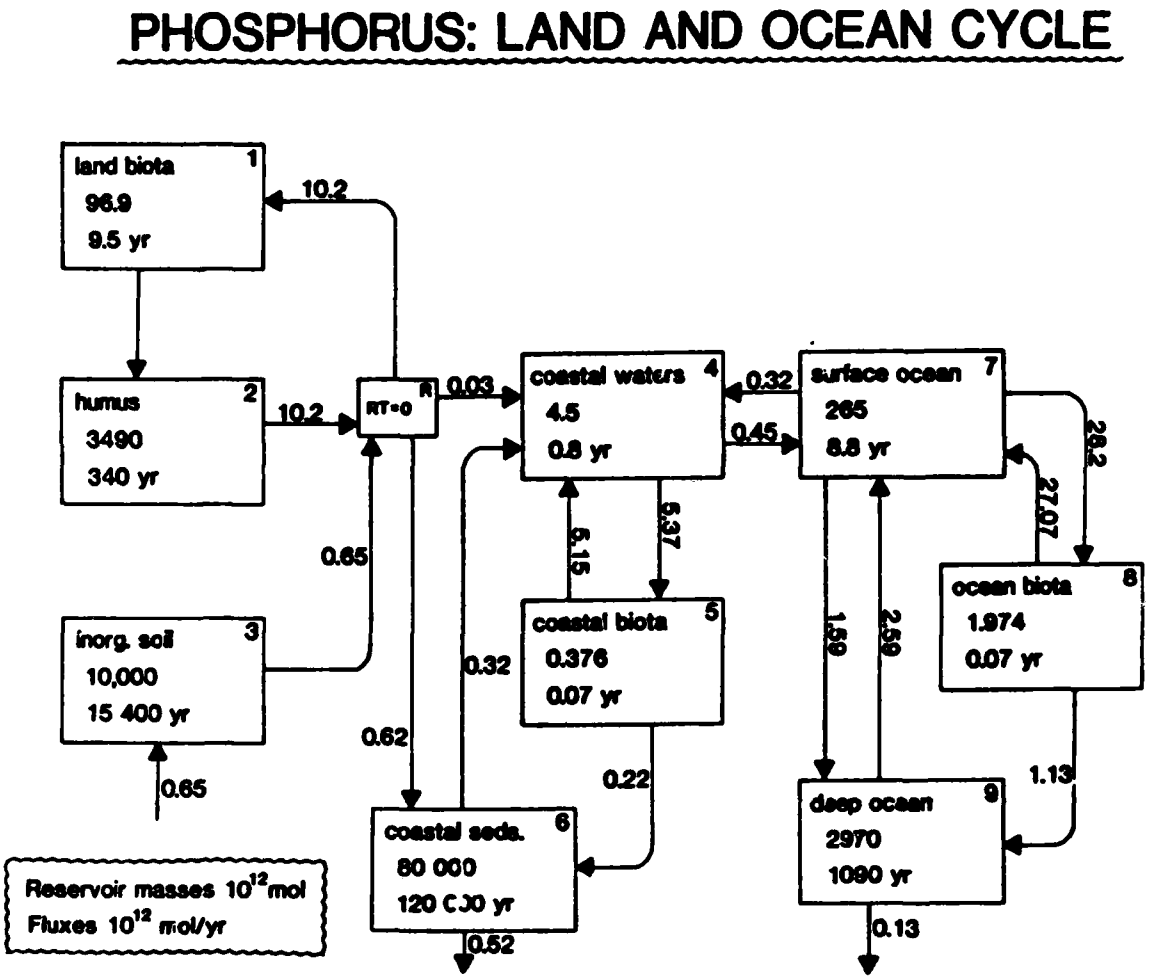

Figure 10. Global coupled land and ocean cycle of phosphorus. Reservoir masses are in units of 10^{12} mol P, and fluxes in units of 10^{12} mol P y^{-1}.

society. Figure 13 is a model calculation for a scenario in which these anthropogenic fluxes increase at a rate of 2% annually. The calculations are done assuming that the As fluxes change globally, and are consistent with projected growth rates in As utilization. Figure 14 shows the results of calculations demonstrating the importance of the rate of global upwelling to exchange of As between the mixed layer and deep ocean. Calculations of this nature provide some idea of the magnitude of compositional changes that might be anticipated in the mixed layer, and other reservoirs, because of society's use of trace metals.

CONCLUSIONS

The major purpose of this paper is to provide some idea of the myriad of chemical interactions between the oceanic mixed layer and other

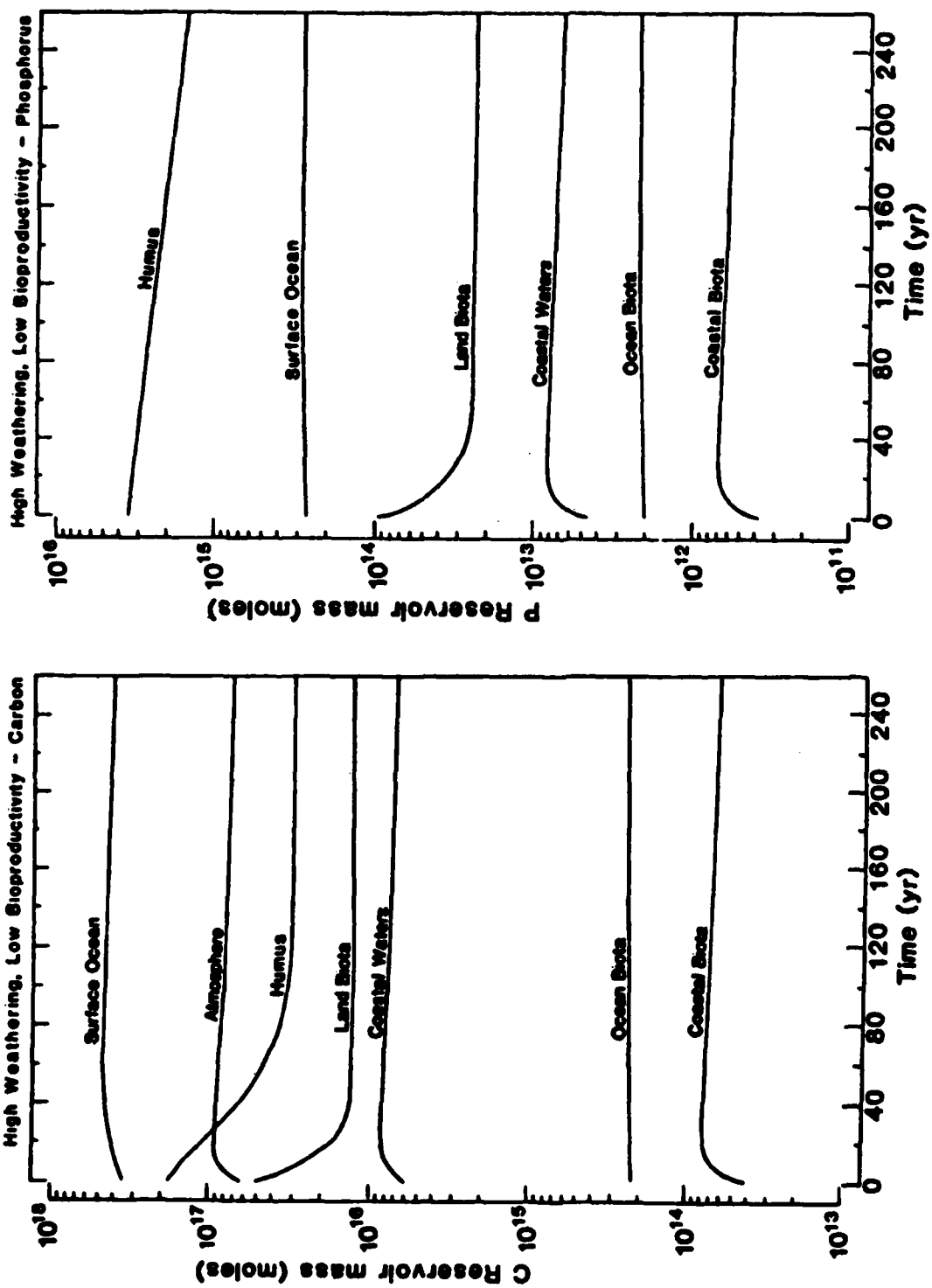

Figure 11. Changes in mass of carbon and phosphorus reservoirs of Figures 9 and 10, because of increased continental weathering and decreased terrigenous organic productivity.

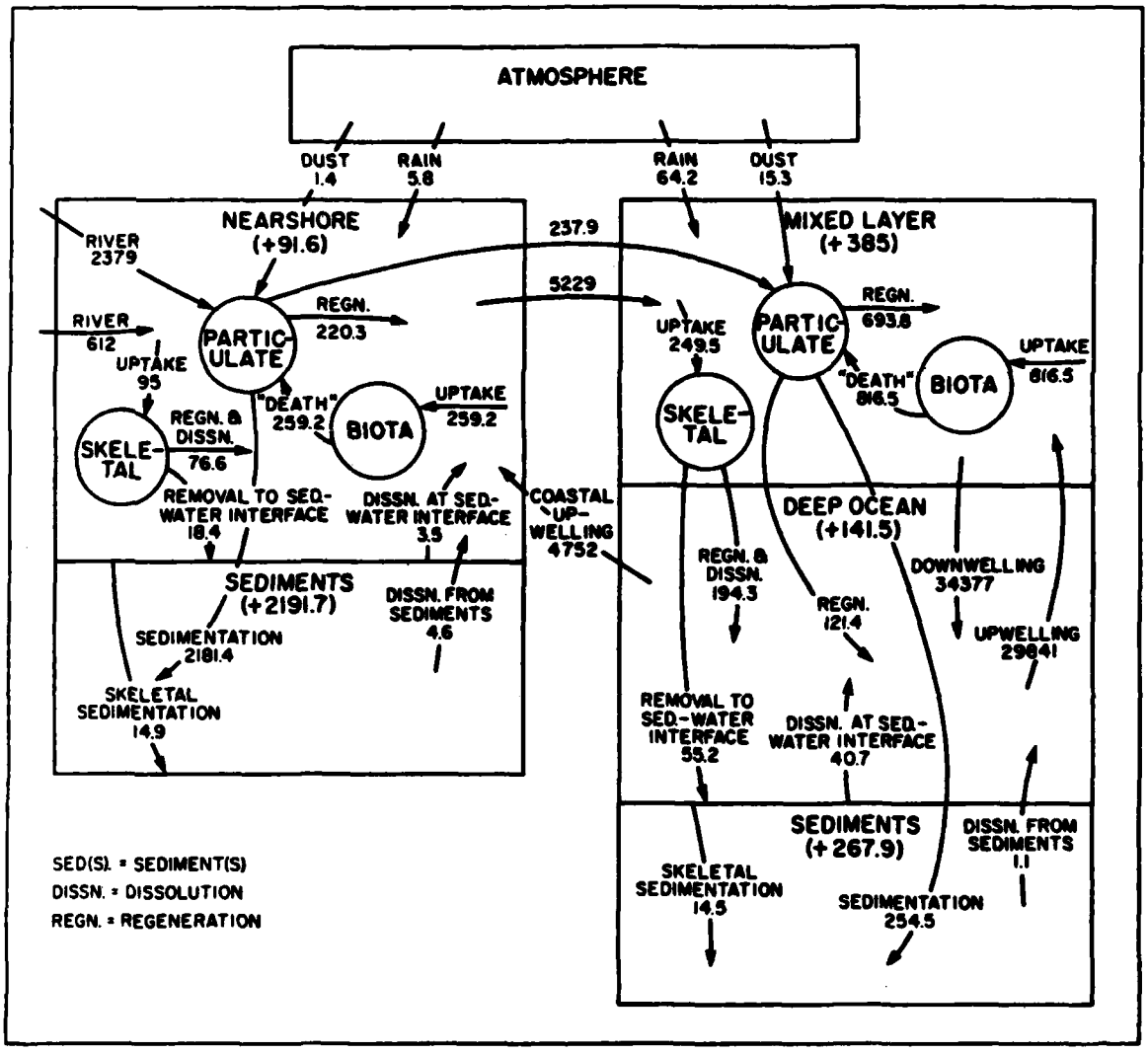

Figure 12. The oceanic biogeochemical cycle of arsenic. All fluxes and reservoir mass changes are in units of 10^8 As y^{-1}. Notice that the various As reservoirs are presumably gaining this element today, because of increased As fluxes from anthropogenic activities.

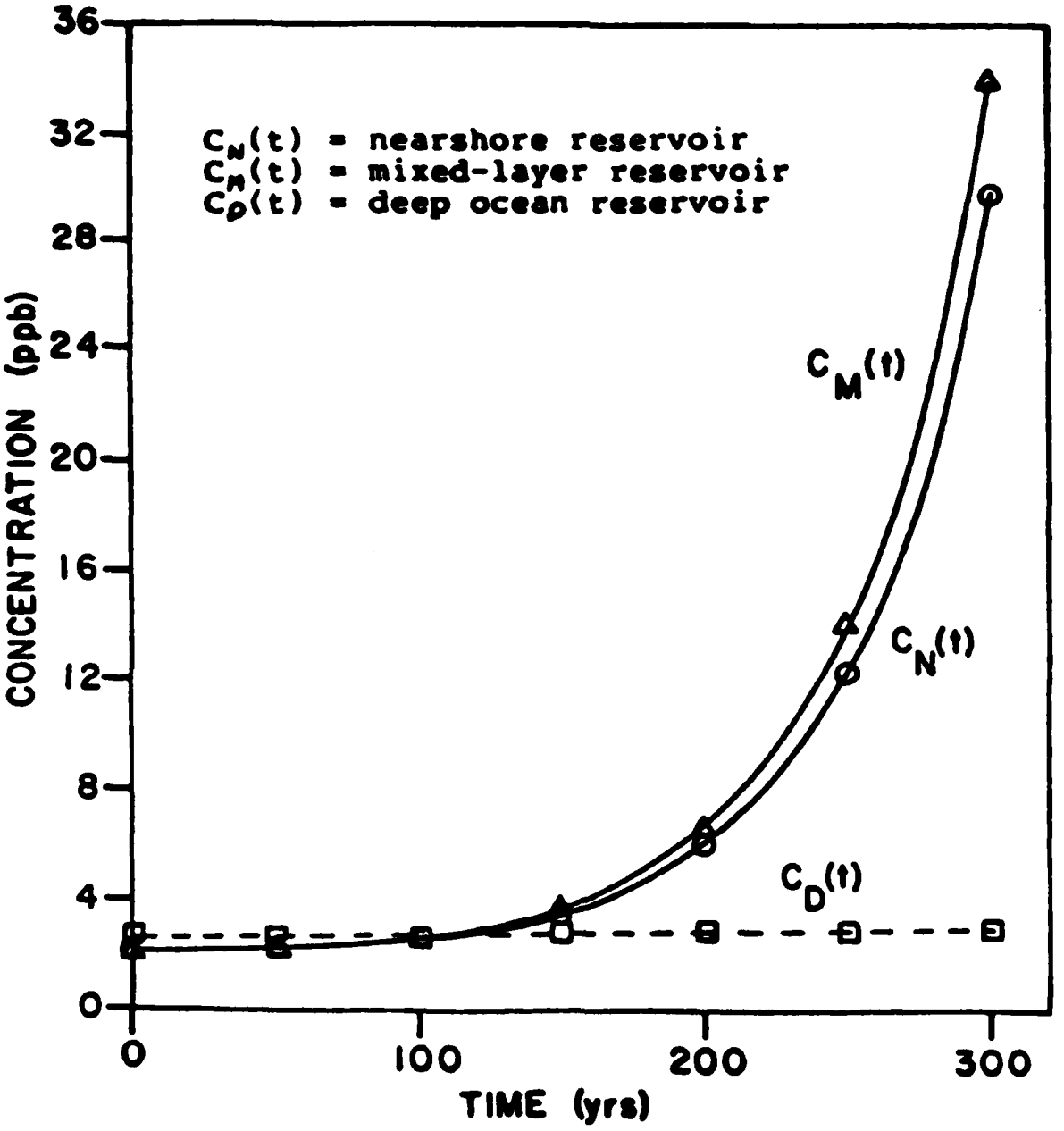

Figure 13. Changes in arsenic concentrations in the nearshore, mixed layer, and deep ocean reservoirs of Figure 12, calculated on the basis of a scenario in which As releases to the environment from society's use of this element increase exponentially at a rate of 2% annually.

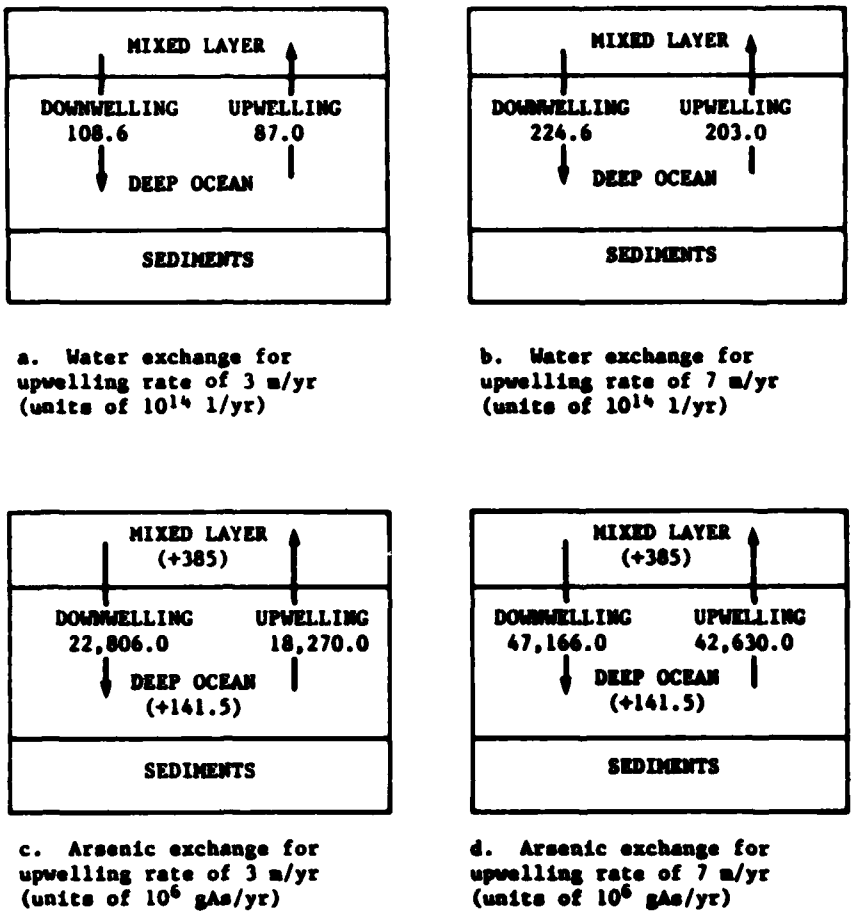

Figure 14. Effect of global upwelling rate on exchange of arsenic between the mixed layer and deep ocean. Fluxes in units of 10^{16} l H_2O y^{-1}, and 10^{8} g As y^{-1}.

environments, and within this important reservoir. The examples presented are only a sampling of the many processes that could be described. An attempt was made to present briefly a methodology employed by chemical oceanographers and geochemists for evaluation of mixed layer chemical changes based on modeling. The physical processes occurring in the mixed layer and responsible for exchange between this reservoir and others exert significant control on mixed layer chemistry, and the overall chemistry of the oceans. There is a strong need to understand these processes and fluxes associated with them before we can hope to answer quantitatively questions concerning global environmental problems, like those related to CO_2 and the greenhouse effect.

ACKNOWLEDGMENTS

This paper derived from an oral presentation given at the 'Aha Huliko'a Hawaiian Winter Workshop, University of Hawaii, January 14-16, 1987 entitled "Dynamics of the Oceanic Mixed Layer". I thank Peter Muller for the invitation to a geochemist to present his thoughts. This research was supported by ACS-PRF, Grant No. 17371-AC2. Hawaii Institute of Geophysics Contribution No. 1875.

REFERENCES

Garrels, R.M., and F.T. Mackenzie, 1971. Evolution of Sedimentary Rocks. W. W. Norton and Co., N. Y., 397 pp.

Garrels, R.M., F.T. Mackenzie, and C. Hunt, 1973. Chemical Cycles and the Global Environment: Assessing Man's Influence. W. Kaufmann, Inc., Los Angeles, 206 pp.

Holland, H.D., 1978. The Chemistry of the Atmosphere and Oceans. John Wiley and Sons, N.Y., 351 pp.

Lantzy, R., and F.T. . Mackenzie, 1987, Oceanic biogeochemical cycle of arsenic. In Scope Metals Cycling Workshop, T.C. Hutchinson, ed., John Wiley and Sons, N.Y. (in press)

Lantzy, R., F.T. Mackenzie, and V. Paterson, 1979. Global trace metal cycles and predictions. Mathematical Geology, 11, 99-140.

Lasaga, A.C., 1981. Dynamic treatment of geochemical cycles. In Kinetics of Geochemical Processes. A.C. Lasaga and R.J. Kirkpatrick, eds., Mineral Soc. America, Reviews in Mineral., 9, 69-110.

Lerman, A., 1979. Geochemical Processes, Water and Sediment Environments. John Wiley and Sons, N.Y., 436 pp.

Lerman, A., R.M. Garrels, and F.T. Mackenzie, 1975. Modeling of geochemical cycles: Phosphorus as an example. In Quantitative Studies in the Geological Sciences, E.H.T. Whittenden, ed., Geol. Soc. America Memoir 142, Boulder, 205-218.

Lerman, A., F.T. Mackenzie, and R.G. Geiger, 1987. Environmental chemical stress effects in carbon and phosphorus cycles. In Ecotoxicology, S.A. Levin, ed. (in press).

Mackenzie, F.T., and R. Wollast, 1977. Sedimentary cycling models of global processes. In The Sea, 6, E.D. Goldberg et al., eds., John Wiley and Sons, N.Y., 739-785.

Mackenzie, F.T., W.D. Bischoff, and V. Paterson, 1983. Biogeochemical cycles and trends in estimates of inputs of anthropogenic chemical

constituents to the environment. Ecosystem Research Center Public, 027, Cornell Univ., 57 pp.

Wollast, R., 1986. Basic concepts in geochemical modeling. In The Role of Air-Sea Exchange in Geochemical Cycling, P. Buat-Menard, ed., D. Reidel Publishing Co., 1-34.

unclassified

SECURITY CLASSIFICATION OF THIS PAGE (When Data Entered)

REPORT DOCUMENTATION PAGE	READ INSTRUCTIONS BEFORE COMPLETING FORM
1. REPORT NUMBER	2. GOVT ACCESSION NO. ADA188348 / 3. RECIPIENT'S CATALOG NUMBER
4. TITLE (and Subtitle) Dynamics of the Oceanic Surface Mixed Layer	5. TYPE OF REPORT & PERIOD COVERED
	6. PERFORMING ORG. REPORT NUMBER
7. AUTHOR(s) Peter Muller, Diane Henderson (eds.)	8. CONTRACT OR GRANT NUMBER(s) N-00014-87-G-0091
9. PERFORMING ORGANIZATION NAME AND ADDRESS Hawaii Institute of Geophysics 2525 Correa Road Honolulu, HI 96822	10. PROGRAM ELEMENT, PROJECT, TASK AREA & WORK UNIT NUMBERS
11. CONTROLLING OFFICE NAME AND ADDRESS Office of Naval Research	12. REPORT DATE 1987
	13. NUMBER OF PAGES
14. MONITORING AGENCY NAME & ADDRESS(if different from Controlling Office) Office of Naval Research Department of the Navy 800 N. Quincy St. Arlington, VA 22217	15. SECURITY CLASS. (of this report) unclassified
	15a. DECLASSIFICATION/DOWNGRADING SCHEDULE

16. DISTRIBUTION STATEMENT (of this Report)

Approved for public release; distribution unlimited

17. DISTRIBUTION STATEMENT (of the abstract entered in Block 20, if different from Report)

18. SUPPLEMENTARY NOTES

Proceedings, 'Aha Huliko'a, Hawaiian Winter Workshop, January 1987, Honolulu, Hawaii

19. KEY WORDS (Continue on reverse side if necessary and identify by block number)

mixed layer, mixing layer, turbulent boundary layer, convective layer, turbulence, Langmuir circulation, inertial motions, surface gravity waves, seasonal thermocline, fronts, subduction, similarity theories.

20. ABSTRACT (Continue on reverse side if necessary and identify by block number)

These proceedings contain the lectures given at the fourth 'Aha Huliko'a Hawaiian Winter Workshop on "Dynamics of the Oceanic Surface Mixed Layer." The lectures cover the major aspects of the state of the art and of the plans for future research concerning observation, theory, modeling, and monitoring of the oceanic surface mixed layer.

DD FORM 1 JAN 73 1473 EDITION OF 1 NOV 65 IS OBSOLETE S/N 0102-014-6601

unclassified

SECURITY CLASSIFICATION OF THIS PAGE (When Data Entered)

END

DATE

FILMED

3-88

DTIC